Revisiting Inverse Spinels: Structure, Electrochemical Properties and Li-ion Diffusion Mechanisms in $Li_{2+x}Ni_{2-2x}Cr_xV_2O_8$ ($0 \leq x \leq 1$)

Daniel Ziggy Chadney Martin

Thesis

Submitted for the degree of Doctor of Philosophy

Supervisors: Dr Nik Reeves-McLaren

Dr Rebecca Boston

September 2021

Department of Materials Science and Engineering

The University of Sheffield

Acknowledgements

This thesis is dedicated to my father, I miss you dearly. I hope I have made you proud.

I would firstly wish to express my gratitude to my supervisors, Dr Nik Reeves-McLaren and Dr Rebecca Boston for their guidance and support throughout my PhD. To Nik, I still remember when you pitched the PhD project by saying that we both won't know what we're doing, hopefully we've learnt a thing or two along the way. Thank you for enabling me to participate on the many beamtime experiments over the years and especially the ISIS neutron and muon training schools.

Secondly, I would like to thank all the current and former members of the L-floor labs who have helped me along this journey. In particular, thank you to Prof. Anthony R. West and his group for their helpful discussions throughout. I am deeply grateful to Dr Karen Johnston and Dr Abby Haworth for accommodating me during my visit to Durham University. I hope we can continue to work together in the future.

My sincere gratitude to the instrumental scientists, Dr Ron Smith, Dr Peter Baker, Dr Maria Diaz-Lopez and Dr Veronica Celorrio, much of this work would not be possible without their guidance and assistance during the several beamtime experiments.

Furthermore, I would like to thank the "Sheffield boys", notably Chris, Jack and Rich. My experience and love of Sheffield would not be the same without them.

Thank you to my mother and two sisters, Anesa and Zara. I would not be the person I am without their love, support and understanding.

Finally, I am especially grateful to Kate for her love and support throughout these challenging few years. You will forever and always be my greatest discovery during my PhD journey. I look forward to our next adventures together.

Contents

Abstract

Materials based on the normal spinel structure have attracted significant interest due to the wide number of elements that can be incorporated and the interesting electrical properties which they display. This, as well as the open three-dimensional framework that they contain, has led to the successful commercialisation of several Li-based spinel materials *e.g.* $LiMn_2O_4$ and $Li_4Ti_5O_{12}$ in Li-ion batteries. Materials based on the inverse spinel structure have also been investigated. However, their continued development and optimisation has been restricted by the lack of a complete understanding of how Li-ions diffuse through such materials.

This thesis explores the synthesis, structural and electrical characterisation as well as the electrochemical properties of a series of novel inverse spinels with the formula $Li_{2+x}Ni_{2-2x}Cr_xV_2O_8$ ($0 \leq x \leq 1$) for potential Li-ion battery applications. In Chapter 1, an introduction to the theory that underpins battery materials is outlined. Chapter 2 details a comprehensive review of the literature to date regarding spinel structures, as well as other common structure types of interest for Li-ion battery applications. Chapter 3 reports the experimental methods utilised within this work, including synthesis and characterisation techniques. The synthesis of $Li_{2+x}Ni_{2-2x}Cr_xV_2O_8$ ($0 \leq x \leq 1$) via solid-state and citric acid sol-gel routes is investigated in Chapter 4. In analysis of combined X-ray and neutron powder diffraction refinements, the materials adopt an inverse spinel structure with no evidence of cation ordering on octahedral sites. Meanwhile, impedance measurements indicate that the total conductivity increases with increasing Li/Cr content. The determined activation energies are found to be comparable to those in normal spinels. In Chapter 5, the Li-ion diffusion is determined to be via a $16c$-$8a$-$16c$ pathway using variable-temperature neutron powder diffraction measurements. Alongside this, muon spectroscopy is used as a complementary technique to probe the local Li-ion diffusion kinetics. The electrochemical properties of the solid solution as potential cathode and anode materials are investigated in Chapter 6 using galvanostatic cycling and in-situ cycling XANES. The cathodic performance is shown to be limited due to the irreversible capacity loss caused by oxidation of Cr^{3+} to Cr^{6+}. The anodic performance, however, shows promising capacity retention after 30 cycles for samples excluding Ni. Finally, the main findings of this work, as well as potential future avenues, are summarised in Chapter 7.

Chapter 1: Introduction

1.1.   Introduction

Lithium-ion batteries (LiBs) have become prevalent within society since they were first commercialised by Sony in 1991 due to the growth of consumer electronics such as laptops and mobile phones. In recent years the demand for LiBs has increased significantly due to the shift away from fossil fuels towards greener alternatives such as wind and solar energy. Emerging markets *e.g.* electric vehicles are expected to rapidly dominate the market for LiB technologies and as of 2019 make up 60 % of the LiB market (Figure 1.1).[1], [2] This is despite electric vehicles accounting for just 1 % of automotive sales in 2019. New initiatives to tackle climate change, such as the UK's target to become carbon neutral by 2050 and the ban on new petrol and diesel cars from 2030, will mean the global market for LiBs could exceed €200 billion per year by 2040.[3]

Because of the wide variety of applications that LiBs are expected to fill, different LiB technologies will be desired *e.g.* for long-range electric vehicles, LiBs which have high energy densities are required, whereas for mass transit applications, faster charging speeds may be more desirable. These differing requirements mean a range of materials with varying properties are necessary. As such, the properties of potential LiB materials needs to be fully understood at different length-scales if they are to be further optimised.
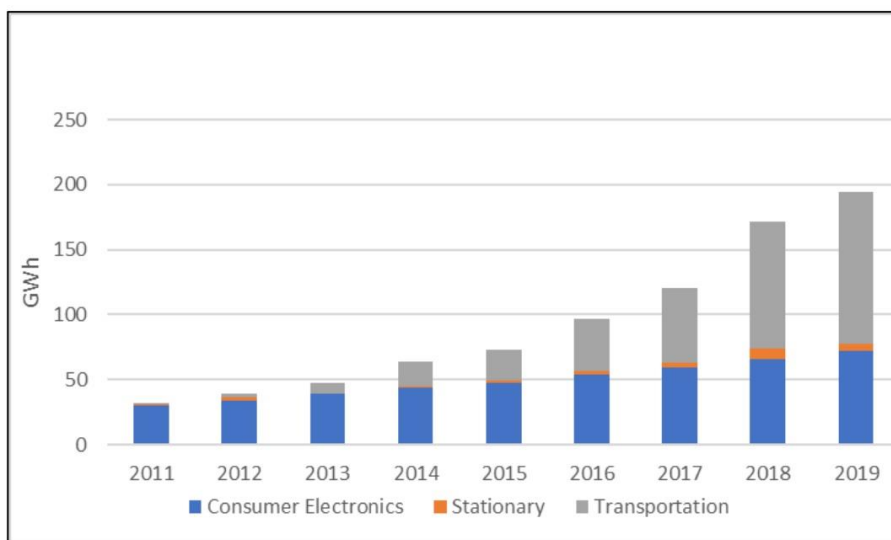
Figure 1.1. Global market for LiB technologies between 2011 to 2019.[2]

1.2. Batteries

Batteries are devices containing one or more electrochemical cell that converts stored chemical energy into electricity. When connected to a circuit, electrochemical cells can utilise redox reactions to generate electrical energy. Each cell is comprised of three main components, the anode, cathode, and electrolyte. The two electrodes (anode and cathode), have differing electrode potentials, defined as the oxidising, or reducing strength of the electrode. The anode acts as a source of electrons (reducing agent) and the cathode as a sink of electrons (oxidising agent). During discharge, ions move from the anode (the more negative potential), through the electrolyte, to the cathode (the more positive potential). The electrolyte separates the two electrodes and is electronically insulating therefore, electrons must flow through an external circuit providing electrical energy and then recombining at the cathode to maintain charge neutrality. The overall cell potential or open-circuit voltage (V_{oc}) is the difference between the electrode potentials of the anode (μ_A) and cathode (μ_C) (Equation 1.1), with a higher voltage allowing the battery to generate greater power. An example of the two half reactions for a Zinc-alkaline battery are shown in Equations 1.2 to 1.4.

$$V_{oc} = \frac{\mu_A - \mu_C}{e} \hspace{3cm} \text{(Equation 1.1)}$$

$$Zn_{(s)} + 2OH^-_{(aq)} \rightarrow ZnO_{(s)} + H_2O_{(l)} + 2e^- \hspace{1cm} E = 1.28\ V \hspace{0.5cm} \text{(Equation 1.2)}$$

$$2MnO_{2(s)} + H_2O_{(l)} + 2e^- \rightarrow Mn_2O_{3(s)} + 2OH^-_{(aq)} \hspace{0.3cm} E = 0.15\ V \hspace{0.5cm} \text{(Equation 1.3)}$$

$$\text{Overall: } Zn_{(s)} + 2MnO_{2(s)} = ZnO_{(s)} + Mn_2O_{3(s)} \hspace{0.5cm} E = 1.43\ V \hspace{0.5cm} \text{(Equation 1.4)}$$

Batteries are generally divided into two types, primary and secondary. In primary batteries, the reaction that converts stored chemical energy into electrical energy during discharge is irreversible. Examples of primary batteries include zinc-alkaline and zinc-carbon batteries. Secondary, or rechargeable batteries can be charged by applying a large voltage, enabling ions to move from the cathode to the anode. Examples of secondary batteries

include lead-acid, nickel-cadmium, nickel-metal hydride, and lithium-ion. Figure 1.2 summarises the main secondary batteries in terms of energy density per unit of volume and mass.[4] Alongside energy density, there are several other performance parameters that batteries can be measured by, summarised in Table 1.1. Ideally, a battery would also be inexpensive, environmentally friendly, and safe over repeated use. Lithium is the most electropositive element (3.04 V *vs* a standard hydrogen electrode) and is the lightest metal. This mean LIBs can typically operate at higher voltages (*ca.* 3.7 V), power and energy densities than other secondary battery technologies such as lead-acid and nickel-based.[4]–[6]
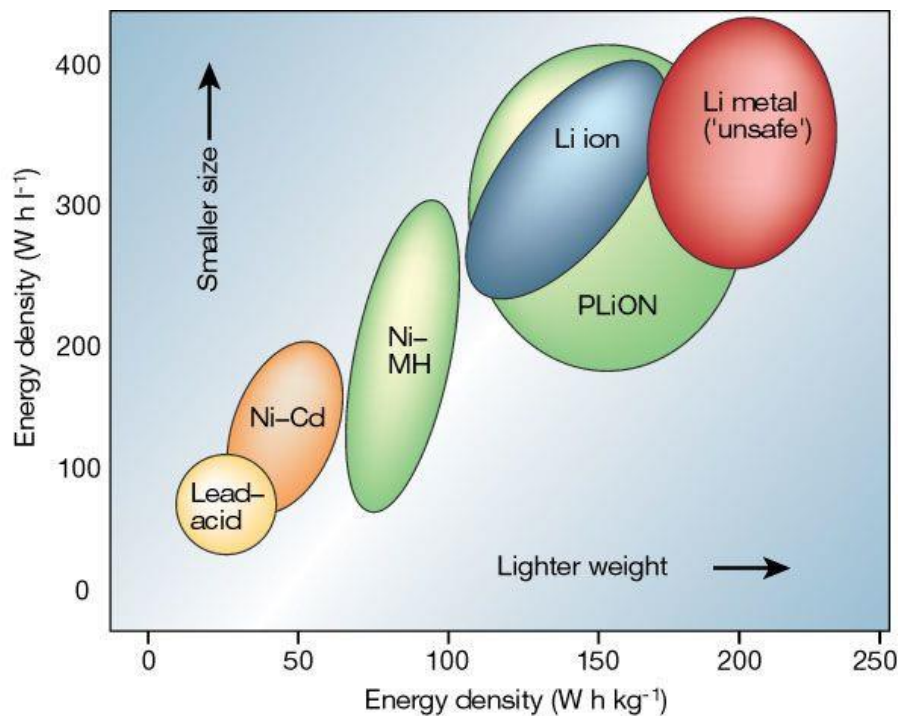
Figure 1.2. Comparison of the main secondary battery materials in terms of energy densities per unit of volume and weight.[4]

Table 1.1. Summary of important battery characteristics and their definition.

Performance Characteristic	Definition
Capacity	The amount of current the battery/active material can store. It is usually measured in mAh (capacity = current x time)
Specific capacity	Capacity divided by mass (gravimetric) or volume of active material (mAh/g or mAh/l). The specific capacity is often less than the theoretical as not all the active material may be accessible.
Energy density	The amount of energy a battery can store by weight (g) or volume (l). Units are typically given in Wh/kg or l.
Power density	The amount of power (power = current x volts) a battery can delivery per gram/litre (W/g, W/l).
Open-circuit voltage	Electrode potential$_{(cathode)}$ - Electrode potential$_{(anode)}$. The energy of cell can be related to the cell voltage by $\Delta G = -nFE$, where n = number of electrons, F = Faraday constant and E = charge of an electron.
Cycle life	The maximum number of times the battery can be charged/discharged.
C-rate	The rate which a battery is (dis)charged relative to its maximum capacity over a specific time *e.g.* 1C = a discharge rate of one hour.
Coulombic Efficiency (CE)	The ratio between charge and discharge capacities. The discharge capacity is often lower than the charge discharge due to irreversible reactions between the electrodes and electrolyte during initial cycles.

A key feature of many battery materials is their ability to change their composition by the process of (de)intercalation. Intercalation is the ability of a host structure to accept ions or molecules without altering the basic structure. Materials in which (de)intercalation can occur typically have either open layers, tunnels, or a three-dimensional framework. For example, in commercial LIBs both the anode and cathode are often layered structures that allow Li-ions to diffuse in-between the layers during charge/discharge.

1.3.   The Spinel Structure

The spinel structure, with the general formula AB_2O_4, has attracted significant attention since it was first reported in 1915.[7], [8] This is due to the vast number of cations which can combine to form the spinel structure. The physical properties of spinel oxides are strongly influenced by the arrangement of these cations. The spinel structure consists of a cubic close-packed array of O^{2-} anions, with 1/8 of the tetrahedral (Wyckoff site 8*a* or 8*b*) and 1/2 of the octahedral (Wyckoff site 16*d* or 16*c*) sites occupied by A and B cations, respectively. A Wyckoff site or position describes a collection of points within the crystal structure which can be related by symmetry. They can be used to describe how atoms are distributed and therefore are also an important tool for describing how mobile cations diffuse through the unit cell. Typically, the general formula is written as $[A_{1-i}B_i]^{tet}[B_{2-i}A_i]^{Oct}O_4$, where *i* is the degree of inversion. Spinel oxides with an inversion equal to zero are referred to as 'normal' spinels, while a material with an inversion degree equal to one is referred to as an 'inverse' spinels. Materials with a degree of inversion between zero and one are described as random or mixed spinels.[9] It should be noted for Li-containing ternary spinels, the distinction between normal and inverse spinels are typically described by the distribution of Li-ions, either in tetrahedral sites (normal spinels) or octahedral sites (inverse spinels).[10]

A and B cations are connected in a three-dimensional framework of edge-sharing BO_6 octahedra, which share corners with AO_4 tetrahedra. The three-dimensional framework structure, alongside the large number of empty sites (56 tetrahedral and 16 octahedral) offer a wide array of options for ions to migrate with ease (Figure 1.3). It is for this reason a great deal of Li-containing spinels have been researched as potential electrode materials in LIBs *e.g.* the anode material $Li_4Ti_5O_{12}$ ($[Li]^{tet}[Li_{1/3}Ti_{5/3}]^{oct}O_4$), as well as the cathode materials $Li_2NiMn_3O_8$ ($[Li]^{tet}[Ni_{0.5}Mn_{1.5}]^{oct}O_4$) and $Li_2Ni_2V_2O_8$ ($[V]^{tet}[LiNi]^{oct}O_4$).[11]–[13]
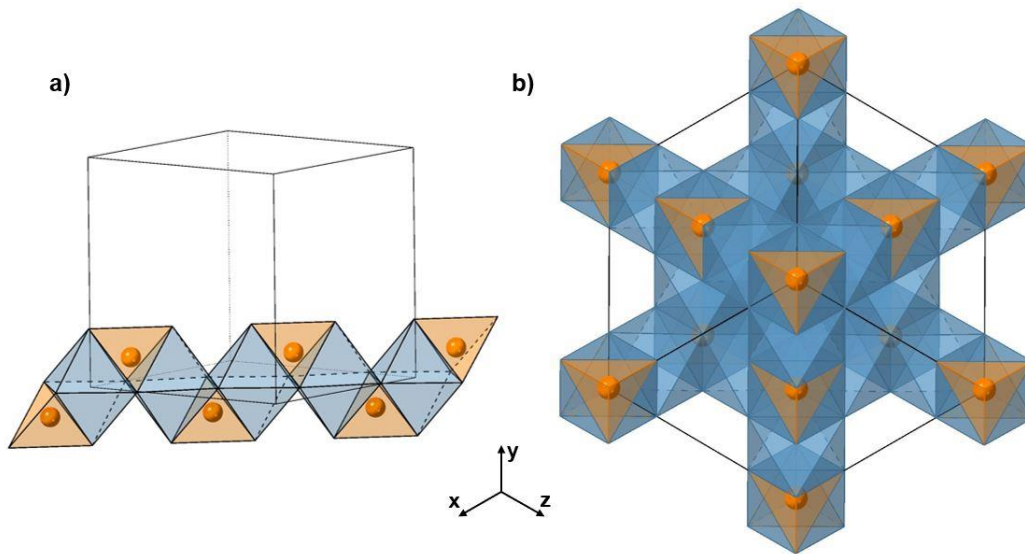
Figure 1.3. a) Portion of the spinel crystal structure, showing the possible Li-ion conduction pathway through the tetrahedral face of 8*a* sites (orange) into intermediate 16*c* sites (blue); b) Simplified crystal structure, orientated in the {111} plane, showing all possible Li positions in the spinel structure, which form ribbons of empty edge sharing octahedra connected to tetrahedra via face sharing.
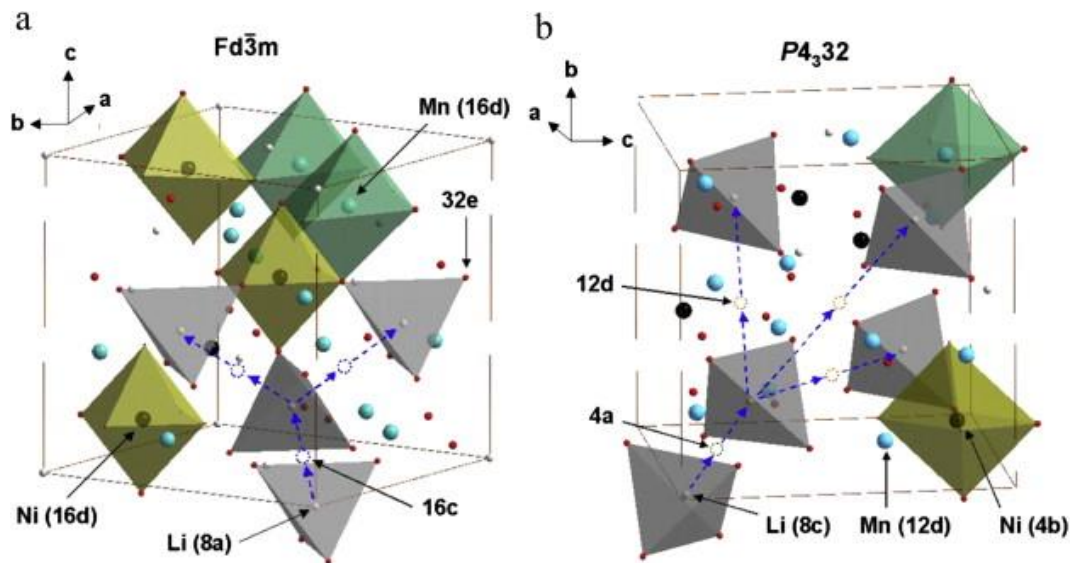
Figure 1.4. Structure and Li-ion diffusion pathway (as shown by the blue dashed line) in the spinel $Li_2NiMn_3O_8$. a) disordered structure and b) ordered structure.[16]

Ternary spinel oxides such as $Li_2NiMn_3O_8$ are commonly referred to as complex spinels due to the occupancy of tetrahedral or octahedral sites by more than one cation.[14] The distribution of cations in these sites can be disordered or ordered for instance, a 1:3 (Ni:Mn) ordering is observed in $Li_2NiMn_3O_8$ at low temperatures (<750 °C).[15] This 1:3 ordering leads

6

to a splitting of the octahedral (16d or 16c) site into two distinct sites (Wyckoff sites 4b and 12d), and results in a relatively lower symmetry $P4_3 32$ space group, compared to the high symmetry $Fd\overline{3}m$ space group for disordered spinel oxides (Figure 1.4).[16] Differences in the cation distributions have been explained by factors such as site preference of cations, electrostatic repulsion between cations and anion polarisation *i.e.* the degree of ionic/covalent bonding between anion and cations.[10], [14] The degree of ordering in these structures can affect the Li-ion conduction pathway and therefore influence electrochemical properties such as how fast a battery can be charged/discharged. A greater understanding of how Li-ion conduction pathways differ in these materials can help design new electrode materials with improved electrochemical characteristics.

1.3.1. Crystal Field Theory

The coordination environment of transition metals in many battery materials can contribute significantly to the observed electrochemical properties, as previously discussed. Crystal and ligand field theories can often be used to predict whether a transition metal will occupy an octahedral or tetrahedral coordination.[17] Crystal field theory is an electrostatic model which predicts that if a transition metal ion is in a crystal field *e.g.* octahedral, or tetrahedral, then the d orbitals are not degenerate, *i.e.* not of equal energy. The model treats ligands (*e.g.* OH$^-$) as point charges which create an electric field around the metal centre. This assumes there is an electrostatic attraction between the ligands and metal cation as well as a repulsive interaction between the d orbitals and ligand electrons; covalent interactions between ligands and metal cations are not accounted for d orbitals that point towards the ligands (3dz^2 and 3dx^2-y^2) are destabilised because of the repulsive electron interactions, whilst d orbitals in-between (3dxy, 3dxz and 3dyz) are stabilised. Figure 1.5 summarises the energy difference, Δ_{oct} and Δ_{tet}, between sets of d orbitals for a metal cation in octahedral and tetrahedral fields, respectively. The magnitude of Δ_{oct} is determined by the strength of the crystal field and is governed by the nature of transition metal, ligands, and oxidation state.
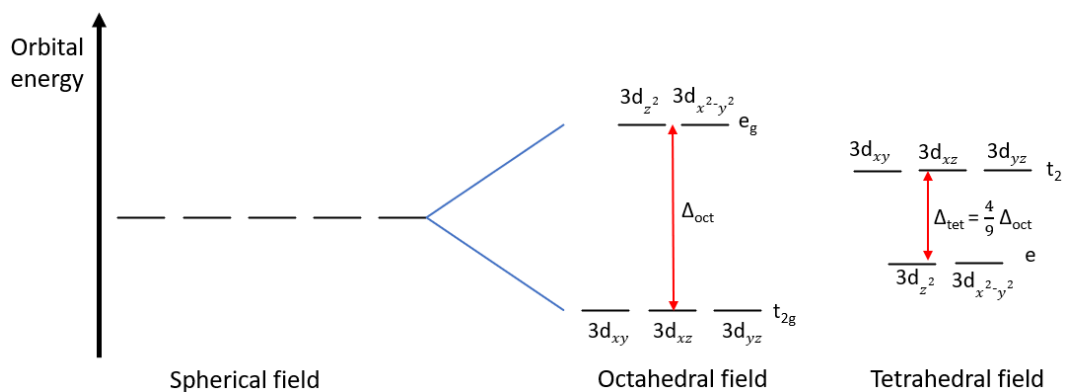
Figure 1.5. Crystal field splitting diagrams for spherical, octahedral, and tetrahedral fields. Adapted from [17].

For transition metal cations with a d^4 to d^7 electron configuration the complex may be high-spin or low-spin. In a high-spin arrangement all d electrons are unpaired, while in low spin arrangements, *d* electrons may pair if the pairing energy is lower than the crystal field stabilisation energy between sets of *d* orbitals (t_{2g} and e_g). For example, Co^{2+} (d^7) and Co^{3+} (d^6) can both be in either high or low spin configurations depending on the ligands.

Ligand field theory is an extension of crystal field theory which incorporates covalent and electrostatic interactions between transition metal cations and ligands. The ligand field stabilisation energies (LFSE) of d^0 to d^{10} electrons in high-spin octahedral and tetrahedral systems are presented in Figure 1.6. This indicates that d^0, d^5 and d^{10} cations have no LFSE and therefore no preference between tetrahedral and octahedral environments, while d^3 and d^8 cations *e.g.* Cr^{3+} and Ni^{2+} respectively, have the largest preference for octahedral environments. Both ligand and crystal field theories are often used to rationalise the distribution of metal cations in the spinel structure. For example, in $LiMn_2O_4$, Mn^{+3} (d^4) has a higher LFSE in octahedral sites compared to tetrahedral sites, thus $LiMn_2O_4$ is a normal spinel ($[Li]^{tet}[Mn_2]^{oct}O_4$). In $LiNiVO_4$, Ni^{2+} (d^8) has a strong preference for octahedral sites, while V^{5+} (d^0) has no LFSE effect and therefore the site preference will be biased on other factors such as ionic radius. As a result, V^{5+} occupies tetrahedral sites in the inverse spinel structure ($[V]^{tet}[LiNi]^{oct}O_4$).
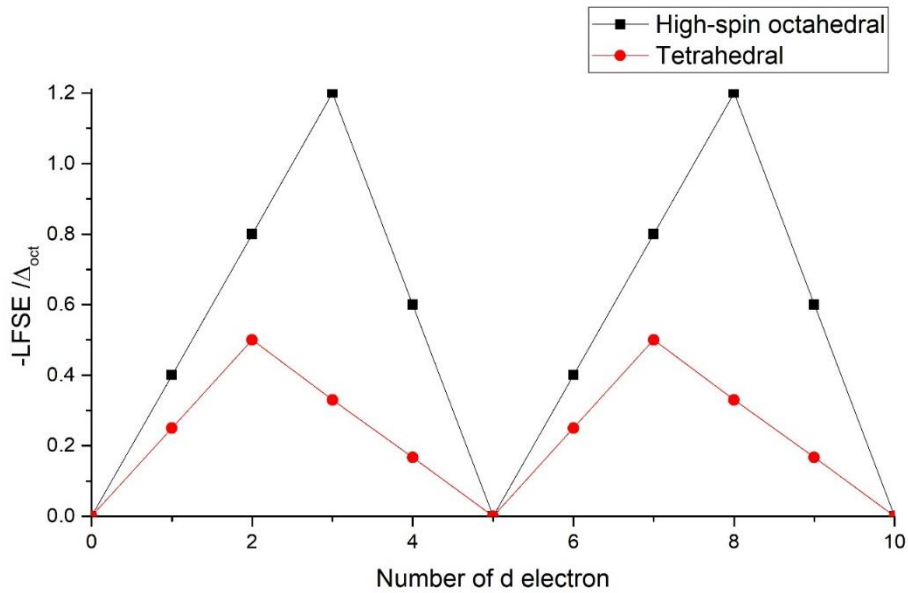
Figure 1.6. Ligand field stabilisation energies (LFSE) *vs.* number of d electrons for high-spin octahedral and tetrahedral configurations. Adapted from [17].

1.4.   Conduction Mechanisms

How quickly Li-ions can diffuse through a material is extremely important for the kinetics and charging rate of LIBs. There are two main mechanisms by which ions can diffuse through a material, via either (i) cation vacancies (Schottky defects), or (ii) Interstitial sites (Frenkel defects), Figure 1.7.[18] In the case of cation vacancies, mobile ions can diffuse through the lattice via randomly hopping into empty sites. For interstitial defects, mobile ions can either hop into empty interstitial site (sites in-between the lattice of ions) or by knocking adjacent ions into empty interstitial sites and subsequently occupying the now empty lattice site. Ions within the crystal structure are trapped in their lattice sites until they can absorb enough thermal energy to become mobile. The conductivity, σ, of a material is related to the number, n, charge, e, and mobility, μ, of carriers by Equation 1.5. The mobility of carriers is governed by the diffusion rate, D_{Li} and activation energy of hopping, E_a.

$$\sigma = n \times e \times \mu$$
(Equation 1.5)
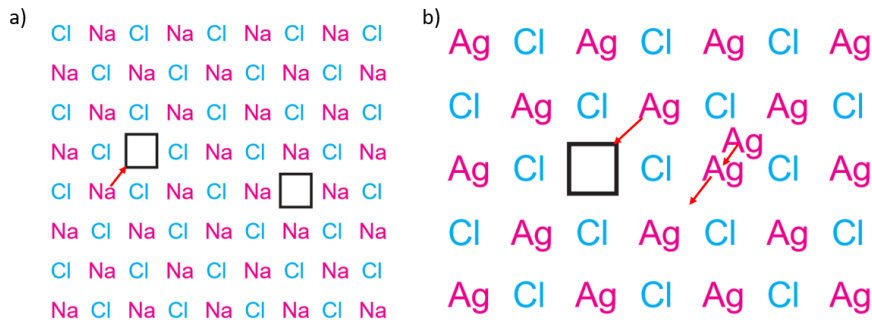
Figure 1.7. 2D schematic of ionic conduction mechanisms in NaCl and AgCl showing a) Schottky defects and b) Frenkel defects. Adapted from [18].

There is a temperature dependence on conductivity because ions require enough thermal energy to activate hopping and become mobile. The relationship between conductivity and temperature is given by the Arrhenius equation (Equation 1.6):

$$\sigma = \sigma_0 e^{(\frac{-E_a}{k_b T})} \qquad \text{(Equation 1.6)}$$

Where σ is conductivity, σ_0 is the pre-exponential factor, E_a is the activation energy, k_b is the Boltzmann constant and T is the temperature in Kelvin.

The activation energy of long-range hopping is governed by the energy associated with the formation of defects (E_f) and defect migration (E_m). Figure 1.8 summarises the variations of conductivity with temperature. At high temperatures, intrinsic ionic conduction dominates, and the number of carriers and mobility increases with temperature. The next stage is extrinsic ionic conduction, which arises due to dopants or impurities in the material. In this case, the number of carriers is constant, and the mobility increases with increasing temperature. A third stage can sometimes occur, whereby at even lower temperatures defects of opposite charge can associate to form defect complexes that are then trapped.
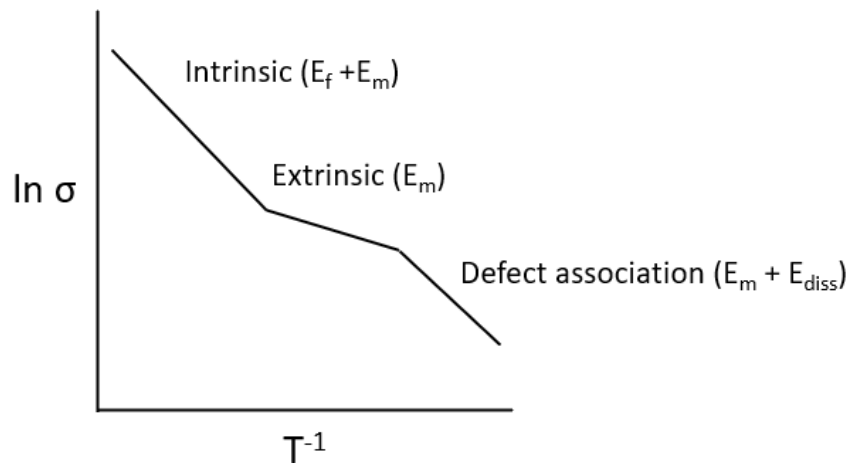
Figure 1.8. Summary of the general variation in ionic conduction with temperature. Activation energy for intrinsic conduction is governed by the formation of defects (Ef) and defect migration (Em). Extrinsic conduction is governed by defect migration and defect association is governed by defect formation and association of defects with opposite charge. Adapted from [18].

For a high ionic conductivity (>10^{-7} S cm^{-1}) a number of requirements must be met:

1. There should be a high number of mobile ions *i.e.* n is large.

2. There should be an equally high number of empty sites for mobile ions to hop into.

3. Neighbouring sites (empty and occupied) should have similar potential energies with a low activation energy for hopping between sites. *i.e.* the hopping windows between sites should be sufficiently large to enable easy migration and ions around the defect should be able to relax. The hopping window cannot be too large, or the ions will need to travel longer distances which requires more energy.

4. The crystal structure should have an open framework or channels which mobile ions can diffuse through.

Requirements one and two are related to the term c(1-c), where c is the concentration of mobile carriers and (1-c) is the number of vacant sites. The pre-exponential factor in the Arrhenius equation is proportional to c(1-c). Ionic conductivity will be low if the concentration of mobile carriers and vacancies are low *i.e.* c and (1-c) is small. However, the conductivity will be higher when there is an equal amount of vacant sites and mobile ions *i.e.* c ≈ (1-c). The number of cation vacancies and interstitials can be altered via aliovalent doping to form solid-solutions. For example, substituting for a higher valence cation, will charge balance by

creating cation vacancies or interstitial anions whilst, substituting for a lower valence cation will generate anion vacancies or interstitial cations.[18] In the following chapter, the most common battery materials are reviewed, with a particular emphasis on conduction mechanisms within these materials.

1.5. References

[1]   U.S. Department of Energy, "Energy Storage Grand Challenge Energy Storage Market Report 2020," *U.S. Dep. Energy*, vol. Technical, no. December, p. 65, 2020.

[2]   "Electric Vehicle Outlook 2020," *Bloomberg New Energy Finance*, 2020. [Online]. Available: https://about.bnef.com/electric-vehicle-outlook/.

[3]   Ioannis Tsiropoulos, Dalius Tarvydas, and Natalia Lebedeva, *Li-ion batteries for mobility and stationary storage applications - Scenarios for costs and market growth* . 2018.

[4]   J. M. Tarascon and M. Armand, "Issues and challenges facing rechargeable lithium batteries.," *Nature*, vol. 414, no. 6861, pp. 359–367, 2001.

[5]   D. R. Sadoway and A. M. Mayes, "Portable Power : Advanced Rechargeable Lithium Batteries," *Mat. Res. Bull.*, vol. 27, no. 8, pp. 590–596, 2002.

[6]   M. Armand and J.-M. Tarascon, "Building better batteries.," *Nature*, vol. 451, no. 7179, pp. 652–657, 2008.

[7]   W. H. Bragg, "The structure of the spinel group of crystals," *London, Edinburgh, Dublin Philos. Mag. J. Sci.*, vol. 30, no. 176, pp. 305–315, 1915.

[8]   S. Nishikawa, "Structure of some crystals of spinel group," *Proc. Tokyo Math. Soc. 2nd Ser.*, vol. 8, no. 3, pp. 199–109, 1915.

[9]   N. Reeves-Mclaren, R. I. Smith, and A. R. West, "Lithium-ion conduction pathways in complex lithium spinels $Li_2MGe_3O_8$ (M = Ni or Zn)," *Chem. Mater.*, vol. 23, no. 15, pp. 3556–3563, 2011.

[10]   J. Liu *et al.*, "Unified View of the Local Cation-Ordered State in Inverse Spinel Oxides," *Inorg. Chem.*, vol. 58, no. 21, pp. 14389–14402, 2019.

[11]   G. T.-K. Fey, W. Li, and J. R. Dahn, "$LiNiVO_4$: A 4.8 volt electrode material for lithium cells," *J. Electrochem. Soc.*, vol. 141, no. 9, pp. 2279–2282, 1994.

[12]   H. Kawai, M. Nagata, H. Tukamoto, and A. R. West, "High-voltage lithium cathode materials," *J. Power Sources*, vol. 81–82, pp. 67–72, 1999.

[13]   A. Laumann, H. Boysen, M. Bremholm, K. T. Fehr, M. Hoelzel, and M. Holzapfel,

"Lithium migration at high temperatures in $Li_4Ti_5O_{12}$ studied by neutron diffraction," *Chem. Mater.*, vol. 23, no. 11, pp. 2753–2759, 2011.

[14] H. Kawai, M. Tabuchi, M. Nagata, H. Tukamoto, and A. R. West, "Crystal chemistry and physical properties of complex lithium spinels $Li_2MM'_3O_8$ (M=Mg, Co, Ni, Zn; M'=Ti, Ge)," *J. Mater. Chem.*, vol. 8, no. 5, pp. 1273–1280, 1998.

[15] B. Aktekin *et al.*, "How Mn/Ni Ordering Controls Electrochemical Performance in High-Voltage Spinel $LiNi_{0.44}Mn_{1.56}O_4$ with Fixed Oxygen Content," *ACS Appl. Energy Mater.*, vol. 3, no. 6, pp. 6001–6013, 2020.

[16] M. Hu, X. Pang, and Z. Zhou, "Recent progress in high-voltage lithium ion batteries," *J. Power Sources*, vol. 237, pp. 229–242, 2013.

[17] D. F. Shriver and P. Atkins, *Inorganic Chemistry*, 5th Ed, OUP Oxford, 2010.

[18] A. R. West, *Solid State Chemistry and its Applications*, Student Ed. Wiley, 2014.

Chapter 2: Literature Review

2.1. Lithium-ion Batteries (LiBs)

The first iteration of the modern Li-ion battery was commercialised by Sony in 1991, consisting of $LiCoO_2$ as the cathode, coke (coal product) as the anode and a lithium salt ($LiPF_6$) in an organic solvent as the electrolyte (Figure 2.1).[1], [2] This followed nearly two decades of fundamental research into LIBs. The slow development of LIB technologies was partly attributed to the reactivity of Li metal and the thermodynamic instability of the electrolyte.[3] The open-circuit voltage (V_{oc}) is constrained by the electrolyte window, *i.e.* the energy separation (E_g) between the lowest unoccupied molecular orbital (LUMO) and the highest occupied molecular orbital (HOMO) of the electrolyte. As shown in Figure 2.2, an anode with an electrochemical potential (μ_a) above the LUMO will reduce the electrolyte; likewise, a cathode with an electrochemical potential (μ_c) below the HOMO will oxidise the electrolyte. These reactions can decrease the amount of Li-ions available for (de)intercalation.[2], [4] Aqueous electrolytes are not suitable in these systems due to the small electrolyte window of 1.5 V, which would limit the achievable energy density and voltage.

In the 1970s, Whittingham demonstrated a rechargeable LIB with the layered intercalation compound TiS_2 as the cathode, Li metal as the anode and lithium perchlorate in dioxolane as the electrolyte.[5] However, these systems were not viable as the voltage was limited to 2.2 V *vs* Li/Li^+. Li metal can react with the organic electrolyte forming a secondary electrode interface (SEI) made up of several Li-containing salts. This SEI layer would continuously breakdown and reform during subsequent charge/discharge cycles, reducing the overall capacity. Uneven Li metal growth (dendrites) can also deposit on the SEI layer, and over time can grow across the separator, resulting in an internal short circuit.[2] In practice, the formation of an SEI layer can be beneficial as it can act as a protective barrier, stopping further breakdown of the electrolyte. However, if possible an SEI layer would not be necessary as its formation reduces the available capacity of the battery. Ideally, Li metal would be used as the anode material as it allows for the widest chemical potential difference and therefore the largest overall cell voltage.[6] However, due to the safety shortcomings of Li metal, lithium alloys were proposed instead.[7] These alloys could only survive a limited number of cycles due to large volume changes and thus intercalated compounds such as pyrolytic carbon (Li_xC_6) were developed.[8]

In 2019 the Nobel prize in chemistry was awarded to John B. Goodenough, M. Stanley Whittingham, and Akira Yoshino for the development of the lithium-ion battery. Whittingham's contribution was awarded due to his research into titanium disulphide as an intercalated cathode material; Goodenough's for his research into lithium cobalt oxide as a cathode material, which increased the voltage of LIBs from 2.2 V to 3.7 V (Section 1.2); and Yoshino's for the creation of the first LIB using pyrolytic carbon as the anode instead of lithium metal in 1985. This substantially increased the cycle life and safety of LIBs; thus, it was the first commercially viable LIB produced.[9]

The subsequent sections aim to give an overview of the main contenders for the anode, electrolyte, and cathode materials in LIBs, with an emphasis on Li-based spinels.
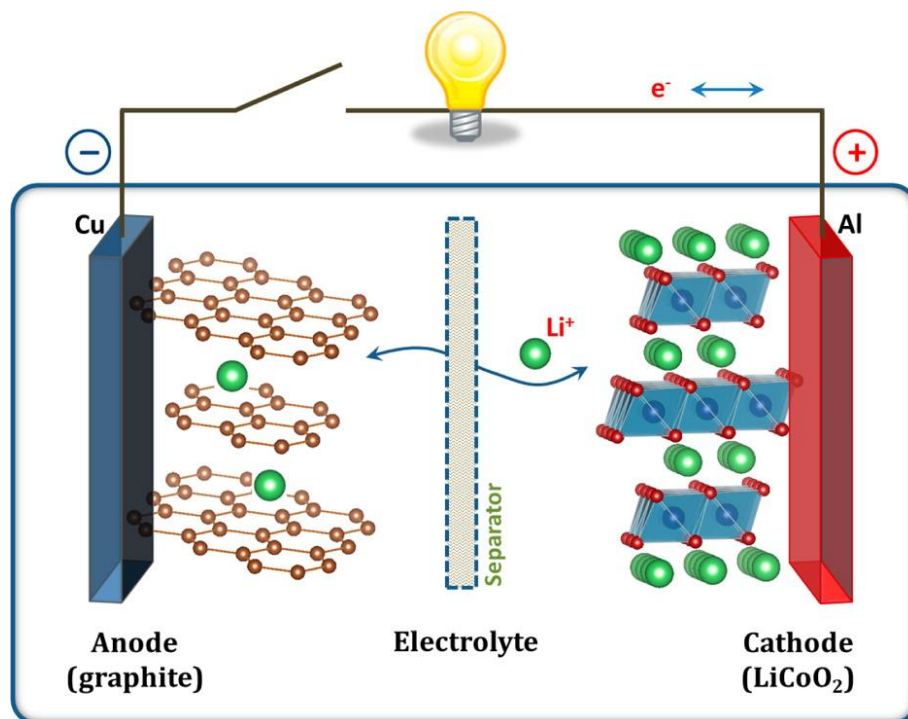
Figure 2.1. Schematic of a lithium-ion battery, comprising of a graphite (Li_xC_6) anode and a $LiCoO_2$ cathode, separated by an electrolyte ($LiPF_6$ in a non-aqueous organic solvent).[2]
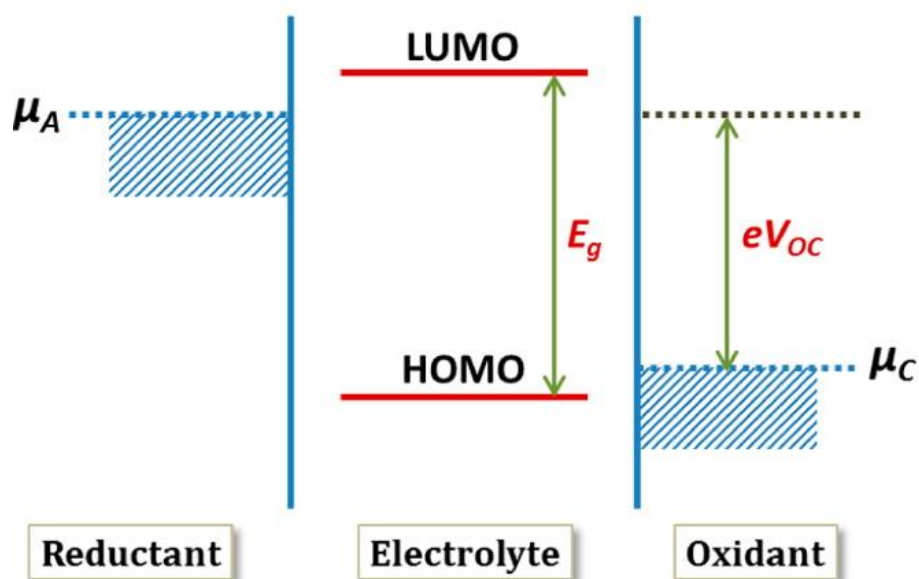
Figure 2.2. Schematic showing the relative energy separation (E_g) of an electrolyte, compared to the electrochemical potential of the anode (μ_A) and cathode (μ_C).[2]

2.2. Anode Materials

The ideal anode material for LIBs would have the following characteristics: little to no volume change during cycling, good mechanical stability, reasonable electronic and ionic conductivity ($>10^{-3}$ S cm^{-1}), high volumetric and gravimetric capacity, low cost, and a low electrochemical potential *vs.* Li.[10] As previously discussed, (Section 2.1), Li metal cannot currently be used in LIBs due to the inherent safety concerns, although it is commonly used as a reference material for the majority of fundamental research in the area.[6], [11] Current anode materials are significantly safer than metallic lithium, yet they sacrifice capacity and have a larger electrochemical potential *vs.* Li. The main contenders can be categorised into three distinct groups: intercalation materials *e.g.* graphitic carbon and $Li_4Ti_5O_{12}$, alloying metals *e.g.* Sn and Si, and conversion materials, such as Co_3O_4.[12], [13]

2.2.1. Intercalation Anodes

Intercalation-type anode materials are the most commercially successful employed in LIBs.[12] During charge in a full cell, lithium-ions are inserted into the host structure with little volume change and therefore the basic structure of the host material is maintained. Graphitic carbon can accommodate Li-ions between graphene sheets, enabling one Li-ion per six-

membered ring of carbon atoms (LixC$_6$).[14] It is typically the anode material of choice, owing to its many advantageous properties. For instance, good mechanical stability, reasonable electrical and Li-ion conductivity, availability, low cost, low electrochemical potential *vs.* Li (0.1-0.3 V) and low volume change during cycling (*ca.* 10 %).[15], [16] Little to no volume change is required to maintain the SEI layer which would otherwise consume more Li-ions, leading to greater irreversible capacity loss. Although graphite displays excellent mechanical and electrochemical stability, it is limited by its relatively low specific capacity (370 mAh g^{-1}).[16], [17] Graphitic carbon also limits the choice of electrolyte, as some solvents such as propylene carbonate (PC) can intercalate between the graphene sheets, further reducing capacity.[18] Another drawback of graphitic carbon is its limited rate capability, *i.e.* how fast the battery can be charged, due to the tendency for plating Li metal on the anode surface at higher charge rates. This can lead to SEI breakdown, resulting in capacity loss and safety concerns due to the potential for the battery to short circuit as Li metal continues to grow across the separator during subsequent cycles.[19]

Li$_4$Ti$_5$O$_{12}$ (LTO) has been developed as an anode material within LIBs due to its greatly improved safety characteristics over other candidates. LTO crystallises in the normal spinel structure: a close-packed array of O^{2-} anions with tetrahedral 8*a* sites fully occupied by Li-ions and octahedral 16*d* sites also fully occupied, one sixth with Li-ions, with the remaining five sixths with Ti^{4+}. The LTO spinel structure has several empty tetrahedral (8*b* and 48*f*) and octahedral (16*c*) sites which enable lithium to be inserted.[20], [21] During lithiation (discharge *vs.* Li), a solid solution between the two end members Li$_4$Ti$_5$O$_{12}$ and Li$_7$Ti$_5$O$_{12}$ is formed in the following reaction:

$$[Li]_{8a}[Li_{1/3}Ti_{5/3}]_{16d}[O_4]_{32e} + 3Li^+ + 3e^- \rightarrow [Li_2]_{16c}[Li_{1/3}Ti_{5/3}]_{16d}[O_4]_{32e}$$
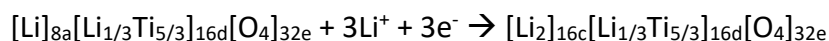
The additional Li-ions cause a shift in lithium occupation from tetrahedral 8*a* to 16*c* octahedral sites, due to the small interatomic distance between lithium sites (1.81 Å).[21]–[23] To accommodate the additional lithium-ions three out of five Ti atoms are reduced from Ti^{4+} to Ti^{3+} and a phase change occurs from the Li-poor spinel Li$_4$Ti$_5$O$_{12}$ to the Li-rich rocksalt Li$_7$Ti$_5$O$_{12}$ (Figure 2.3). The corresponding volume change is negligible, at *ca.* 0.2 – 0.3 %, compared to approximately 10 % for graphite due to the very similar lattice parameters between end-members.[20] LTO also displays a flat voltage plateau at 1.5 V and is capable of fast (dis)charge rates. The higher potential *vs.* Li means there is little to no SEI or dendrite

formation on charging.[24] Whilst this enables an extremely large cycle life, it also means that the overall cell voltage is lower, at *ca.* 2.5 V compared the to 3.7 V obtained when using graphite-based anodes.[24], [25] The main disadvantages of LTO over other anode candidates are its low electronic conductivity ($<10^{-13}$ S cm^{-1}) and relatively low theoretical capacity (175 mAh g^{-1}).[21] To overcome its poor electronic conductivity, research has focused on fabricating $Li_4Ti_5O_{12}$ nanoparticles and carbon-based surface coatings.[21], [26], [27] These research efforts have enabled LTO-based anodes with extremely fast charging rates, e.g. a specific capacity of 156 mAh g^{-1} was observed on charge at a C-rate of 50C for 20 nm sized LTO nanoparticles.[26]
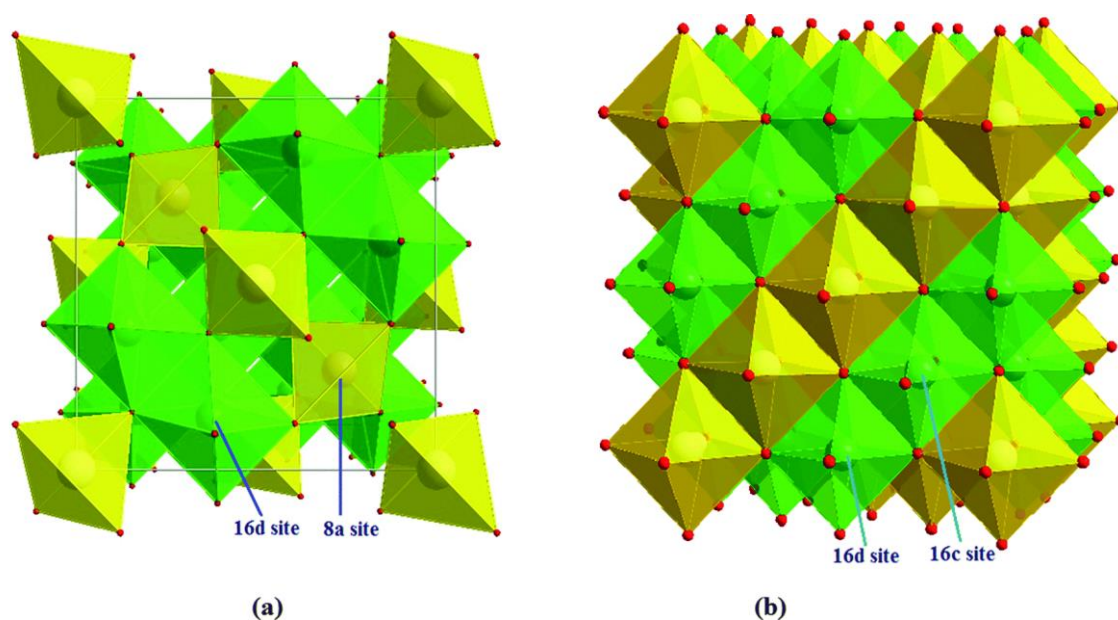
Figure 2.3. Crystal structure of a) spinel $Li_4Ti_5O_{12}$ and b) rocksalt $Li_7Ti_5O_{12}$. Li and Ti atoms on octahedral 16*d* sites are shown in green and Li atoms on tetrahedral 8*a* and octahedral 16*c* sites are shown in yellow.[21]

Anode materials based on the inverse spinel structure have also been demonstrated with the general formula $LiMVO_4$ (M = Ni, Cu, Mg and Zn).[28]–[30] The inverse spinel structure can be described as a close packed array of O^{2-} anions with Li and M^{2+} cations distributed randomly over octahedral 16*c* sites with the tetrahedral 8*b* sites occupied by V^{5+} ions. For example, the compounds $LiMg_{1-x}Zn_xVO_4$ (*x* = 0 to 1) were investigated by Uyama *et al.* as anode materials due to the potential of a two electron $V^{5+/3+}$ redox process. Compositions with *x* = 0 displayed an initial discharge (lithiation) capacity of *ca.* 581 mAh g^{-1}

and an operating voltage of *ca.* 0.8 V *vs.* Li. The subsequent charge (delithiation) was, however, significantly lower at *ca.* 200 mAh g^{-1}, suggesting a large irreversible reaction had occurred.[30] The proposed overall reaction mechanism can be described by:

$$[V^{5+}]_{8b}[LiM]_{16c}O_4 + 2Li^+ + 2e^- \rightarrow [Li]_{8b}[LiV^{3+}]_{16d}[LiM]_{16c}O_4$$
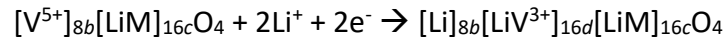
The large irreversible capacity loss was attributed to vanadium being unable to be oxidised back to V^{5+} during delithiation; instead, a one-electron process occurs in subsequent cycles.[30] For compounds containing Zn, the rocksalt phase (Li$_a$Zn$_b$V$_c$)O was observed alongside [Li]$_{8b}$[LiV^{3+}]$_{16d}$[LiM]$_{16c}$O$_4$ using ex-situ X-ray powder diffraction, resulting in the reaction mechanism:

$$[Li]_{tet}[LiV^{3+}]_{oct}[LiM]_{oct}O_4 + xLi^+ + xe^- \rightarrow x(Li_a,Zn_b,V_c)O$$
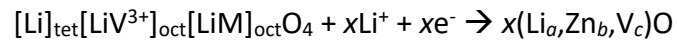
This reaction mechanism differs from LTO and other normal spinels, with vanadium cations shifting from tetrahedral to octahedral sites to enable Li diffusion through 8*b* tetrahedral sites to 16*d* octahedral sites (Figure 2.4), followed by a conversion-like mechanism (Section 2.2.3). The formation of the rocksalt phase enabled significantly larger capacities with increasing *x*, up to 1008 mAh g^{-1} for *x* = 1. However, the formation of this phase was also suggested to cause poor capacity retention (ca. 42 % after 30 cycles for *x* = 1) due to isolation of active material from the conducting carbon.[30] These materials were only measured for a limited number of cycles with a slow charge/discharge rate of 0.05 C.[30] Their practical use is also limited by the large irreversible capacity loss seen during the first cycle. Nevertheless, they are promising anodes due to their lower operating voltage *vs.* Li and slightly larger capacity compared to LTO.
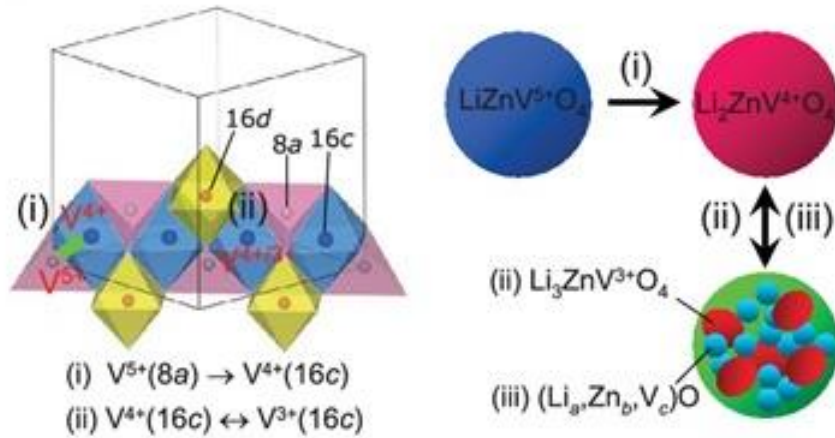
Figure 2.4. Reaction mechanism of the inverse spinel LiZnVO$_4$ anode during lithiation.[30]

2.2.2. Alloying Metals

Si and Sn are examples of metals which can form alloys with lithium and have low electrochemical potentials, as well as extremely large volumetric and specific capacities. Si has an operating voltage range of 0.1 – 0.4 V *vs.* Li and a theoretical capacity of *ca.* 4200 mAh g^{-1}. Meanwhile, Sn has an operating voltage of *ca.* 0.4 V and a theoretical capacity of 960 mAh g^{-1}.[10], [12], [31] They act as anode materials via an alloying mechanism, where during lithiation, they can react with Li-ions to form various lithium-based alloys such as Li$_{12}$Si$_{17}$.[32] This process can by described by:

$$M + xLi^+ + xe^- \rightarrow Li_xM \text{ (M = metal)}$$

Both Si and Sn suffer from huge volume changes during lithium insertion (>400 and 255 %, respectively), which results in loss of contact between the electrode/electrolyte interface.[15], [25] This can damage the SEI layer, leading to greater consumption of the electrolyte and Li-ions. The huge volume change during cycling means these materials have low coulombic efficiencies and poor cycling stability, thus severely limiting their commercial application. For example, Si powder has an initial coulombic efficiency of only *ca.* 36 % during the first charge/discharge cycle, which continues to decrease during subsequent cycles.[33] To overcome these issues, carbon composites with small additions of the alloying element have been investigated to increase cycle life.[13], [34], [35] These nanocomposite materials can accommodate large volume changes during cycling, resulting in greater capacity retention over time (up to 97 % after 1000 cycles). [13], [35], [36] As a result, Si/carbon nanocomposite

materials are seen as the next generation anode materials, offering improved specific capacities (up to 500 mAh g^{-1}) over their graphitic carbon counterparts.[37]

2.2.3. Conversion Anodes

Many transition metal oxides can react with Li-ions and are potential anode materials. The mechanism differs from intercalation-type metal oxides such as LTO, where the basic structure is maintained, and instead follows a conversion-type mechanism which can be described by the following process:

$$M_xO_y + 2yLi^+ + 2ye^- \rightarrow yLi_2O + {}_xM \text{ (M = metal)}$$

During lithiation, the metal oxides are reduced to metallic clusters which are surrounded in a Li_2O matrix. During delithiation, the process is reversible, and the metallic clusters react with Li_2O to reform the corresponding metal oxide.[31] Examples of conversion-type anodes include CuO, Co_3O_4, Fe_2O_3/Fe_3O_4 and Mn_3O_4, many of which are based on the spinel structure.[38]–[41] The main advantage of these materials over intercalation-type are their high theoretical capacity (*e.g.* CuO = 674 mAh g^{-1}, Co_3O_4 = 890 mAh g^{-1} and Fe_3O_4 = 1007 mAh g^{-1}). However, a large hysteresis in the voltage during cycling is observed *e.g.,* Co_3O_4 has an operating voltage of 1.1 V and 2.1 V *vs.* Li during lithiation/delithiation, respectively (Figure 2.5).[31], [40] The overpotential significantly limits the capacity and thus the energy density, alongside columbic efficiency (*ca.* <70 %). This is due to a large irreversible capacity loss observed during the first cycle, as not all the Li_2O can be oxidised on delithiation.[40] Like alloying-type anodes, strategies such as lowering the particle size (increasing surface area), multiphase composites and thin films have been implemented to increase cycling stability.[13], [31], [41] However, these are yet to produce a high capacity anode with the cycle life required for commercialisation.
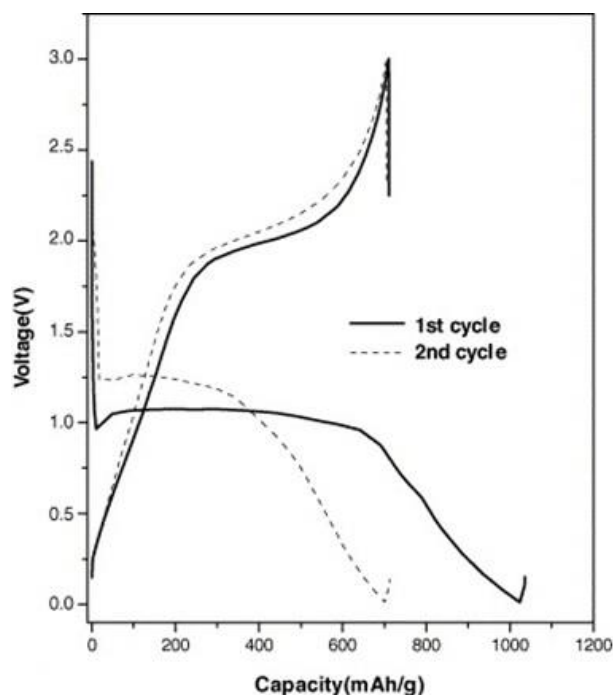
Figure 2.5. Charge/discharge curves of Co_3O_4 *vs.* Li, demonstrating the large overpotential seen in conversion anodes during cycling.[40]

2.3. Electrolyte Materials

The choice of electrolyte used in LIBs greatly influences the operating voltage, power density, cycle life and critically, the safety parameters in these systems. The safety aspects of LIBs are frequently governed by the chemical stability (electrolyte window) of the electrolyte used, especially since it is in close proximity with the electrodes. As such, advances in new cathode and anode materials are often limited practically by their compatibility with current electrolyte materials. These compatibility issues have led to more attention being placed on the choice of electrolyte, but it is imperative that cathode, anode, and electrolyte materials be developed in tandem to overcome the challenges associated with LIBs.

Electrolyte materials are typically classed into three main groups: organic and inorganic liquids, polymers, and inorganic solids.[42]–[44] Regardless of the type, several criteria must be fulfilled for practical viability:

1) A large electrolyte window, and thus thermodynamically stability in contact with the electrodes used.

2) Kinetic stability if the electrode potentials lie outside the thermodynamic stability range.

3) Ionically conductive, i.e. an ionic conductivity, $\sigma_i \geq 10^{-3}$ S cm^{-1} at 25 °C.

4) Electronically insulating, i.e. an electronic conductivity, $\sigma_e < 10^{-10}$ S cm^{-1} at 25 °C.

5) Chemical and mechanical stability over an operating temperature range of typically -20 °C to 60 °C.

6) Preferably materials that are non-flammable, non-toxic, whilst also being sustainable and relatively cheap to fabricate.

Meeting all of these conditions demonstrates why the development of new electrolytes is such a challenging task.

2.3.1. Organic and Polymer Electrolytes

Depending on the required properties, the organic electrolyte is typically comprised of the lithium salt, LiPF$_6$, in a carbonate-based solvent mixture of ethylene carbonate (EC) and either propylene carbonate (PC), dimethyl carbonate (DMC), ethyl methyl carbonate (EMC) and/or diethyl carbonate (DEC).[42] The most common blend used in commercial LIBs is a 1:1 molar mixture of EC and DMC. Lithium salts are highly soluble in the cyclic carbonate EC and more importantly, EC enables the formation of the solid-electrolyte interface layer. DMC is a linear carbonate used for its relatively low viscosity, which results in better Li-ion diffusion due to the lower activation energy.[43], [45]–[47] The combination of these electrolyte solutions can give ionic conductivities between 5-10 mS cm^{-1} and is one of the main reasons they are still widely used today. Despite this, carbonate-based solvents and lithium salts have several drawbacks; they are volatile and highly flammable; the ionic conductivity can drop significantly below -15 °C, limiting the operating temperature range; whilst the lithium salts used are expensive and toxic.[46]

The most common electrolyte solution of 1:1 EC and DMC (generation one) is thermodynamically stable with current commercial cathode materials however, this is not the case on the anode side. To enable the use of graphitic carbon as the anode, a passivating SEI layer must form for the electrolyte to be stable (Section 2.2.1). During this process, approximately 10 % of the battery's capacity is lost and the resulting interface formed may

impede Li-ion mobility. Nevertheless, the SEI layer provides kinetic stability via enlarging of the electrolyte window thus, preventing further chemical reactions between the electrolyte and electrodes.[17], [48] The main drawback with carbonate-based electrolytes are their relatively low operating voltage stability. Generation one based electrolytes are unstable when charging above 4.5 V *vs.* Li; generation two (1.2 M $LiPF_6$ in 3:7 EC/EMC) increased the stability to 4.9 V *vs.* Li however, this is still incompatible with many high voltage cathode materials, with cells made using materials that operate at high potentials still suffering from significantly limited cycle life (Section 2.4.4).[49], [50]

Over time, the lithium salt can also undergo chemical side reactions. $LiPF_6$ can decompose to LiF and PF_5, which are involved in surface reactions on the anode, disrupting the SEI layer. The decomposition product, PF_5 can react with water or carbonate solvents to release PF_3O and HF. HF can then interact with the cathode, leading to reductions in capacity, cycle life, as well as additional safety concerns.[45], [48], [51]

Polymer electrolytes can be treated as composite materials consisting of a polymer such as polyethylene oxides (PEOs) and a lithium containing salt ($LiPF_6$) or inorganic solid electrolyte. They have the advantages of being low-cost, less toxic and display good chemical stability and mechanical properties.[43], [52] Unfortunately, they are poor Li-ion conductors at room temperature and have yet to be implemented into LIBs.[53] Confusingly, systems based on so-called lithium polymer batteries (LiPo) are already a commercial reality. These use polymer-gel electrolyte materials that can be described as hybrid systems which aim to exploit the advantages of both solid-polymer and organic carbonate electrolytes. Polymer-gel electrolytes use a microporous membrane separator and are infused with liquid electrolytes to form a gel (Figure 2.6).[3] Unlike their solid polymer counterparts, they offer comparable ionic conductivities to carbonate-based electrolytes, whilst also offering additional benefits such as flexibility, lightweight, and lower the chances of leakage.[54] The nature of these hybrid systems means that they also exhibit many of the same disadvantages as organic carbonate-based electrolytes such as flammability, continued capacity loss and reduced mechanical properties compared to solid polymers.[43], [53] LiPo batteries are used extensively in portable devices however, ongoing incidents for example, the Samsung Note 7 recall, reignite the debate around the safety of these systems and highlight the growing need for new, safer electrolyte materials.[42], [55]
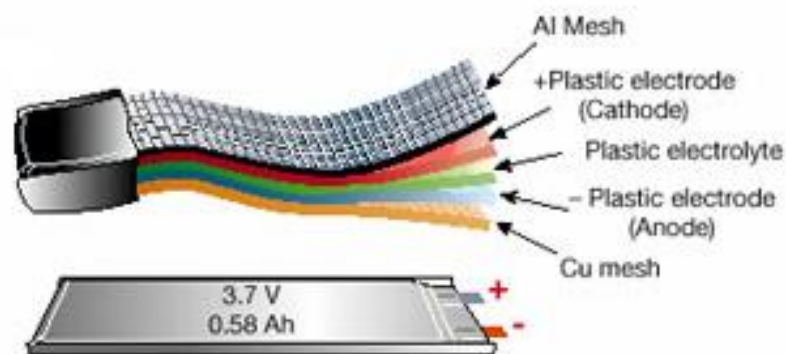
Figure 2.6. Schematic of a commercial Li-ion polymer battery that is used within portable devices. Adapted from [3].

2.3.2. Inorganic Solid Electrolytes

Inorganic solid electrolytes can potentially solve many of the problems previously discussed concerning liquid electrolytes. The use of a solid electrolyte with a wide electrochemical stability window would enable Li metal and high voltage cathode materials (> 4.5 V) to be used, thus improving many performance characteristics for instance operating temperature range, cycle life, power output, energy density, and capacity. A wide electrochemical stability window would also eliminate the need for an SEI layer (assuming Li metal dendrites do not form).[56] In addition, solid electrolytes present other advantages in terms of overall design and safety of LIBs when compared to their liquid and polymer-gel counterparts; they would remove the need for a separator, therefore simplifying cell design, whilst likewise creating a battery that is durable, leakage free and non-flammable.[4], [54]

The main ceramic materials under focus are LISICON-based, NASICON-based, perovskites, and garnet-type Li-ion conductors. Ceramic-based electrolytes meet many of the criteria outlined in Section 2.3. However, the general ongoing challenges include, relatively low Li-ion conduction, electrode/electrolyte interfacial resistance, volume changes during cycling, and difficult synthesis conditions (particularly for sulphur and halide-containing electrolytes, as they are reactive under ambient conditions). Reported room temperature Li-ion conductivity ranges for many common ceramic electrolyte structural families are presented in Figure 2.7.[54], [57]–[62]
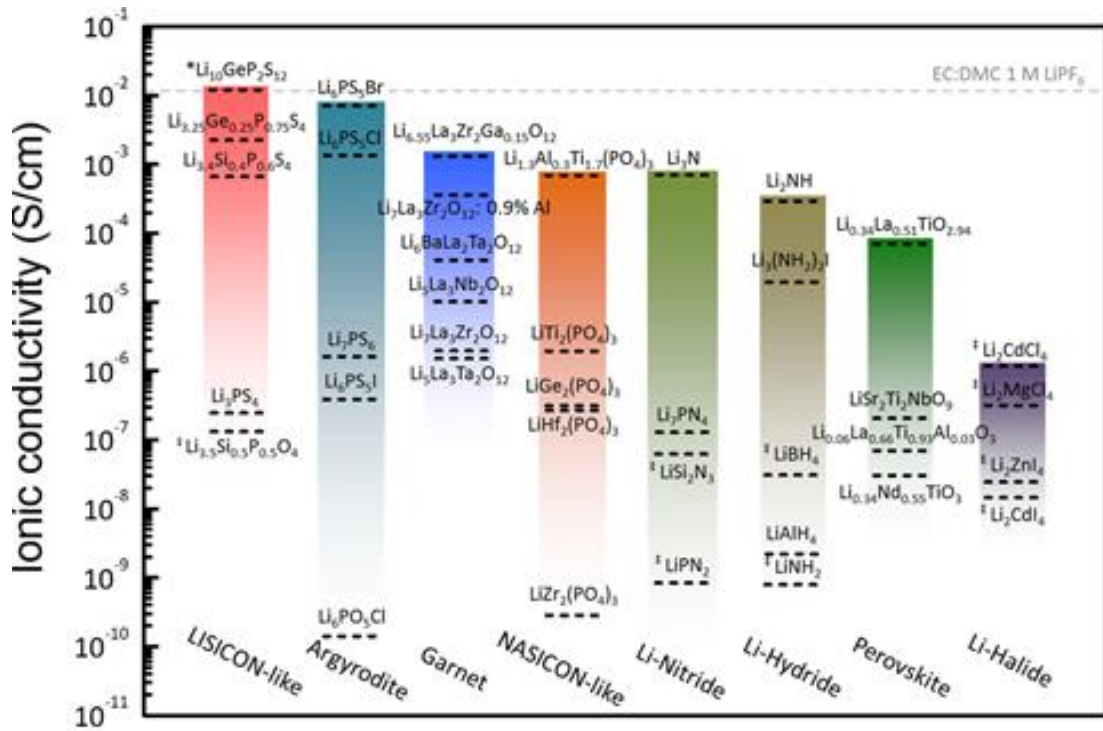
Figure 2.7. Total ionic conductivity for many of the most well-known structures under investigation as potential solid electrolyte materials.[59]

2.3.2.1 LISICONs

The Lithium Super Ionic Conductor (LISICON) family were first described by Hong for the compound $Li_{14}ZnGe_4O_{16}$, and later by Bruce *et al.* for the solution solid $Li_{2+2x}Zn_{1-x}GeO_4$.[63], [64] LISICON compounds adopt a three-dimensional (3D) framework structure similar to γ-Li_3PO_4, with all cations located in tetrahedral sites (Figure 2.8).[65] Mobile Li-ions can diffuse between LiO_4 tetrahedra and octahedral interstitial sites. $Li_{14}ZnGe_4O_{16}$ exhibits a high Li-ion conduction of 0.125 S cm^{-1} at 300 °C however, the Li-ion conductivity is only 1 x 10^{-7} S cm^{-1} at room temperature.[57], [59], [63] Phosphorus in γ-Li_3PO_4 can be substituted by Si, Ge or V to create the solid solution $Li_{3+x}Y_{1-x}X_xO_4$, (x = Si, Ge and Y = V, P). The excess Li, required to charge balance, occupy interstitial octahedral sites and increases the Li-ion conductivity in these systems; the highest of which is seen for the compound, $Li_{3.6}Ge_{0.6}V_{0.4}O_4$ (4 x 10^{-5} S cm^{-1} at 25 °C).[66] Besides their relatively low conductivity, LISICON materials are reactive with lithium metal and CO_2, limiting their usage in LIBs.[58]
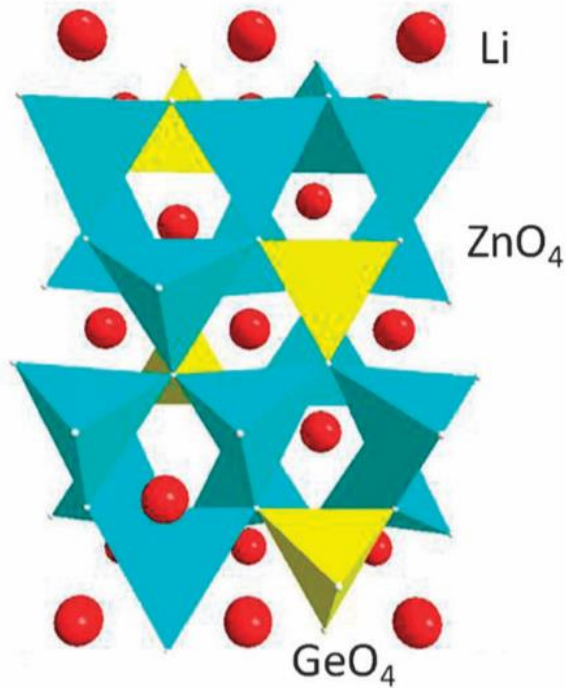
Figure 2.8. Crystal structure of the Lithium Super Ionic Conductor (LISICON), $Li_{14}ZnGe_4O_{16}$. Li atoms at shown in red, with ZnO_4 and GeO_4 tetrahedra in blue and yellow, respectively.[65], [67]

Replacing oxygen for sulphur in LISICON-based materials has led to the biggest increase in Li-ion conduction. The thio-LISICON family of materials can achieve conductivities comparable or even higher than current organic-based electrolytes (e.g. $Li_{10}GeP_2S_{12}$, 1.2 x 10^{-2} S cm^{-1} and $Li_{3.25}Ge_{0.25}P_{0.75}S_4$, 2.2 x 10^{-3} S cm^{-1} at room temperature).[68]–[70] Although, Ge is expensive and can be reduced at low voltages (between 1.7 and 1.6 V).[71] Attempts to substitute Ge for Sn or Si can give conductivities as high as 4 x 10^{-3} S cm^{-1}.[61], [69], [72] The main drawbacks to thio-LISICON materials are: They are unstable in air (decomposing to form toxic H_2S), they can decompose at cell voltages above 4 V (by side reactions with the cathode), and many can react with lithium metal to form a mixed conductive SEI layer which continues to grow during cycling, leading to a potential short circuit.[56], [59], [62]

2.3.2.2. NASICONs

The Sodium Super Ionic Conductor (NASICON) term was first given to the solid solution $Na_{1+x}Zr_2Si_xP_{3-x}O_{12}$ by Hong *et al.* in 1976.[73] The end-member, $NaZr_2P_3O_{12}$ consists of corner-sharing PO_4 tetrahedra and ZrO_6 octahedra. There are two interstitial sites, with Na ions fully occupying one, and the other remaining empty. Replacement of P^{5+} by Si^{4+} and Na^+ causes excess sodium to partially fill empty interstitial sites, shortening the Na^+ hopping distance and enabling a 3D conduction pathway. The lithium analogue, $LiM_2(PO_4)_3$ (where M = Zr, Ti, Ge and Hf) likewise adopts a NASICON framework, Figure 2.9.[67], [74] However, these materials display low total (bulk and grain boundary) conductivity (*ca.* 10^{-7} S cm^{-1} at 25 °C) due to high grain boundary resistance and difficult sintering conditions.[57], [74], [75] Creating Li interstitials via substituting Ti^{4+} ions for lower valance cations e.g. Al^{3+} has a pronounced effect on ionic conductivity, with $Li_{1.3}Al_{0.3}Ti_{1.7}(PO_4)_3$ exhibiting the highest conductivity of 3 x 10^{-3} S cm^{-1} at 25 °C for these materials.[76] Unlike sulphur-based electrolytes, NASICON-based materials are also typically stable in air and water. Nevertheless, they cannot be used with lithium metal due to the reduction of Ti^{4+} to Ti^{3+} during cycling.[77], [78]
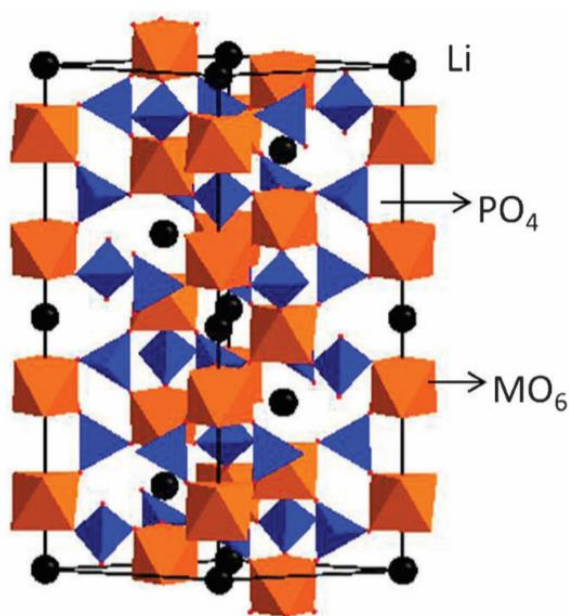
Figure 2.9. Crystal structure of the Sodium Super Ionic Conductor (NASICON), $LiM_2(PO_4)_3$ (where M = Zr, Ti, Ge and Hf).[67], [74]

2.3.2.3. Perovskites

Materials based on the perovskite structure (ABO_3) have been widely investigated in the solid-state community and are used extensively in applications such as capacitors, piezoelectrics, solar cells and oxygen-conductors in solid oxide fuel cells. The A-site deficient perovskite, $Li_{0.34}La_{0.51}TiO_{2.94}$ currently exhibits the highest bulk Li-ion conductivity for perovskite-based materials (1×10^{-3} S cm^{-1} at room temperature).[79] The structure consists of Li and La on the A-site in a 12-fold coordination and corner-sharing TiO_6 in the B-site (Figure 2.10).[67] The high bulk Li-ion conduction makes Li-containing titanate perovskites a promising class of materials for use as a solid electrolyte in LIBs. Despite this, these materials have several disadvantages such as low total Li-ion conduction (7×10^{-5} S cm^{-1}) due to grain boundary resistance. They also require high sintering temperatures (>1200 °C), which can lead to difficulties in controlling the lithium and oxygen content.[80] Ti-containing perovskites also cannot be used with Li metal for the same reason as Ti-based NASICON structures.[81], [82]
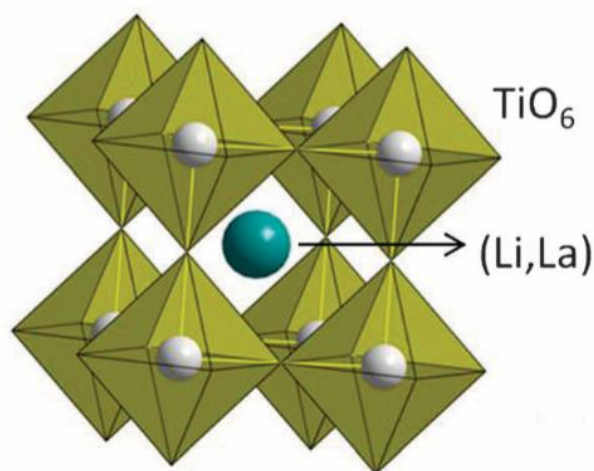
Figure 2.10. Crystal structure of the A-site deficient perovskite, (La/Li)TiO$_3$.[67]

2.3.2.4. Li-stuffed Garnets

Li-stuffed garnets have been under extensive research since their discovery in 2003, owing to their high Li-ion conductivity (between 10^{-6} to 10^{-3} S cm^{-1} at room temperature) and stability with Li metal.[83] The ideal garnet with a general formula, $A_3B_2C_3O_{12}$, can host a range of elements with A-site ions typically being group two alkali earth or rare earth elements (*e.g.* Ca, Mg, Y or La), in an eight-fold coordination; B-sites are typically +3 transition metal ions (*e.g.* Al, Fe, Ga, Ge, Mn, Ni or V), in a six-fold coordination, and C-site ions are either Si, Ge or Al in a four-fold coordination.[67], [84], [85] Lithium-based garnets can also incorporate many different elements onto A, B and C sites. Figure 2.11 highlights the compositional variation in Li-based garnet with cation substitution. In Li-stuffed garnets excess lithium can occupy mobile octahedral sites (Figure 2.12) which contribute to the high ionic conductivity seen, *ca.* 10^{-4} to 10^{-3} S cm^{-1} at 25 °C.[85]
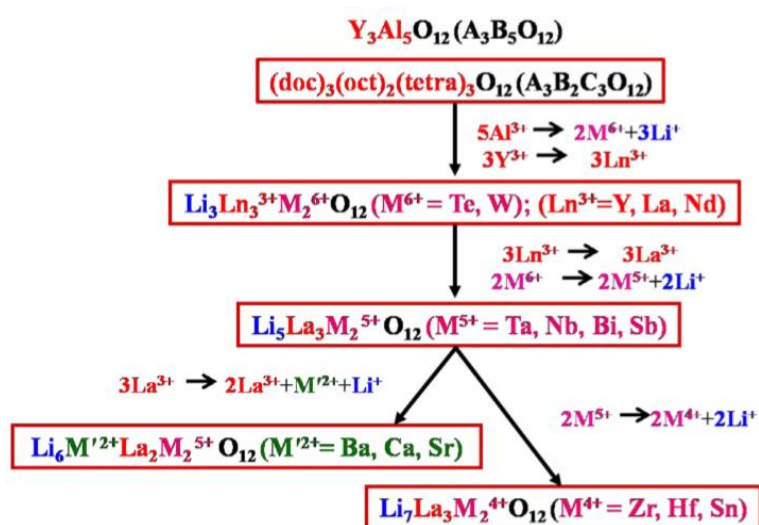
Figure 2.11. Evolution of Li-stuffed garnets with cationic substitution.[84]
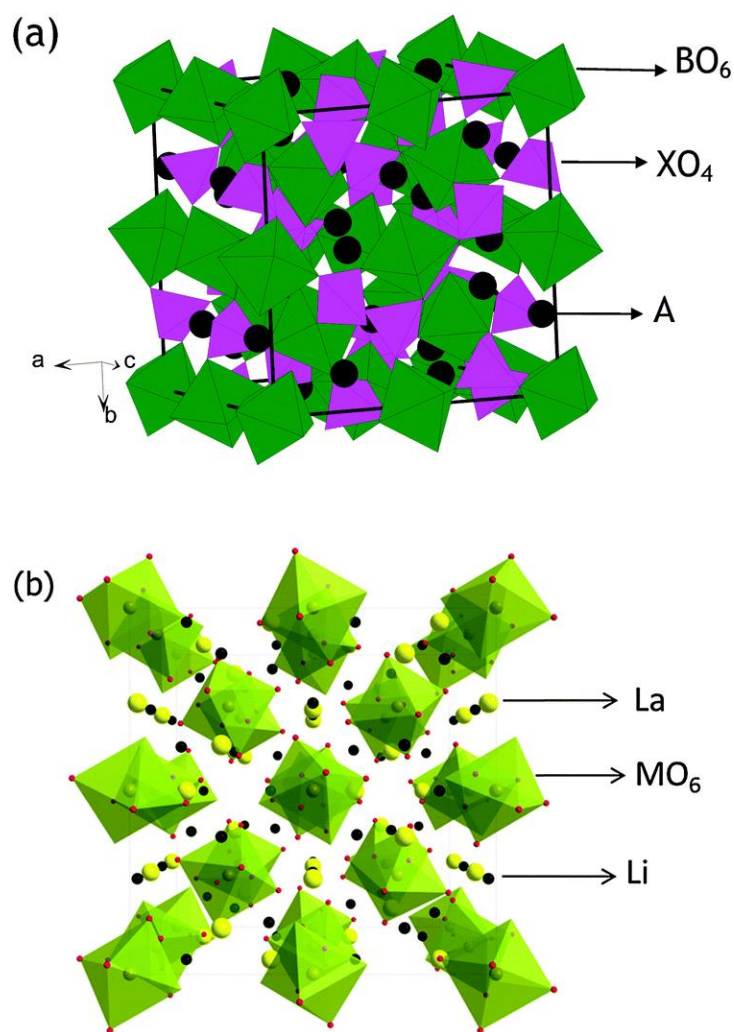
Figure 2.12. Crystal structure of a) an ideal garnet structure, $A_3B_2X_3O_{12}$ (A = rare earth element, B = Te and X = Li) consisting of AO_8, BO_6 and XO_4 units and b) a Li-stuffed garnet-type structure, $Li_5La_3M_2O_{12}$, (M = Ta, Nb, Bi or Sb) consisting of LiO_4, LiO_6, LaO_8 and MO_6 units.[67]

Li_7 phases were first reported in 2007 by Murugan *et al.* by substituting Zr^{4+} for M^{5+} ions in $Li_5La_3M_2O_{12}$ (M = Ta, Nb) to give $Li_7La_3Zr_2O_{12}$ (LLZO).[86] Initial fabrication of these materials reported a cubic Li-stuffed garnet structure and the highest conductivity in the garnet family of 7.74×10^{-4} S cm^{-1} at 25 °C, up to this point.[86] Cubic LLZO was synthesised at 1230 °C for 36 h, with temperatures below this producing tetragonal LLZO. The tetragonal phase exhibits a bulk ionic conductivity two orders of magnitude lower than its cubic counterpart (1.63×10^{-6} S cm^{-1} at 27 °C).[87] The lower Li-ion conductivity was attributed to numerous reasons for instance, lower densities and the difference between the occupancy of Li-ions within tetragonal and cubic LLZO. Three main strategies have been adopted to stabilise the highly conductivity cubic LLZO phase: 1) partially replacing Li^+ with 3+ metal ions to form the general

formula, $Li_{7-3x}M_xLa_3Zr_2O_{12}$ (M = Al, Fe or Ga), 2) substituting Zr^{4+} for 5+ metal ions to form the general formula, $Li_{7-x}La_3Zr_{2-x}M_xO_{12}$ (M = Ta or Nb) and 3) substitution of La^{3+} for 2+ cations to form the general formula $Li_{7-x}La_{3-x}M_xZr_2O_{12}$ (M = Ba, Ca or Sr).[84], [88]–[93] To date, the highest room temperature Li-ion conductivities have resulted because of these strategies, for example $Li_{6.4}La_3Zr_{1.4}Ta_{0.6}O_{12}$ (1.0×10^{-3} S cm^{-1}), and $Li_{6.55}La_3Zr_2Ga_{0.15}O_{12}$ (1.3×10^{-3} S cm^{-1}).[89], [92], [94]

Despite the high ionic conduction seen, Li-stuffed garnets face numerous challenges to overcome before they can be used as solid electrolytes in LIBs. They can undergo proton exchange (H_3O^+/Li^+) and CO_2 absorption when handled under ambient atmospheres, substantially reducing levels of Li-ion conductivity.[67], [84], [95] CO_2 absorption can also lead to $LiCO_3$ formation on the surface of pellets which greatly increases interfacial resistance with electrode materials during charge/discharge. While they are not reduced by Li metal, dendrites can form leading to safety concerns and limited cycle life. Finally, like many Li-based ceramics, they require sintering at high temperatures (>1000 °C) for up to 36 hours which can lead to difficulty in controlling lithium content and unwanted secondary phases.[96]

2.3.2.4. The Complex Spinel, Li$_2$NiGe$_3$O$_8$

Numerous spinel structured materials have been considered for both the cathode and anode (*e.g.* LiNi$_{0.5}$Mn$_{0.5}$O$_4$ and Li$_4$Ti$_5$O$_{12}$). Many of these spinel-structured electrodes exhibit little to no volume change during cycling. This gives the possibility of all-spinel solid-state batteries with excellent lattice matching if a solid electrolyte material with the spinel crystal structure could be developed.

Some such materials have indeed been investigated such as the complex spinel, Li$_2$NiGe$_3$O$_8$.[97], [98] Complex spinel structures have the general formula A$_2$BB'$_3$O$_8$. These phases allow tetrahedral and/or octahedral sites to be occupied by more than one cation. Octahedral sites exhibit a 1:3 cation ordering, which causes a splitting of the octahedral site in normal spinels into two separate octahedral sites (Section 1.3). Complex spinel phases may also have cation mixing between octahedral and tetrahedral sites, to give the general formula (Li$_{2-y}$M$_y$)^{tet}(A$_y$M$_{1-y}$)^{oct1}(M')^{oct2}O$_8$.[99] Several lithium-based complex spinels have previously been reported with the general formula, Li$_2$MM'$_3$O$_8$ (where M = Mg, Co, Ni, Zn and M' = Ti, Ge or Mn). Examples of normal and partially inverse complex spinels are Li$_2$NiGe$_3$O$_8$ and Li$_2$ZnGe$_3$O$_8$, respectively. Li$_2$NiGe$_3$O$_8$ was previously reported with moderate Li-ion conductivity of *ca.* 10^{-7} S cm^{-1} at 60 °C, and crucially is not redox active up to 5 V.[99] At room temperature, the crystal structure for Li$_2$NiGe$_3$O$_8$ consists of lithium in tetrahedral 8*c* sites, nickel and germanium on 4*b* and 12*d* octahedral sites, with oxygen split over 8*c* and 24*e* sites (Figure 2.13).[99] Reeves-McLaren *et al.* used variable-temperature time-of-flight neutron powder diffraction (ToF ND) to investigate the conduction pathway of Li$_2$NiGe$_3$O$_8$, finding the addition of a second Li site (12*d* octahedral site) at high temperatures.[97] The conduction pathway was proposed to be a 3D 8*c*-12*d*-8*c* hopping mechanism (Figure 2.14).[97] Further computational work by Nakayama *et al.* confirmed the activation energy for this hopping pathway was lower than others proposed and therefore more likely.[100] On the other hand, Li$_2$ZnGe$_3$O$_8$ exhibits extremely low Li-ion conduction. This is because zinc in Li$_2$ZnGe$_3$O$_8$ partially occupies 8*c* tetrahedral sites ([Li/Zn]^{tet8c}[Li]^{oct4b}[Ge$_3$]^{oct12d}O$_8$) that block the 8*c*-12*d*-8*c* pathway for Li-ion to migrate through, thus a more complex mechanism is required that limits Li-ion conduction.[97], [99]

If the Li-ion conductivity of these complex spinel phases could be improved, then they may be utilised as solid electrolytes in LIBs or in composite materials with a faster Li-ion

conducting electrolyte. This would help minimise interfacial resistance between the electrode/electrolyte, which many materials currently suffer from.[101]
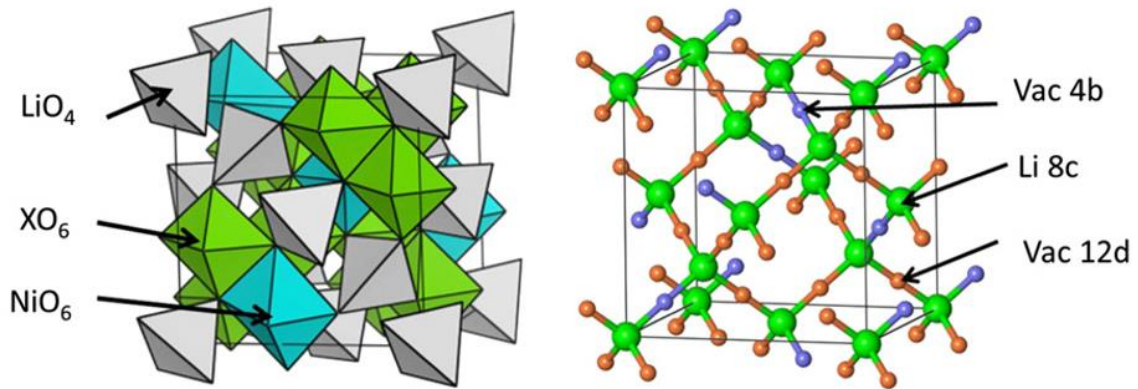
Figure 2.13. Crystal structure and 3D migration network in the complex spinel, $Li_2NiX_3O_8$ (X = Ge).[100]
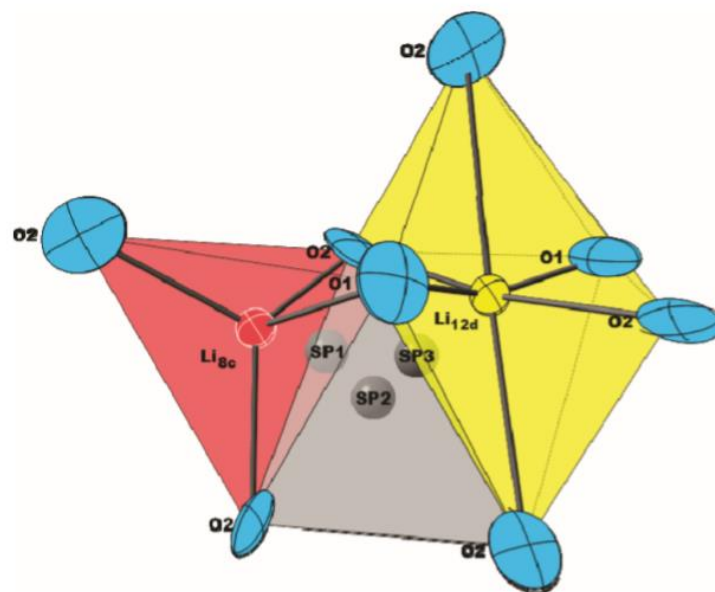
Figure 2.14. 8c-12d-8c conduction pathway in the complex spinel, $Li_2NiGe_3O_8$.[97]

2.4. Cathode Materials

Since the commercialisation of LIBs in 1991, the development and understanding of cathode materials have arguable seen the most improvement, compared to their anode and electrolyte counterparts. This is partly due to the cathode often being the limiting component of full cells in terms of capacity, energy density and cycle life.[45] The main contenders are often drawn from a small number of structural families that include: 1) Layered transition metal oxides, 2) Li-rich metal oxides, 3) Olivine-type and 4) spinel-based structures. These materials all consist of a host framework, which enables Li-ions to shuttle in-between the framework during charge/discharge. Research into state-of-the-art materials have focused of improving operating voltage, capacity, cycle life and safety aspects.

2.4.1. *Layered Transition Metal Oxides*

The layered transition metal oxide family $LiMO_2$ (M = Co, Ni, Mn) was first proposed by Goodenough *et al.* in 1989.[102] This new family of materials resulted in LIBs with higher voltages (3.7 V) and energy densities (120-150 W h/kg) than previously seen.[4] The structure is comprised of a cubic close-packed anion array, (O^{2-}), with cations (Li and M) occupying octahedral sites in ordered alternating layers.[103] During cycling, Li-ions can diffuse via a two-dimensional conduction pathway, in which they can hop into adjacent octahedral sites through empty tetrahedral sites (Figure 2.15). $Li_{1-x}CoO_2$ has a theoretical capacity of 275 mAh g^{-1} however, its specific capacity is only half of this at *ca.* 140 mAh g^{-1} in practice.[2], [104] Attempting to extract more Li-ions, beyond x ≥ 0.5, leads to a phase transition from a rhombohedral to monoclinic crystal structure. Over time, this structural change can result in cracking and other defects of the electrode material.[105] Besides capacity loss over time, delithiation greater than x = 0.5 can cause oxygen gas evolution, which can then react with the organic electrolyte, generating heat and leading to thermal runaway in extreme cases.[4] The use of cobalt means these materials are often toxic and expensive to produce due to cobalt's unstable and limited supply. These supply limitations are expected to greatly increase due to the rapid growth of electric vehicles.[106] Attempts to transition to the lower cost and more environmentally compatible $LiNiO_2$ were unsuccessful due to mixing between Li and Ni layers during synthesis and cycling.[25], [104], [107] This interlayer mixing blocks Li-ion diffusion, thereby limiting capacity, and cycling performance. $LiNiO_2$ also suffers from low

thermal stability and ordered layered structure can be difficult to synthesise.[108] The manganese analogue, LiMnO$_2$, has greatly improved thermal stability although, it also has several drawbacks such as being difficult to synthesise in its layered form, converting to the spinel LiMn$_2$O$_4$ on charge and interlayer mixing between Mn and Li layers.[104], [109]
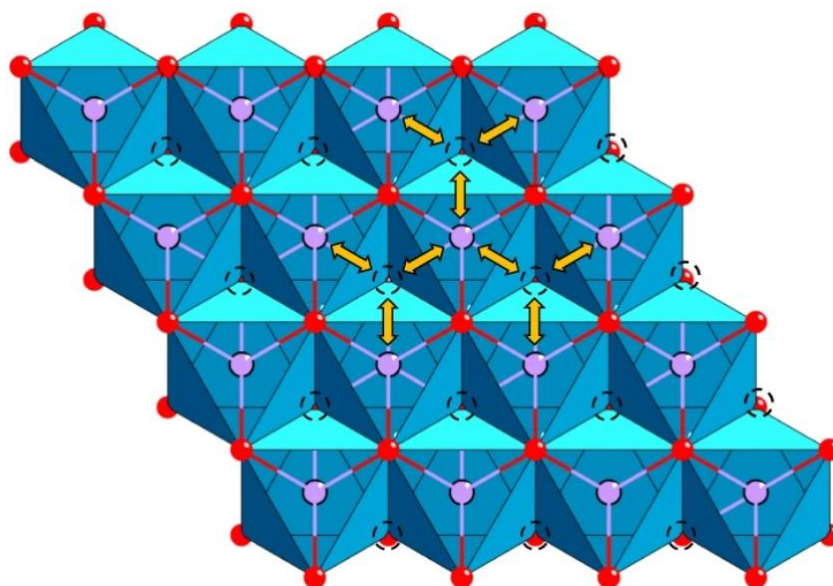
Figure 2.15. Two-dimensional Li-ion conduction pathway (shown by the yellow arrows) in the layered transition metal oxides LiMO$_2$ (M = Co, Ni, or Mn). Li-ion (purple) can diffuse through the lithium layers via hopping into adjacent octahedral site.[103]

Layered transition metal oxides have been studied extensively, with researchers endeavouring to combine the various strengths of Ni, Co, and Mn whilst minimising the drawbacks (Figure 2.16).[104] Doping with Mn has been shown to improve thermal stability, higher Ni content increases discharge capacity however, it also leads to larger volume changes and cracking, reducing cycle life.[110] Despite the increase in cost, Co stabilises the ordered layered structure, preventing intermixing of cations within individual layers as well as improving rate performance.[25], [111], [112] These efforts have led to compounds such as Li[Ni$_{1/3}$Co$_{1/3}$Mn$_{1/3}$]O$_2$, commonly referred to as NMC-111 or NMC-333, which show improved thermal stability and specific capacity (up to 170 mAh g^{-1}) over their LiMO$_2$ counterparts.[104], [113] More current research has focussed on reducing the reliance of Co in NMC, while increasing Ni content due to the higher discharge capacities seen (> 200 mAh g^{-1} in NMC-811).[114] Other strategies include doping with small amounts of non-redox active cations such as Al in an effort to minimise interlayer mixing and increase structural

stability.[111] For example, $Li[Ni_{0.80}Co_{0.15}Al_{0.05}]O_2$ (NCA) has a discharge capacity of 199 mAh g^{-1} and has been successfully commercialised.[114]
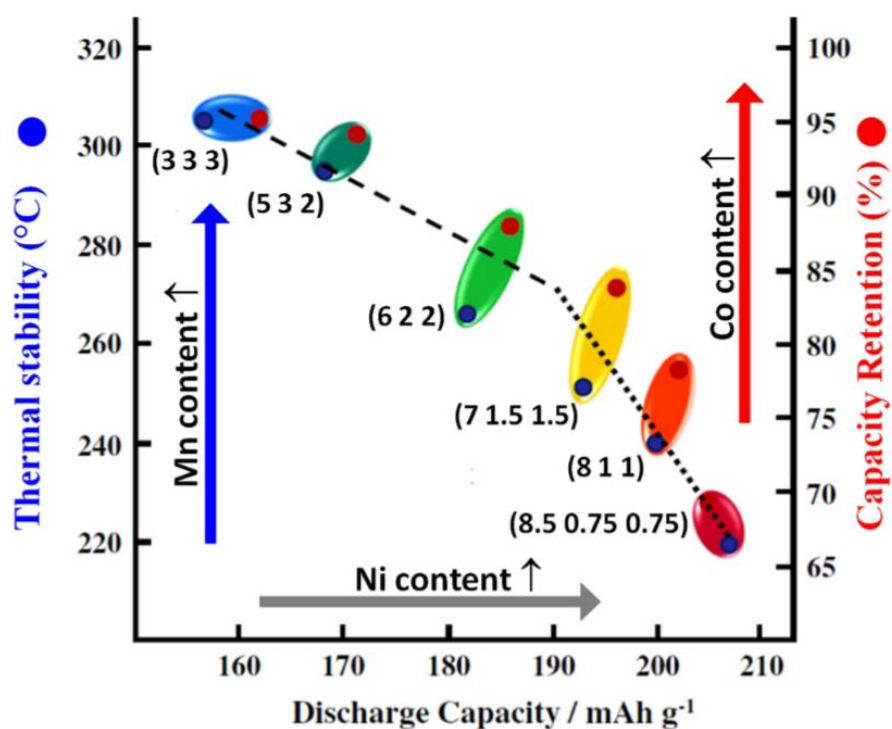
Figure 2.16. Summary of the effects of dopants in the layered transition metal oxide, NMC. The numbers in brackets indicate the Ni, Mn and Co fractional content, showing that Mn governs thermal stability, Ni discharge capacity and Co capacity retention.[104]

2.4.2. Li-rich Cathode Materials

Li-rich oxides are seen as some of the next generation cathode materials due to their large specific capacity, in excess of 250 mAh g^{-1}, with average discharge voltages of *ca.* 3.5 V *vs.* Li/Li+.[104], [115], [116] Li-rich oxides have the general $Li_{1+x}M_{1-x}O_2$ (M = transition metal) with a Li/M ratio greater than one. They are typically classified into two groups: layered Li-rich oxides (*e.g.* Li_2MnO_3 and Li_2RuO_3) and disordered Li-rich oxides (*e.g.* $Li_4Mn_2O_5$ and Li_2VO_2F).[117]–[120] Layered Li-rich oxides adopt a similar structure to $LiMO_2$ (M = Mn, Ni or Co), where additional Li-ions partially occupy the transition metal layer. In contrast, all cations are randomly distributed in disordered Li-rich oxides, Figure 2.17.[116]
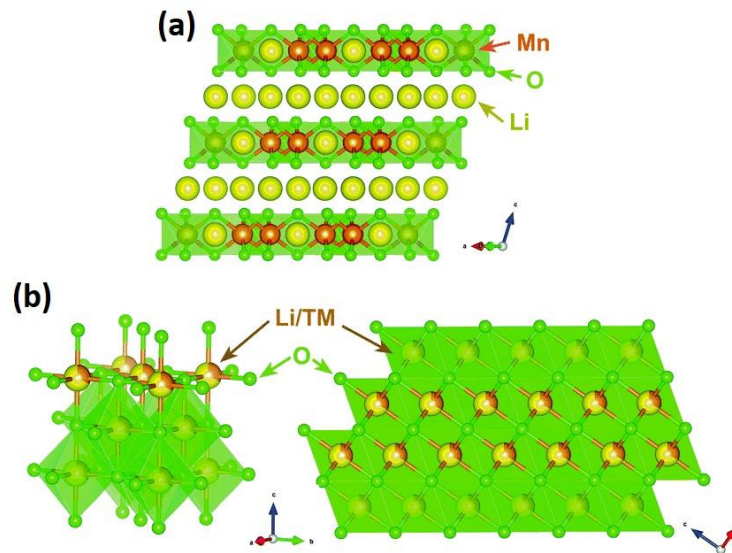
Figure 2.17. Structure of Li-rich oxides a) ordered b) disordered.[116]

Layered Li-rich oxides tend to display greater cycling stability and higher discharge voltages, whereas disordered Li-rich oxides tend to show higher specific capacities.[116] The larger observed capacity seen in these materials, compared to their layered transition metal counterparts, is due to their ability to undergo anionic (O^{2-}/O_2^{2-}), as well as cationic redox reactions. These redox processes are typically observed in charge/discharge voltage profiles by a smooth slope below 4.5 V, followed by a voltage plateau between 4.5 to 4.6 V during the initial charge. On discharge, a single slope is typically seen from 4.6 to 3 V, Figure 2.18.[121] This highlight's one of the significant challenges in developing Li-rich cathode materials due to voltage fade over subsequent cycles, reducing energy density. Additional drawbacks include capacity fade and low initial coulombic efficiency due to irreversible structural changes and severe O_2 loss, which currently limits their commercialisation.[116]
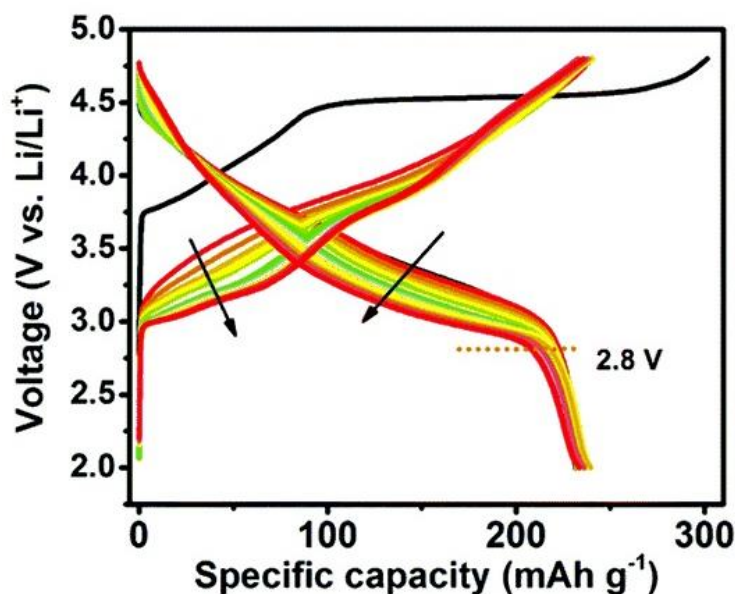
Figure 2.18. Charge/discharge voltage profile of the layered Li-rich oxide $Li_{1.2}Ni_{0.2}Mn_{0.6}O_2$, highlighting the challenge of voltage fade in Li-rich cathode materials.[121]

2.4.3. Olivine-type Cathode Materials

Olivine-type materials (theoretical capacity ≈ 170 mAh g^{-1}), with general formula $LiMPO_4$ (M = Fe, Mn, Co and Ni) are promising cathodes due to their potential use in applications requiring high power density and thermal stability e.g. electric vehicles.[122]–[124] The olivine-type structure consists of a distorted hexagonal close-packed framework in which Li^+ and M^{2+} ions occupy octahedral sites, with P^{5+} in tetrahedral sites, Figure 2.19.[125] Li^+ ions can only travel through one-dimensional (1D) tunnels, which together with the lack of a continuous network of MO_6 octahedra, results in low electronic and ionic conductivity.[124], [126], [127] This is one of the major drawbacks of this class of materials. Of the different olivine-type materials $LiCoPO_4$ and $LiNiPO_4$ are considered high voltage cathodes, operating at 4.8 V and 5.1 V respectively. $LiMnPO_4$ and $LiFePO_4$ operate at lower potentials of 4.1 V and 3.4 V, respectively.[124] The higher voltage of Co and Ni- olivine materials enables larger energy densities, though these are currently incompatible with current organic electrolytes, limiting cycle life and practical uses.[124], [128] Likewise, $LiMnPO_4$ has a higher theoretical energy density than $LiFePO_4$ but suffers from lower electronic conductivity (reducing rate performance) and capacity fade over time due to structural changes caused by the presence of Mn^{3+} and associated Jahn-Teller distortions, which limit Li-ion diffusion at the $LiMnPO_4/MnPO_4$ interface.[128]

40

LiFePO$_4$ has received the most attention due to its low toxicity, low cost, inclusion of high abundance materials, and excellent thermal stability.[126], [129] Despite the lower energy density compared to other olivine-type materials, LiFePO$_4$ has the highest electronic and ionic conductivity and is the easiest to prepare. Since its conception, researchers have focused on improving its electrochemical properties via carbon coating, reduction of particle size and partial cation or anion substitution.[126], [130]–[134] LiFePO$_4$ has been successfully commercialised in applications that require long cycle life at moderate voltages.[124]
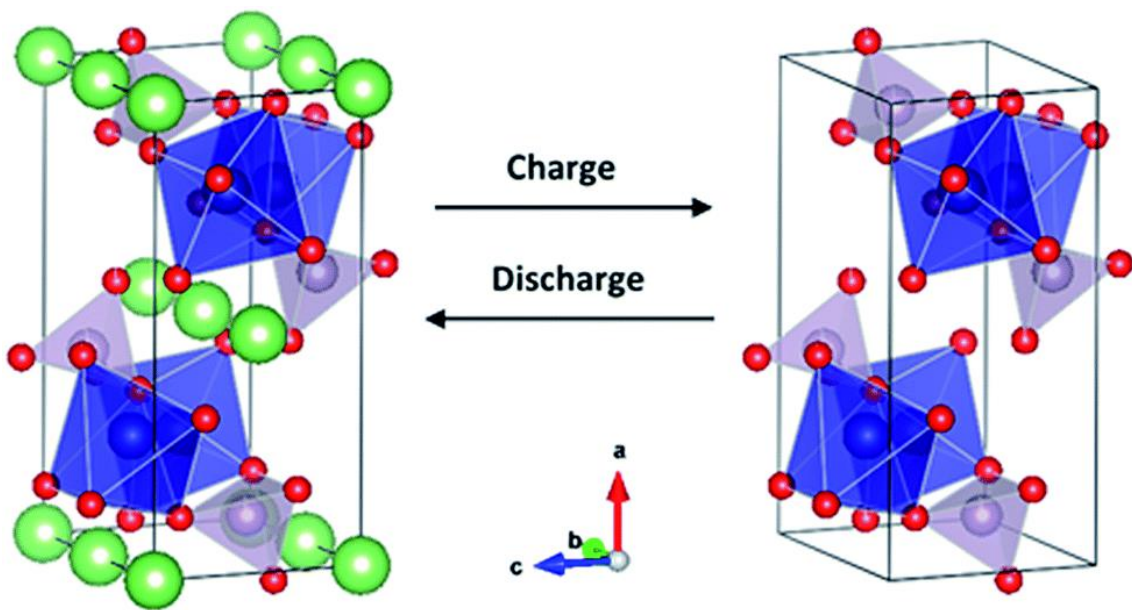
Figure 2.19. Structure of Olivine-type LiMPO$_4$ (M = Fe, Co or Ni) during charge and discharge, showing Li-ion in green, MO$_6$ octahedra in blue and PO$_4$ tetrahedra in purple.[123]

2.4.4. Li-containing Normal Spinels

$LiMn_2O_4$ was first reported as a potential cathode material in 1984, with a theoretical capacity of *ca.* 148 mAh g^{-1}.[135] It benefits from many of the same safety, cost, and environmental factors as $LiFePO_4$, whilst operating at a slightly higher voltage of 3.9 V vs Li/Li$^+$.[136], [137] $LiMn_2O_4$ adopts a cubic spinel structure (Section 1.3), which enables Li-ions to follow a three-dimensional conduction pathway through empty 16*c* octahedral sites, adjacent to their typical 8*a* sites, before migrating on to the next tetrahedral site forming an 8*a*-16*c*-8*a* route (Figure 2.20). $LiMn_2O_4$ was successfully commercialised in the first-generation electric vehicles *e.g.* Nissan Leaf. Nevertheless, $LiMn_2O_4$ suffers from significant capacity loss over time at elevated temperatures due to 1) disproportionation of Mn^{3+} to Mn^{2+} and Mn^{4+} and 2) Jahn-Teller distortion of Mn^{3+} ions. The Jahn-Teller distortions can cause a phase transition from cubic to orthorhombic; while Mn^{2+} can react with the electrolyte and SEI layer in side-reactions that consume Li-ions, thus reducing capacity.[136]–[138] Partial substitution of Mn with other transition metal ions to form $LiMn_{2-x}M_xO_4$ (M = Ni, Fe, Cr, Cu and Co), Table 2.1, can limit the disproportionation reaction and improve cycle life, whilst also increasing the operating voltage from 3.9 V to *ca.* 5.0 V depending on the transition metal used.[139]–[144] This offers an alternative route towards superior energy densities relative to pure $LiMn_2O_4$.[142], [145]
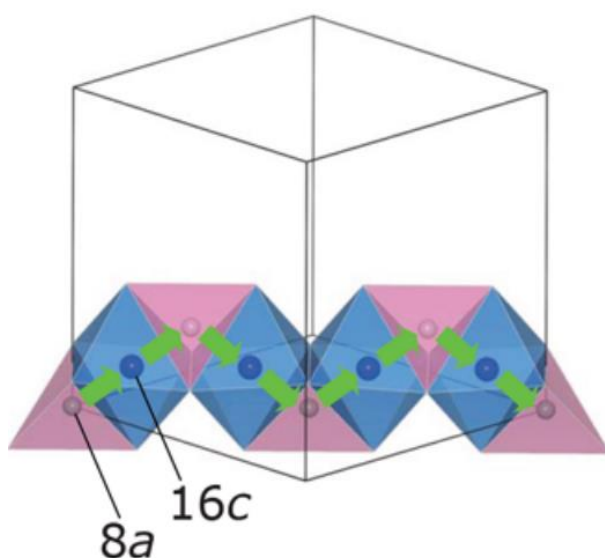
Figure 2.20. Li-ion conduction pathway in normal disordered spinels.[30]

Table 2.1. Electrochemical data for potential high voltage spinel-based cathode materials.[145]–[147]

Cathode Material	Structure Type	Redox couple and Discharge voltage *vs.* Li/Li$^+$	Theoretical Capacity (mAh g^{-1})
LiNi$_{0.5}$Mn$_{1.5}$O$_4$	Normal Spinel	Ni$^{2+/3+/4+}$, 4.7 V	147
LiCr$_x$Mn$_{2-x}$O$_4$ (x = 0.5 to 1)	Normal Spinel	Cr$^{3+/4+}$, 4.8 V Mn$^{3+/4+}$ 3.9 V	151
LiCo$_x$Mn$_{2-X}$O$_4$ (x = 0.5 to 1)	Normal Spinel	Co$^{3+/4+}$, 5.0 V Mn$^{3+/4+}$ 3.9 V	145
LiFe$_{0.5}$Mn$_{1.5}$O$_4$	Normal Spinel	Fe$^{3+/4+}$, 5.1 V Mn$^{3+/4+}$ 3.9 V	148
LiCu$_{0.5}$Mn$_{1.5}$O$_4$	Normal Spinel	Cu$^{2+/3+}$, 4.9 V	145
LiNiVO$_4$	Inverse Spinel	Ni$^{2+/3+}$, 4.8 V	148

These doped LiMn$_2$O$_4$ materials have the general formula LiMMNO$_4$ (M = Cr or Co) or Li$_2$MMn$_3$O$_8$ (M = Cr, Cu, Co, Fe, or Ni).[145] Several of these materials exhibit cationic ordering on the octahedral sites, *e.g.* 3:1 order of Li$_2$NiMn$_3$O$_8$. Sigala *et al.* reported Cr substitution for Mn in the formula LiCr$^{3+}_x$Mn$^{3+}_{1-x}$Mn^{4+}O$_4$ (*x* = 0 to 1) gave rise to two voltage plateaus, one at 3.9 V due to Mn$^{3+/4+}$ and another at 4.8 V due to Cr$^{3+/4+}$. Cr-substitution was observed to improved cyclability up to *x* = 0.5 compared to LiMn$_2$O$_4$.[139] This improvement is likely due to the replacement of Mn^{3+} ions, limiting disproportionation and Jahn-Teller distortions. Above *x* = 0.5 Sigala *et al.* noticed a detrimental effect of Cr-substitution, which was explained by structural defects during cycling. These structural defects can lead to partial occupancy of Lithium tetrahedral sites by Cr^{6+} ions that block the 8*a*-16*c*-8*a* conduction pathway.[140] Substitution of Mn by Cu, Co and Fe with the formulas Li$_2$CuMn$_3$O$_8$, Li$_2$CoMn$_3$O$_8$, and Li$_2$FeMn$_3$O$_8$ also leads to the observation of two voltage plateaus at 3.9 V and 4.9 V for Fe and Cu and 5.1 V for Co.[141]–[145] As previously mentioned, Mn^{3+} ions can have a detrimental effect on cyclability and thus the 3.9 V plateau should be avoided. On cycling,

$LiCoMnO_4$ and $Li_2NiMn_3O_8$ both exhibit a single (dis)charge plateau at 5.0 V and 4.7 V respectively, with Mn ions all ideally being in the 4+ oxidation state. Initial reports show that $LiCoMnO_4$ and $Li_2NiMn_3O_8$ exhibit discharge capacities of *ca.* 95 mAh g^{-1}, with theoretical capacities of 145 and 147 mAh g^{-1} respectively.[145] Despite the slightly lower voltage, $Li_2NiMn_3O_8$ have received a greater deal of attention because nickel is cheaper and more environmentally friendly than cobalt, as previously discussed.

The disordered $Fd\bar{3}m$ phase of $Li_2NiMn_3O_8$ is considered to have improved long term cyclability over the ordered $P4_332$ phase. This has been attributed to greater electronic conductivity and charge-transfer kinetics of the disordered phase.[136], [138] However, preparation of phase-pure $Li_2NiMn_3O_8$ can be difficult due to the formation of rocksalt impurity phases, such as NiO and Li_2MnO_3.[147], [148] The ordered phase is typically synthesised at 700 °C, while the disordered phase is typically prepared by sintering at 900 °C. The elevated temperatures required can result in oxygen loss and the reduction of Mn^{4+} to Mn^{3+}.[138], [148] In this instance, the formation of an $Li_2MnO_{3-\delta}$ phase with a small amount of Mn^{3+} has been shown to improve rate performance due to increased electronic conductivity.[138] Small amounts of substitution of Ni and/or Mn by M^{3+} ions for instance, Fe and Cr, have been shown to be beneficial to long term cycling (Figure 2.21).[149] Such dopants can reduce oxygen vacancies and rocksalt impurities, whilst also generating small amounts of Mn^{3+} to charge balance, increasing charge-transfer kinetics.[150]

Other significant problems with lithium manganate spinels are the dissolution of Mn at high voltages and the breakdown of the organic electrolytes. Both doping and surface coating, *e.g.* with Al_2O_3, have been demonstrated to be beneficial and limit these concerns.[151], [152] However, these strategies do not eliminate the drawbacks of high voltage cathodes with current electrolytes completely; more robust liquid electrolytes and/or solid electrolytes need to be developed to make high voltage cathodes commercially viable.
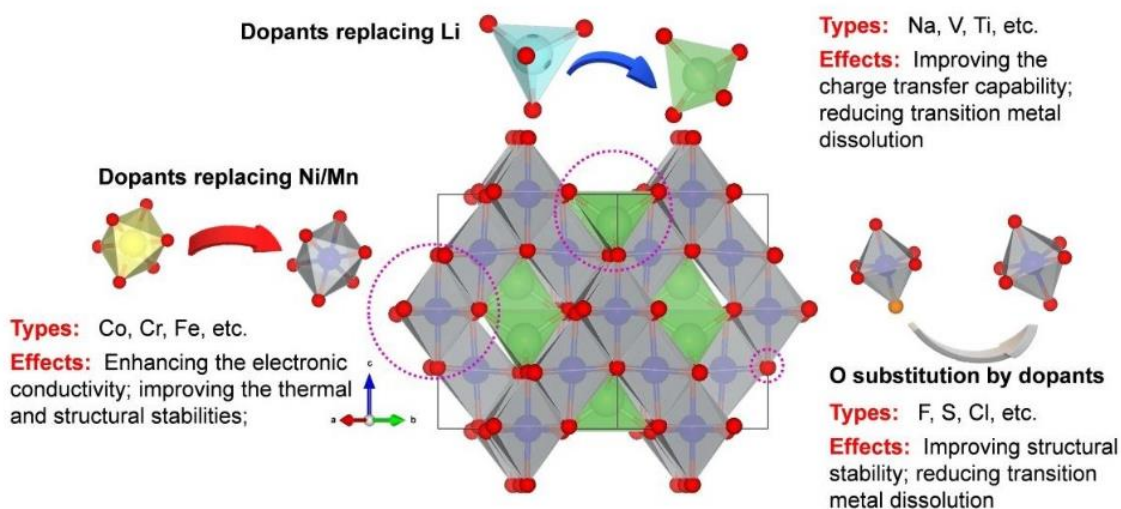
Figure 2.21. Summary of doping strategies for the high voltage cathode $Li_2NiMn_3O_8$.[149]

2.4.5. Li-containing Inverse Spinels

Cathode materials based on the inverse spinel structure have received less attention than their normal spinel counterparts. The three main materials investigated are $LiMnVO_4$, $LiCoVO_4$ and $LiNiVO_4$, operating at 3.8 V, 4.2 V and 4.8 V *vs.* Li/Li$^+$, respectively.[153], [154] These vanadate-based inverse spinels have theoretical capacities of *ca.* 148 mAh g^{-1} however, their observed capacity is significantly lower at between 40 to 50 mAh g^{-1}.[155] $LiMnVO_4$ displays the highest observed capacity at *ca.* 90 mAh g^{-1}, though the phase can only be formed at high pressures (5.5 GPa), instead forming an olivine structure at ambient pressures.[154], [156] Another drawback is the significant and irreversible capacity loss over time. Explanations for this have been limited, with low electronic conductivity and cation mixing over octahedral and tetrahedral sites during charge/discharge cycles suggested to be major factors.[156]–[158]

In an effort to improve cycling performance, several doping strategies have been carried out, which includes: 1) mixed solid solutions between $LiNiVO_4$ and $LiCoVO_4$ ($LiNi_{1-x}Co_xVO_4$, x = 0 to 1), 2) partial substitution of Co^{2+} for Cr, Cu and Fe ($LiCo_{0.9}M_{0.1}VO_4$), and 3) Partial substitution of $LiNiVO_4$ and $LiCoVO_4$ by Mn to form the general formula $Li(Ni/Co)_{1-x}Mn_xVO_4$.[159]–[161] The first strategy had little effect on the overall cycling performance. However, strategies two and three have been shown to improve electronic conductivity and

overall cycling performance, increasing initial (dis)charge capacities, and improving cyclability.[160], [161] Following on from these strategies, several groups have tried co-doping of LiNiVO$_4$ with Mn and Co to produce the composition LiNi$_{1/3}$Co$_{1/3}$Mn$_{1/3}$VO$_4$.[156], [162] Unlike the parent phase LiNiVO$_4$, only Mn and Co in LiNi$_{1/3}$Co$_{1/3}$Mn$_{1/3}$VO$_4$ appears to be redox active, operating at between 3.6 to 4.2 V for Mn$^{2+/4+}$ and between 4.3 to 4.6 V for Co$^{2+/3+}$. Kitajou *et al.* reported that the initial capacity of LiNi$_{1/3}$Co$_{1/3}$Mn$_{1/3}$VO$_4$ can be increased further by the introduction of transition metal vacancies to give the general formula Li(Ni$_{1/3}$Co$_{1/3}$Mn$_{1/3}$)$_{1-x}$V$_{1-x}$O$_4$ (x = 0.1 and 0.2).[156] This material has the highest observed discharge capacity in an inverse spinel, at 120 mAh g^{-1} on the first cycle, decreasing to *ca.* 100 mAh g^{-1} after 20 cycles. Despite the relatively high voltage inverse spinels can operate at, the dramatic capacity fade over the limited number of charge/discharge cycles (20 to 30 cycles) investigated is a significant hindrance to their practical use.

Unlike normal spinels such as LiMn$_2$O$_4$, Li-ion diffusion in inverse spinels is unexpected as there are no obvious tunnels through which Li-ions can diffuse. This is due to the random distribution of octahedral sites by both Li and transition metal cations. For example, once Li-ions hop into adjacent empty tetrahedral sites, their diffusion may be blocked by the presence of the transition metal cations in octahedral sites. Nevertheless, the limited reversible charge/discharge capacities suggest the Li-ion conduction pathway in inverse spinels is not completely blocked by the shared occupancy of octahedral sites. Page *et al.* used neutron and X-ray total scattering to investigate the local ordering in a number of inverse spinels.[163] It was suggested that inverse spinels such as LiNiVO$_4$ adopted an ordered structure (space group P4$_1$22) up to 8 Å, in which Li$^+$ and Ni^{2+} cations order alternatively in 4*a* and 4*b* octahedral sites, Figure 2.22.[163] However, these octahedral sites are not fully ordered, with *ca.* 25 % cation site mixing observed in the local structure. In contrast, no ionic conduction is reported in the long range ordered inverse spinel LiZnNbO$_4$ (P4$_1$22), in which Zn^{2+} cations occupy tetrahedral 4*c* sites, with Li$^+$ and Nb^{5+} cations fully ordered over 4*a* and 4*b* octahedral sites.[164]
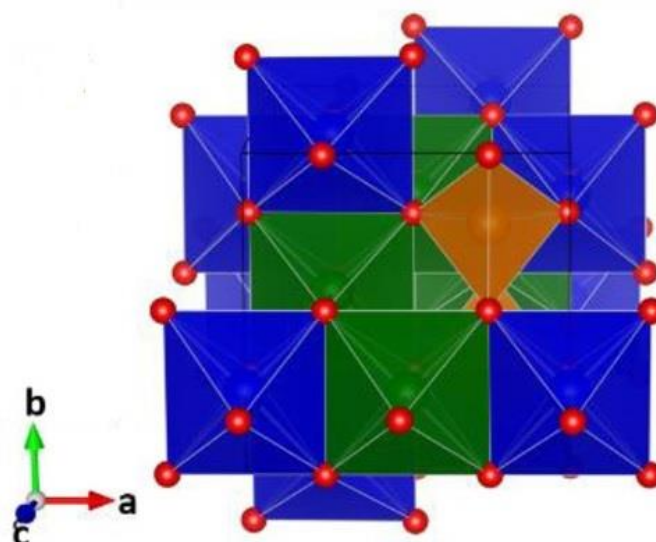
Figure 2.22. Short range ordered (P4$_1$22) structure of LiM^{2+}VO$_4$. LiO$_6$ and MO$_6$ octahedra are shown in green and blue, respectively, with VO$_4$ tetrahedra in orange.[163]

Several other inverse spinels have previously been reported in the 1960's with the general formula Li$_3$M^{3+}V$_2$O$_8$ (M = Cr or Ga). Blasse reported an Li$_3$CrV$_2$O$_8$ phase crystallising in an inverse spinel structure, [Li$_{1.5}$Cr$_{0.5}$]^{oct}[V]^{tet}O$_4$,[165] suggesting a 1:3 ordering on octahedral sites was evident from X-ray diffraction patterns. At a similar time, Joubert and Durif reported the same Li$_3$CrV$_2$O$_8$ phase to be a disordered inverse spinel (space group $Fd\overline{3}m$).[166] The aforementioned study by Page *et al.* indicated that there is a correlation between the ionic radii and cation charge difference on the presence of ordering on octahedral sites. For instance, an inverse spinel with a larger charge and ionic radius difference is likely to possess long range ordering, as is the case for LiZnNbO$_4$ (charge and ionic radius difference = 4 and 0.12 Å respectively).[163], [164] Considering this, Li$_3$CrV$_2$O$_8$, where the charge and ionic radius difference are 2 and 0.14 Å, respectively, may exhibit short-range ordered or long-range ordering depending on the synthetic conditions. No electrochemical data have been reported for this inverse spinel material. The cation ordering and thus Li-ion conduction pathway in these materials are likely to be complex.

It is clear that there is a need to investigate a range of inverse spinel compositions to better understand how Li-ions diffuse through these complex materials, and to expand the understanding of their electrochemical properties.

47

2.5. Aims

As seen throughout this literature review, materials with the spinel structure have great potential to be used in LiBs. Several of these, such as $LiMn_2O_4$ and $Li_4Ti_5O_{12}$, are already available for commercial use. Investigations into materials with the inverse spinel structure have also shown promise as both high voltage cathodes and high capacity anodes. Nevertheless, the continued development of such materials has been restricted by the lack of a complete understanding of the structural and Li-ion diffusion properties. The overall aim of this thesis is to evaluate the crystal structures, Li-ion diffusion kinetics and electrochemical properties within novel inverse spinel structures. As a result, this work will enable future researchers to develop new strategies and materials with greatly improved electrochemical properties, thus leading to their commercialisation within future LiB technologies.

The aims of Chapter 4 were to revisit the inverse spinel, $Li_3CrV_2O_8$ and fully characterise its crystal structure through the use of combined X-ray and neutron refinements. The synthesis of a novel solid solution between $Li_2Ni_2V_2O_8$ and $Li_3CrV_2O_8$ was also investigated. Subsequently, the effect of altering the Li and transition metal ratio on the electrical properties were investigated through impedance spectroscopy in the compositions $Li_{2+x}Ni_{2-2x}Cr_xV_2O_8$ ($0 \leq x \leq 1$).

In Chapter 5 the average Li-ion diffusion mechanisms within the inverse spinels, $Li_3CrV_2O_8$ and $Li_{2.5}NiCr_{0.5}V_2O_8$, were investigated through variable-temperature neutron powder diffraction Rietveld refinements. Alongside this, the local Li-ion kinetics were investigated using muon spectroscopy.

Finally, the aims of Chapter 6 were to evaluate the electrochemical properties of $Li_{2+x}Ni_{2-2x}Cr_xV_2O_8$, x = 0, 0.25, 0.5, 0.75 and 1 as potential cathode and anode materials for LiBs. This was attempted through the use of galvanostatic cycling and in-situ cycling X-ray absorption near edge structure (XANES). This is of interest because the substitution of Ni^{2+} for Cr^{3+} and Li^+ may influence cycle life, as well as improving the capacity of inverse spinels by increasing the number of charge carriers available.

2.6. References

[1]   B. Scrosati and J. Garche, "Lithium batteries: Status, prospects and future," *J. Power Sources*, vol. 195, no. 9, pp. 2419–2430, 2010.

[2]   J. B. Goodenough and K. Park, "The Li-Ion Rechargeable Battery: A Perspective," *J. Am. Chem. Soc.*, vol. 135, no. 4, pp. 1167–1176, 2013.

[3]   J. M. Tarascon and M. Armand, "Issues and challenges facing rechargeable lithium batteries.," *Nature*, vol. 414, no. 6861, pp. 359–367, 2001.

[4]   J. B. Goodenough, "Batteries and a Sustainable Modern Society," *Electrochem. Soc. Interface*, vol. 25, no. 3, pp. 67–70, 2016.

[5]   M. S. Whittingham, "Electrical energy storage and intercalation chemistry.," *Science (80-.).*, vol. 192, no. 4244, pp. 1126–1127, 1976.

[6]   B. Horstmann *et al.*, "Strategies towards enabling lithium metal in batteries: interphases and electrodes," *Energy Environ. Sci.*, 2021.

[7]   R. W. Francis and H. A. Christopher, "Lithium-Aluminum Electrode," *J. Electrochem. Soc.*, vol. 124, no. 10, pp. 1490–1492, 1977.

[8]   M. Mohri *et al.*, "Rechargeable lithium battery based on pyrolytic carbon as a negative electrode," *J. Power Sources*, vol. 26, pp. 545–551, 1989.

[9]   "The Nobel Prize in Chemistry 2019.," *NobelPrize.org. Nobel Prize Outreach AB*, 2021. [Online]. Available: https://www.nobelprize.org/prizes/chemistry/2019/press-release/. [Accessed: 28-Aug-2021].

[10]   A. Eftekhari, "Low voltage anode materials for lithium-ion batteries," *Energy Storage Mater.*, vol. 7, no. December 2016, pp. 157–180, 2017.

[11]   J.-G. Zhang, W. Xu, and J. Wang, "Lithium metal anodes for rechargeable batteries," *Energy Environ. Sci.*, vol. 7, pp. 513–537, 2014.

[12]   J. Lu, Z. Chen, F. Pan, Y. Cui, and K. Amine, "High-Performance Anode Materials for Rechargeable Lithium-Ion Batteries," *Electrochem. Energy Rev.*, vol. 1, no. 1, pp. 35–53, 2018.

[13]   H. Cheng, J. G. Shapter, Y. Li, and G. Gao, "Recent progress of advanced anode materials of lithium-ion batteries," *J. Energy Chem.*, vol. 57, pp. 451–468, 2021.

[14]   J. R. Dahn, T. Zheng, Y. Liu, and J. S. Xue, "Mechanisms for lithium insertion in carbonaceous materials," *Science (80-.).*, vol. 270, no. 5236, pp. 590–593, 1995.

[15]   C. K. Chan *et al.*, "High-performance lithium battery anodes using silicon nanowires," *Nat. Nanotechnol.*, vol. 3, pp. 31–35, 2007.

[16]   N. A. Kaskhedikar and J. Maier, "Lithium Storage in Carbon Nanostructures," *Adv. Mater.*, vol. 21, pp. 2664–2680, 2009.

[17]   R. Yazami, "Surface chemistry and lithium storage capability of the graphite ± lithium electrode," *Electrochim. Acta*, vol. 45, no. 1–2, pp. 87–97, 1999.

[18]   D. Aurbach, B. Markovsky, I. Weissman, E. Levi, and Y. Ein-eli, "On the correlation between surface chemistry and performance of graphite negative electrodes for Li ion batteries," *Electrochim. Acta*, vol. 45, pp. 67–86, 1999.

[19]   A. Tomaszewska *et al.*, "Lithium-ion battery fast charging: A review," *eTransportation*, vol. 1, p. 100011, 2019.

[20]   T. Ohzuku, A. Ueda, and N. Yamamota, "Zero-Strain Insertion Material of $Li[Li_{4/3}Ti_{5/3}]O_4$ for Rechargeable Lithium Cells," *J. Electrochem. Soc.*, vol. 142, no. 5, pp. 1431–1435, 1995.

[21]   X. Sun, P. V. Radovanovic, and B. Cui, "Advances in spinel $Li_4Ti_5O_{12}$ anode materials for lithium-ion batteries," *New J. Chem.*, vol. 39, no. 1, pp. 38–63, 2015.

[22]   W. J. H. Borghols, M. Wagemaker, U. Lafont, and E. M. Kelder, "Li-Ion Diffusion in the Equilibrium Nanomorphology of Spinel $Li_{4+x}Ti_5O_{12}$," *J. Phys. Chem. B*, vol. 12, no. 9, pp. 17786–17792, 2009.

[23]   J. Shu, "Electrochemical behavior and stability of $Li_4Ti_5O_{12}$ in a broad voltage window," *J. Solid State Electrochem.*, vol. 13, no. 10, pp. 1535–1539, 2009.

[24]   B. M. Wagemaker *et al.*, "A Kinetic Two-Phase and Equilibrium Solid Solution in Spinel $Li_{4+x}Ti_5O_{12}$," *Adv. Mater.*, vol. 18, pp. 3169–3173, 2006.

[25]   N. Nitta, F. Wu, J. T. Lee, and G. Yushin, "Li-ion battery materials : present and future," *Materialstoday*, vol. 18, no. 5, pp. 252–264, 2015.

[26]   B. Gangaja, S. Nair, and D. Santhanagopalan, "Surface-Engineered $Li_4Ti_5O_{12}$ Nanostructures for High-Power Li-Ion Batteries," *Nano-Micro Lett.*, vol. 12, no. 1, pp. 1–11, 2020.

[27]   J. C. Daigle *et al.*, "Boosting Ultra-Fast Charge Battery Performance: Filling Porous nano $Li_4Ti_5O_{12}$ Particles with 3D Network of N-doped Carbons," *Sci. Rep.*, vol. 9, no. 1, pp. 1–9, 2019.

[28]   R. Kanno, Y. Takeda, M. Hasegawa, Y. Kawamoto, and O. Yamamoto, "Mechanistic studies on the electrochemically lithiated spinel $LiCuVO_4$," *J. Solid State Chem.*, vol. 94, no. 2, pp. 319–328, 1991.

[29]   C. Rossignol, G. Ouvrard, and E. Baudrin, "X-Ray Absorption Spectroscopy Study of the Structural and Electronic Changes upon Cycling of $LiNiVO_4$ as a Battery Electrode," *J. Electrochem. Soc.*, vol. 148, no. 8, p. A869, 2001.

[30]   T. Uyama, K. Mukai, and I. Yamada, "Structure, Magnetism, and Electrochemistry of $LiMg_{1-x}Zn_xVO_4$ Spinels with $0 \leq x \leq 1$," *Inorg. Chem.*, vol. 59, no. 1, pp. 777–789, 2020.

[31]   C. Liang, M. Gao, H. Pan, Y. Liu, and M. Yan, "Lithium alloys and metal oxides as high-capacity anode materials for lithium-ion batteries," *J. Alloys Compd.*, vol. 575, pp. 246–256, 2013.

[32]   C. J. Wen and R. A. Huggins, "Chemical diffusion in intermediate phases in the lithium-silicon system," *J. Solid State Chem.*, vol. 37, no. 3, pp. 271–278, 1981.

[33]   J. H. Ryu, J. W. Kim, Y.-E. Sung, and S. M. Oh, "Failure Modes of Silicon Powder Negative

Electrode in Lithium Secondary Batteries," *Electrochem. Solid-State Lett.*, vol. 7, no. 10, p. A306, 2004.

[34]   W. Wang and P. N. Kumta, "Nanostructured Hybrid Silicon / Carbon," *ACS Nano*, vol. 4, no. 4, pp. 2233–2241, 2010.

[35]   A. Magasinski, P. Dixon, B. Hertzberg, A. Kvit, J. Ayala, and G. Yushin, "High-performance lithium-ion anodes using a hierarchical bottom-up approach," *Nat. Mater.*, vol. 9, no. 4, pp. 353–358, 2010.

[36]   P. J. Yang, "Engineering the Distribution of Carbon in Silicon Oxide Nanospheres at the Atomic Level for Highly Stable Anodes," *Angew. Chemie - Int. Ed.*, vol. 58, no. 20, pp. 6669–6673, 2019.

[37]   J. Sourice *et al.*, "One-step synthesis of Si@C nanoparticles by laser pyrolysis: High-capacity anode material for lithium-ion batteries," *ACS Appl. Mater. Interfaces*, vol. 7, no. 12, pp. 6637–6644, 2015.

[38]   A. Débart, L. Dupont, P. Poizot, J.-B. Leriche, and J. M. Tarascon, "A Transmission Electron Microscopy Study of the Reactivity Mechanism of Tailor-Made CuO Particles toward Lithium," *J. Electrochem. Soc.*, vol. 148, no. 11, p. A1266, 2001.

[39]   D. Pasero, N. Reeves, and A. R. West, "Co-doped Mn_3O_4: A possible anode material for lithium batteries," *J. Power Sources*, vol. 141, no. 1, pp. 156–158, 2005.

[40]   Y. M. Kang *et al.*, "A study on the charge-discharge mechanism of Co_3O_4 as an anode for the Li ion secondary battery," *Electrochim. Acta*, vol. 50, no. 18, pp. 3667–3673, 2005.

[41]   Q. Wu, R. Jiang, L. Mu, and S. Xu, "Fe_3O_4 anodes for lithium batteries: Production techniques and general applications," *Comptes Rendus Chim.*, vol. 22, no. 1, pp. 96–102, 2019.

[42]   J. B. Goodenough and Y. Kim, "Challenges for Rechargeable Li Batteries," *Chem. Mater.*, vol. 22, no. 3, pp. 587–603, 2010.

[43]   Q. Li, J. Chen, L. Fan, X. Kong, and Y. Lu, "Progress in electrolytes for rechargeable Li-based batteries and beyond," *Green Energy Environ.*, vol. 1, no. 1, pp. 18–42, 2016.

[44]   D. R. Sadoway and A. M. Mayes, "Portable Power : Advanced Rechargeable Lithium Batteries," *Mat. Res. Bull.*, vol. 27, no. 8, pp. 590–596, 2002.

[45]   V. Etacheri, R. Marom, R. Elazari, G. Salitra, and D. Aurbach, "Challenges in the development of advanced Li-ion batteries: a review," *Energy Environ. Sci.*, vol. 4, no. 9, pp. 3243–3262, 2011.

[46]   K. Xu, "Electrolytes and Interphases in Li-Ion Batteries and Beyond," *Chem. Rev.*, vol. 114, no. 23, pp. 11503–11618, 2014.

[47]   M. T. Ong, O. Verners, E. W. Draeger, A. C. T. Van Duin, V. Lordi, and J. E. Pask, "Lithium Ion Solvation and Diffusion in Bulk Organic Electrolytes from First Principles and Classical Reactive Molecular Dynamics," *J. Phys. Chem. B*, vol. 119, no. 4, pp. 1535–1545, 2015.

[48] E. Peled and S. Menkin, "Review—SEI: Past, Present and Future," *J. Electrochem. Soc.*, vol. 164, no. 7, pp. A1703–A1719, 2017.

[49] J. R. Croy, A. Abouimrane, and Z. Zhang, "Next-generation lithium-ion batteries: The promise of near-term advancements," *Mat. Res. Bull.*, vol. 39, no. 5, pp. 407–415, 2014.

[50] L. Hu, Z. Zhang, and K. Amine, "Electrochemical investigation of carbonate-based electrolytes for high voltage lithium-ion cells," *J. Power Sources*, vol. 236, pp. 175–180, 2013.

[51] S. Sloop, "Chemical Reactivity of PF_5 and $LiPF_6$ in Ethylene Carbonate/Dimethyl Carbonate Solutions," *Electrochem. Solid-State Lett.*, vol. 4, no. 4, pp. A42–A44, 2001.

[52] A. M. Stephan, "Review on gel polymer electrolytes for lithium batteries," *Eur. Polym. J.*, vol. 42, no. 1, pp. 21–42, 2006.

[53] K. S. Ngai, S. Ramesh, K. Ramesh, and J. C. Juan, "A review of polymer electrolytes: fundamental , approaches and applications," *Ionics (Kiel).*, vol. 22, no. 8, pp. 1259–1279, 2016.

[54] J. W. Fergus, "Ceramic and polymeric solid electrolytes for lithium-ion batteries," *J. Power Sources*, vol. 195, no. 15, pp. 4554–4569, 2010.

[55] Samsung, "Samsung Expands Recall to All Galaxy Note7 Devices," *http://www.samsung.com/us/note7recall/*, 2016. .

[56] A. C. Luntz, J. Voss, and K. Reuter, "Interfacial Challenges in Solid-State Li Ion Batteries," *J. Phys. Chem. Lett.*, vol. 6, no. 22, pp. 4599–4604, 2015.

[57] A. D. Robertson, A. R. West, and A. G. Ritchie, "Review of crystalline lithium-ion conductors suitable for high temperature battery applications," *Solid State Ionics*, vol. 104, no. 1–2, pp. 1–11, 1997.

[58] P. Knauth, "Inorganic solid Li ion conductors: An overview," *Solid State Ionics*, vol. 180, no. 14–16, pp. 911–916, 2009.

[59] J. C. Bachman *et al.*, "Inorganic Solid-State Electrolytes for Lithium Batteries : Mechanisms and Properties Governing Ion Conduction," *Chem. Rev.*, vol. 116, no. 1, pp. 140–162, 2016.

[60] B. V. Lotsch and J. Maier, "Relevance of solid electrolytes for lithium-based batteries: A realistic view," *J. Electroceramics*, vol. 38, no. 2–4, pp. 128–141, 2017.

[61] C. Sun, J. Liu, Y. Gong, D. P. Wilkinson, and J. Zhang, "Recent advances in all-solid-state rechargeable lithium batteries," *Nano Energy*, vol. 33, no. January, pp. 363–386, 2017.

[62] J. Kasemchainan and P. G. Bruce, "All-Solid-State Batteries and their Remaining Challenges," *Johnson Matthey Technol. Rev.*, vol. 62, no. 2, pp. 177–180, 2018.

[63] P. G. Bruce and A. R. West, "Ionic conductivity of LISICON solid solutions, $Li_{2+2x}Zn_{1-x}GeO_4$," *J. Solid State Chem.*, vol. 44, no. 3, pp. 354–365, 1982.

[64] H. Y. P. Hong, "Crystal structure and ionic conductivity of $Li_{14}Zn(GeO_4)_4$ and other new Li+ superionic conductors," *Mater. Res. Bull.*, vol. 13, no. 2, pp. 117–124, 1978.

[65] I. Abrahams, P. G. Bruce, W. I. F. David, and A. R. West, "A re-examination of the lisicon structure using high-resolution powder neutron diffraction: evidence for defect clustering," *Acta Crystallogr. Sect. B*, vol. 45, no. 5, pp. 457–462, 1989.

[66] J. Kuwano and A. R. West, "New Li^+ ion conductors in the system, Li_4GeO_4-Li_3VO_4," *Mat. Res. Bull*, vol. 15, pp. 1661–1667, 1980.

[67] V. Thangadurai, S. Narayanan, and D. Pinzaru, "Garnet-type solid-state fast Li ion conductors for Li batteries: critical review," *Chem. Rev.*, vol. 43, no. 13, pp. 4714–4727, 2014.

[68] R. Kanno and M. Murayama, "Lithium Ionic Conductor Thio-LISICON," *J. Electrochem. Soc.*, vol. 148, no. 7, pp. 742–746, 2001.

[69] J. M. Whiteley, J. H. Woo, E. Hu, K. Nam, and S. Lee, "Empowering the Lithium Metal Battery through a Silicon-Based Superionic Conductor," *J. Electrochem. Soc.*, vol. 161, no. 12, pp. 1812–1817, 2014.

[70] N. Kamaya *et al.*, "A lithium superionic conductor," *Nat. Mater.*, vol. 10, no. 9, pp. 682–686, 2011.

[71] Y. Zhu, X. He, and Y. Mo, "Origin of Outstanding Stability in the Lithium Solid Electrolyte Materials: Insights from Thermodynamic Analyses Based on First-Principles Calculations," *ACS Appl. Mater. Interfaces*, vol. 7, no. 42, pp. 23685–23693, 2015.

[72] B. Roling, "$Li_{10}SnP_2S_{12}$: An Affordable Lithium Superionic Conductor," *J. Am. Chem. Soc.*, vol. 135, pp. 15694–15697, 2013.

[73] H. Y.-P. Hong, "Crystal structures and crystal chemistry in the system $Na_{1+x}Zr_2Si_xP_{3-x}O_{12}$," *Mater. Res. Bull.*, vol. 11, no. 2, pp. 173–182, 1976.

[74] J. Kuwano, N. Sato, M. Kato, and K. Takano, "Ionic conductivity of $LiM_2(PO_4)_3$ (M=Ti, Zr, Hf) and related compositions," *Solid State Ionics*, vol. 70–71, no. PART 1, pp. 332–336, 1994.

[75] B. V. R. Chowdari, K. Radhankrishnan, K. A. Thomas, and G. V. Subba Rao, "Ionic conductivity studies on $Li_{1-x}M_{2-x}M'_xP_3O_{12}$ (H = Hf, Zr; M' = Ti, Nb)," *Mater. Res. Bull.*, vol. 24, no. 2, pp. 221–229, 1989.

[76] H. Sugimoto, E Sadaoka, Y Imanaka, N Adachi, G Aono, "Ionic Conductivity of Solid Electrolytes Based on Lithium Titanium Phosphate," *J. Electrochem. Soc.*, vol. 137, no. 4, pp. 1023–1027, 1990.

[77] H. Xu, S. Wang, H. Wilson, F. Zhao, and A. Manthiram, "Y-Doped NASICON-type $LiZr_2(PO_4)_3$ Solid Electrolytes for Lithium-Metal Batteries," *Chem. Mater.*, vol. 29, no. 17, pp. 7206–7212, 2017.

[78] H. El-Shinawi, A. Regoutz, D. J. Payne, E. J. Cussen, and S. A. Corr, "NASICON $LiM_2(PO_4)_3$ electrolyte (M = Zr) and electrode (M = Ti) materials for all solid-state Li-ion batteries with high total conductivity and low interfacial resistance," *J. Mater. Chem. A*, vol. 6, no. 13, pp. 5296–5303, 2018.

[79] Y. Inaguma *et al.*, "High ionic conductivity in lithium lanthanum titanate," *Solid State*

Commun., vol. 86, no. 10, pp. 689–693, 1993.

[80] V. Thangadurai and W. Weppner, "Effect of B-Site Substitution of $(Li,La)TiO_3$ Perovskites by Di- ,Tri- ,Tetra- and Hexavalent Metal Ions on the Lithium Ion Conductivity," *Ionics (Kiel).*, vol. 6, pp. 70–77, 2000.

[81] O. Bohnke, "The fast lithium-ion conducting oxides $Li_{3x}La_{2/3-x}TiO_3$ from fundamentals to application," *Solid State Ionics*, vol. 179, no. 1–6, pp. 9–15, 2008.

[82] W. Nan and A. Mei, "Enhanced ionic transport in lithium lanthanum titanium oxide solid state electrolyte by introducing silica," *Solid State Ionics*, vol. 179, no. 39, pp. 2255–2259, 2008.

[83] V. Thangadurai, H. Kaack, and W. J. F. Weppner, "Novel Fast Lithium Ion Conduction in Garnet-Type $Li_5La_3M_2O_{12}$," *J. Am. Ceram. Soc.*, vol. 86, no. 3, pp. 437–440, 2003.

[84] S. Ramakumar, C. Deviannapoorani, L. Dhivya, L. S. Shankar, and R. Murugan, "Lithium garnets: Synthesis, structure, Li+ conductivity, Li^+ dynamics and applications," *Prog. Mater. Sci.*, vol. 88, pp. 325–411, 2017.

[85] E. J. Cussen, "Structure and ionic conductivity in lithium garnets," *J. Mater. Chem.*, vol. 20, no. 25, pp. 5167–5173, 2010.

[86] R. Murugan, V. Thangadurai, and W. Weppner, "Fast Lithium Ion Conduction in Garnet-Type $Li_7La_3Zr_2O_{12}$," *Angew. Chemie - Int. Ed.*, vol. 4, pp. 7778–7781, 2007.

[87] J. Awaka, N. Kijima, H. Hayakawa, and J. Akimoto, "Synthesis and structure analysis of tetragonal $Li_7La_3Zr_2O_{12}$ with the garnet-related type structure," *J. Solid State Chem.*, vol. 182, no. 8, pp. 2046–2052, 2009.

[88] X. Tong, V. Thangadurai, and E. D. Wachsman, "Highly Conductive Li Garnets by a Multielement Doping Strategy," *Inorg. Chem.*, vol. 54, pp. 3600–3607, 2015.

[89] Y. Li, J.-T. Han, C.-A. Wang, and J. B. Goodenough, "Optimizing Li+ conductivity in a garnet framework," *Chem, J Mater*, vol. 3, pp. 15357–15361, 2012.

[90] J. L. Allen, J. Wolfenstine, E. Rangasamy, and J. Sakamoto, "Effect of substitution (Ta , Al, Ga) on the conductivity of $Li_7La_3Zr_2O_{12}$," *J. Power Sources*, vol. 206, pp. 315–319, 2012.

[91] S. Ohta, T. Kobayashi, and T. Asaoka, "High lithium ionic conductivity in the garnet-type oxide $Li_{7-x}La_3(Zr_{2-x}, Nb_x)O_{12}$ (X = 0–2)," *J. Power Sources*, vol. 196, pp. 3342–3345, 2011.

[92] C. Bernuy-lopez, W. Manalastas, J. Miguel, A. Aguadero, F. Aguesse, and J. A. Kilner, "Atmosphere Controlled Processing of Ga-Substituted Garnets for High Li-Ion Conductivity Ceramics," *Chem. Mater.*, vol. 26, pp. 3610–3617, 2014.

[93] R. Wagner *et al.*, "Fast Li-Ion-Conducting Garnet-Related $Li_{7-3x}Fe_xLa_3Zr_2O_{12}$ with Uncommon $I\bar{4}$ 3d Structure," *Chem. Mater.*, vol. 28, pp. 5943–5951, 2016.

[94] M. Kotobuki, K. Kanamura, Y. Sato, and T. Yoshida, "Fabrication of all-solid-state lithium battery with lithium metal anode using Al_2O_3-added $Li_7La_3Zr_2O_{12}$ solid electrolyte," *J. Power Sources*, vol. 196, no. 18, pp. 7750–7754, 2011.

[95] E. Yi, W. Wang, J. Kieffer, and R. M. Laine, "Key parameters governing the densification of cubic-$Li_7La_3Zr_2O_{12}$ Li+ conductors," *J. Power Sources*, vol. 352, pp. 156–164, 2017.

[96] C. Deviannapoorani, S. Ramakumar, N. Janani, and R. Murugan, "Synthesis of lithium garnets from $La_2Zr_2O_7$ pyrochlore," *Solid State Ionics*, vol. 283, pp. 123–130, 2015.

[97] N. Reeves-Mclaren, R. I. Smith, and A. R. West, "Lithium-ion conduction pathways in complex lithium spinels $Li_2MGe_3O_8$ (M = Ni or Zn)," *Chem. Mater.*, vol. 23, no. 15, pp. 3556–3563, 2011.

[98] D. Z. C. Martin *et al.*, "Evaluating lithium diffusion mechanisms in the complex spinel $Li_2NiGe_3O_8$," *Phys. Chem. Chem. Phys.*, vol. 21, no. 41, pp. 23111–23118, 2019.

[99] H. Kawai, M. Tabuchi, M. Nagata, H. Tukamoto, and A. R. West, "Crystal chemistry and physical properties of complex lithium spinels $Li_2MM'_3O_8$ (M=Mg, Co, Ni, Zn; M'=Ti, Ge)," *J. Mater. Chem.*, vol. 8, no. 5, pp. 1273–1280, 1998.

[100] M. Nakayama, R. Jalem, and T. Kasuga, "Electronic structure of spinel-type $LiNi_{1/2}Ge_{3/2}O_4$ and $LiNi_{1/2}Mn_{3/2}O_4$ as positive electrodes for rechargeable Li-ion batteries studied by first-principles density functional theory," *Solid State Ionics*, vol. 262, pp. 74–76, 2014.

[101] F. Rosciano, P. P. Pescarmona, K. Houthoofd, A. Persoons, P. Bottke, and M. Wilkening, "Towards a lattice-matching solid-state battery: Synthesis of a new class of lithium-ion conductors with the spinel structure," *Phys. Chem. Chem. Phys.*, vol. 15, no. 16, pp. 6107–6112, 2013.

[102] K. Mizushima, P. C. Jones, P. J. Wiseman, and J. B. Goodenough, "$LiCoO_2$: A new cathode material for batteries of high energy density," *Mat. Res. Bull.*, vol. 15, pp. 783–789, 1980.

[103] A. Manthiram, "A reflection on lithium-ion battery cathode chemistry," *Nat. Commun.*, vol. 11, no. 1, pp. 1–9, 2020.

[104] P. Rozier and J.-M. Tarascon, "Review — Li-Rich Layered Oxide Cathodes for Next-Generation Li-Ion Batteries : Chances and Challenges," *J. Electrochem. Soc.*, vol. 162, no. 14, pp. 2490–2499, 2015.

[105] J. Tan *et al.*, "Electrochemically driven phase transition in $LiCoO_2$ cathode," *Materials (Basel).*, vol. 14, no. 2, pp. 1–10, 2021.

[106] M. Azevedo, N. Campagnol, T. Hagenbruch, K. Hoffman, A. Lala, and O. Ramsbottom, "Lithium and cobalt-a tale of two commodities," *McKinsey&Company Met. Min.*, no. June, pp. p1-25, 2018.

[107] J. R. Dahn, U. VonSacken, and C. A. Michal, "Structure and electrochemistry of $LiNiO_2$ and a new Li_2NiO_2 phase with the $Ni(OH)_2$ structure," *Solid State Ionics*, vol. 44, no. 1–2, pp. 87–97, 1990.

[108] A. Mesnier and A. Manthiram, "Synthesis of $LiNiO_2$ at Moderate Oxygen Pressure and Long-Term Cyclability in Lithium-Ion Full Cells," *ACS Appl. Mater. Interfaces*, vol. 12, no. 47, pp. 52826–52835, 2020.

[109] G. Vitinc and K. West, "Lithium Intercalation into Layered $LiMnO_2$," *J. Electrochem. Soc.*, vol. 144, no. 8, pp. 2587–2592, 1997.

[110] S. Schweidler *et al.*, "Investigation into Mechanical Degradation and Fatigue of High-Ni NCM Cathode Material: A Long-Term Cycling Study of Full Cells," *ACS Appl. Energy Mater.*, vol. 2, no. 10, pp. 7375–7384, 2019.

[111] C. H. Chen, J. Liu, M. E. Stoll, G. Henriksen, D. R. Vissers, and K. Amine, "Aluminum-doped lithium nickel cobalt oxide electrodes for high-power lithium-ion batteries," *J. Power Sources*, vol. 128, pp. 278–285, 2004.

[112] P. Kalyani, N. Kalaiselvi, P. Kalyani, and N. Kalaiselvi, "Various aspects of $LiNiO_2$ chemistry: A review," *Sci. Technol. Adv. Mater.*, vol. 6996, pp. 689–703, 2005.

[113] N. Yabuuchi and T. Ohzuku, "Novel lithium insertion material of $LiCo_{1/3}Ni_{1/3}Mn_{1/3}O_2$ for advanced lithium-ion batteries," *J. Power Sources*, vol. 121, pp. 171–174, 2003.

[114] W. Li, E. M. Erickson, and A. Manthiram, "High-nickel layered oxide cathodes for lithium-based automotive batteries," *Nat. Energy*, vol. 5, no. 1, pp. 26–34, 2020.

[115] M. M. Thackeray, S. Kang, C. S. Johnson, and J. T. Vaughey, "Li_2MnO_3-stabilized $LiMO_2$ (M = Mn , Ni , Co) electrodes for lithium-ion batteries," *J. Mater. Chem.*, vol. 17, no. 30, pp. 3112–3125, 2007.

[116] W. Zuo *et al.*, "Li-rich cathodes for rechargeable Li-based batteries: Reaction mechanisms and advanced characterization techniques," *Energy Environ. Sci.*, vol. 13, no. 12, pp. 4450–4497, 2020.

[117] M. Diaz-Lopez *et al.*, "Operando X-ray Absorption Spectroscopy and Emission Kβ 1,3 Study of the Manganese Redox Activity in High-Capacity $Li_4Mn_2O_5$ Cathode," *J. Phys. Chem. C*, vol. 122, no. 51, pp. 29586–29597, 2018.

[118] J. Huang *et al.*, "Non-topotactic reactions enable high rate capability in Li-rich cathode materials," *Nat. Energy*, vol. 6, no. 7, pp. 706–714, 2021.

[119] R. Chen *et al.*, "Li+ intercalation in isostructural Li_2VO_3 and Li_2VO_2F with O^{2-} and mixed O^{2-}/F^- anions," *Phys. Chem. Chem. Phys.*, vol. 17, no. 26, pp. 17288–17295, 2015.

[120] P. J. Reeves, I. D. Seymour, K. J. Griffith, and C. P. Grey, "Characterizing the Structure and Phase Transition of Li_2RuO_3 Using Variable-Temperature ^{17}O and ^7Li NMR Spectroscopy," *Chem. Mater.*, vol. 31, no. 8, pp. 2814–2821, 2019.

[121] J. Zheng *et al.*, "Structural and chemical evolution of Li- and Mn-rich layered cathode material," *Chem. Mater.*, vol. 27, no. 4, pp. 1381–1390, 2015.

[122] V. Aravindan, J. Gnanaraj, Y. S. Lee, and S. Madhavi, "$LiMnPO_4$ - A next generation cathode material for lithium-ion batteries," *J. Mater. Chem. A*, vol. 1, no. 11, pp. 3518–3539, 2013.

[123] M. Zhang, N. Garcia-Araez, and A. L. Hector, "Understanding and development of olivine $LiCoPO_4$ cathode materials for lithium-ion batteries," *J. Mater. Chem. A*, vol. 6, no. 30, pp. 14483–14517, 2018.

[124] A. Mauger and C. M. Julien, "Olivine positive electrodes for Li-ion batteries: Status and

perspectives," *Batteries*, vol. 4, no. 3, 2018.

[125] W. J. Zhang, "Structure and performance of LiFePO$_4$ cathode materials: A review," *J. Power Sources*, vol. 196, no. 6, pp. 2962–2970, 2011.

[126] Y. Zhang *et al.*, "Advances in new cathode material LiFePO$_4$ for lithium-ion batteries," *Synth. Met.*, vol. 162, no. 13–14, pp. 1315–1326, 2012.

[127] Z. Li, D. Zhang, and F. Yang, "Developments of lithium-ion batteries and challenges of LiFePO$_4$ as one promising cathode material," *J. Mater. Sci.*, vol. 44, no. 10, pp. 2435–2443, 2009.

[128] T. Muraliganth and A. Manthiram, "Understanding the shifts in the redox potentials of olivine LiM$_{1-y}$M$_y$PO$_4$ (M = Fe, Mn, Co, and Mg) solid solution cathodes," *J. Phys. Chem. C*, vol. 114, no. 36, pp. 15530–15540, 2010.

[129] A. K. Padhi, K. S. Nanjundaswamy, and J. B. Goodenough, "Phospho-olivines as Positive-Electrode Materials for Rechargeable Lithium Batteries," *Journal of The Electrochemical Society*, vol. 144, no. 4. pp. 1188–1194, 1997.

[130] A. Goren, C. M. Costa, M. M. Silva, and S. Lanceros-Menndez, "State of the art and open questions on cathode preparation based on carbon coated lithium iron phosphate," *Compos. Part B Eng.*, vol. 83, pp. 333–345, 2015.

[131] S. Wu, M.-S. Chen, C.-J. Chien, and Y.-P. Fu, "Preparation and characterization of Ti4+-doped LiFePO$_4$ cathode materials for lithium-ion batteries," *J. Power Sources*, vol. 189, no. 1, pp. 440–444, 2009.

[132] T. K. Pietrzak, M. Wasiucionek, I. Gorzkowska, J. L. Nowinski, and J. E. Garbarczyk, "Novel vanadium-doped olivine-like nanomaterials with high electronic conductivity," *Solid State Ionics*, vol. 251, pp. 40–46, 2013.

[133] G. X. Wang, S. L. Bewlay, K. Konstantinov, H. K. Liu, S. X. Dou, and J. H. Ahn, "Physical and electrochemical properties of doped lithium iron phosphate electrodes," *Electrochim. Acta*, vol. 50, no. 2-3 SPEC. ISS., pp. 443–447, 2004.

[134] M. Koltypin, D. Aurbach, L. Nazar, and B. Ellis, "More on the performance of LiFePO4 electrodes-The effect of synthesis route, solution composition, aging, and temperature," *J. Power Sources*, vol. 174, no. 2, pp. 1241–1250, 2007.

[135] M. M. Thackeray, P. . Johnson, P. G. Bruce, and J. B. Goodenough, "Electrochemical extraction of lithium from LiMn$_2$O$_4$," *Mater. Res. Bull.*, vol. 19, no. 2, pp. 179–187, 1984.

[136] R. Santhanam and B. Rambabu, "Research progress in high voltage spinel LiNi$_{0.5}$Mn$_{1.5}$O$_4$ material," *J. Power Sources*, vol. 195, no. 17, pp. 5442–5451, 2010.

[137] K. Raju, F. P. Nkosi, E. Viswanathan, M. K. Mathe, K. Damodaran, and K. I. Ozoemena, "Microwave-enhanced electrochemical cycling performance of the LiNi$_{0.2}$Mn$_{1.8}$O$_4$ spinel cathode material at elevated temperature," *Phys. Chem. Chem. Phys.*, vol. 18, pp. 13074–13083, 2016.

[138] A. Manthiram, K. Chemelewski, and E. Lee, "A perspective on the high-voltage LiMn$_{1.5}$Ni$_{0.5}$O$_4$ spinel cathode for lithium-ion batteries," *Energy Environ. Sci.*, vol. 7, pp.

1339–1350, 2014.

[139] C. Sigala, D. Guyomard, A. Verbaere, Y. Piffard, and M. Tournoux, "Positive electrode materials with high operating voltage for lithium batteries : $LiCr_yMn_{2-y}O_4$ (0 < y < 1)," *Solid State Ionics*, vol. 81, pp. 167–170, 1995.

[140] C. Sigala, A. Verbaere, J. L. Mansot, D. Guyomard, Y. Piffard, and M. Tournoux, "The Cr-Substituted Spinel Mn Oxides $LiCr_yMn_{2-y}O_4$ (0< y <1): Rietveld Analysis of the Structure Modifications Induced by the Electrochemical Lithium Deintercalation," *J. Solid State Chem.*, vol. 132, pp. 372–381, 1997.

[141] K. Amine, H. Tukamoto, H. Yasuda, and Y. Fujita, "Preparation and electrochemical investigation of $LiMn_{2-x}Me_xO_4$ (Me: Ni, Fe, and x = 0.5, 1) cathode materials for secondary lithium batteries," *J. Power Sources*, vol. 68, pp. 604–608, 1997.

[142] H. Kawai, M. Nagata, H. Tukamoto, and A. R. West, "A new Lithium cathode $LiCoMnO_4$: Toward Practical 5V Lithium Batteries," *Electrochem. Solid-State Lett.*, vol. 1, pp. 212–214, 1998.

[143] H. Kawai, M. Tabuchi, H. Tukamoto, and A. R. West, "Novel 5 V Spinel Cathode $Li_2FeMn_3O_8$ for Lithium Ion Batteries," *Chem. Mater.*, vol. 10, no. 11, pp. 3266–3268, 1998.

[144] Y. Ein-eli *et al.*, "$LiMn_{2-x}Cu_xO_4$ Spinels (0.1 < x < 0.5): A new Class of 5 V Cathode Materials for Li Batteries," *J. Electrochem. Soc.*, vol. 145, no. 4, pp. 1238–1244, 1998.

[145] H. Kawai, M. Nagata, H. Tukamoto, and A. R. West, "High-voltage lithium cathode materials," *J. Power Sources*, vol. 81–82, pp. 67–72, 1999.

[146] C. M. Julien and A. Mauger, "Review of 5-V electrodes for Li-ion batteries: status and trends," *Ionics (Kiel).*, vol. 19, pp. 951–988, 2013.

[147] M. Hu, X. Pang, and Z. Zhou, "Recent progress in high-voltage lithium ion batteries," *J. Power Sources*, vol. 237, pp. 229–242, 2013.

[148] Q. Zhong, A. Bonakdarpour, M. Zhang, Y. Gao, and J. R. Dahn, "Synthesis and electrochemistry of $LiNi_xMn_{2-x}O_4$," *J. Electrochem. Soc.*, vol. 144, no. 1, pp. 205–213, 1997.

[149] G. Liang, V. K. Peterson, K. W. See, Z. Guo, and W. K. Pang, "Developing high-voltage spinel $LiNi_{0.5}Mn_{1.5}O_4$ cathodes for high-energy-density lithium-ion batteries: current achievements and future prospects," *J. Mater. Chem. A*, no. 8, pp. 15373–15398, 2020.

[150] S. H. Oh, S. H. Jeon, W. Il Cho, C. S. Kim, and B. W. Cho, "Synthesis and characterization of the metal-doped high-voltage spinel $LiNi_{0.5}Mn_{1.5}O_4$ by mechanochemical process," *J. Alloys Compd.*, vol. 452, no. 2, pp. 389–396, 2008.

[151] M. Xu, D. Lu, A. Garsuch, and B. L. Lucht, "Improved performance of $LiNi_{0.5}Mn_{1.5}O_4$ cathodes with electrolytes containing dimethylmethylphosphonate (DMMP)," *J. Electrochem. Soc.*, vol. 159, no. 12, pp. 2130–2134, 2012.

[152] X. Xiao, D. Ahn, Z. Liu, J. H. Kim, and P. Lu, "Atomic layer coating to mitigate capacity fading associated with manganese dissolution in lithium ion batteries," *Electrochem.*

commun., vol. 32, pp. 31–34, 2013.

[153] G. T.-K. Fey, W. Li, and J. R. Dahn, "LiNiVO$_4$: A 4.8 volt electrode material for lithium cells," *J. Electrochem. Soc.*, vol. 141, no. 9, pp. 2279–2282, 1994.

[154] a K. Padhi, W. B. Archibald, K. S. Nanjundaswamy, and J. B. Goodenough, "Ambient and High-Pressure Structures of LiMnVO$_4$ and Its Mn$^{3+/2+}$ Redox Energy," *J. Solid State Chem.*, vol. 128, pp. 267–272, 1997.

[155] G. T. K. Fey and D. L. Huang, "Synthesis, characterization and cell performance of inverse spinel electrode materials for lithium secondary batteries," *Electrochim. Acta*, vol. 45, no. 1, pp. 295–314, 1999.

[156] A. Kitajou *et al.*, "Capacity improvement by deficit of transition metals in inverse spinel LiNi$_{1/3}$Co$_{1/3}$Mn$_{1/3}$VO$_4$ cathodes," *J. Power Sources*, vol. 302, pp. 240–246, 2016.

[157] R. S. Liu, Y. C. Cheng, R. Gundakaram, and L. Y. Jang, "Crystal and electronic structures of inverse spinel-type LiNiVO$_4$," *Mater. Res. Bull.*, vol. 36, no. 7–8, pp. 1479–1486, 2001.

[158] P. E. Stallworth *et al.*, "A solid-state ^{51}V NMR characterization of vanadium sites in LiCo$_x$Ni$_{1-x}$VO$_4$," *Solid State Ionics*, vol. 170, no. 3–4, pp. 181–186, 2004.

[159] G. T. K. Fey, K. S. Wang, and S. M. Yang, "New inverse spinel cathode materials for rechargeable lithium batteries," *J. Power Sources*, vol. 68, no. 1, pp. 159–165, 1997.

[160] A. Kitajou, J. Yoshida, S. Nakanishi, S. Okada, and J. I. Yamaki, "Cathode properties of Mn-doped inverse spinels for Li-ion battery," *J. Power Sources*, vol. 244, pp. 658–662, 2013.

[161] N. Van Landschoot, E. M. Kelder, and J. Schoonman, "Citric acid-assisted synthesis and characterization of doped LiCoVO$_4$," *Solid State Ionics*, vol. 166, no. 3–4, pp. 307–316, 2004.

[162] G. T. K. Fey, P. Muralidharan, and C. Z. Lu, "Synthesis and characterization of a new inverse spinel LiNi$_{1/3}$Co$_{1/3}$Mn$_{1/3}$VO$_4$ for lithium-ion batteries," *Mater. Lett.*, vol. 60, no. 9–10, pp. 1209–1212, 2006.

[163] J. Liu *et al.*, "Unified View of the Local Cation-Ordered State in Inverse Spinel Oxides," *Inorg. Chem.*, vol. 58, no. 21, pp. 14389–14402, 2019.

[164] M. L. Veiga and C. Pico, "Relationship between crystal structure and electric properties for lithium-containing spinels," *Pergamon*, vol. 29, no. 8, pp. 903–910, 1994.

[165] G. Blasse, "The structure of some new mixed metal oxides containing lithium (II)," *J. Inorg. Nucl. Chem.*, vol. 26, pp. 1473–1474, 1964.

[166] J.-C. Joubert and A. Durif-Varambon, "Étude Cristallographique D'Un Vanadate De Lithium-Chrome," *Bull. la Société française Minéralogie Cristallogr.*, vol. 86, no. 4, p. 430, 1963.

Chapter 3: Experimental Theory and Methodology

3.1. Synthesis Methods

3.1.1. Solid State Synthesis

Solid-state synthesis is the process whereby powder precursors are mixed and subsequently heated at high temperatures (> 800 °C) over many hours to produce an end product. Solid-state methods are typically easy to replicate and can be used to produce large batches of material. For this reason, it is the most commonly used synthesis method for inorganic oxide materials. Nevertheless, it has several disadvantages. For instance, it is an inherently slow and high energy process due to the slow interdiffusion of different ions in solids. Intimate mixing of precursors before and between heating steps can promote reaction by increasing the homogeneity of particles at the micron scale. However, the reaction mixtures are still generally inhomogeneous on the atomic scale. The two stages of the solid-state method are nucleation and growth. In the nucleation stage, counterions must diffuse through and arrange at the interfaces of precursors to form small crystals (nucleation sites) of the new phase. Nucleation is facilitated if it is heterogeneous *i.e.,* nucleation is easier at the interface between precursors and products as well as if the product and precursors have similar structures (lattice matching). For growth of subsequent crystals, they must reach a critical size at which there is a balance between the free energy of formation of the product and the surface energy of the crystal nucleus.[1] Further growth of the product becomes increasingly more difficult as the path length for counter diffusion of ions to the reaction interface increases. Because of this, reactions often require multiple steps of mixing and heating to form a single phase product.

3.1.2 Soft Chemical Synthetic Routes

There are various different synthesis methods which employ soft or wet chemistry processes, such as alkoxide and citric acid sol-gel methods.[1], [2] The reactants used during these processes are typically in the liquid phase and therefore mix well on the atomic scale. This is a significant advantage over solid-state synthesis and often results in lower temperatures being required during the final heating process. Products produced using wet chemistry methods have a high chemical homogeneity and typically smaller particle sizes than if synthesised *via* a solid-state route. Materials can also be fabricated into different particle

morphologies *e.g.,* nanowires.[2], [3] These qualities often lead to improved electrochemical properties and lower energy cost associated with synthesis.[4] Disadvantages of wet chemistry methods are that they can be more complex and are difficult to use on larger scales due to reagents often being expensive and/or requiring special handling.

Sol-gel synthesis methods differ depending on the solvents, cation species, and the chelating and/or polymerisation agents used. However, the stages of sol-gel methods are similar, with the first stage being to produce a homogenous solution. Traditional sol-gel methods use metal-organic liquid reagents such as titanium isopropoxide, $Ti(O^iPr)_4$, as a Ti source.[2] The alkoxides are mixed in the desired ratios with water and either an acid or base to speed up hydrolysis. Alcohol is also added to promote mixing between the alkoxides and water. Hydrolysis occurs by first replacement of an -OR group by -OH e.g., replacement of a O^iPr group in $M(O^iPr)_4$ to form $M(O^iPr)_3OH$. Two $M(O^iPr)_3OH$ groups can then react in a condensation polymerisation reaction. The resulting gel is heated to decompose the organic species forming an oxide product. In this thesis, the citric acid sol-gel method was utilised. This method differs slightly to conventional sol-gel synthesis by first dissolving metal salts, typically nitrates, in water before slowly adding citric acid under heating. The citric acid is a chelating agent which acts as a ligand to bind the cationic species. As the water is evaporated, a gel and finally foam is produced which again can be heated to produce an oxide product. The complexity of these reactions can be increased with the addition of aids, such as alcohols to facilitate polymerisation or nitric acid to control pH and avoid precipitation of insoluble precursors. The citric acid method was particularly useful in this work as it can react with insoluble V_2O_5 in water to form a vanadium-citric acid complex.[5]

3.2. X-ray Powder Diffraction

The following section was written with the aid of the references [1], [6].

X-ray powder diffraction (XRD) is one of the fundamental techniques for materials characterisation. A diffraction pattern contains a wealth of information on the crystal structure of the material studied and can often be used as a fingerprint to help identify different phases present within a sample. X-rays are part of the electromagnetic spectrum with wavelengths in the magnitude of 1 Å, which is comparable to the interatomic spacing of many typical solid state materials. They can be treated as electromagnetic waves or as high energy particles which can be described by Equations 3.1 and 3.2.

$$\nu = \frac{c}{\lambda} \text{ and } E = h\nu \qquad \text{(Equation 3.1 and 3.2)}$$

Where ν is frequency (s^{-1}), λ is wavelength (m), c is the speed of light in a vacuum (ms^{-1}), E is energy and h is Planck's constant (Js).

Laboratory X-rays are generated by accelerating a beam of electrons produced from a filament to impact a metal target made from *e.g.* Cu. Below a certain energy, continuous (white) radiation is produced through the deceleration of electrons within the metal target. However, above a critical energy, the incident electrons have sufficient kinetic energy to ionise some core (1s) electrons, which results in transfer of outer shell electrons, from higher energy 2p or 3p orbitals, to replenish the vacated core shell. This is accompanied by the emission of characteristic radiation - an X-ray photon of a fixed energy determined by the specific metal species and electronic transition.

There are a number of ways that X-rays can interact with matter. These include absorption, and scattering, which may be inelastic or elastic. For diffraction experiments elastic scattering is required, where no energy is lost during the scattering process and the scattered X-rays are coherent ('in phase') with the incident X-rays. Crystals can be described using repeating arrays of atoms, often referred to as lattice planes. The scattering of X-rays by these lattice planes are described by Bragg's law (nλ = 2$d$sinƟ, where n is the diffraction order, λ is the wavelength, d is the interplanar spacing and $Ɵ$ is the angle of the scattered X-ray), which treats these planes as semi-transparent mirrors running through the crystal structure. Figure 3.1 shows the derivation of Bragg's law, which shows that Bragg's law is satisfied when the diffracted X-rays are in-phase and interfere constructively. Bragg's law can

be used to predict the direction of the diffracted X-rays from the lattice planes which describe the crystal structure. The angle an X-ray is diffracted by, is determined by the interatomic distances (d-spacing, d) between repeating lattice planes; this angle 2Θ can be measured using a detector and gives a characteristic pattern obtained for a given material. For example, in a cubic system the interatomic distance is related to the unit cell dimensions (a = b = c) and the Miller indices (orientation, *hkl*) of a given lattice plane by Equation 3.3.

$$\frac{1}{d^2} = \frac{h^2 + k^2 + l^2}{a^2} \qquad \text{(Equation 3.3)}$$
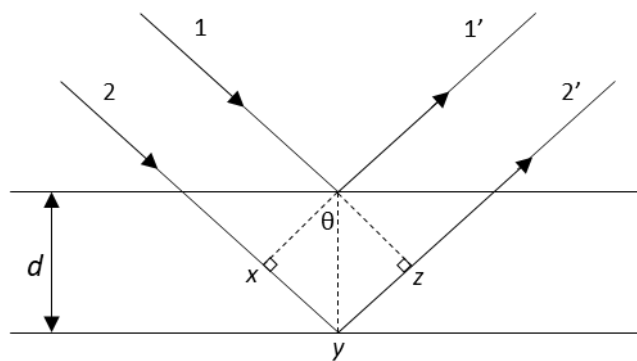
Figure 3.1. Derivation of Bragg's law (*nλ = 2dsinΘ*, where n is the diffraction order *e.g.* 1 or 2, λ is the wavelength (related to the distance between point *x*, *y* and *z*) , *d* is the interplanar spacing and *Θ* is the angle of the scattered X-ray).

In principle, Bragg's law and *e.g.,* Equation 3.3 for cubic systems can be used to calculate all possible d-spacing values and every lattice plane should give rise to a diffraction peak. However, certain reflections from sets of lattice planes may have zero intensity due to systematic absences, which are a result of extreme destructive interference. Systematic absences are observed when one set of atoms diffract X-rays exactly out of phase with another set of the same atoms and is dependent on the type of Bravais lattice.

Characteristic radiation results in photons with specific wavelengths *e.g.,* with a Cu metal target, the transition from a 2p shell to a 1s shell results in the emission of X-rays with an average wavelength of 1.5418 Å and is called Kα. Some transitions are more probable than others and therefore are more intense e.g., Kα radiation is *ca.* five times as intense as Kβ (3p to 1s). For most diffraction experiments, a monochromatic beam is desired to avoid additional

complexity in the diffraction pattern. For X-rays generated by a Cu target this is accomplished using a Ni filter. The energy required to ionise the 1s core shell of Ni lies between the wavelengths (and hence energies, based on Equation 3.2) of the Kβ and Kα lines. Therefore, the Kβ emission lines are preferentially absorbed by the Ni filter alongside most of the continuous radiation. Such 'filtration' results in the suppression of both Kα and Kβ lines, but the ratio between the two is increased from 5:1 to around 200:1 or even greater, depending on the thickness of Ni foil used. Ni filtration cannot separate lines with very similar wavelengths, such as $K\alpha_1$ and $K\alpha_2$. In this case, a primary beam monochromator would be the most suitable method for generating monochromatic $K\alpha_1$ radiation, with removal of both $K\alpha_2$ and Kβ radiation.

A typical schematic diagram of a laboratory reflection (Bragg-Brentano) X-ray diffraction setup is shown in Figure 3.2. At a fundamental level, the setup includes a source (X-ray tube), sample and detector, though modern diffractometers also include several means of managing the beam pathway using slits, filters and/or monochromators. Examples of focusing 'optics' are Soller slits, divergence slits and diffracted beam slits. These are used to suppress the divergence of the X-ray beam, both from the source and sample. This can help reduce instrumental errors such as flat plate specimen error which occurs when the flat sample deviates slightly from the diffraction circle, resulting in a systematic shift in 2Ө of the diffraction pattern. They are also used to control the beam path such as to reduce axial divergence, improving the shape of the observed Bragg peaks.

Monochromators are devices that diffract the X-ray beam with single crystals to select for specific desired wavelengths, or to operate similarly to filters by removing unwanted wavelengths of X-rays such as Kβ and white radiation. Other variations of diffractometers include transmission geometry where the incident X-rays pass through a very thin sample. However, the fundamental setup is similar to Bragg-Brentano geometry.
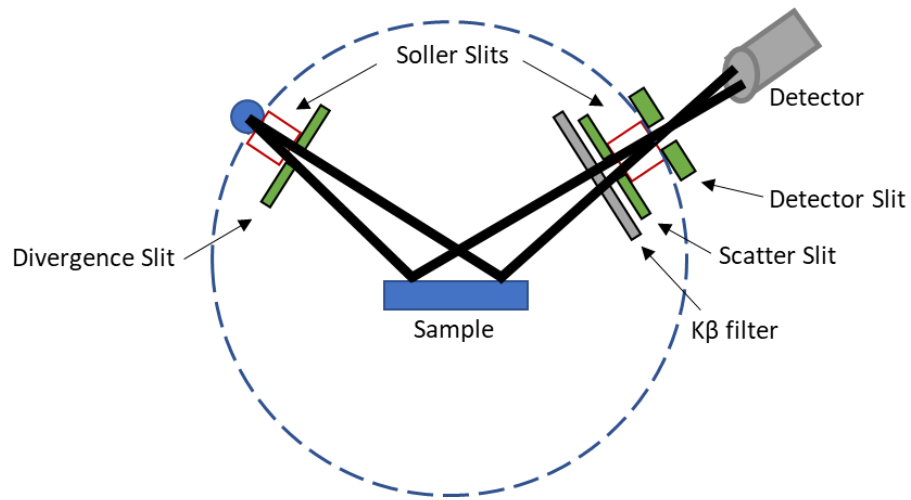
Figure 3.2. Schematic of a Bragg-Brentano geometry diffractometer setup.

There are numerous factors which can affect the peak position, intensity, and shape of a diffraction pattern. Peak positions depend on the crystal structure and lattice planes as well as instrumental contributions such as sample height displacement. The contributions to peak intensity can be classified into instrumental, phase chemistry, and specimen factors. Instrumental contributions include the intensity of generated X-rays, the distance between the sample and detector as well as the energy or wavelength of generated X-rays. Phase chemistry factors include the unit cell volume, reflection multiplicity and structure factor (F_{hkl}) of diffracting lattice (*hkl*) planes for a given phase. Multiplicity is the result of peak overlap due to crystal symmetry of a given phase *e.g.,* in a cubic system *h00* has a multiplicity of six, resulting from the presence of six symmetrically equivalent reflections.

The structure factor is a function of the scattering factor (*f*) of atoms and their relative positions. The X-ray scattering factor of an atom is proportional to the number of electrons, i.e. denser atoms scatter X-rays with greater intensity. The effect of scattering factors also leads to intensity decreasing at higher 2Θ angles. This is because X-rays scattered by an atom are the summation of the scattering by each electron in the atom. As a result, scattering at 2Θ angles greater than zero in relation to the incident X-rays will have some small degree of phase difference between the X-rays scattered by different electrons and therefore partial destructive interference will occur. Finally, specimen factors include the absorption of X-rays by the sample, and the volume fraction of a particular phase in a specimen.

The peak shapes of a diffraction pattern are typically described using one of three functions, Gaussian, Lorentzian or Pseudo-Voigt (a combination of Gaussian and Lorentzian functions). Peak shapes may also be asymmetric. Similarly to peak position and intensity, peak shape is affected by both instrumental (typically Gaussian) and sample factors (typically Lorentzian). Instrumental contributions include divergence of X-ray beam *e.g.,* due to flat plate specimen error or misalignment of the diffractometer, and the finite width of the beam *i.e.,* the beam is not a perfectly sharp spot or line. These contributions are generally constant for a given diffractometer, and as such they can be accounted for using a standard which has negligible or known sample contributions to peak shape. Sample contributions arise from factors such as sample transparency, crystallite size, and microstrain (lattice distortions). Sample transparency occurs in samples with low absorption coefficients *e.g.,* organic materials.

In this work, a Bruker D2 Phaser diffractometer and PANalytical X'Pert[3] (Cu Kα, λ = 1.5418 Å) diffractometer in Bragg-Brentano geometry was used for initial phase characterisation and collection of diffraction data at high temperatures, respectively. A STOE STADI P, fitted with a linear PSD detector and primary beam monochromator to give a highly pure Mo Kα1 beam (λ = 0.7107 Å, was used in transmission geometry to collect data for lattice parameter refinements (Section 3.4).

3.3. Neutron Powder Diffraction

Neutron powder diffraction (ND) is often used as a complimentary technique to XRD. It is particularly useful when studying crystal structures containing light atoms, which are poor scatterers of X-rays, such as Li and O, as well as atoms which have a similar number of electrons *e.g.* adjacent d-block atoms, and therefore can be difficult to distinguish using X-rays alone. This is because neutrons are scattered by the nucleus of atoms and the coherent neutron scattering length (*b*) of atoms does not vary proportionally with atomic number (Figure 3.3). The effective area of a nucleus which can scatter a neutron is known as the scattering cross-section ($\sigma = 4\pi b^2$, where *b* is a measure of the strength between the interactions of the nucleus and neutron).[7] The scattering of neutrons can be described by Bragg's Law and the de Broglie equation (Equation 3.4).

$$\lambda = \frac{h}{mv} = \frac{ht}{mL}$$

(Equation 3.4)

Where λ is the wavelength, h is Planck's constant, m is the neutron mass, t is the total time of flight, v is the frequency and L is the total slight path from moderator to sample detector.
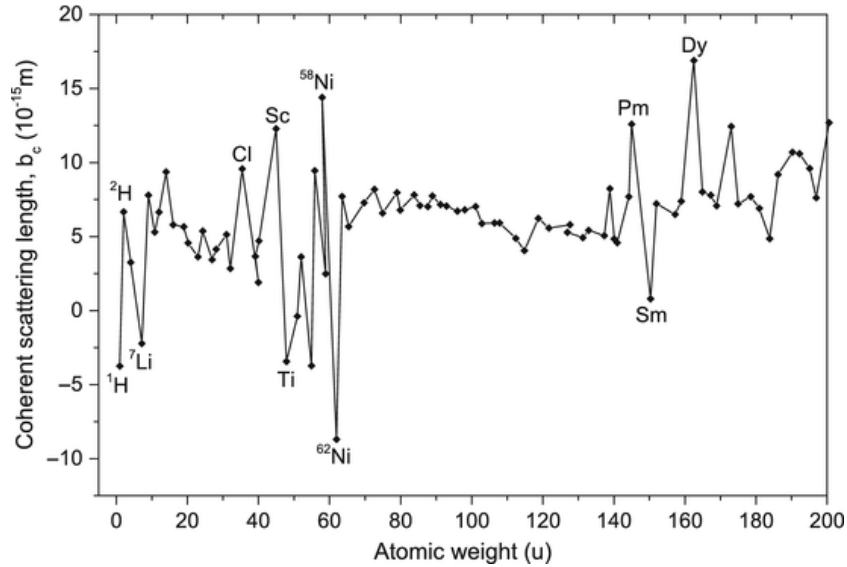
Figure 3.3. Variation of the coherent scattering length of neutrons with atomic weight.[8]

Neutrons are produced in large quantities using two different types of sources, reactor or spallation. Examples of facilities with reactor and spallation sources are the High-Flux reactor at the ILL, Grenoble, France and the ISIS Neutron and Muon Facility, Rutherford Appleton Laboratory, UK respectively. At reactor sources, neutrons are produced by nuclear fission using uranium fuel rods. The resulting neutrons are of varying wavelength which are then monochromated to produce a beam of neutrons of constant wavelength for experiments. Constant wavelength neutrons are a directly analogous to XRD, as discussed in Section 3.2. On the other hand, spallation sources produce neutrons using a particle accelerator to accelerate protons, which then bombard a metal target *e.g.* tungsten. This process causes an ejection of neutrons of differing velocities. Experiments at spallation sources make use of the time taken (t) to reach a fixed detector over a defined path length (l), known as time-of-flight. Using Bragg's law and Equation 3.4, this can then be related to the d-spacing via Equation 3.5.

$$t = \left(\frac{2m}{h}\right) L \; \sin\theta \; d \qquad\qquad \text{(Equation 3.5)}$$

The total scattering lengths for the elements studied, *i.e.* the summation of the coherent scattering lengths of different isotopes of the same atom, are -1.90 fm, 10.30 fm, 3.60 fm, -0.38 fm and 5.80 for Li, Ni, Cr, V and O, respectively.[9] The large variation in total scattering length of different atoms can mean it is easier to distinguish between them. Generally, a larger magnitude means the atom is a better scatterer of neutrons. A positive scattering length indicates the interaction between the nucleus and scattered neutron is a repulsive interaction, with the opposite being true for negative scattering lengths.[7] The neutron powder diffraction data used in this thesis was collected using the Polaris instrument at the ISIS Neutron and Muon Facility. Polaris collects data on five detector banks that are able to measure d-spacings between 0.2 and 40 Å. Data collected on detector banks 5, 4 and 3 (the backscattering, 90° and low angle detector banks) were used for Rietveld refinements, as these offered the highest resolution. For room temperature datasets, vanadium cans were used due to the small scattering length of vanadium.

3.4. The Rietveld Method

The Rietveld method is a computational technique that utilises a least squares approach to fit and refine modelled crystal structures to measured diffraction patterns. Over the course of the refinement, sample and instrumental parameters, *e.g.* lattice parameters and peak shape terms are iteratively refined until the calculated diffraction pattern more closely resembles the experimentally derived dataset.[10], [11] The quality of the resulting fit is acceptable if the weighted profile, R_{wp} and goodness-of-fit, χ^2, are small alongside a sensible refined structural model *e.g.* the interatomic distances are appropriate. The statistical measures, R_{wp}, R_{exp} and χ^2, are defined in Equations 3.6, 3.7 and 3.8:

$$R_{wp}^2 = \frac{\sum_i w_i (y_{oi} - y_{ci})^2}{\sum_i y_{oi}} \qquad\qquad \text{(Equation 3.6)}$$

$$R_{exp}^2 = \frac{N-P}{\sum_i w_i y_{oi}^2}$$

(Equation 3.7)

$$\chi^2 = \left(\frac{R_{wp}}{R_{exp}}\right)$$

(Equation 3.8)

Where R_{wp} and R_{exp} are the weighted and expected profile R-factor for the full diffraction pattern, respectively. y_{oi} and y_{ci} are the observed and calculated intensities at each point *i*. w_i is the weighting factor. *N* is the number of data points and finally, *P* is the number of least-squares variables.

Parameters may be related to the crystal structure of the phase(s) present within a sample or to instrumental effects on peak shape and position, and are typically refined or kept at fixed values. Fixed parameters include instrumental factors such as the wavelength used. For the refinements in this thesis, the data was imported alongside an appropriate starting model, and parameters were then usually refined in the following order:

1) Background and scale factors. The background function, as the name suggests, models the background in the observed diffraction pattern, excluding the Bragg peaks. The scale factors can be separated into an overall histogram scale factor, or individual phase fraction scale factors in a multi-phase refinement.

2) Lattice parameters and diffractometer constants. Both the lattice parameters and diffractometer constants define the position of Bragg peaks. For accurate lattice parameter calculations, data collected using a standard sample (*e.g.* Si powder) is required to determine the diffractometer constants. The diffractometer constants account for contributions such as sample height displacement. For time-of-flight neutron diffraction data the diffractometer constants refined are DIFC and DIFA, which relate the time-of-flight of a Bragg reflection to its d-spacing.

3) Peak shape parameters (*U*, *V*, *W*, *X* and *Y*). The peak shapes were modelled using a Pseudo-Voigt function, which uses a combination of Gaussian (terms *U*, *V* and *W*) and Lorentzian (terms *X* and *Y*) functions to describe the peak shape.

4) Atomic positions (*x, y, z*). The atomic positions describe where an atom sits within the crystal structure. The atomic positions of an atom may be refined if it is not on a special position. Special positions are occupied by atoms placed on a point symmetry element and depend on the space group of the material studied.

5) Thermal displacement parameters (*U*, Å^2) and fractional occupancies. The thermal displacement parameters are usually refined in order of scattering length magnitude *i.e.* larger scattering lengths are refined first. It is a measure of an atom's vibration and/or displacement off a crystallographic site and can be described either as isotropic or anisotropic, with a common starting value of 0.005 Å^2. Fractional occupancies are also usually refined in order of scattering length magnitude. Fractional occupancies and thermal displacement parameters should typically be refined independently of each other due to the correlated effect they have on Bragg peak intensities.

3.4.1. Difference Fourier Maps

Difference Fourier maps can be used during a refinement to locate atoms that may be missing from, or poorly described by a structural model and are analogous to contour maps. Difference Fourier maps can be obtained by subtracting the observed structure factors from the calculated structure factors.[1] For example, difference Fourier maps generated during a refinement using XRD data may show regions of positive electron density, associated with a missing atom; or may show regions of negative electron density associated with a poorly placed atom. For Fourier maps generated using ND data, negative density may also be observed as a result of missing atoms with a negative scattering length *e.g.* Li. This fact is particularly useful in identifying interstitial sites along the Li-ion diffusion pathway of a given material using variable-temperature neutron diffraction data. At higher temperatures, Li-ions may have sufficient thermal energy to become mobile and hop off their ideal crystallographic site(s) into interstitial conduction sites. During a Rietveld refinement using the resulting collected data, difference Fourier maps can be generated once a base model has been determined. Any new Li sites due to thermally activated hopping may then appear in generated Fourier maps as negative contours. This technique has previously been used to

investigate the Li-ion conduction pathway(s) of several battery materials, such as $Li_4Ti_5O_{12}$ and $Li_2NiGe_3O_8$.[12], [13]

3.5. Differential Scanning Calorimetry (DSC)

DSC is an analytical technique used to examine the different thermal events that may occur within a sample on heating and/or cooling *e.g.* melting or decomposition. In DSC experiments, the sample and an inert reference are maintained at the same temperature. Subsequently, the amount of energy required to maintain the sample temperature compared to the reference is recorded. For endothermic events, extra heat will be input to the sample to increase the temperature at the same rate as the reference. For exothermic events, the reverse will occur, *i.e.* the sample will require less heat to maintain the temperature compared to the reference. In this work, DSC was used to measure the thermal stability of synthesised materials up to 900 °C. Powder samples were analysed using a SDT Q600 Simultaneous DSC-TGA in air over the temperature range of 20 to 900 °C, using a heating rate of 10 °C min^{-1}.

3.6. Impedance Spectroscopy

Impedance spectroscopy is a commonly used technique to measure the resistance of Li-ion conductors.[14] It is especially useful for distinguishing different electrical components *e.g.* bulk, grain boundaries and surface effects (assuming these components can be separated).[15] Impedance measurements are carried out by applying a small alternating current (ac) voltage over a wide frequency range (typically 10^{-2} to 10^6 Hz), the phase shift and magnitude of the resulting current (at each frequency) can then be recorded. The phase shift is related to the reactive component (capacitance and/or inductive components) and the magnitude to the resistive component.[16] The data is most commonly expressed through complex impedance (Z*) plots, with both real (Z′) and imaginary (Z″) components. The complex formalism for impedance is given in Equation 3.9, however three other formalisms can be used to represent the same data, the admittance (Y*), electric modulus (M*) and permittivity (ε*).[16] These complex formalisms can by interrelated through Equations 3.10 to 3.12:

$$Z^* = Z' \text{ (resistive)} - jZ'' \text{ (reactive)} \qquad \text{(Equation 3.9)}$$

$$Y^* = (Z^*)^{-1} = Y' + Y'' \qquad \text{(Equation 3.10)}$$

$$M^* = j\omega C_o Z^* = M' + M'' \qquad \text{(Equation 3.11)}$$

$$\varepsilon^* = (M^*)^{-1} = Y^*(j\omega C_o)^{-1} = \varepsilon' + \varepsilon'' \qquad \text{(Equation 3.12)}$$

Where $j = \sqrt{-1}$, $C_o = \varepsilon_o A/l$ (ε_o is the permittivity of free space, 8.854 x 10^{-14} Fcm^{-1}, A and l are the area and separation between the electrodes, respectively). ω is the angular frequency ($2\pi f$).

The four complex formalisms may be plotted either as complex plane plots (imaginary *vs.* real components) or as spectroscopic plots (imaginary or real components *vs.* frequency). The plotting of multiple formalisms can be useful in distinguishing the different electrical components of a system *e.g.* bulk and grain boundary, as they emphasis different regions of the material under study.

The different electrical components or regions of a material will be ideally represented in impedance data by distinct semicircles, which can be modelled by a resistor (R) and capacitor (C) in parallel. Each component can be characterised by its relaxation time or time constant, τ, which is the product of the separate RC elements ($\tau = RC$). Differing RC elements are able to be separated over a measured frequency range if $\omega_{max}RC = 1$, where ω_{max} is the frequency of maximum loss (relaxation maxima).[15], [16] An example of a complex impedance plot with two semicircles (R_1C_1 and R_2C_2) is shown in Figure 3.4. Resistance values can be extracted from the high intercepts on the real axis (Z'), where the highest intercept will be R_{total} and is equal to R_1+R_2. Capacitance values can be calculated by using the frequency at the maximum of each semicircle with Equation 3.13.

$$C = \frac{1}{2\pi f \times R} \qquad \text{(Equation 3.13)}$$
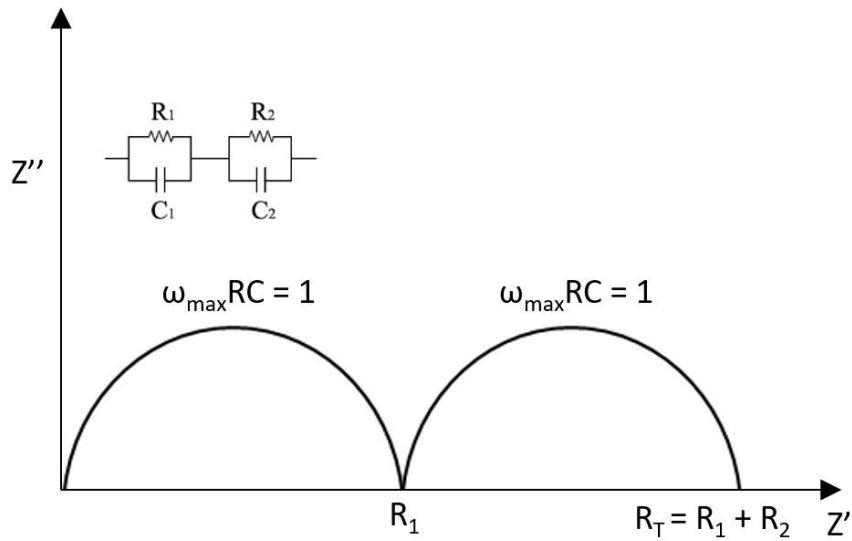
Figure 3.4. Ideal impedance complex plane plot for a material containing two different components.

The capacitance values can then be used to distinguish the different regions of the sample. This can be calculated using Equation 3.14, assuming the different regions of the sample vary in thickness (l) but have the same permittivity (ε') and therefore the capacitance values for each region differ only in l, Figure 3.5. The capacitance values for different region of a sample are summarised in Table 3.1.[15], [16]

$$C = \varepsilon' \, \varepsilon_0 \frac{A}{l} \qquad \text{(Equation 3.14)}$$
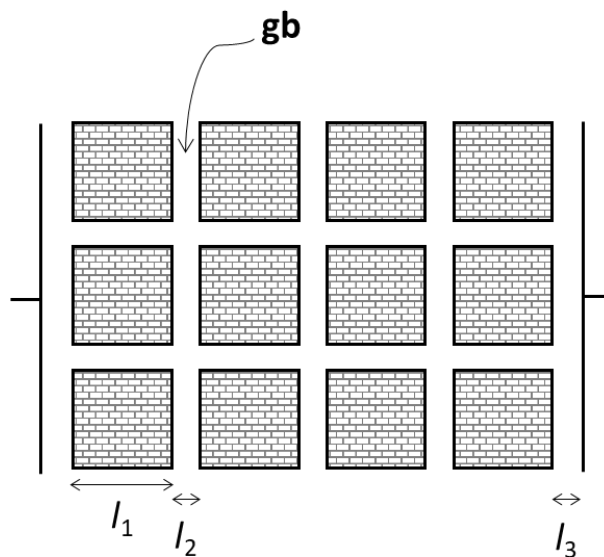
Figure 3.5. Brickwork model for different regions in a ceramic sample.[15]

Table 3.1. Summary of capacitance values and their possible interpretations.[15]

Capacitance $(F\ cm^{-1})$	Phenomenon or Region
10^{-12}	Bulk
10^{-11}	Minor, second phase
10^{-11} to 10^{-8}	Grain boundary
10^{-10} to 10^{-9}	Bulk ferroelectric
10^{-9} to 10^{-7}	Surface layer
10^{-4} to 10^{-5}	Sample-electrode interface
10^{-4}	Electrochemical reactions

When using impedance spectroscopy to measure Li-ion conductors, Pellets of the sample are typically pressed, sintered at high temperatures and subsequently coated on opposite sides with conductive metal electrodes, often gold. Gold electrodes are blocking in Li-ion conductors, meaning the Li-ions are unable to pass through the gold electrode layer. As a results, Li-ions will form a layer at the electrode-sample interface when a current is applied. This is shown in complex impedance plots by a vertical 'Warburg' spike at low frequencies. However, commonly the electrode interface is not ideal and may only be partially blocking. These cases are often observed within complex impedance plots by an inclined low frequency spike and is associated with ionic conduction.[16]

In practice, the observed semicircles in complex impedance plots may also be non-ideal and instead appear as depressed or partially resolved semicircles. The non-ideal behaviour may be due to the presence of multiple relaxations with the bulk *e.g.* successive Li-ion hops are dependent on previous hops and thus may have differing relaxation times. Partially resolved semicircles occur when the time constants of different regions are similar and is due to the small differences in capacitance values between regions *e.g.* in poorly sintered samples.[1], [16] Nevertheless, impedance spectroscopy can be a powerful technique for measuring the resistance of Li-ion conductors over a wide temperature range and thus, can be used to extract the conductivity and activation energy of Li-ion diffusion.

3.7. Muon Spectroscopy

Muon spectroscopy is a commonly used technique to study magnetic properties in materials and more recently ionic diffusion of cations (*e.g.* Li-ions) in battery materials. This is due to its sensitivity to local internal fields such as electronic and nuclear moments.[17]–[20] How quickly Li-ions can diffuse through a material is extremely important for the kinetics and (dis)charge rates of LIBs. Ionic diffusion properties are defined by the diffusion rate, D_{Li}, and activation energy, E_a, associated with diffusion (Section 1.4). Impedance spectroscopy is a widely used technique to measure bulk and grain boundary conductivity in electroceramics, as discussed above. However, the measured ionic conductivity can vary greatly depending on processing conditions such as sintering temperature and time, density of pellets as well as the electrodes or pressing techniques employed. Separation of bulk and grain boundary components can be difficult unless these parameters are fully controlled and understood.[21] Solid-state NMR is another technique used to measure bulk ionic motion within battery materials and is a direct probe of the ions under investigation.[18] Nevertheless, the presence of paramagnetic ions in many battery materials adds additional complexity in the interpretation of ionic diffusion rates due to broadening of the peaks this information is derived from. The changes in ionic diffusion at different length scales (bulk and grains) means a variety of techniques should be used to better understand LIB materials.[21]

Muons are fundamental particles that can be considered as heavy unstable electrons (μ^-) or light unstable protons (μ^+), with a lifetime of 2.197 μs.[17] For ionic diffusion studies, positive muons are used, as when they are implanted *ca.* 200 μm into an oxygen-containing sample they reside approximately $1 - 1.2$ Å away from O^{2-} sites, forming stable $\mu^+ - O^{2-}$ bonds. This enables the implanted muons to be sensitive to nuclear magnetic fields of the ions being investigated *e.g.* Li-ions.[18] The large quantities of muons required for these experiments are produced at large-scale beamline facilities such as ISIS Neutron and Muon Facility, Rutherford Appleton Laboratory, UK. They can be generated when high-energy protons are accelerated into a carbon target producing pions, π^+, which subsequently decay into positive muons (μ^+) and muon-neutrinos (ν_μ).[18] The generated muons are 100 % spin polarised *i.e.* their spins all face the same direction. Before the muons decay, their spin can precess depending on the different magnetic fields it experiences, for instance by an external applied field, the inherent nuclear spin of an element or by the spin of an unpaired electron. The

diffusion of Li-ions leads the muon to undergo a spin flip due to the inherent nuclear magnetic moment of lithium. When the muon decays, positrons are produced and are most likely to be emitted in the direction of the muon spin at the time of its decay (Figure 3.6). By recording the positrons emitted at opposite sides of the sample, the asymmetry, $A(t)$, of positrons can then be followed as a function of time (Equation 3.15).

$$A(t) = \frac{N_{forward} - \alpha N_{backward}}{N_{forward} + \alpha N_{backward}}$$
(Equation 3.15)

Where $N_{forward}$ and $N_{backward}$ are the number of positrons detected by forward and backward detectors and α is a constant which accounts for any efficiency discrepancies between the forward and backward detectors.[18], [22]
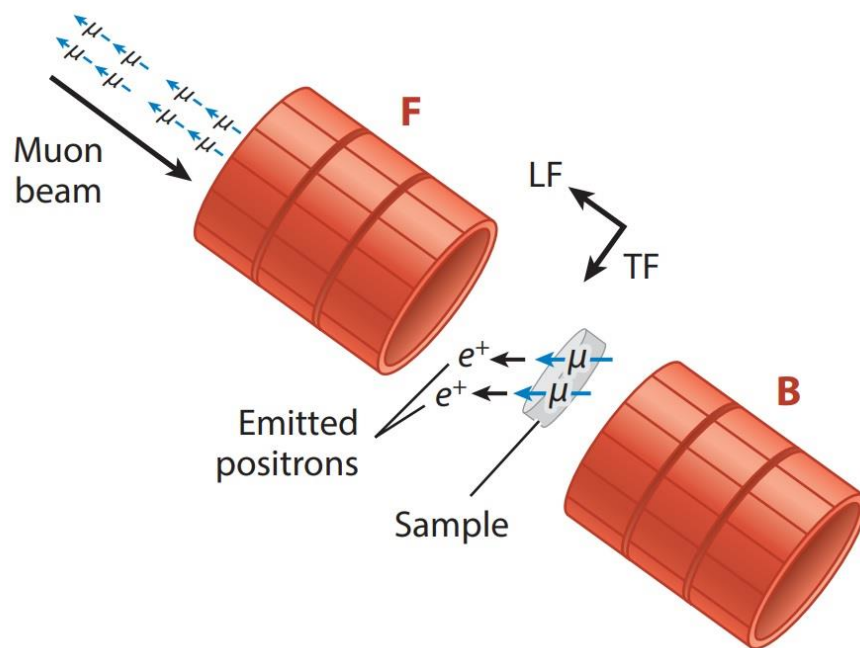
Figure 3.6. Schematic of a typical muon spectroscopy experimental setup. F and B are the forward and backward detectors, with LF and TF indicating the direction of longitudinal and transverse fields. [18]

3.7.1. Experimental Setup and Data Analysis

For a typical muon spectroscopy experiment of battery materials, a disk-shaped Ti sample holder (Figure 3.7) is used due to its small local magnetic field, allowing ingress of muons into the specimen and a negligible background signal. Ideally, *ca.* 2 g of powder sample, with a thickness of *ca.* 1 mm, is required for the highest count rates and smallest background signal. Measurements are then collected under zero applied field (ZF) and a small number of longitudinal fields (LF), *e.g.* 5 and 10 Gauss, over a temperature range of 100 to 500 K. The temperature range is chosen based on the region where the muons are most likely to be affected by Li-ion diffusion. Collection of data in multiple longitudinal fields enables the decoupling of interactions between the implanted muons and any local magnetic field distributions *e.g.,* from nuclear magnetic moments. This is because if the external applied LF is greater than the internal nuclear field contributions, the spin of the implanted muons will be held in their original direction and the muon spin relaxation will be reduced.[17] This affect is particularly useful when analysing materials containing paramagnetic ions, since the weak applied LF used decouples nuclear contributions but not the strong electronic contributions.
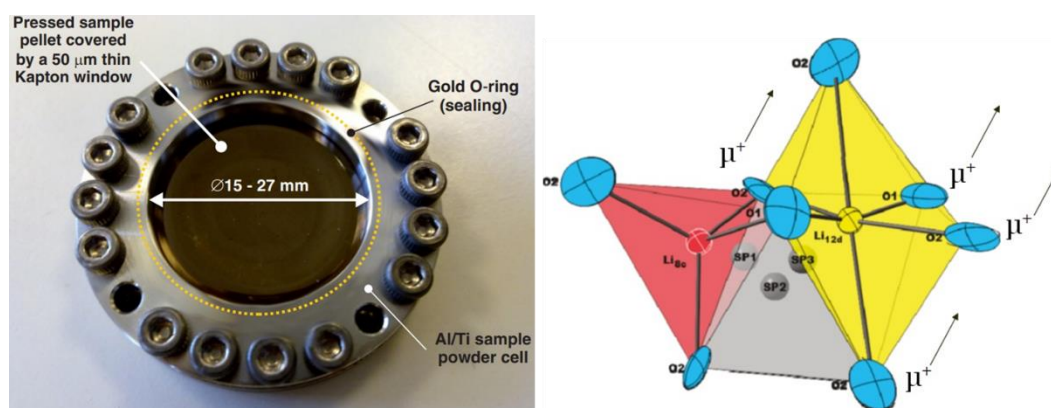
Figure 3.7. Example of a typically sample holder for muon spectroscopy experiments and schematic of implanted muons residing near oxygen sites in the Li-ion conductor, $Li_2NiGe_3O_8$. Adapted from [13], [17]

The raw asymmetry data (Figure 3.8) resulting from the differing interactions that cause the muon spin to depolarise can be described using a model incorporating the Dynamic Kubo Toyabe (DKT) function, such as in Equation 3.16.

$$A(t) = AG^{DKT}(\Delta, \nu, t, H_{LF}) \times e^{(-\lambda t)} + A_{BG} \qquad \text{(Equation 3.16)}$$

The DKT function contains the terms Δ, ν and H_{LF}, which represent the field distribution experienced by the muon, the fluctuation rate due to mobile species e.g. Li-ions, and the applied LF field, respectively. The multiplying factor accounts for paramagnetic species, which causes the muon to depolarise exponentially with a relaxation rate λ. An additional background term, A_{BG}, is also added to account for muons that stop within the sample holder. Δ and ν can be calculated for each temperature point measured, by simultaneously fitting the raw asymmetry data collected in zero and multiple longitudinal fields.
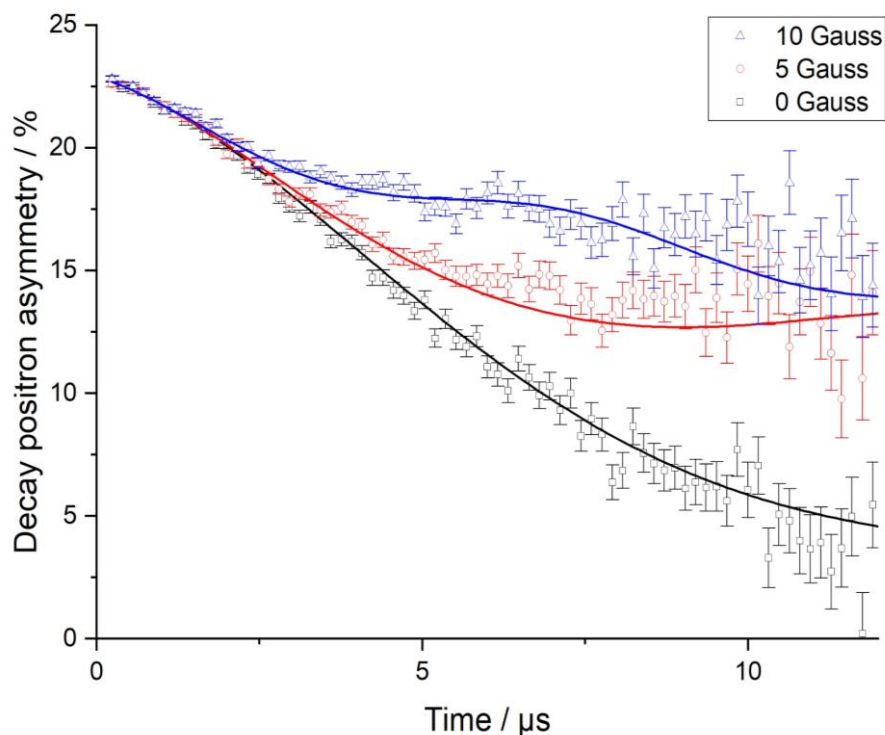
Figure 3.8. Example of raw muon spectroscopy data for $Li_2NiG_3O_8$, collected at 300 K in a zero field (black, squares), and applied longitudinal fields of 5 G (red, circles) and 10 G (blue, triangles).[23]

The activation energy of Li-ion diffusion, E_a, can be derived from the Arrhenius plot of v over the thermally activated region *i.e.* the temperature range for the onset of rapid Li-ion diffusion. v can also be used, alongside structural information, to calculate the Li-ion diffusion rate coefficient (D_{Li}) using Equation 3.17.[24]

$$D_{Li} = \Sigma_{i=1}^{n} \frac{1}{N_i} Z_{v,i} S_i^2 v \qquad \text{(Equation 3.17)}$$

Where N_i is the number of available sites in the conduction pathway. $Z_{v,i}$ is the vacancy fraction of destination sites. S_i is the hopping distance between neighbouring sites. Finally, v is the fluctuation rate, assumed to be a direct measure of the Li-ion hopping rate in the material.[18] The calculation of these parameters using muon spectroscopy can give meaningful insights into the local Li-ion diffusion properties and mechanisms, particularly in the case of paramagnetic-containing battery materials.

3.8. Electrochemical Cells and Battery Cycling

Galvanostatic cycling experiments are widely used to investigate materials for potential battery applications. In these experiments, batteries are first assembled and connected to a potentiostat, and a positive or negative current applied until the voltage reaches a defined limit. This is also known as galvanostatic cycling with a potential limit (GCPL). The main aims of these experiments are typically to 1) investigate the amount of energy (specific capacity) the battery can store during charge/discharge cycles (Section 1.2), 2) investigate the specific capacity over a defined number of cycles (cycle life) and 3) investigate the rate capabilities of the battery i.e. the specific capacity of the battery under increasing higher applied currents.

For this thesis, Swagelok type cells were used as shown in Figure 3.9. Electrodes were first prepared via mixing of the materials under study with conducting carbon (to increase the electronic conductivity) and a binder *e.g.* polyvinylidene fluoride (PVDF). The mixture was then pressed into 10 mm diameter pellets and assembled, together with a separator, liquid electrolyte and a Li metal disk, into cells within an Ar-filled glovebox. The cells were assembled under Ar to avoid the Li metal oxidising in air and to prevent the electrolyte absorbing water,

which can affect the cell performance. These cells are referred to as half-cells due to the use of Li metal as the counter electrode. The voltage limits were decided based on those used for similar materials previously investigated.[25], [26] The current applied was determined by multiplying the theoretical capacity by the mass of active material and C-rate. If the material is being tested as a cathode, a positive current is applied first, and the voltage will increase until the upper voltage limit (charging). Afterwards, a negative current is applied, and the voltage will decrease until the lower limit (discharging). This process is reversed if the material is tested as an anode.
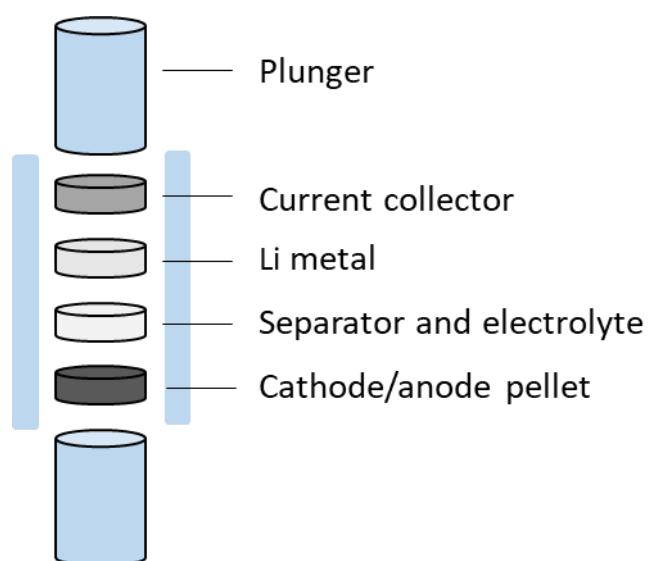
Figure 3.9. Schematic of a Swagelok cell used for Galvanostatic cycling experiments.

3.9. X-ray Absorption Spectroscopy (XANES)

The following section was written with the aid of the references [1], [27].

X-ray absorption spectroscopy (XAS) is a technique used to investigate the local coordination and oxidation state of different elements in a material (e.g. the changing oxidation state of an element in a battery material during charge/discharge processes). The technique works by measuring the absorption of X-rays of specific energies, depending on the element under investigation. In XAS, X-rays of specific energies are fired at a sample and a certain amount of these X-rays will have sufficient energy to ionise a core electron (*e.g.* an electron from the K shell or 1s orbital) into the continuum *i.e.* where the electron is no longer bound to the atom. The energy at which this process occurs is called the adsorption edge. Subsequently, an electron from a higher energy orbital can relax to fill the vacant core orbital,

resulting in the emission of characteristic (fluorescence) radiation. This process is analogous to the generation of laboratory X-rays, described in Section 3.2.

For XAS experiments a broad continuous spectrum of high energy X-rays are required and are typically only available at synchrotron facilities such as the Diamond Light Source synchrotron facility (Harwell Science & Innovation Campus, Oxfordshire, UK). During the experiment, the X-ray absorption coefficient (μ) of a specific element can be followed as a function of X-ray energy. μ is the probability that an X-ray will be absorbed by a sample. The experimental setup can make use of transmission and/or fluorescence sample geometries. In a transmission geometry, the incident X-rays first go through an ionisation chamber detector to measure the incident beam intensity (I_0), before passing through the sample and entering another ionisation chamber detector to measure the intensity of the transmitted X-rays (I_t). μ can then be calculated from the thickness of the measured sample (x), I_0 and I_t using Equation 3.18.

$$\mu x = ln\left(\frac{I_0}{I_t}\right)$$
(Equation 3.18)

μ can also be determined in fluorescence sample geometry (Figure 3.10), because the intensity of the fluorescence X-rays (I_f) produced can be assumed to be proportional to the absorption through Equation 3.19.

$$\mu x \propto \frac{I_f}{I_0}$$
(Equation 3.19)
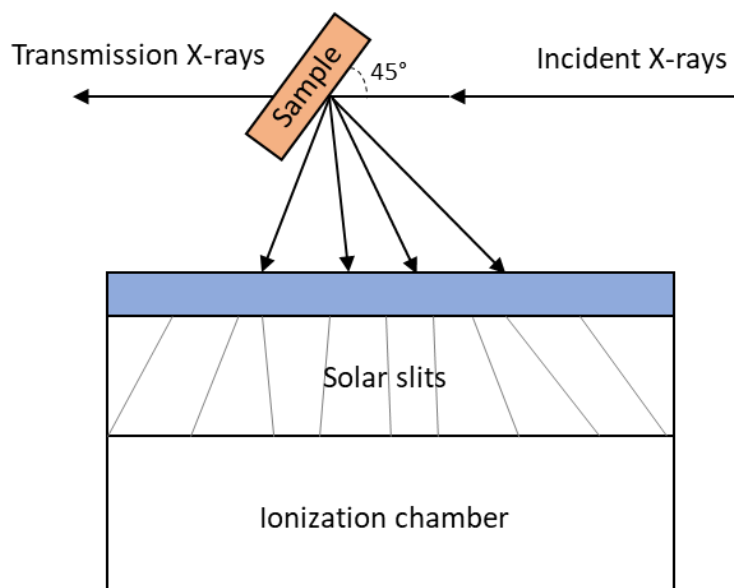
Figure 3.10. Schematic of a fluorescence sample geometry for XAS experiments.[27]

Figure 3.11 highlights the different regions in a XAS spectrum for Cr_2O_3. Each element will have a specific set of absorption edges, with their shape and energy position dependent on oxidation state and coordination environment of the scattering atom. Typically, the absorption edge energy will increase with increasing oxidation state due to the higher effective binding energy experienced by the core electrons. The XAS spectrum is conventionally divided into two regions: the X-ray absorption near edge structure (XANES) and the extended X-ray absorption fine structure (EXAFS). The XANES region usually ranges from -50 to +200 eV away from the absorption edge and can give information on the oxidation state and local atomic coordination. The EXAFS region can extend 1000 eV or more away from the absorption edge and contains information on the types and number of neighbouring atoms in relation to the absorbing atom.

The XANES features of interest for a given sample can be compared to a set of standard reference materials with known oxidation states and coordination, thus these properties can then be determined in the sample under investigation. Certain species may have features at energies below their edge, which are commonly referred to as pre-edge peaks. These pre-edge features are the result of transitions between the core shells and other unoccupied shells. For example, transition metal *K*-edge spectra often display pre-edge features due to core shell to valence shells transitions such as hybridised 3d orbitals.

In this thesis, XANES data were collected in fluorescence geometry for synthesised materials and standard reference samples at room temperature on the B18 beamline at the Diamond Light Source (Chapter 6).
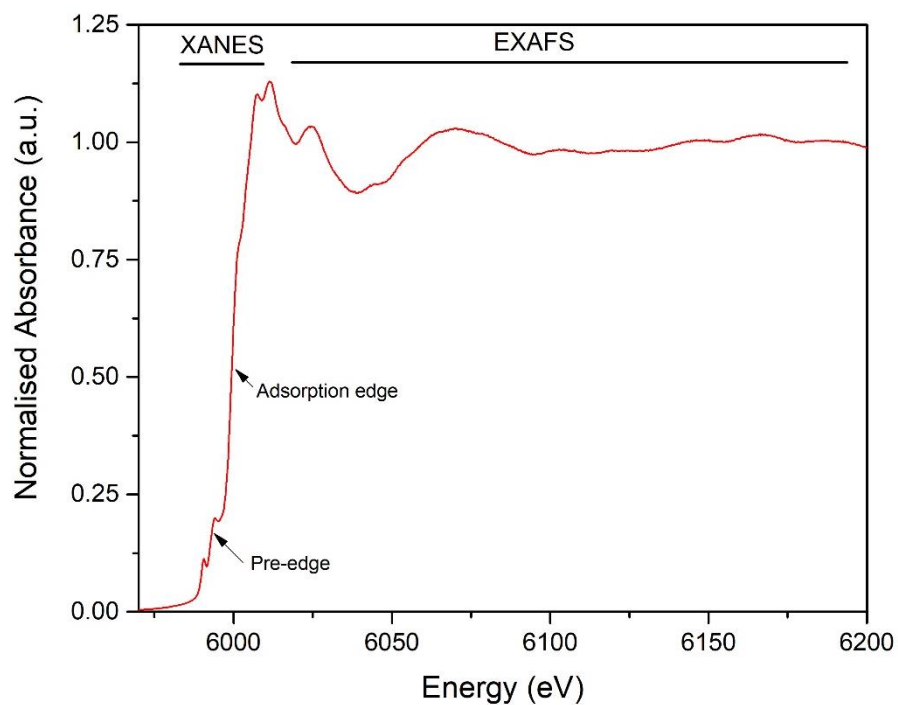
Figure 3.11. Example of an X-ray absorption spectrum of the Cr k-edge for Cr_2O_3 (Cr^{3+}).

3.8. References

[1]   A. R. West, *Solid State Chemistry and its Applications*, Student Ed. Wiley, 2014.

[2]   A. E. Danks, S. R. Hall, and Z. Schnepp, "The evolution of 'sol-gel' chemistry as a technique for materials synthesis," *Mater. Horizons*, vol. 3, pp. 91–112, 2016.

[3]   R. Boston, A. Carrington, and S. R. Hall, "Synthesis of spherical superconductors," *CrystEngComm*, vol. 15, pp. 3763–3766, 2013.

[4]   G. Armstrong, A. R. Armstrong, P. G. Bruce, P. Reale, and B. Scrosati, "TiO$_2$(B) Nanowires as an Improved Anode Material for Lithium-Ion Batteries Containing LiFePO$_4$ or LiNi$_{0.5}$Mn$_{1.5}$O$_4$ Cathodes and a Polymer Electrolyte," *Adv. Mater.*, vol. 18, no. 19, pp. 2597–2600, 2006.

[5]   J. R. Liu, M. Wang, X. Lin, D. C. Yin, and W. D. Huang, "Citric acid complex method of preparing inverse spinel LiNiVO$_4$ cathode material for lithium batteries," *J. Power Sources*, vol. 108, no. 1–2, pp. 113–116, 2002.

[6]   R. E. Dinnenbier and S. J. L. Billinge, *Powder Diffraction: Theory and Practice*. RSC Publishing, 2008.

[7]   R. Pynn, *Neutron Scattering: A Primer*. Los Alamos Science, 1990.

[8]   B. C. Hauback and H. Mauroy, *Neutron Scattering and Other Neclear Techniques for Hydrogen in Materials*. 2016.

[9]   V. F. Sears, "Neutron scattering lengths and cross sections," *Neutron News*, vol. 3, no. 3, pp. 26–37, 1992.

[10]   P. Scardi, L. B. Mccusker, R. B. Von Dreele, D. E. Cox, and D. Louer, "Rietveld refinement guidelines," *J. Appl. Crystallogr.*, vol. 32, pp. 36–50, 1999.

[11]   B. H. Toby, " R factors in Rietveld analysis: How good is good enough? ," *Powder Diffr.*, vol. 21, no. 1, pp. 67–70, 2006.

[12]   A. Laumann, H. Boysen, M. Bremholm, K. T. Fehr, M. Hoelzel, and M. Holzapfel, "Lithium migration at high temperatures in Li$_4$Ti$_5$O$_{12}$ studied by neutron diffraction," *Chem. Mater.*, vol. 23, no. 11, pp. 2753–2759, 2011.

[13]   N. Reeves-Mclaren, R. I. Smith, and A. R. West, "Lithium-ion conduction pathways in complex lithium spinels Li$_2$MGe$_3$O$_8$ (M = Ni or Zn)," *Chem. Mater.*, vol. 23, no. 15, pp. 3556–3563, 2011.

[14]   J. C. Bachman *et al.*, "Inorganic Solid-State Electrolytes for Lithium Batteries : Mechanisms and Properties Governing Ion Conduction," *Chem. Rev.*, vol. 116, no. 1, pp. 140–162, 2016.

[15]   J. T. S. Irvine, D. C. Sinclair, and A. R. West, "Electroceramics: Characterization by Impedance Spectroscopy," *Adv. Mater.*, vol. 2, no. 3, pp. 132–138, 1990.

[16]   D. Sinclair, "Characterization of Electro-materials using ac Impedance Spectroscopy," *Boletín la Soc. Española Cerámica y Vidr.*, vol. 34, no. 2, pp. 55–65, 1995.

[17]   M. Mansson and J. Sugiyama, "Muon-spin relaxation study on Li- and Na-diffusion in

solids," *Phys. Scr.*, vol. 88, no. 068509, pp. 1–13, 2013.

[18] I. McClelland, B. Johnston, P. J. Baker, M. Amores, E. J. Cussen, and S. A. Corr, "Muon Spectroscopy for Investigating Diffusion in Energy Storage Materials," *Annu. Rev. Mater. Res.*, vol. 50, pp. 371–393, 2020.

[19] P. J. Baker *et al.*, "Probing magnetic order in $LiMPO_4$ (M = Ni, Co, Fe) and lithium diffusion in Li_xFePO_4," *Phys. Rev. B*, vol. 84, no. 174403, pp. 1–8, 2011.

[20] K. Tustain *et al.*, "From magnetic order to quantum disorder in the Zn-barlowite series of S = 1/2 kagomé antiferromagnets," *npj Quantum Mater.*, vol. 5, no. 1, 2020.

[21] M. Amores, T. E. Ashton, P. J. Baker, E. J. Cussen, and S. A. Corr, "Fast microwave-assisted synthesis of Li-stuffed garnets and insights into Li diffusion from muon spin spectroscopy," *J. Mater. Chem. A*, vol. 4, no. 5, pp. 1729–1736, 2016.

[22] S. J. Blundell, "Spin-polarized muons in condensed matter physics," *Contemp. Phys.*, vol. 40, no. 3, pp. 175–192, 1999.

[23] D. Z. C. Martin *et al.*, "Evaluating lithium diffusion mechanisms in the complex spinel $Li_2NiGe_3O_8$," *Phys. Chem. Chem. Phys.*, vol. 21, no. 41, pp. 23111–23118, 2019.

[24] J. Sugiyama, K. Mukai, Y. Ikedo, H. Nozaki, M. Månsson, and I. Watanabe, "Li diffusion in Li_xCoO_2 probed by Muon-Spin spectroscopy," *Phys. Rev. Lett.*, vol. 103, no. 14, pp. 1–4, 2009.

[25] G. T.-K. Fey, W. Li, and J. R. Dahn, "$LiNiVO_4$: A 4.8 volt electrode material for lithium cells," *J. Electrochem. Soc.*, vol. 141, no. 9, pp. 2279–2282, 1994.

[26] T. Uyama and K. Mukai, "Synthesis of $LiMg_{1-x}Zn_xVO_4$ with $0 \leq x \leq 1$ for application to the negative electrode of lithium-ion batteries," *Mater. Today Energy*, vol. 14, pp. 1–10, 2019.

[27] S. D. Kelly, D. Hesterberg, and B. Ravel, *Analysis of soils and minerals using x-ray absorption spectroscopy*, vol. 5, no. 5. 2008.

Chapter 4: Synthesis and Characterisation of the $Li_{2+x}Ni_{2-2x}Cr_xV_2O_8$ Solid solution

4.1. Introduction

The composition $Li_3CrV_2O_8$ was first reported in the 1960's separately by Blasse and Joubert and Durif.[1], [2] The structure was described as an inverse spinel with Li and Cr occupying octahedral sites and V occupying tetrahedral sites. However, their conclusions differed on whether 3:1 ordering was observed between Li and Cr on the octahedral sites. Blasse noted the presence of superstructure reflections in the X-ray diffraction patterns, suggesting $Li_3CrV_2O_8$ forms an ordered inverse spinel structure; whereas Joubert and Durif did not observe any reflections indicative of ordering, instead reporting a disordered cubic inverse spinel in the space group $Fd\bar{3}m$ (a = 8.19 Å).[2] Blasse suggested these differences may be due to a difference in reaction kinetics.[1] A later study by Touboul *et al* failed to synthesise $Li_3CrV_2O_8$ from Li_3VO_4 and Cr_2O_3 using the same reaction temperature as the previous studies (550 °C).[3] To date, these limited experiments are the only reports on the synthesis and characterisation of $Li_3CrV_2O_8$. As such, the structural and electrochemical properties of $Li_3CrV_2O_8$ have not yet been fully investigated.

As discussed in Section 2.4.5 of the literature review, several inverse spinel structures with the chemical formula, $[LiTM]^{oct}[V]^{tet}O_4$ (TM = 2+ transition metal *e.g.* Ni, Co, Mn), have previously been investigated as electrode materials for LiB applications.[4]–[6] $LiNiVO_4$ has received significant attention because it was one of the first high voltage (4.8 V *vs.* Li^+/Li) cathode materials reported.[7] Despite this, there is limited information available on Li-ion diffusion behaviour within inverse spinels.[8]–[11] The ionic and electronic conductivity of a material can greatly influence its electrochemical properties in LiBs, for instance how quickly the battery can be charged. Lower electronic conductivity can also mean greater amounts of conductive carbon is required to have sufficient electrical conductivity when producing electrodes, thus reducing the overall energy density (Wh/kg).

In this chapter, attempts are made to synthesise $Li_3CrV_2O_8$ *via* the same solid-state method reported by Blasse as well as via a citric acid sol-gel route.[1], [12] The compositions $Li_{2+x}Ni_{2-2x}Cr_xV_2O_8$ (0 ≤ *x* ≤ 1) were also synthesised *via* the same sol-gel route. Room temperature combined neutron and X-ray powder diffraction refinements were used to fully

characterise their crystal structures. Varying the Li:TM ratio has been shown to dramatically affect electrochemical properties such as capacity, operating voltage and Li-ion conduction of electrode materials (*e.g.* Li-rich transition metal oxide cathode materials, see Section 2.4.2). Therefore, impedance spectroscopy measurements were utilised to investigate the effect of varying the Li:TM ratio on the conductivity of these materials.

4.2. Experimental

4.2.1. Synthesis and thermal analysis

The compositions $Li_{2+x}Ni_{2-2x}Cr_xV_2O_8$ (x = 0, 0.25, 0.5, 0.75, 0.8, 0.85, 0.9, 0.95 and 1) were prepared using a citric acid sol-gel method. Appropriate amounts of the starting materials lithium nitrate ($LiNO_3$, Alfa Aesar, 99 %, dried at 180 °C for 12 h), chromium nitrate nonahydrate ($Cr(NO_3)_3.9H_2O$, Alfa Aesar, 99.99 %), nickel acetate tetrahydrate ($Ni(OCOCH_3)_2 \cdot 4H_2O$, Sigma-Aldrich, 99 %) and vanadium(V) oxide (V_2O_5, Sigma Aldrich, 99.6 %, dried at 180 °C for 12 h) were dissolved in deionised water with constant magnetic stirring at 80 °C, forming a brown suspension. An aqueous solution of citric acid, with a 1:2 ratio of metal ions to citric acid, was slowly added to the suspension, which changed colour from brown to a clear blue solution. This was then stirred at 120 °C until the formation of a dried precursor, which was then ground in an agate mortar, placed into an alumina crucible, and calcined in air at 500 °C for 12 h. Finally, the powder was re-ground, and calcined for a second time in air at 500 °C for 12 h. All heating steps described used heating and cooling rates of 5 °C min^{-1}.

Attempts were also made to synthesis the composition $Li_3CrV_2O_8$ (x = 1) via solid-state routes. Stoichiometric amounts of the starting materials Li_2CO_3 (Acros Organics, 99 %, dried at 180 °C for 12 h), Cr_2O_3 (Sigma Aldrich, 99 %, dried at 900 °C for 12 h), and V_2O_5 (Sigma Aldrich, 99.6 %, dried at 180 °C for 12 h) were ground together with acetone using a mortar and pestle. The mixture was air-dried, placed into an alumina crucible and calcined at 550 °C for 24 h at 5 °C min^{-1}. This process was repeated until the product was observed to remain unchanged via XRD analysis.

Differential scanning calorimetry (DSC) was used to analyse the thermal behaviour of the compositions x = 0, 0.25, 0.5, 0.75 and 1. Powder samples were analysed using a SDT Q600 Simultaneous DSC-TGA in air over the temperature range of 20 to 900 °C, using a heating rate of 10 °C min^{-1}.

4.2.2. X-ray and Neutron Diffraction

All samples were initially characterised by X-ray powder diffraction using a Bruker D2 Phaser diffractometer using Ni-filtered Cu Kα (λ = 1.5418 Å) radiation and a Lynxeye detector. The ICDD PDF-4+ database, 2020 edition, and Sleve+ software was used for phase analysis. For lattice parameter refinements, data were collected using a STOE STADI P (Mo Kα1, λ = 0.7107 Å) powder diffractometer with a linear position sensitive detector. STOE's WinX^{POW} software was used to calibrate the data using a Si NIST 640e line position standard reference material, added as an internal calibrant.

High temperature XRD data were collected on precursor powder (dried at 120 °C) for the compositions $Li_3CrV_2O_8$, $Li_2Ni_2V_2O_8$ and $Li_{2.5}NiCr_{0.5}V_2O_8$ using a PANalytical X'Pert[3] Powder X-ray diffractometer with Cu Kα (λ = 1.5418 Å) radiation. Specimens were heated from 25 to 550 °C in increments of 25 °C. The furnace was heated at 60 °C min^{-1}, with 22 minute dwells at each temperature for data collection.

Room temperature time-of-flight (ToF) neutron powder diffraction data (for x = 0, 0.25, 0.5, 0.75 and 1) were collected on the Polaris powder diffractometer through express access at the ISIS Neutron and Muon Facility, Rutherford Appleton Laboratory.[13] Vanadium cans were filled with *ca.* 2 g of powdered sample and diffraction data was collected for *ca.* 200 μAh. For $Li_3CrV_2O_8$, room temperature data was collected in a silica glass tube as part of variable-temperature ToF experiments (Chapter 5). The EXPGUI interface for GSAS was used for Rietveld refinements using X-ray diffraction data, and neutron diffraction data collected using the backscattering detector bank (bank 5).[14], [15]

4.2.3. Impedance Spectroscopy

For impedance spectroscopy, the reacted powders were pressed into pellets at 1 ton using a cold uniaxial press to yield pellets of approximately 2 to 3 mm thickness and 10 mm diameter. The pellets were sintered in air at 650 °C for x = 0, 0.25, 0.5, 0.75 and 550 °C for x = 1 for 12 h. They were then polished and sputter coated with gold before impedance measurements. Density measurements were collected by hand, measuring the mass and thickness of pellets after sintering. Theoretical densities were calculated from lattice parameters obtained during Rietveld refinement and Equation 4.1.

$$Theortical\ density\ (gcm^{-3}) = \frac{(Z\ x\ Mr)}{(a^3\ x\ Na)} \qquad (Equation\ 4.1)$$

where Z is the number of atoms per unit cell, M_r is molecular weight (g/mol), a^3 (cm^3) is the unit cell volume, and N_a is Avogadro's number (mol^{-1}).

The impedance of each sample was measured using a Solartron 1260 impedance analyser in the frequency range of 10^6 Hz to 0.01 Hz with an applied AC signal of 100 mV. All measurements were corrected using a geometric factor (area/thickness of the pellet). The corrected data was then analysed within the Zview software. Total resistances were recorded as the value where the semicircle intercepts the x-axis. Bulk resistances were calculated by fitting the semicircles and calculating the resistance at the x-axis intercept using the fit circle function within Zview. Measurements were taken during cooling from 250 °C to 75 °C under dry air to avoid moisture, which could conceivably affect the impedance results through the advent of proton conduction.[8]

4.3. Results and Discussion

4.3.1. Synthesis of $Li_{2+x}Ni_{2-2x}Cr_xV_2O_8$ $(0 \leq x \leq 1)$

X-ray powder diffraction patterns, Figure 4.1, show the results of initial attempts to synthesise $Li_3CrV_2O_8$ following the same solid-state routes reported by Blasse.[1] After two days reacting at 550 °C the diffraction patterns showed peaks matching to the inverse spinel $Li_3CrV_2O_8$ (PDF card number 00-016-0735), in the $Fd\overline{3}m$ space group.[2] Significant additional peaks corresponding to $LiVO_3$, Li_3VO_4 and Cr_2O_3 were also observed. The powder was repeatedly heated at 550 °C for 24 h intervals with intermittent regrinding and XRD measurements. However, the XRD patterns after heating showed very little change in the intensity of the Bragg peaks attributed to secondary phases. Even after 7 days of reaction, only a small decrease in intensity was observed for the additional peaks. This suggests the reaction of the intermediate phases to form $Li_3CrV_2O_8$ proceeds very slowly at 550 °C, likely due to slow reaction kinetics of oxides such as Cr_2O_3, which are refractory and therefore result in slow diffusion, as well as the low temperature used for the solid-state reaction. Scope for increasing the reaction temperature was limited by the presence of $LiVO_3$, which reportedly melts at 616 °C.[16] Attempts to increase the reaction temperature above 600 °C resulted in the samples melting and sticking to the reaction vessel. As a single phase material had not

been produced after significant reaction time, an alternative sol-gel citric acid method was adopted, following a previously reported synthesis route for end member $Li_2Ni_2V_2O_8$.[12]
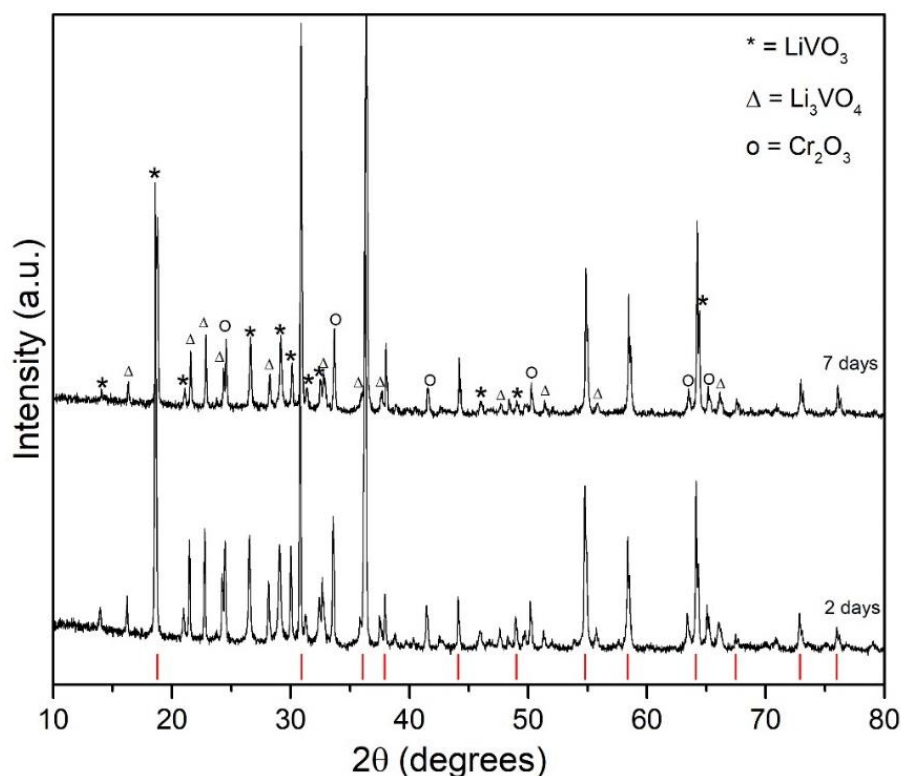
Figure 4.1. XRD patterns after the attempted solid-state synthesis of $Li_3CrV_2O_8$ at 550 °C for 2 and 7 days. Peaks attributed to the $Li_3CrV_2O_8$ inverse spinel phase are highlighted using red tickmarks.

XRD patterns after attempts to synthesise the solid solution $Li_{2+x}Ni_{2-2x}Cr_xV_2O_8$, x = 0 to 1, via sol-gel routes are shown in Figures 4.2 and 4.3. After 24 h at 500 °C, sharp Bragg peaks corresponding to a disordered ($Fd\bar{3}m$) inverse spinel structure were observed for all compositions up to x = 0.9. For compositions between x = 0.9 and 1, small additional peaks matching to Li_3VO_4 were observed. As x increases, the relative intensity of the (111) and related reflections also increases. This is due to the changes in composition leading to an altering of the (F_{111}) structure factor. Assuming the structure factor for the (111) reflection can be approximated for X-ray scattering by Equation 4.2, then for x = 0 (f_A = V, f_B = Li and f_C = TM) the magnitude of F_{111} will be small. As x increases, the ($f_B + f_C$) term decreases and thus the magnitude of F_{111} will increase. This has previously been explained in the context of the differences observed between X-ray diffraction patterns of normal and inverse spinels.[11]

91

$$F_{111} \cong 4\sqrt{2f_A} - 4(f_B + f_c) \qquad \text{(Equation 4.2)}$$

Blasse noted supercell reflections due to Li/Cr ordering when synthesising $Li_3CrV_2O_8$ via solid-state routes however, there was no evidence of any additional reflections in the compositions synthesised in this work.[1] Page *et al.* suggested long duration (>300 h) annealing at low temperatures (500 °C or lower) can increase the degree of ordering between Li/TM sites (TM = transition metals), as this allows sufficient time and energy for the system to reach an ordered state.[11] Because of this, a sample of x = 1 was annealed for 312 h at 500 °C, after which the small impurity peaks associated with Li_3VO_4 were not present, suggesting after enough time the reaction can proceed to completion. Nevertheless, there was still no evidence for any long range ordering observed in diffraction data after this long duration annealing step.

High temperature XRD data for $Li_2Ni_2V_2O_8$ (x = 0), $Li_{2.5}NiCr_{0.5}V_2O_8$ (x = 0.5) and $Li_3CrV_2O_8$ (x = 1) precursors were collected to investigate the mechanism of phase formation during calcination, as shown in Table 4.1. and Figures 4.4. to 4.9. The initial formation temperature for the inverse spinel phase was found to increase with x. For example, for x = 0, broad peaks associated with the target phase, $Li_2Ni_2V_2O_8$, appear at 300 °C. As the temperature is increased, these peaks become narrower and increase in intensity, likely associated with increasing crystallite size. For both x = 0.5 and 1, peaks associated with the inverse spinel phase appear at 325 °C and 375 °C, respectively. Peaks associated with Li_3VO_4 can also be seen at 325 °C and 375 °C. These peaks then decrease in intensity and do not appear after 500 °C for x = 0.5, suggesting that Li_3VO_4 is an intermediate phase which can react to form a single phase spinel in samples containing both Ni and Cr. However, for $Li_3CrV_2O_8$, the peaks corresponding to Li_3VO_4 increase in intensity with increasing temperature. This suggests that Li_3VO_4 may be more stable or Cr-containing samples are less reactive, and significantly more energy is required for it to fully react and form a single phase, as seen in the sample annealed for 312 h.
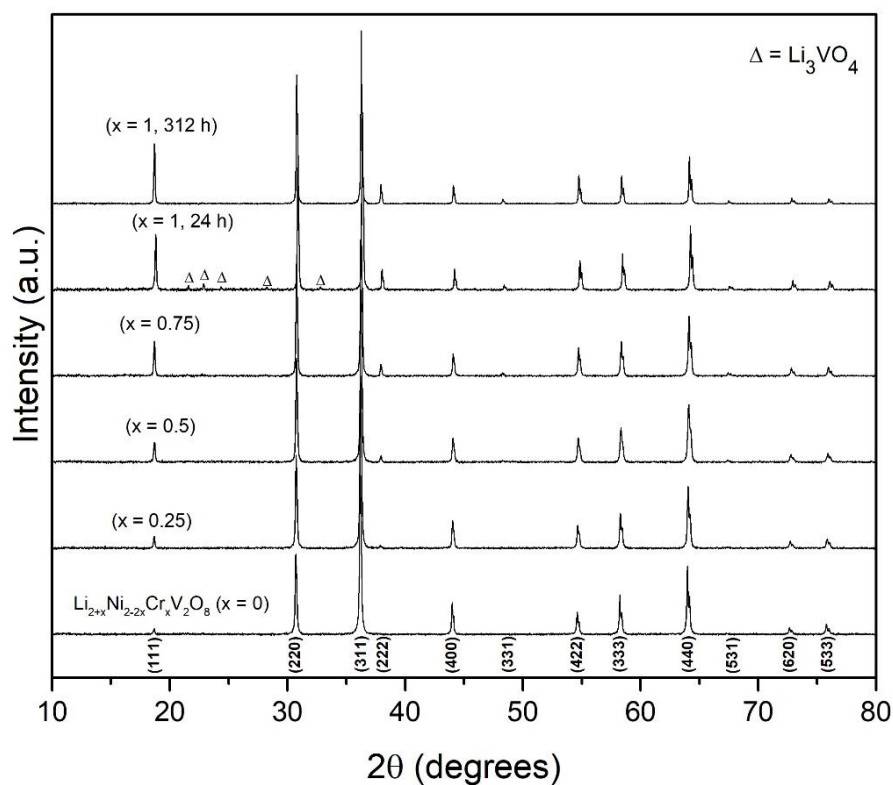
Figure 4.2. XRD patterns of the compositions $Li_{2+x}Ni_{2-2x}Cr_xV_2O_8$ (x = 0, 0.25 0.5 0.75 and 1) synthesised using a citric acid sol gel method at 500 °C for 24 h.
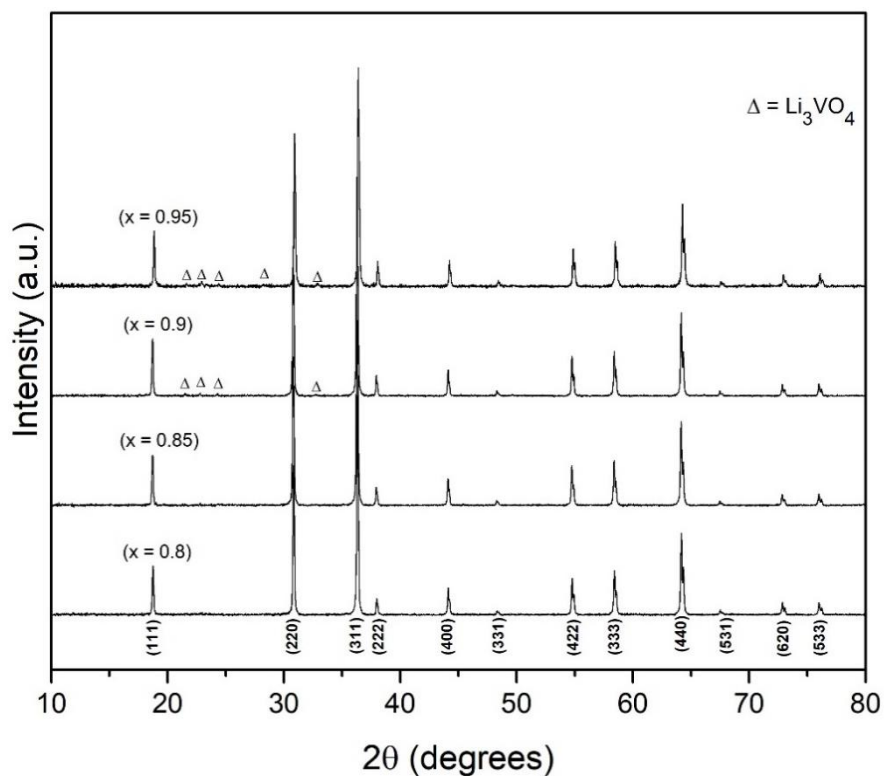
Figure 4.3. XRD patterns of the compositions $Li_{2+x}Ni_{2-2x}Cr_xV_2O_8$ (x = 0.8, 0.85 0.9 and 0.95) synthesised using a citric acid sol gel method at 500 °C for 24 h.

Table 4.1. Summary of phase formation for *x* = 0, 0.5 and 1 using high temperature (300 °C to 550 °C) XRD data of precursor powders before heat treatment.

Composition ($Li_{2+x}Ni_{2-2x}Cr_xV_2O_8$)	Phase formation
0	Broad peaks associated with a spinel phase observed between 300 °C - 550 °C.
0.5	Broad peaks associated with spinel and Li_3VO_4 phases observed between 325 °C - 500 °C. At 300 °C the sample is amorphous and above 500 °C a single phase spinel is observed.
1	Broad peaks associated with spinel and Li_3VO_4 phases observed between 375 °C - 550 °C. Below 375 °C the sample is amorphous.
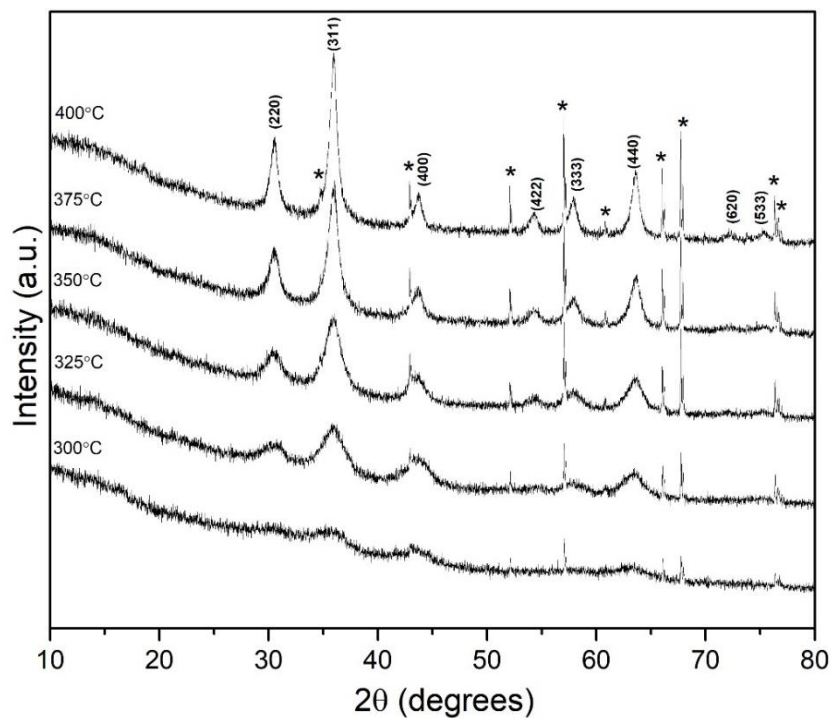
Figure 4.4. High temperature (HT) XRD data for $Li_2Ni_2V_2O_8$ precursor powder between 300 - 400 °C. * indicates additional peaks associated with the Al_2O_3 crucible and indexed peaks are associated with $Li_2Ni_2V_2O_8$.
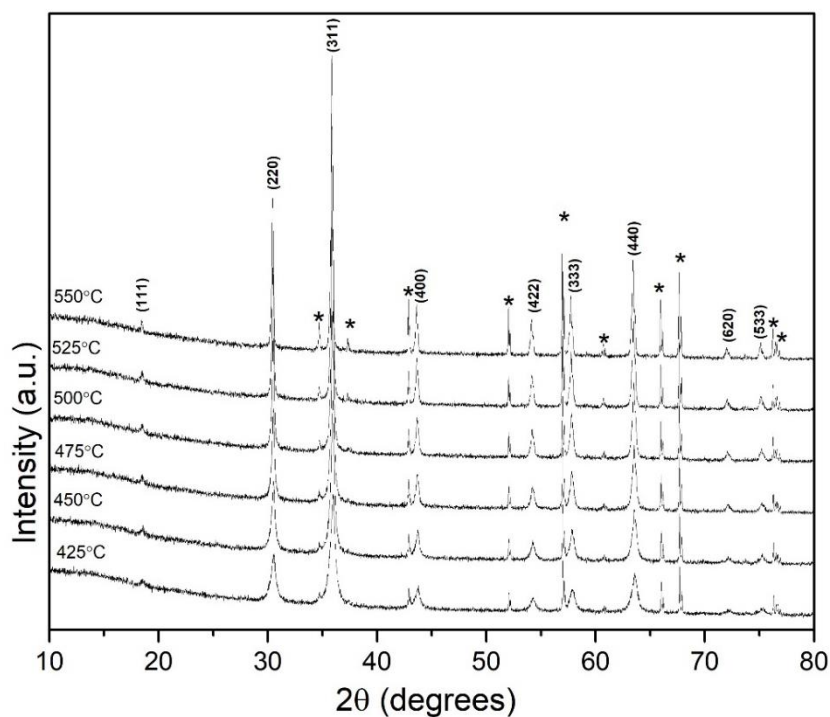
Figure 4.5. HT-XRD data for $Li_2Ni_2V_2O_8$ precursor powder between 425 - 525 °C. * indicates additional peaks associated with the Al_2O_3 crucible and indexed peaks are associated with $Li_2Ni_2V_2O_8$.
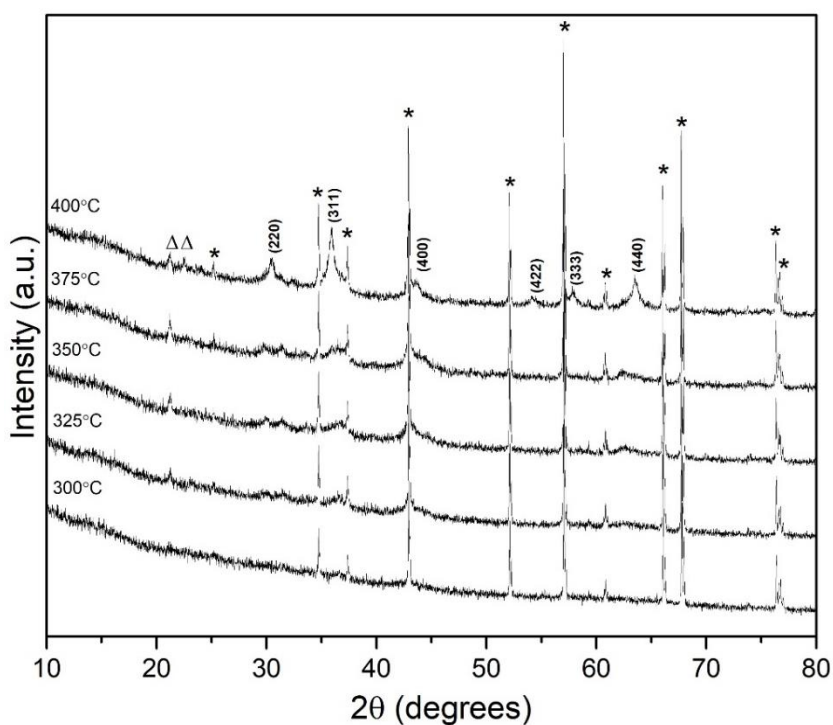
Figure 4.6. HT-XRD data for $Li_{2.5}Cr_{0.5}NiV_2O_8$ precursor powder between 300 - 400 °C. * indicates additional peaks associated with the Al_2O_3 crucible, Δ = peaks associated with Li_3VO_4 and indexed peaks are associated with $Li_{2.5}Cr_{0.5}NiV_2O_8$.
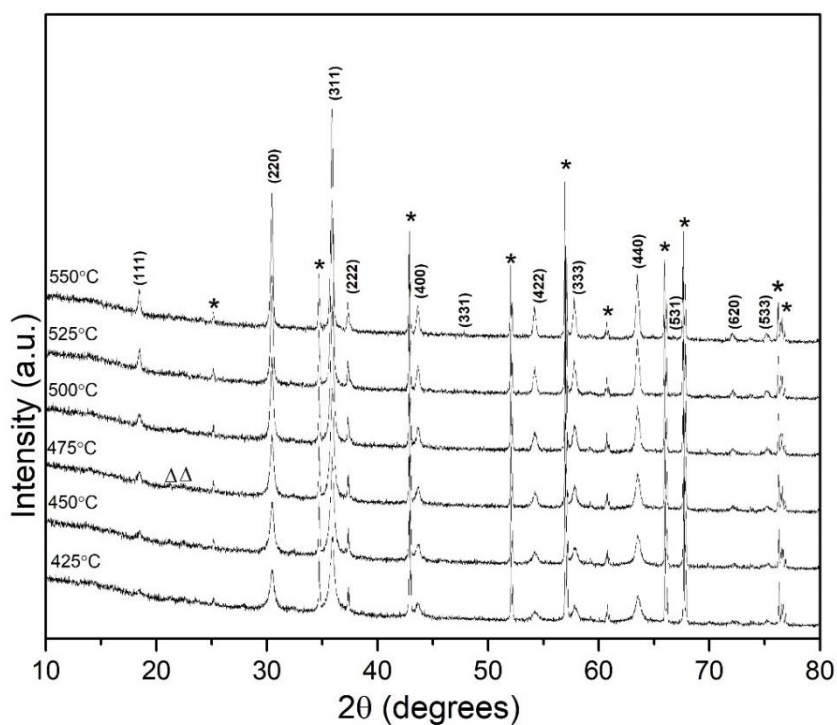
Figure 4.7. HT-XRD data for $Li_{2.5}Cr_{0.5}NiV_2O_8$ precursor powder between 425 - 550 °C. * indicates additional peaks associated with the Al_2O_3 crucible, Δ = peaks associated with Li_3VO_4 and indexed peaks are associated with $Li_{2.5}Cr_{0.5}NiV_2O_8$.
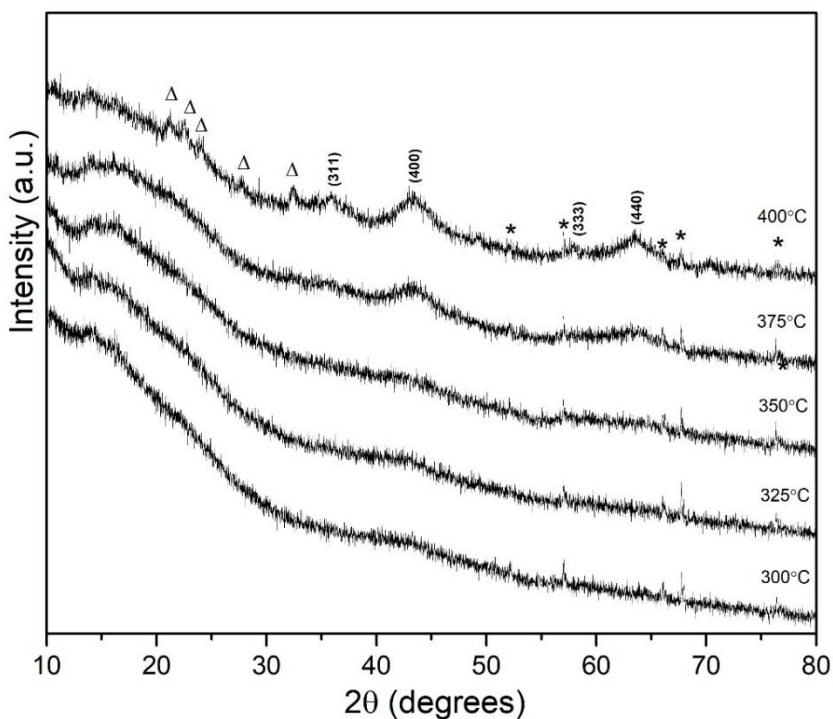
Figure 4.8. HT-XRD data for $Li_3CrV_2O_8$ precursor powder between 300 - 400 °C. * indicates additional peaks associated with the Al_2O_3 crucible, Δ = peaks associated with Li_3VO_4 and indexed peaks are associated with $Li_3CrV_2O_8$.
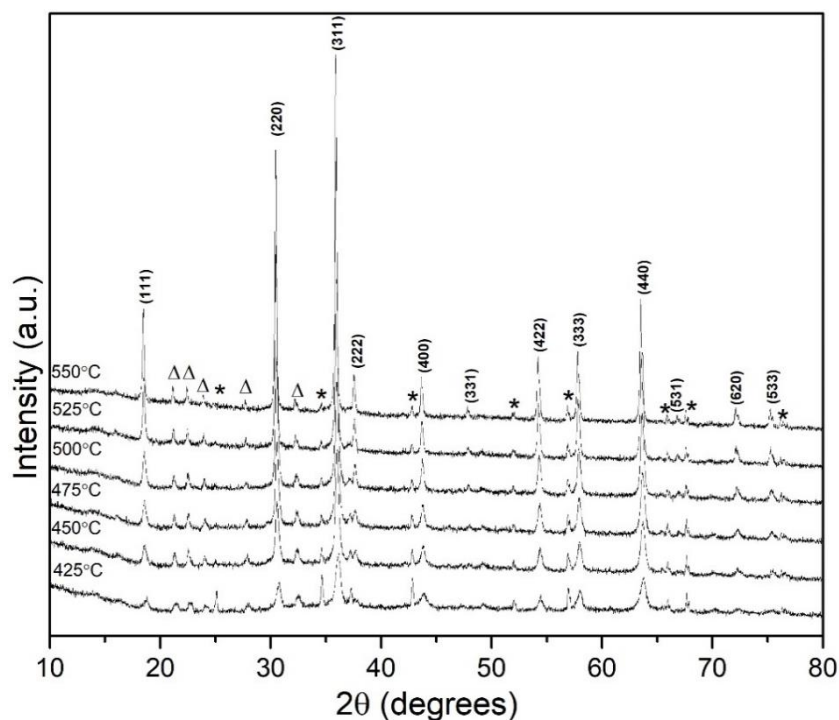
Figure 4.9. HT-XRD data for $Li_3CrV_2O_8$ precursor powder between 425 - 550 °C. * indicates additional peaks associated with the Al_2O_3 crucible, Δ = peaks associated with Li_3VO_4 and indexed peaks are associated with $Li_3CrV_2O_8$.

Figure 4.10 shows DSC heating curves for the compositions $Li_{2+x}Ni_{2-2x}Cr_xV_2O_8$ (x = 0, 0.25, 0.5 0.75 and 1). For x = 1, a sharp endothermic peak is observed at *ca.* 690 °C, with an onset temperature of 650 °C. The sharp endothermic peak is likely indicative of the sample melting.[17] For x = 0.75 and 0.5, the DSC curves can be interpreted as containing a broad endothermic feature between 550 °C and 700 °C. These may be indicative of the samples undergoing partial melting due to the similar compositions to x = 1. Alternatively, a broad exothermic feature between 700 to 750 °C can be observed in the DSC curves of x = 0.75. This could be indicative of the sample undergoing a gradual second order transition such as cation ordering. A similar phenomenon has previously been observed in the DSC for the spinel composition $MgFe_2O_4$ and confirmed by Rietveld refinements.[18] To confirm this, future work could investigate any structural changes that may occur with temperature using complementary techniques e.g. DSC and XRD. For compositions x = 0.25 and 0 there is no indication of decomposition or melting of the spinel phase up to 900 °C. These samples display a gradually decreasing slope, suggesting the materials are absorbing heat. XRD data (Figure

97

4.11) collected after calcination at 650 °C for 6 h showed $Li_3CrV_2O_8$ had decomposed into the oxides Li_3VO_4, $LiVO_3$ and Cr_2O_3. Consequently, it is clear that this phase is less thermally stable than its Ni-containing counterparts. Pellets for impedance measurements were subsequently sintered at 550 °C for $x = 1$ and 650 °C for $x = 0, 0.25, 0.5$, and 0.75. No changes were observed within XRD patterns collected after sintering (Figure 4.12).
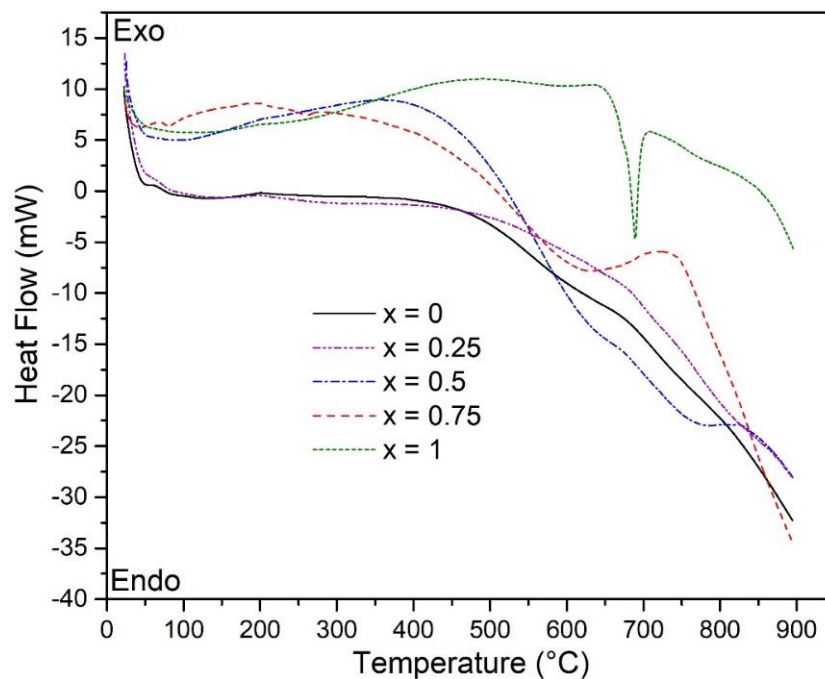
Figure 4.10. DSC heating curves for $Li_{2+x}Ni_{2-2x}Cr_xV_2O_8$ ($x = 0, 0.25, 0.5, 0.75$ and 1.0) from 25 °C to 900 °C.
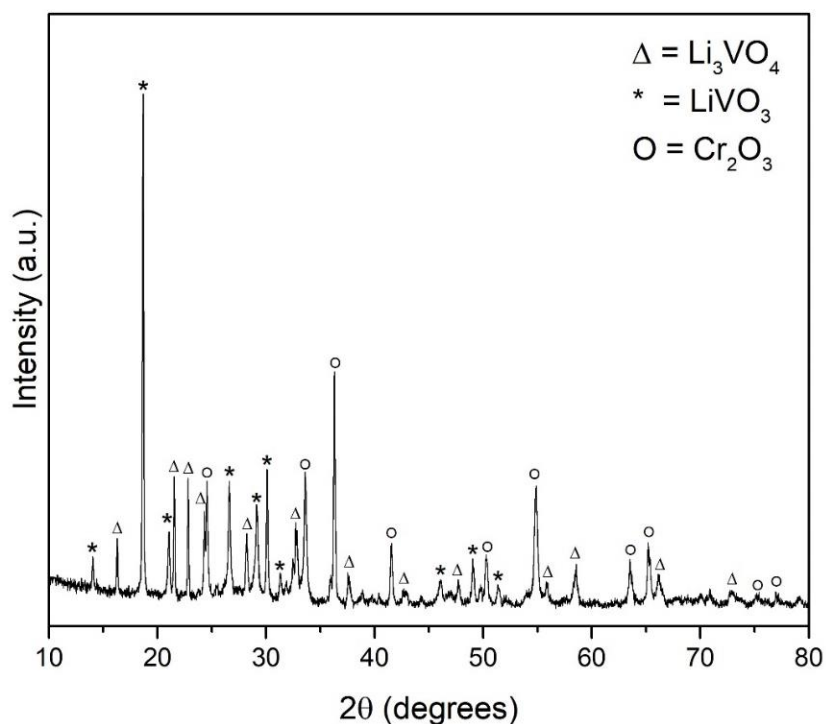
Figure 4.11. XRD data for $Li_3CrV_2O_8$ calcined at 650 °C for 6 h. Δ indicates peaks associated with Li_3VO_4, * = peaks associated with $LiVO_3$ and o = peaks associated with Cr_2O_3.
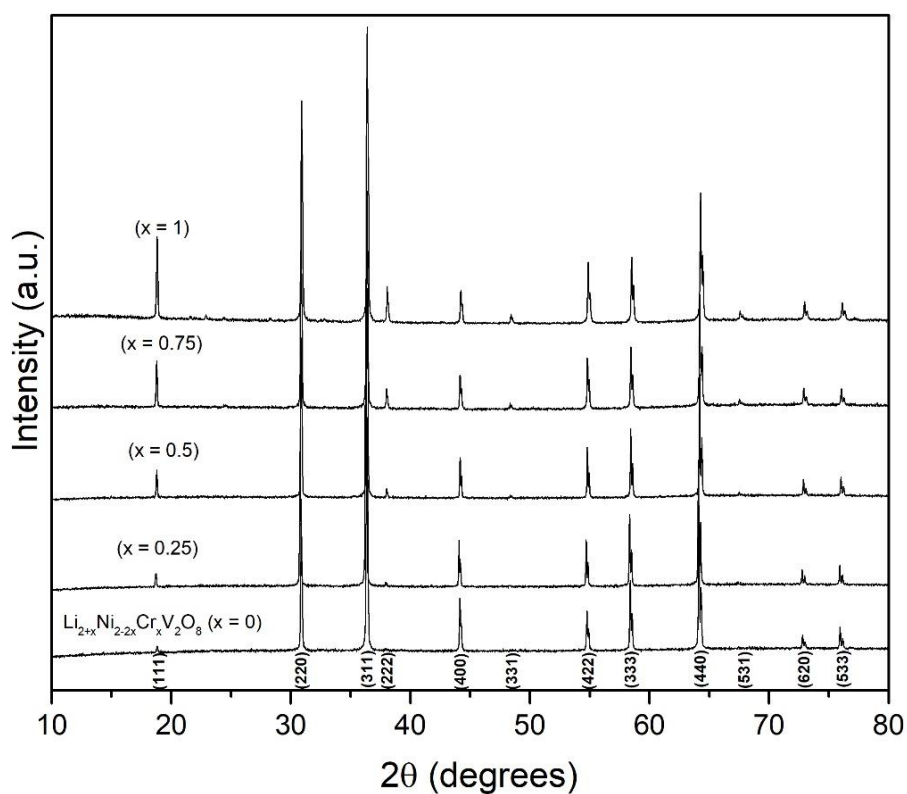
Figure 4.12. XRD data for $Li_{2+x}Ni_{2-2x}Cr_xV_2O_8$ after sintering at 650 °C (x = 0, 0.25, 0.5 and 0.75) and 550 °C for 12 h (x = 1).

4.3.2. Lattice Parameter Variations in $Li_{2+x}Ni_{2-2x}Cr_xV_2O_8$

Lattice parameters for all synthesised compositions in the solid solution $Li_{2+x}Ni_{2-2x}Cr_xV_2O_8$ were calculated from XRD data using an internal Si standard. Room temperature neutron diffraction data were also collected for the compositions x = 0, 0.25, 0.5, 0.75 and 1 (heated for 24 h). The initial structural model assumed a fully inverse spinel which was previously reported for $LiNiVO_4$.[11] The model placed appropriate amounts of Li, Ni and Cr on octahedral 16c sites, V on tetrahedral 8a sites and oxygen on 32e sites. Initial isotropic thermal displacement parameters, U_{iso}, were fixed to the default value of 0.005 $Å^2$. For the initial stages of the refinement, the XRD data was imported first, refining the background and phase fraction using a shifted Chebyschev function with twelve terms. This was followed by lattice parameters and zero point correction (to account for any specimen displacement error or misalignment of the detector). The peak profile parameters were then refined until convergence. The (111) peak in the XRD data was excluded from the refinement due to peak asymmetry at low angles (<18° 2Θ) caused by axial divergence. This resulted in an improved fit as the peak shape can be described using one model for both lower and higher angles. Subsequent calculated lattice parameters are plotted as a function of composition in Figure 4.13. The lattice parameters for both end members $Li_2Ni_2V_2O_8$ (a = 8.2204(1) Å) and $Li_3CrV_2O_8$ (500 °C, 312 h) (a = 8.1992(1) Å) were in good agreement with previous reports.[1], [2], [11], [19] For single phase compositions, the lattice parameters were found to decrease slightly with increasing x and follow a linear relationship. This is likely due to the differences in the ionic radius of Ni^{2+} (0.69 Å), Li^+ (0.76 Å) and Cr^{+3} (0.615 Å). The slight deviation from Vegard's law (which states the lattice parameters of a solid solution is the weighted average of the two end members) at higher values of x from the linear fit may be due to small discrepancies in composition. Further evidence for this is observed for x = 1 samples heat treated for 24 h and 312 h; data for the 24 h sample showed the presence of a small amount of Li_3VO_4, and as such the spinel composition is likely off-stoichiometric and the lattice parameter slightly higher than anticipated from the linear fit. However, the sample heated for 312 h, and where no secondary phase was observed, fits well with expectations from Vegard's Law. Nevertheless, the close relationship to the linear fit (R^2 = 0.999) indicates a solid solution can exist for the whole compositional range, allowing for appropriate reaction times.
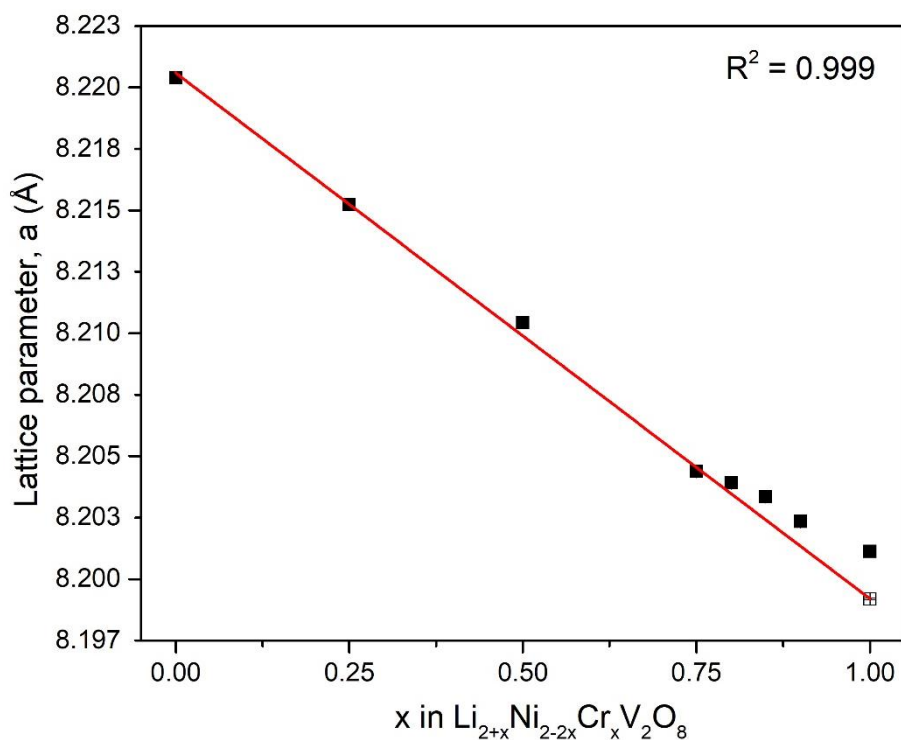
Figure 4.13. Lattice parameter, a, *vs. x* in $Li_{2+x}Ni_{2-2x}Cr_xV_2O_8$ inverse spinels, calculated errors are smaller than displayed points. For x = 1, the annealed (312 h) sample is shown with an open square. Linear fit was calculated using compositions that appeared single phase *via* XRD analysis.

4.3.3. *Combined X-ray and Neutron Refinements*

For the compositions x = 0, 0.25, 0.5, 0.75 and 1 (24 h) the refinement was continued with the addition of neutron diffraction (ND) data. The lattice parameters were fixed to that calculated from XRD data and the background and scale factors for ND data refined. DIFC, DIFA and the peak profile parameters where than refined until convergence. Atomic positions for oxygen were refined first, followed by U_{iso} values in order of decreasing scattering length magnitude. U_{iso}s for the single crystallographic site occupied by a disordered mix of Li, Ni and Cr were constrained together. For x = 0.75, all attempts to refine U_{iso}s for the 16*c* site using combined neutron and X-ray datasets led to negative values (-0.00475 $Å^2$), therefore this site was refined and fixed to values obtained from XRD data only. The process was repeated until convergence, and a good fit for all datasets achieved. Convergence is defined by a relatively flat difference (observed – calculated diffraction pattern) profile, alongside a minimal change in structural parameters and the statistical measures R_{wp} and χ^2. The fits, structural parameters and bond lengths for compositions *x* = 0, 0.25, 0.5, 0.75 and 1 are summarised in Tables 4.2 to 4.6 and Figures 4.14 to 4.18. The refinement yields a structure which is in good agreement with that expected of an inverse spinel, with Li, Ni and Cr on 16*c* octahedral sites,

V on 8*b* tetrahedral sites and oxygen on 32*e* sites for all studied compositions. The goodness-of-fit parameters for X-ray datasets are slightly poorer at low angles due to the mismatch in intensity between the calculated and observed diffraction patterns. This can be observed for both the sample and the internal Si standard and is likely because low angle peaks are more asymmetric, leading to variations in the peak shape caused by axial divergence.

Previously for $Li_2Ni_2V_2O_8$, some cation site mixing has been reported between Ni octahedral and V tetrahedral sites of up to 8 %.[19] However, in the present combined refinements there was no observation of mixing between Ni/V sites. Initial efforts placed 8 % of Ni/V atoms on tetrahedral 8*b* and octahedral 16*c* sites, respectively, resulting in a greatly increased χ^2 (6.337) compared to the ideal inverse spinel structure. Attempts to refine the fractional occupancies (constraining the total occupancy to one on each site) resulted in negative occupancies of Ni in tetrahedral 8*b* sites.

A small decrease in the Li/TM-O_6 bond lengths with increasing Cr content was observed, likely due to the replacement of two Ni^{2+} (0.69 Å) cations with one Li^+ (0.76 Å) and Cr^{3+} (0.615 Å). Alongside this, a linear increase in the oxygen U_{iso} values and a decrease in the oxygen fractional coordinates were also observed with increasing x. This may be because there is a larger ionic radius difference between atoms on the 16*c* site as *x* increases, therefore resulting in a slight distortion of the oxygen atom positions on average. Refined 16*c* site U_{iso}s for $Li_3CrV_2O_8$ were significantly higher than those refined for all other compositions. This could be indicative of greater distortion on the 16*c* site due to the larger ionic radius difference and/or the poorer total scattering contribution from both neutrons and X-rays. For example, the effective neutron scattering length for atoms occupying the 16*c* site in $Li_3CrV_2O_8$ is -0.53 fm, compared to 4.2 fm for $Li_2Ni_2V_2O_8$.

Table 4.2. Refined structure parameters and calculated bond lengths from combined neutron and X-ray refinements for $Li_2Ni_2V_2O_8$ at 25 °C.

Atom	Site	x	y	z	Occ.	U_{iso} (Å²)	Bond Length	(Å)
$Li_2Ni_2V_2O_8$, 25 °C, Fd$\bar{3}$m a = 8.2204(1) Å, Total R_{wp} = 2.47%, χ^2 = 2.323								
V	8*b*	0.375	0.375	0.375	1	0.00474(49)	V-O x 4	1.7362(4)
Li	16*c*	0	0	0	0.5	0.00361(5)	(Li/Ni)-O x 6	2.0806(3)
Ni	16*c*	0	0	0	0.5	0.00361(5)		
O	32*e*	0.2531(1)	0.2531(1)	0.2531(1)	1	0.00773(4)		

Table 4.3. Refined structure parameters and calculated bond lengths from combined neutron and X-ray refinements for $Li_{2.25}Ni_{1.5}Cr_{0.25}V_2O_8$ at 25 °C.

Atom	Site	x	y	z	Occ.	U_{iso} ($Å^2$)	Bond Length	($Å$)
$Li_{2.25}Ni_{1.5}Cr_{0.25}V_2O_8$, 25 °C, $Fd\overline{3}m$ $a = 8.2152(1)$ Å, Total $R_{wp} = 2.59\%$, $\chi^2 = 2.594$								
V	8b	0.375	0.375	0.375	1	0.00515(50)	V-O x 4	1.7360(5)
Li	16c	0	0	0	0.5625	0.00292(6)	(Li/Ni/Cr)-O x 6	2.0787(3)
Ni	16c	0	0	0	0.3750	0.00292(6)		
Cr	16c	0	0	0	0.0625	0.00292(6)		
O	32e	0.2530(1)	0.2530(1)	0.2530(1)	1	0.00826(4)		

Table 4.4. Refined structure parameters and calculated bond lengths from combined neutron and X-ray refinements for $Li_{2.5}NiCr_{0.5}V_2O_8$ at 25 °C.

Atom	Site	x	y	z	Occ.	U_{iso} ($Å^2$)	Bond Length	($Å$)
$Li_{2.5}NiCr_{0.5}V_2O_8$, 25 °C, $Fd\overline{3}m$ $a = 8.2104(1)$ Å, Total $R_{wp} = 2.76\%$, $\chi^2 = 2.729$								
V	8b	0.375	0.375	0.375	1	0.00574(50)	V-O x 4	1.7365(6)
Li	16c	0	0	0	0.625	0.00099(9)	(Li/Ni/Cr)-O x 6	2.0766(4)
Ni	16c	0	0	0	0.250	0.00099(9)		
Cr	16c	0	0	0	0.125	0.00099(9)		
O	32e	0.2529(1)	0.2529(1)	0.2529(1)	1	0.00928(5)		

Table 4.5. Refined structure parameters and calculated bond lengths from combined neutron and X-ray refinements for $Li_{2.75}Ni_{0.5}Cr_{0.75}V_2O_8$ at 25 °C. U_{iso} values for the 16c site were refined using X-ray data only.

Atom	Site	x	y	z	Occ.	U_{iso} ($Å^2$)	Bond Length	($Å$)
$Li_{2.75}Ni_{0.5}Cr_{0.75}V_2O_8$, 25 °C, $Fd\overline{3}m$ $a = 8.2044(1)$ Å, Total $R_{wp} = 3.43\%$, $\chi^2 = 3.385$								
V	8b	0.375	0.375	0.375	1	0.0067(6)	V-O x 4	1.7375(7)
Li	16c	0	0	0	0.6875	0.00287(7)	(Li/Ni/Cr)-O x 6	2.0739(4)
Ni	16c	0	0	0	0.1250	0.00287(7)		
Cr	16c	0	0	0	0.1875	0.00287(7)		
O	32e	0.2527(1)	0.2527(1)	0.2527(1)	1	0.01042(5)		

Table 4.6. Refined structure parameters and calculated bond lengths from combined neutron and X-ray refinements for $Li_3CrV_2O_8$ at 25 °C.

Atom	Site	x	y	z	Occ.	U_{iso} ($Å^2$)	Bond Length	($Å$)
$Li_3CrV_2O_8$, 25 °C, $Fd\overline{3}m$ $a = 8.2011(1)$ Å, Total $R_{wp} = 3.84\%$, $\chi^2 = 2.377$								
98.5(1) % $Li_3CrV_2O_8$, 1.5(1) % Li_3VO_4								
V	8b	0.375	0.375	0.375	1	0.0045(6)	V-O x 4	1.7395(12)
Li	16c	0	0	0	0.75	0.0329(10)	(Li/Cr)-O x 6	2.0713(7)
Cr	16c	0	0	0	0.25	0.0329(10)		
O	32e	0.2525(1)	0.2525(1)	0.2525(1)	1	0.01136(6)		
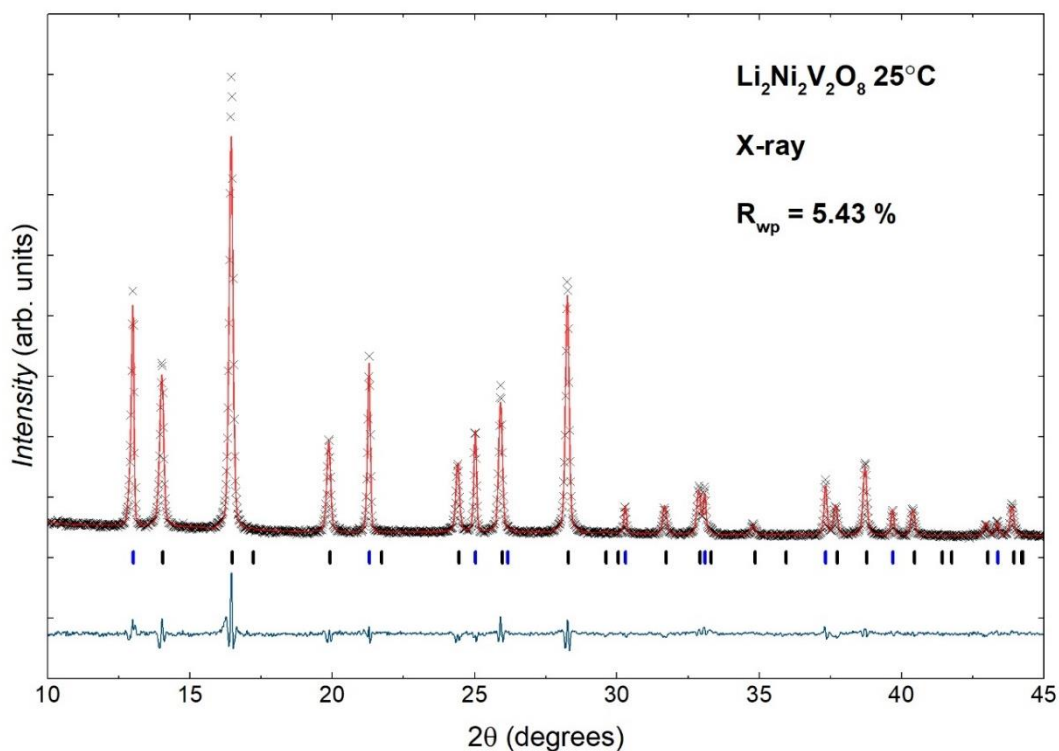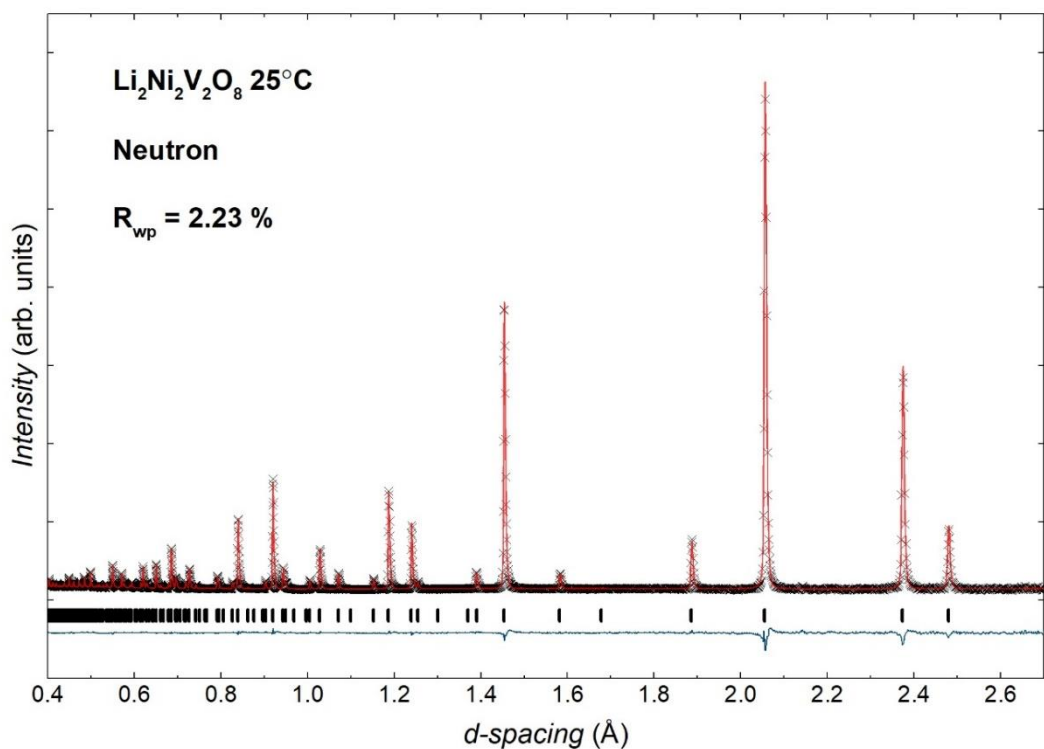
Figure 4.14. Observed, calculated and difference profiles of combined X-ray and Neutron diffraction data for Li$_2$Ni$_2$V$_2$O$_8$ at 25 °C. Observed data are shown in black crosses, calculated in red, difference in blue and calculated reflection positions as black (spinel phase) and blue (Si standard) tickmarks.
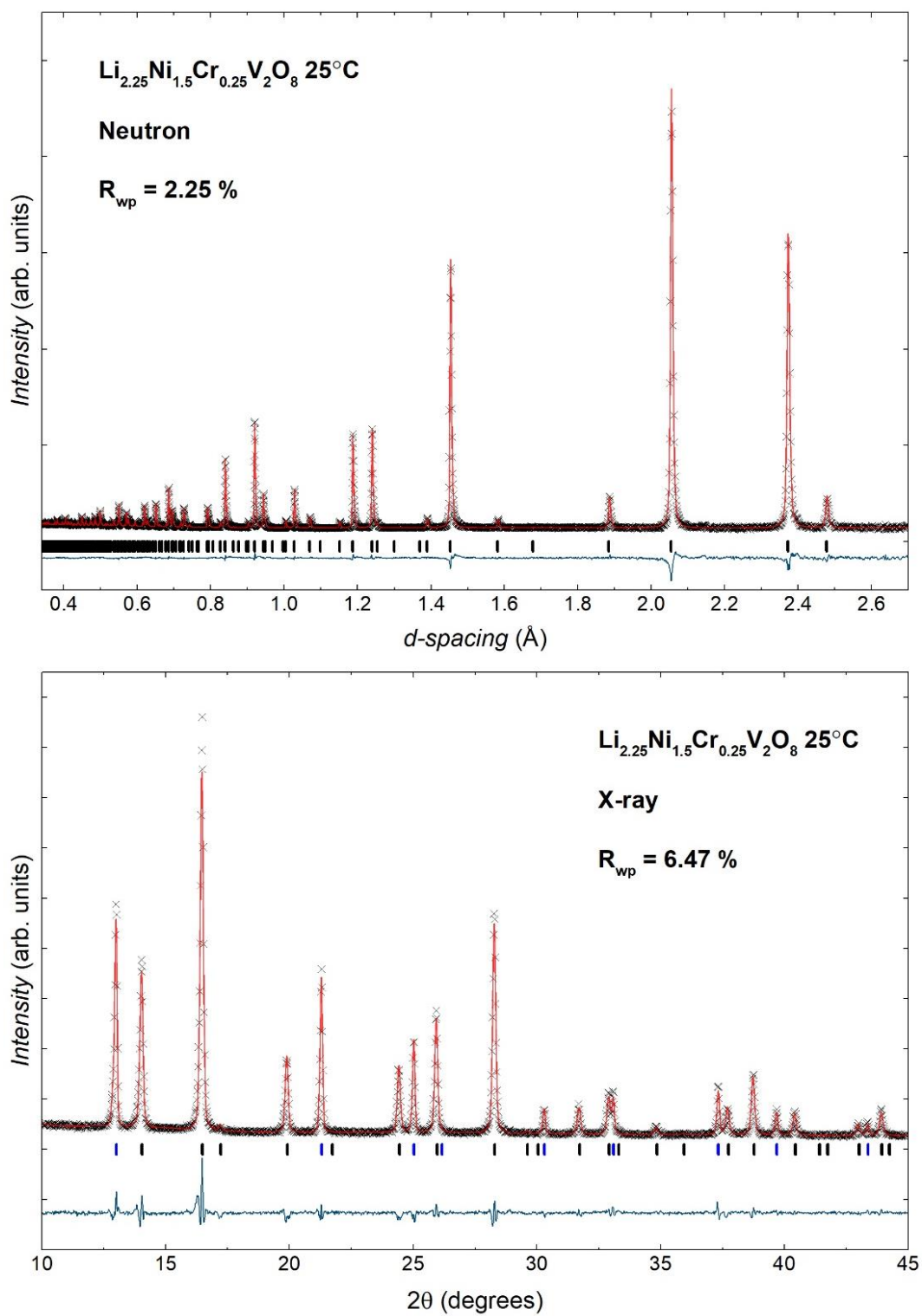
Figure 4.15. Observed, calculated and difference profiles of combined X-ray and Neutron diffraction data for Li$_{2.5}$NiCr$_{0.5}$V$_2$O$_8$ at 25 °C. Observed data are shown in black crosses, calculated in red, difference in blue and calculated reflection positions as black (spinel phase) and blue (Si standard) tickmarks.
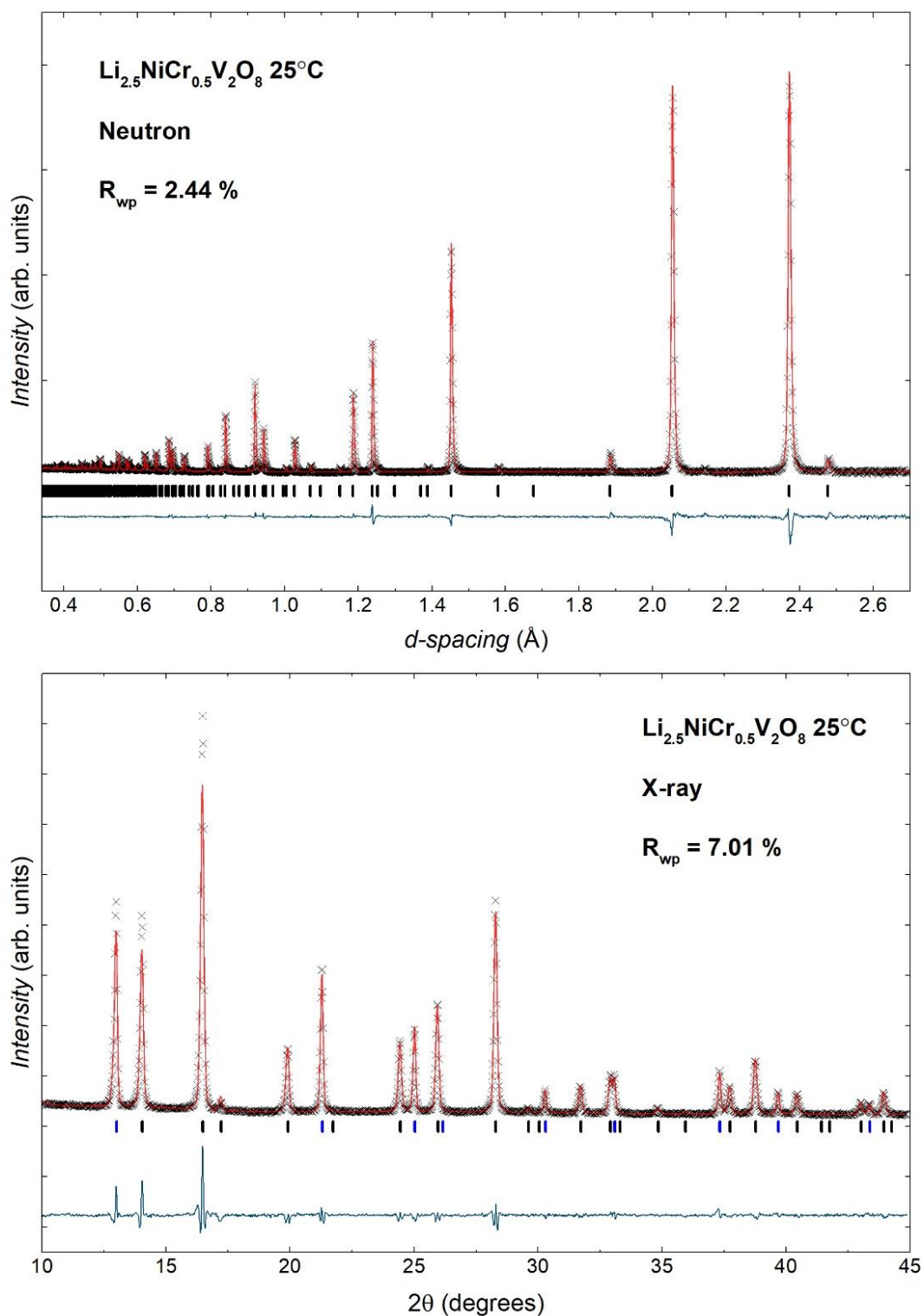
Figure 4.16. Observed, calculated and difference profiles of combined X-ray and Neutron diffraction data for $Li_{2.75}Ni_{0.5}Cr_{0.75}V_2O_8$ at 25 °C. Observed data are shown in black crosses, calculated in red, difference in blue and calculated reflection positions as black (spinel phase) and blue (Si standard) tickmarks.
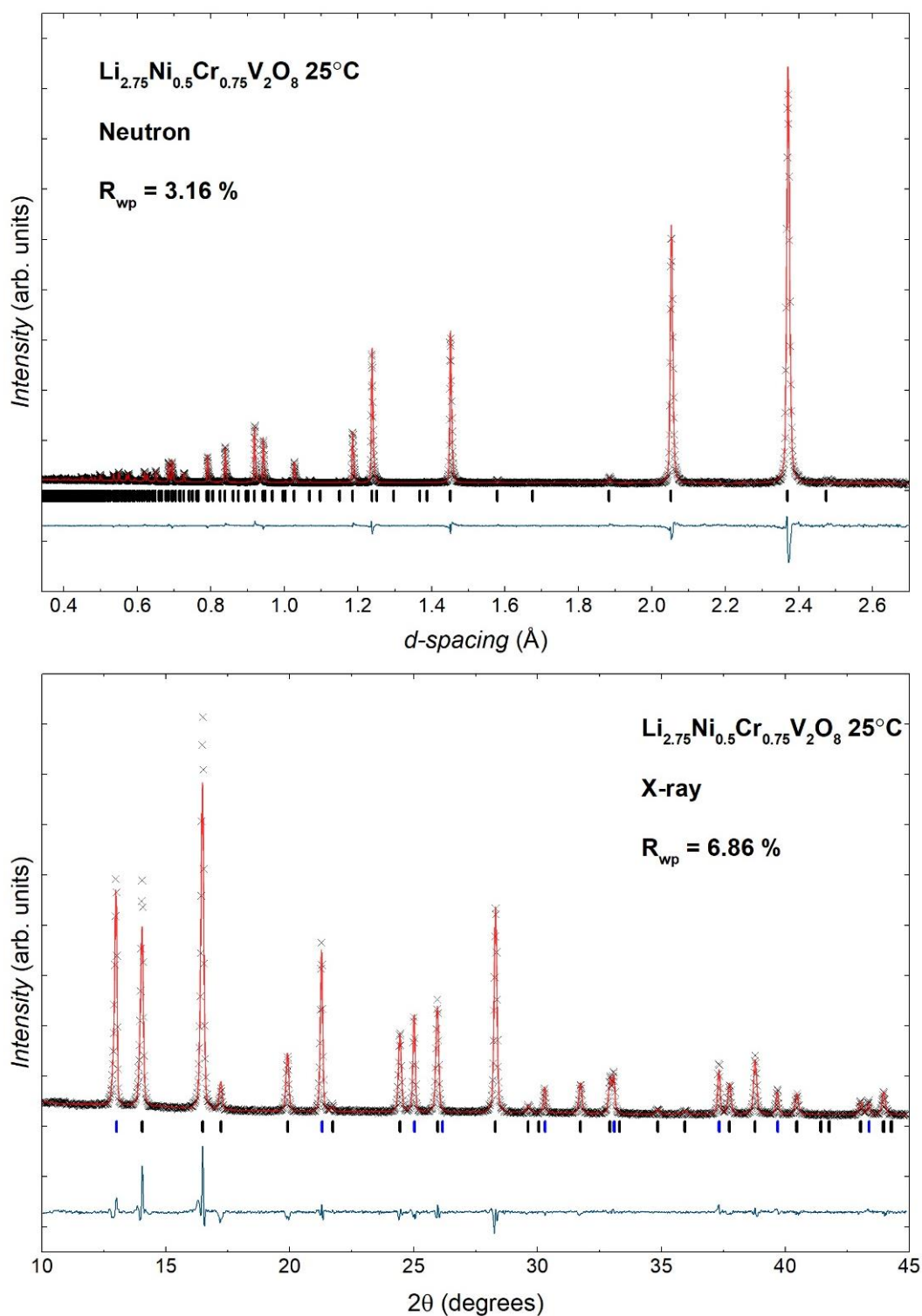
Figure 4.17. Observed, calculated and difference profiles of combined X-ray and Neutron diffraction data for Li$_{2.75}$Ni$_{0.5}$Cr$_{0.75}$V$_2$O$_8$ at 25 °C. Observed data are shown in black crosses, calculated in red, difference in blue and calculated reflection positions as black (spinel phase) and blue (Si standard) tickmarks.
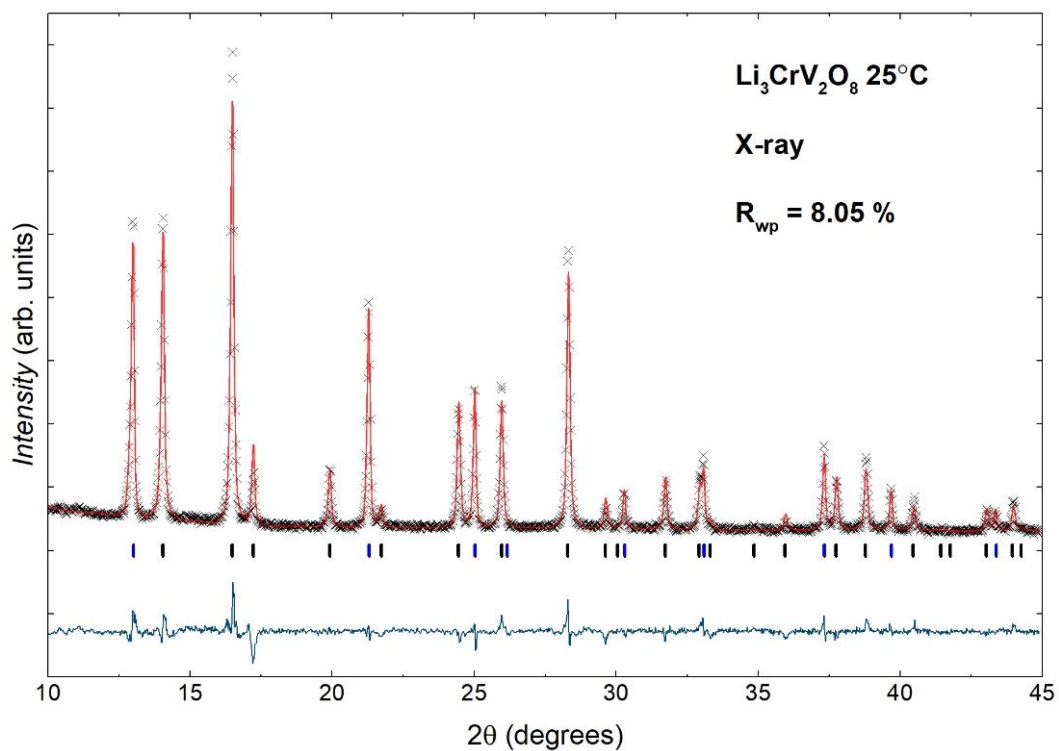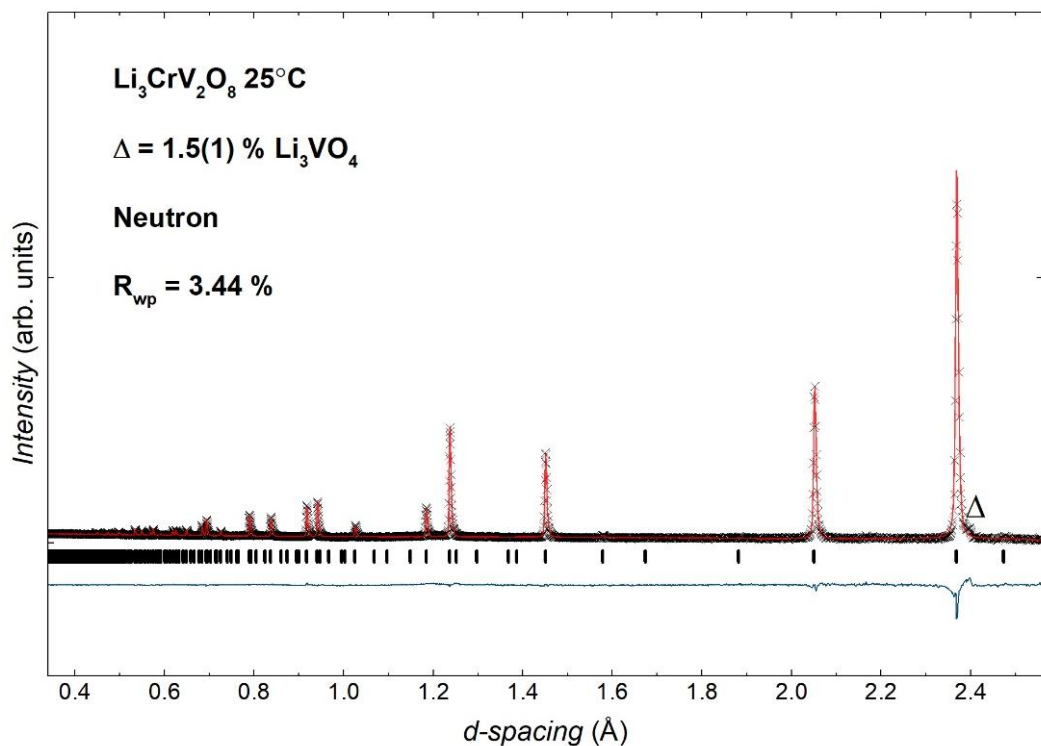
Figure 4.18. Observed, calculated and difference profiles of combined X-ray and Neutron diffraction data for Li$_3$CrV$_2$O$_8$ at 25 °C. Observed data are shown in black crosses, calculated in red, difference in blue and calculated reflection positions as black (spinel phase) and blue (Si standard) tickmarks.

4.3.4. Impedance Spectroscopy

Impedance complex plane plots and spectroscopic plots of C', Z" and M" for the $Li_{2+x}Ni_{2-2x}Cr_xV_2O_8$ (*x* = 0, 0.25, 0.5, 0.75 and 1) solid solution at 75 °C, 125 °C, and 250 °C are presented in Figures 4.19 to 4.23. Measured densies are summarised in Table 4.7. Compositions *x* = 0, 0.25 and 0.5 all had the same density of 76 % after sintering at 650 °C for 12 h. For *x* = 0.75, a slightly higher density of 84 % was achieved after sintering under the same conditions as the previous compositions. *x* = 1 had the lowest measured density at 59 % due to the lower sintering temperature used to avoid decomposition and/or melting, as previously discussed. Complex impedance plots for *x* = 0 and 0.75 both displayed a single, broad semicircle at low temperature (75 °C) which shifted to higher frequencies with increasing temperature, and eventually out of the frequency window measured. *x* = 0.25, 0.5 and 1 all showed two partially resolved semicircles at high and intermediate frequencies, suggesting two resistive components can be seen within the complex impedance plots. Every measured composition displayed a low frequency spike, which was better resolved with increasing temperature. This low frequency spike is indicative of complete or partial blocking at the gold electrodes by Li^+ ions.[20]

Combined spectroscopic plots of Z"/M" for *x* = 0 display single broad peaks and their maxima do not overlap. Ideally in a material with multiple components, the M" plot highlights the components with the lowest capacitance and the Z" plot highlights the components with the highest resistance.[21], [22] Therefore, if the M" peak overlaps with a Z" peak, it is possible to identify the component with the smallest capacitance, usually associated with the bulk.[22] The single broad peak in Z" plots indicates that the time constant (relaxation time), τ, of the different elements present are similar. These results suggest the sample is electrically inhomogeneous and the broad (> 1.5 decades) nature may be due to multiple resistive components which cannot be resolved.[21], [23] Further work could investigate the effect of sintering temperature to better resolve the different components or attempt to model the different components with an equivalent circuit analysis. For *x* = 0.75, single broad Z" and M" peaks can also be seen, however, unlike *x* = 0 there is a better overlap in the maxima of Z" and M" peaks, indictive of greater electrical homogeneity within the sample.[24] Similar to *x* = 0, the broad nature of the Z" peak may suggest multiple components which cannot be resolved. *x* = 0.25, 0.5 and 1 display a single broad peak for M" and two broad peaks for Z"

which correspond to those seen in the complex plane impedance plots. The high frequency Z" peak overlaps with the M" peak, suggesting this component may be associated with a bulk response phenomenon.

Spectroscopic plots of C' for all compositions complement combined Z"/M" plots and complex plane impedance plots. For x = 0 and 0.75, a plateau at high frequencies can be seen, corresponding to a capacitance of *ca.* 10^{-12} F cm^{-1} for the M" peak maxima. At higher temperatures, a low frequency dispersion approaching capacitance values between 10^{-7} and 10^{-5} F cm^{-1} is also observed for all compositions. Capacitances of 10^{-12} can be interpreted as a bulk response phenomenon, while a capacitance between 10^{-7} to 10^{-5} F cm^{-1} is typically associated as a sample-electrode interface response due to the partial blocking effect of Li$^+$ ion at the gold electrodes.[20], [22], [25] It should be noted, at high frequencies for x = 0 a capacitance of ca. 10^{-13} F cm^{-1} is observed. This is likely to be linked to the higher porosity instead of a sample effect, as this would mean the sample has a permittivity value close to that of a vacuum (based on the equation, $\varepsilon' = C(l/A)\varepsilon_o^{-1}$). For x = 0.25, 0.5 and 1, two plateaus are observed at high and intermediate frequencies, coinciding with the two semicircles seen within complex plane impedance plots. These plateaus have a capacitance of *ca.* 10^{-12} F cm^{-1} for the first semicircle (high frequencies) and *ca.* 10^{-11} F cm^{-1} for the second semicircle (intermediate frequencies). The second plateau can also be observed for x = 0 and 0.75 at 125 °C and 250 °C, respectively. A capacitance of 10^{-11} F cm^{-1} is associated with a grain boundary response, minor secondary phase. However, since the XRD after sintering (Figure 4.12) revealed no impurity phases it is likely the responses seen here are due to grain boundary responses.

Table 4.7. Summary of sintering conditions and calculated densities of Li$_{2+x}$Ni$_{2-2x}$Cr$_x$V$_2$O$_8$ (x = 0, 0.25, 0.5, 0.75 and 1)

Composition (Li$_{2+x}$Ni$_{2-2x}$Cr$_x$V$_2$O$_8$) and Sintering Conditions	Density, g/cm^3	Theoretical Density, g/cm^3	Density, %
0 (650 °C, 12 h)	3.270	4.319	76
0.25 (650 °C, 12 h)	3.140	4.153	76
0.5 (650 °C, 12 h)	3.040	3.984	76
0.75 (650 °C, 12 h)	3.217	3.816	84
1 (550 °C, 12 h)	2.160	3.644	59
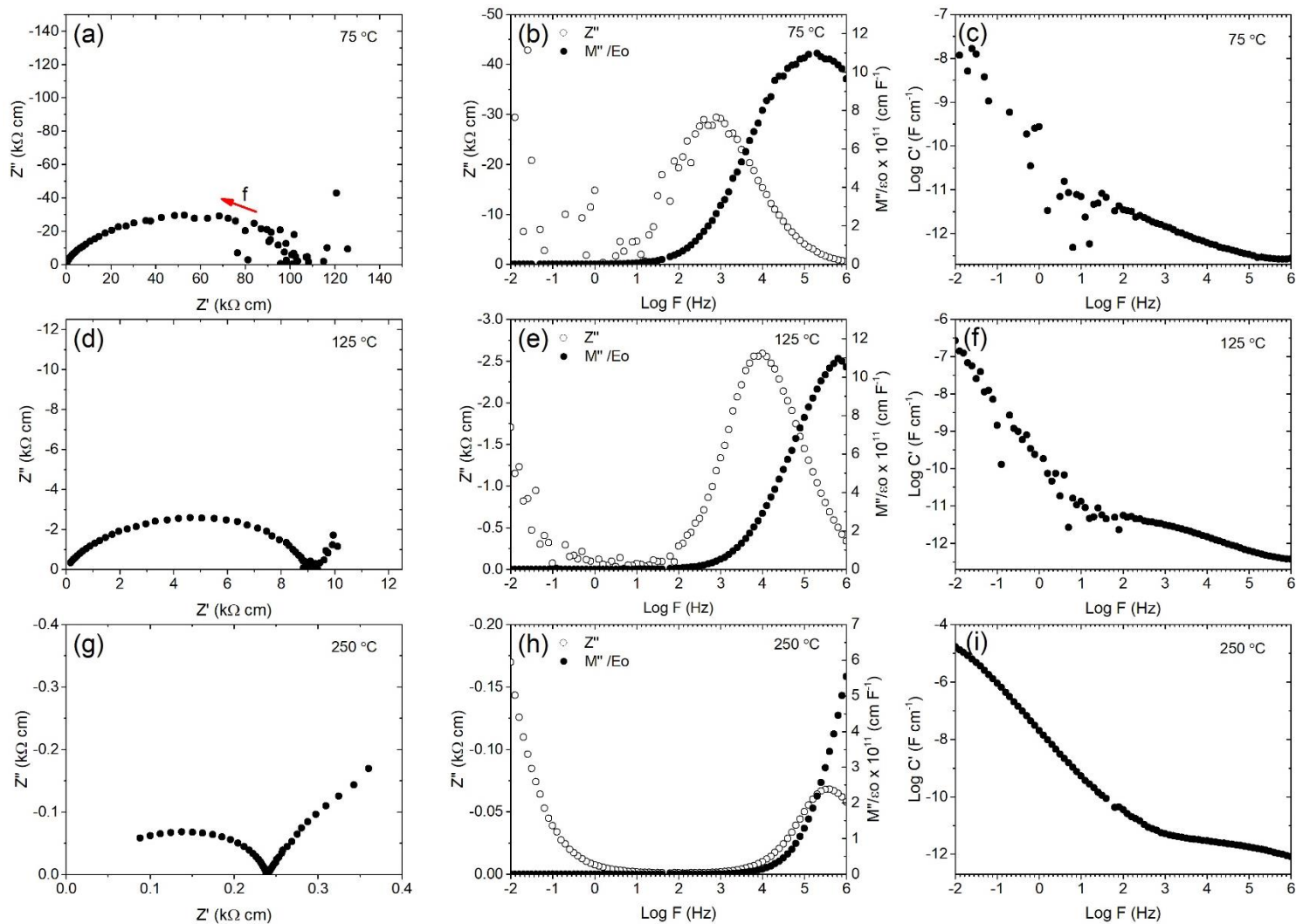
Figure 4.19. Impedance complex plane plots (a, d, g) and spectroscopic plots of C'(c, f, i), M" and -Z" (b, e, h) for Li$_2$Ni$_2$V$_2$O$_8$ at 75 °C, 125 °C and 250 °C.
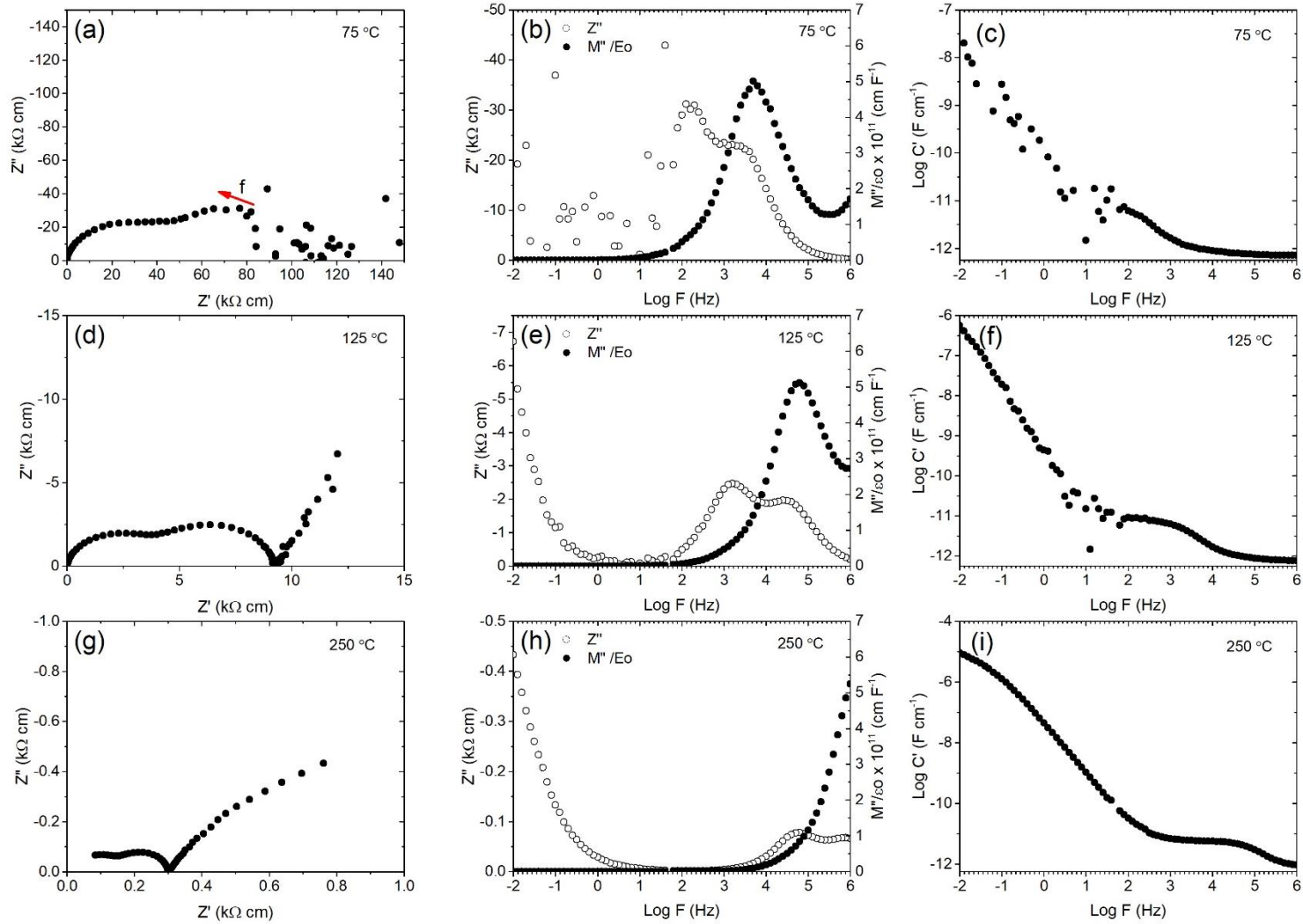
Figure 4.20. Impedance complex plane plots and spectroscopic plots of C', M" and -Z" for $Li_{2.25}Ni_{1.5}Cr_{0.25}V_2O_8$ at 75 °C, 125 °C and 250 °C.
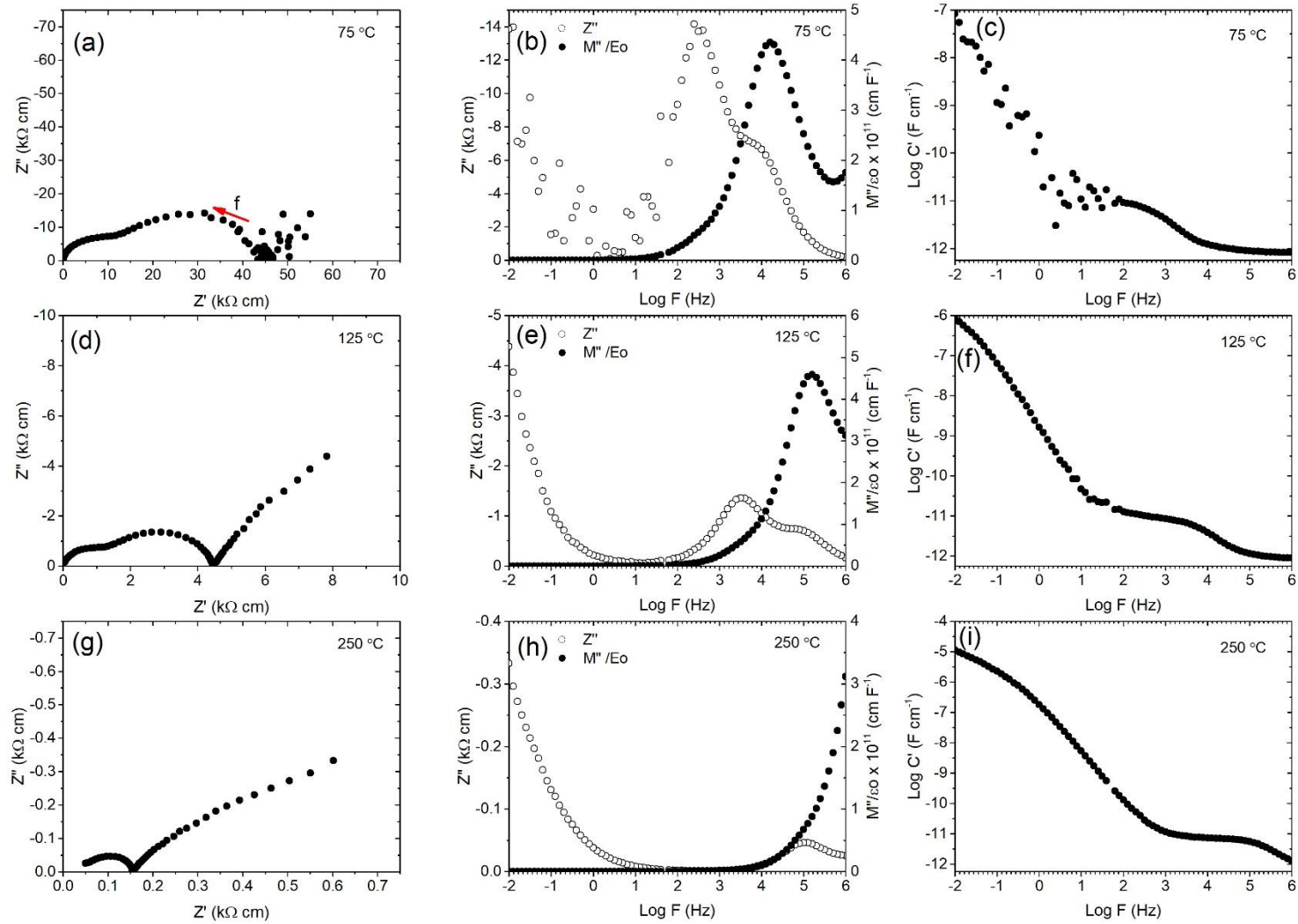
Figure 4.21. Impedance complex plane plots and spectroscopic plots of C', M" and -Z" for $Li_{2.5}NiCr_{0.5}V_2O_8$ at 75 °C, 125 °C and 250 °C.
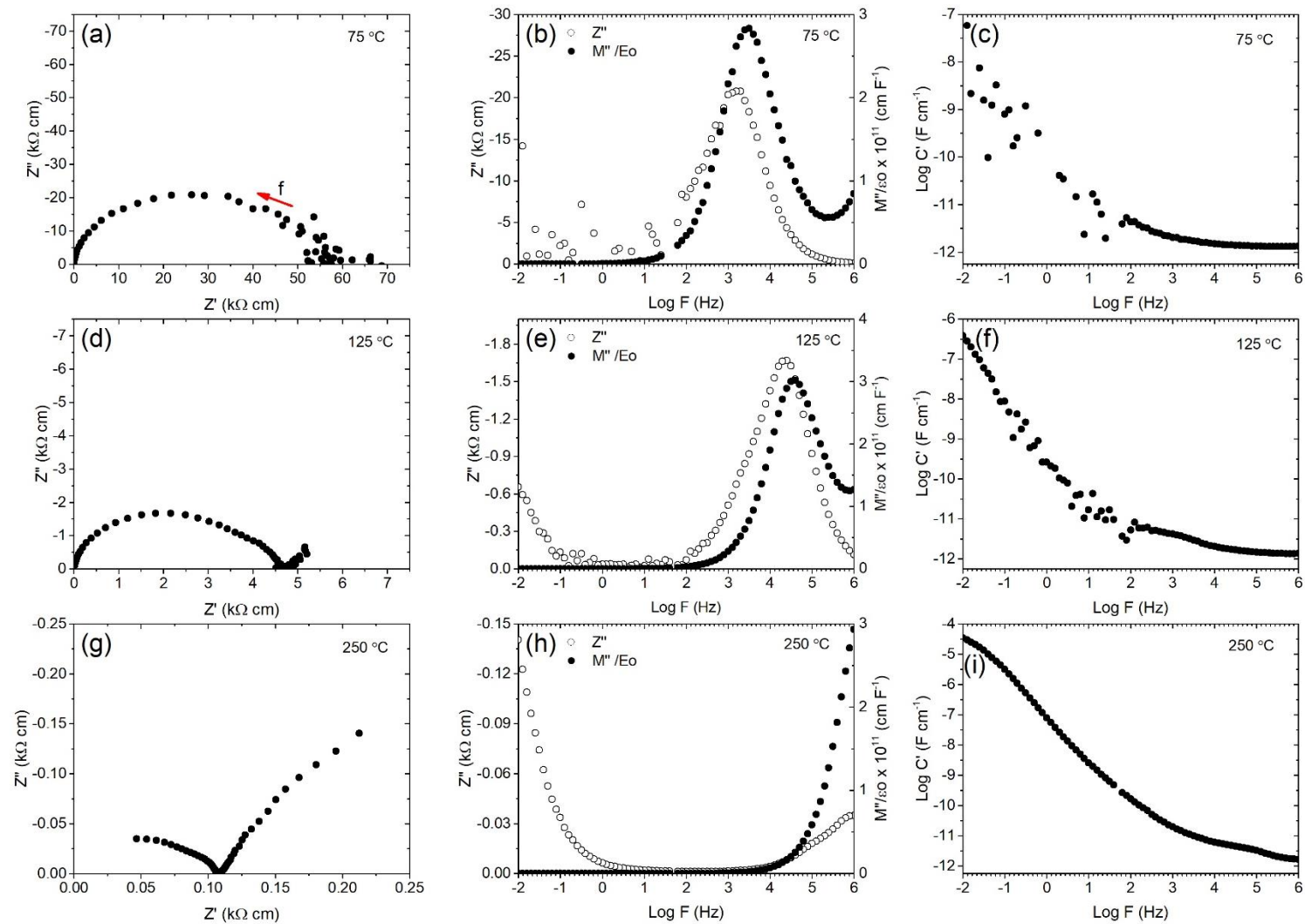
Figure 4.22. Impedance complex plane plots and spectroscopic plots of C', M" and -Z" for $Li_{2.75}Ni_{0.5}Cr_{0.75}V_2O_8$ at 75 °C, 125 °C and 250 °C.
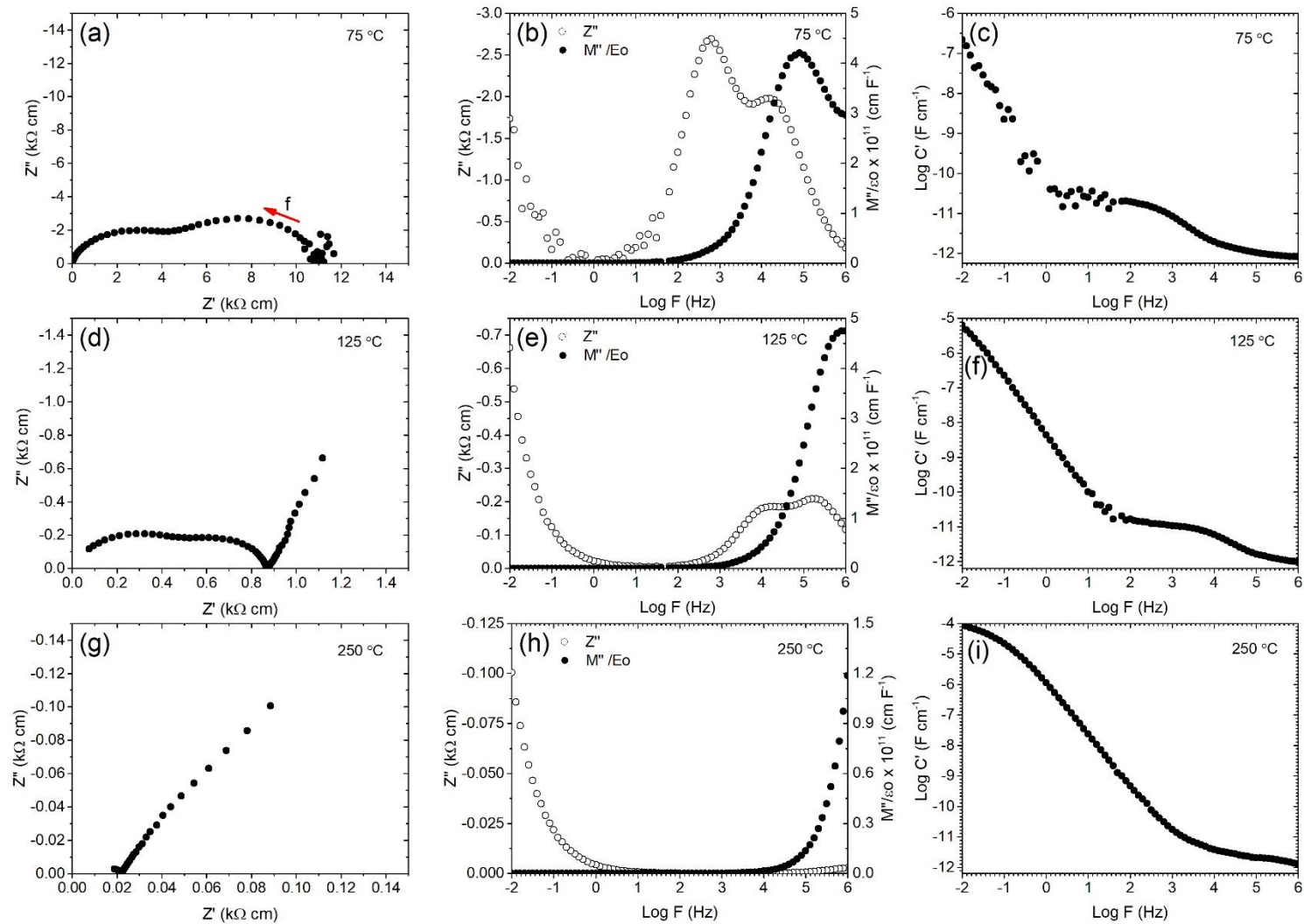
Figure 4.23. Impedance complex plane plots and spectroscopic plots of C', M" and -Z" for Li$_3$CrV$_2$O$_8$ at 75 °C, 125 °C and 250 °C.

Arrhenius plots of total and bulk conductivity versus 1000/T for the solid solution $Li_{2+x}Ni_{2-2x}Cr_xV_2O_8$ are shown in Figures 4.24 and 4.25. For x = 0, 0.25, 0.5, 0.75 and 1, total conductivities were calculated to be 1.02 x 10^{-8}, 9.56 x 10^{-9}, 2.29 x 10^{-8}, 1.78 x 10^{-8} and 9.14 x 10^{-8} S cm^{-1} at 75 °C, respectively. Bulk conductivities of 2.04 x 10^{-8}, 6.15 x 10^{-8}, 1.68 x 10^{-7} S cm^{-1} at 75 °C were determined for x = 0.25, 0.5 and 1, respectively. Activation energies for total conduction ranges between 0.50 eV and 0.56 eV, whilst activation energies for the bulk range from 0.49 eV to 0.53 eV. The small difference in calculated activation energies is likely insignificant considering the poor density of the sintered pellets and the resulting poor resolution of the different components within complex plane impedance plots. For x = 0.25, 0.5 and 1, the bulk conductivity values were calculated from impedance plots by fitting the first semicircle at high frequencies (C' *ca.* 10^{-12} F cm^{-1}) with a parallel RC circuit, using the fit circle function in the Zview software package. The resistance was then taken from the intercept with the x-axis (Z'). Total and bulk activation energies were similar for all compositions, and the subtle differences observed are likely due to factors such as differences in density or charge carriers. The similar activation energies seen indicates a similar barrier for diffusion between the different compositions, which is expected as they have the same inverse spinel structure confirmed via combined X-ray/neutron Rietveld refinements. This suggests the conduction mechanism is likely the same in all compositions and the slightly higher conductivity observed with increasing x could potentially be due to the increase in charge carriers (Li$^+$ ions).

The conductivities reported in Figures 4.24 and 4.25 are comparable to those previously reported for the inverse spinels, $Li_2Ni_2V_2O_8$ (ca. 10^{-8} S cm^{-1} at 25 °C) and $Li_2Co_2V_2O_8$ (ca. 10^{-7} S cm^{-1} at 80 °C).[10], [26] Interestingly, they also have similar activation energies to several normal and complex spinel structures such as $Li_4Ti_5O_{12}$ (0.53 eV), $LiMn_2O_4$ (0.52 eV) and $Li_2NiGe_3O_8$ (0.46 to 0.55 eV).[27]–[31] This is in contrast to the partially inverse complex spinel, $Li_2ZnGe_3O_8$ which is a poor Li-ion conductor and has an activation energy 2.14 eV measured between 562 °C to 838 °C. In $Li_2ZnGe_3O_8$, Zn and Li share tetrahedral sites, therefore the conduction pathway is significantly blocked by Zn^{+2} metal ions and as such only Li-ions in octahedral sites are involved in the conduction pathway.[30], [32] The results shown herein suggest the conduction pathway in inverse spinels are not significantly impacted by the shared occupancy of octahedral sites by Li-ions and transition metal ions.
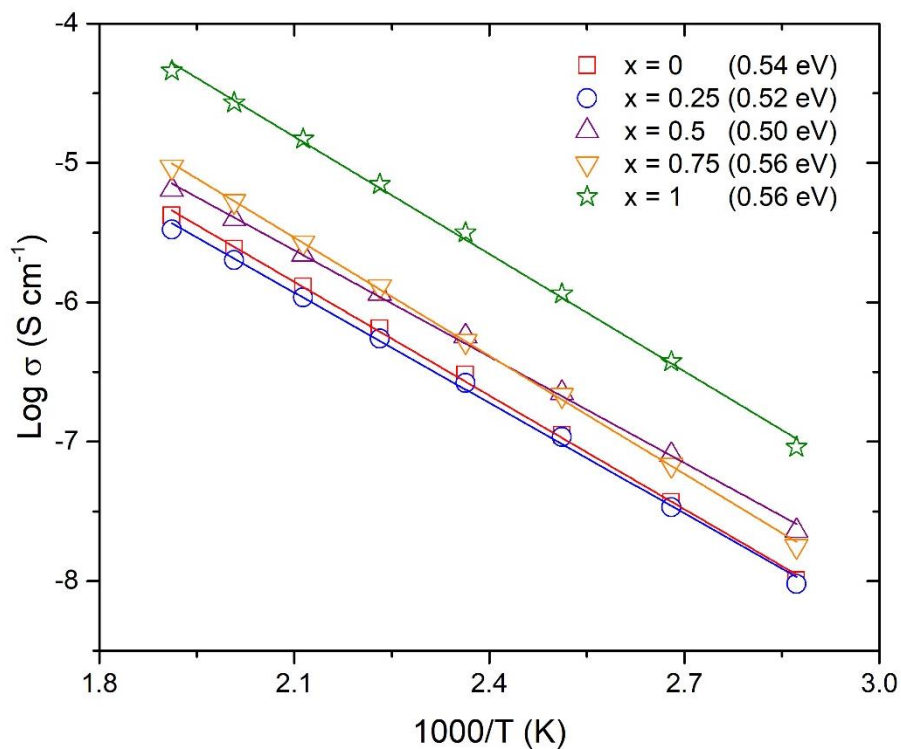
Figure 4.24. Arrhenius plots of total conductivity versus 1000/T for $Li_{2+x}Ni_{2-2x}Cr_xV_2O_8$ (x = 0, 0.25, 0.5 0.75, and 1) measured under dry air. All errors were +/- 0.01 eV, calculated from the error in the slope.
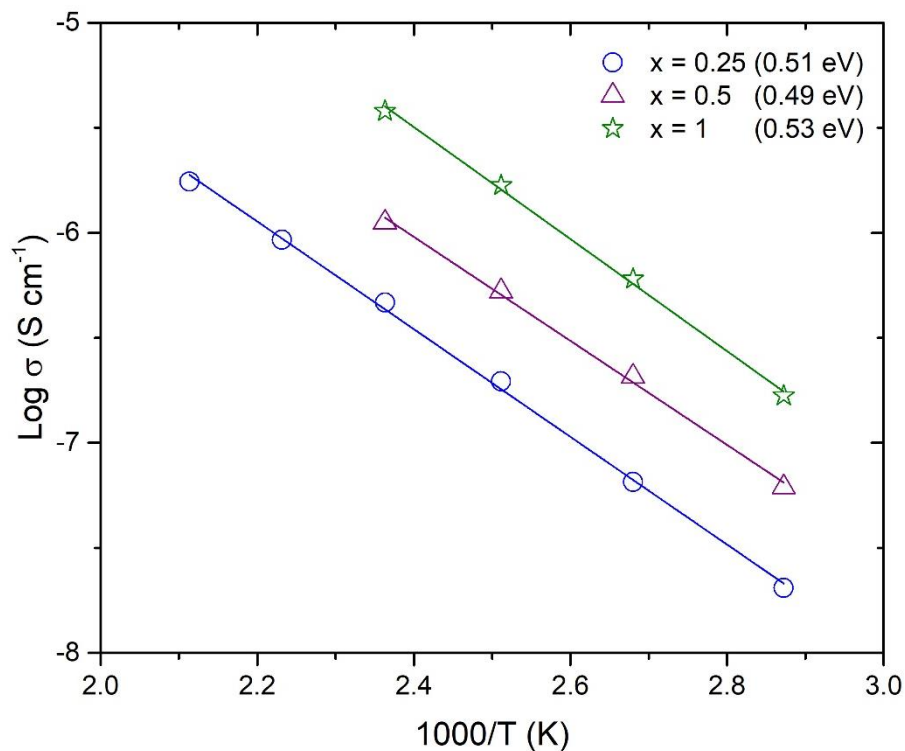
Figure 4.25. Arrhenius plots of bulk conductivity versus 1000/T for $Li_{2+x}Ni_{2-2x}Cr_xV_2O_8$ (x = 0.25, 0.5, and 1) measured under dry air. All errors were +/- 0.01 eV, calculated from the error in the slope.

4.4. Conclusions

In this Chapter, initial attempts to synthesise the previously reported inverse spinel, $Li_3CrV_2O_8$ via solid-state routes did not succeed in producing a single phase material. Instead, a phase mixture of $Li_3CrV_2O_8$, Li_3VO_4, $LiVO_3$ and Cr_2O_3 were found after 7 days total at 550 °C. DSC and XRD data revealed the synthesis temperature was limited by the decomposition and/or melting of $Li_3CrV_2O_8$ at *ca.* 650 °C into Li_3VO_4, $LiVO_3$ and Cr_2O_3. As a consequence, the synthesis method was altered to a citric acid sol-gel route which enabled the synthesis of a novel solid solution between the two end members $Li_2Ni_2V_2O_8$ and $Li_3CrV_2O_8$. Single phase materials were synthesised after 24 h at 500 °C using a citric acid sol-gel method for all compositions up to $Li_{2+x}Ni_{2-2x}Cr_xV_2O_8$ $x = 1$. For $x = 1$, small impurity peaks corresponding to Li_3VO_4 (1.5 wt %) were visible within XRD patterns after 24 h. However, annealing a portion of the x = 1 sample for 312 h at 500 °C resulted in a single phase material by XRD analysis. For all single phase compositions, the calculated lattice parameters were found to follow a linear relationship, decreasing with increasing *x* and suggests a full solid solution exist.

Subsequently, room-temperature combined X-ray and neutron powder diffraction Rietveld refinements were conducted for $x = 0$, 0.25, 0.5, 0.75 and 1. The refinements yielded an inverse spinel structure, with Li, Ni and/or Cr randomly distributed over octahedral 16*c* sites. There was no evidence of any long range ordering or cation mixing between octahedral and tetrahedral sites contrary to previous reports by Blasse.[1]

Impedance spectroscopy measurements were used to investigate how the conductivity changed with varying Li and transition metal content. Total and bulk conductivities was found to increase slightly with increasing *x*. Activation energies for total conductivity were between 0.50 eV to 0.56 eV. The similar activation energies likely indicates these materials have the same conduction pathway. The calculated activation energies are also comparable to normal spinels where Li-ions are able to travel freely through empty interstitial sites within the spinel framework. This suggest the random distribution of Li and Cr and/or Ni on 16c octahedral sites does not significantly impact the diffusion pathway.

Regarding future work, the broad endothermic peak between 700 °C and 750 °C observed within DSC data of *x* = 0.75 requires further investigation. This could be accomplished through the use of high temperature XRD to study any structural changes which may occur in this composition. DSC data should also be collected beyond 900 °C for

compositions containing both Ni and Cr, to examine the effect that altering the transition metal may have on the melting point of these inverse spinels.

4.5. References

[1]   G. Blasse, "The structure of some new mixed metal oxides containing lithium (II)," *J. Inorg. Nucl. Chem.*, vol. 26, pp. 1473–1474, 1964.

[2]   J.-C. Joubert and A. Durif-Varambon, "Étude Cristallographique D'Un Vanadate De Lithium-Chrome," *Bull. la Société française Minéralogie Cristallogr.*, vol. 86, no. 4, p. 430, 1963.

[3]   M. Touboul and A. Popot, "Caractérisation de la solution solide $In_{1-x}Li_{3x}VO_4$ ($0 < x \leq 0,4$) dans le système $InVO_4$-Li_3VO_4 et examen des systèmes $CrVO_4$-Li_3VO_4 et $InVO_4$-$CrVO_4$," *J. Solid State Chem.*, vol. 65, no. 3, pp. 287–292, 1986.

[4]   T. Uyama and K. Mukai, "Synthesis of $LiMg_{1-x}Zn_xVO_4$ with $0 \leq x \leq 1$ for application to the negative electrode of lithium-ion batteries," *Mater. Today Energy*, vol. 14, pp. 1–10, 2019.

[5]   G. T. K. Fey, K. S. Wang, and S. M. Yang, "New inverse spinel cathode materials for rechargeable lithium batteries," *J. Power Sources*, vol. 68, no. 1, pp. 159–165, 1997.

[6]   A. K. Padhi, W. B. Archibald, K. S. Nanjundaswamy, and J. B. Goodenough, "Ambient and High-Pressure Structures of $LiMnVO_4$ and Its $Mn^{3+/2+}$ Redox Energy," *J. Solid State Chem.*, vol. 128, pp. 267–272, 1997.

[7]   G. T. Fey, W. Li, and J. R. Dahn, "$LiNiVO_4$: A 4.8 Volt Electrode Material for Lithium Cells," *J. Electrochem. Soc.*, vol. 141, no. 9, pp. 2279–2282, 1994.

[8]   A. Kazakopoulos, C. Sarafidis, K. Chrissafis, and O. Kalogirou, "Synthesis and characterization of inverse spinel $LiNiVO_4$ and $LiCoVO_4$ with impedance spectroscopy," *Solid State Ionics*, vol. 179, no. 35–36, pp. 1980–1985, 2008.

[9]   H. Kawai, M. Nagata, H. Tukamoto, and A. R. West, "High-voltage lithium cathode materials," *J. Power Sources*, vol. 81–82, pp. 67–72, 1999.

[10]   G. T. K. Fey and D. L. Huang, "Synthesis, characterization and cell performance of inverse spinel electrode materials for lithium secondary batteries," *Electrochim. Acta*, vol. 45, no. 1, pp. 295–314, 1999.

[11]   J. Liu *et al.*, "Unified View of the Local Cation-Ordered State in Inverse Spinel Oxides," *Inorg. Chem.*, vol. 58, no. 21, pp. 14389–14402, 2019.

[12]   J. R. Liu, M. Wang, X. Lin, D. C. Yin, and W. D. Huang, "Citric acid complex method of preparing inverse spinel LiNiVO4 cathode material for lithium batteries," *J. Power Sources*, vol. 108, no. 1–2, pp. 113–116, 2002.

[13]   R. I. Smith *et al.*, "The upgraded Polaris powder diffractometer at the ISIS neutron source," *Rev. Sci. Instrum.*, vol. 90, no. 11, 2019.

[14]   T. Brian. H, "EXPGUI, a graphical user interface for GSAS," *J. Appl. Crystallogr.*, vol. 34, no. 2, pp. 210–213, 2001.

[15]   A. C. Larson and R. B. Von Dreele, "General Structure Analysis System (GSAS)," *Los Alamos National Laboratory Report LAUR*. pp. 86–748, 2004.

[16] S. Das, X. M. Zong, A. Niazi, and D. C. Johnston, "Phase Relations in the Li_2O-V_2O_3-V_2O_5 System at 700 $°C$: Correlations with Magnetic Defect Concentration in Heavy Fermion LiV_2O_4," *Phys. Rev. B*, vol. 74, no. 18, p. 184417, 2006.

[17] A. R. West, *Solid State Chemistry and its Applications*, Student Ed. Wiley, 2014.

[18] S. M. Antao, I. Hassan, and J. B. Parise, "Cation ordering in magnesioferrite, $MgFe_2O_4$, to 982 °C using in situ synchrotron X-ray powder diffraction," *Am. Mineral.*, vol. 90, no. 1, pp. 219–228, 2005.

[19] R. S. Liu, Y. C. Cheng, R. Gundakaram, and L. Y. Jang, "Crystal and electronic structures of inverse spinel-type $LiNiVO_4$," *Mater. Res. Bull.*, vol. 36, no. 7–8, pp. 1479–1486, 2001.

[20] J. T. S. Irvine, D. C. Sinclair, and A. R. West, "Electroceramics: Characterization by Impedance Spectroscopy," *Adv. Mater.*, vol. 2, no. 3, pp. 132–138, 1990.

[21] S. Dutta, R. N. P. Choudhary, and P. K. Sinha, "Impedance spectroscopy studies on Fe^{3+} ion modified PLZT ceramics," *Ceram. Int.*, vol. 33, no. 1, pp. 13–20, 2007.

[22] D. C. Sinclair, "Characterization of Electro-materials using ac Impedance Spectroscopy," *Boletín la Soc. Española Cerámica y Vidr.*, vol. 34, no. 2, pp. 55–65, 1995.

[23] M. Belal Hossen and A. K. M. Akther Hossain, "Complex impedance and electric modulus studies of magnetic ceramic $Ni_{0.27}Cu_{0.10}Zn_{0.63}Fe_2O_4$," *J. Adv. Ceram.*, vol. 4, no. 3, pp. 217–225, 2015.

[24] R. Gerhardt, "Impedance and dielectric spectroscopy revisited: Distinguishing localized relaxation from long-range conductivity," *J. Phys. Chem. Solids*, vol. 55, no. 12, pp. 1491–1506, 1994.

[25] A. R. West, D. C. Sinclair, and N. Hirose, "Characterization of Electrical Materials, Especially Ferroelectrics, by Impedance Spectroscopy," *J. Electroceramics*, vol. 1, no. 1, pp. 65–71, 1997.

[26] N. V Landschoot, "Synthesis and characterization of inverse spinels, intercalation materials for Li-ion batteries," 2006.

[27] H. Shiiba, M. Nakayama, and M. Nogami, "Ionic conductivity of lithium in spinel-type $Li_{4/3}Ti_{5/3}O_4$-$LiMg_{1/2}Ti_{3/2}O_4$ solid-solution system," *Solid State Ionics*, vol. 181, no. 21–22, pp. 994–1001, 2010.

[28] K. Hoang, "Understanding the electronic and ionic conduction and lithium over-stoichiometry in $LiMn_2O_4$ spinel," *J. Mater. Chem. A*, vol. 2, no. 43, pp. 18271–18280, 2014.

[29] B. Vikram Babu *et al.*, "Structural and electrical properties of $Li_4Ti_5O_{12}$ anode material for lithium-ion batteries," *Results Phys.*, vol. 9, pp. 284–289, 2018.

[30] H. Kawai, M. Tabuchi, M. Nagata, H. Tukamoto, and A. R. West, "Crystal chemistry and physical properties of complex lithium spinels $Li_2MM'_3O_8$ (M=Mg, Co, Ni, Zn; M'=Ti, Ge)," *J. Mater. Chem.*, vol. 8, no. 5, pp. 1273–1280, 1998.

[31] D. Z. C. Martin *et al.*, "Evaluating lithium diffusion mechanisms in the complex spinel $Li_2NiGe_3O_8$," *Phys. Chem. Chem. Phys.*, vol. 21, no. 41, pp. 23111–23118, 2019.

[32] N. Reeves-Mclaren, R. I. Smith, and A. R. West, "Lithium-ion conduction pathways in complex lithium spinels $Li_2MGe_3O_8$ (M = Ni or Zn)," *Chem. Mater.*, vol. 23, no. 15, pp. 3556–3563, 2011.

Chapter 5: Diffusion Mechanisms in Li-based Inverse Spinels

5.1. Introduction

As previously seen throughout this work, numerous materials based on the spinel structure have been investigated as potential battery materials for LiBs. This is due to the wide variety of possible elements which can combine to form the spinel structure, as well as the number of empty interstitial sites enabling potential three-dimensional conduction pathways for Li-ions to travel through the crystal structure. How cations are distributed within the spinel structure has been shown to affect the activation energy for Li-ion diffusion, and potentially the route along which Li-ions can migrate through the structure, which in turn influences key electrochemical properties such as rate capability.[1], [2] Therefore, a greater understanding of the Li-ion diffusion mechanisms in spinel materials is crucial if these materials are to be fully optimised. An improved understanding of existing battery materials would also help facilitate the design of new materials.

The lithium migration and high temperature (> 700 °C) crystal structure of the Li-containing spinels $Li_4Ti_5O_{12}$ and $Li_2MGe_3O_8$ (M = Ni or Zn) have previously been investigated utilising variable-temperature neutron powder diffraction data.[1], [3] In $Li_4Ti_5O_{12}$, it was revealed that at high temperatures Li-ions occupy split 32e tetrahedral sites around the 16c octahedral positions, suggesting that an 8a-32e-32e-8a diffusion pathway plays a key role in Li-ion migration. However, for $Li_2NiGe_3O_8$, Li-ions diffuse from 8c tetrahedral sites through vacant 12d octahedral sites in an 8c-12d-8c conduction pathway. In contrast, in the partially inverse complex spinel $Li_2ZnGe_3O_8$, the conduction pathway is significantly longer due to the presence of both Li and Zn on 8c tetrahedral sites. As a result, the remaining Li, which occupy 4b octahedral sites, diffuse *via* a longer and more tortuous 4b-24e-4a-24e-4b mechanism; the activation energy for ionic hopping is significantly larger as a result.

The results for $Li_2ZnGe_3O_8$ would imply Li-ions which randomly occupy sites alongside other atoms *e.g.* Zn are blocked from taking part in the conduction pathway. Despite this, some fully inverse spinels, $LiMVO_4$ (M = Ni, Mn and/or Co), where Li and M cations are randomly distributed over octahedral sites, display limited charge/discharge capacities.[4]–[6] The impedance results in Chapter 4 also suggest the inverse spinels, $Li_{2+x}Ni_{2-2x}Cr_xV_2O_8$ (0 ≤ x ≤ 1), are modest Li-ion conductors and have similar activation energies for Li-ion hopping to their normal spinel counterparts such as $Li_4Ti_5O_{12}$. As previously discussed, this has been

suggested as evidence for local ordering between Li and transition metal cations.[7] Nevertheless, studies on the crystal structures and Li-ion migration pathways in these materials have not yet been reported in-depth.

In this chapter, the crystal structures of $Li_{2+x}Ni_{2-2x}Cr_xV_2O_8$, where $x = 0.5$ and 1, were investigated as a function of temperature using variable-temperature neutron powder diffraction with a view on identifying active Li-ion conduction pathway(s). These two samples were chosen because of their novel composition and high ionic conductivity, meaning they were the most promising samples for identifying mobile Li-ions at high temperatures. Structural information obtained from neutron diffraction refinements is then used alongside data obtained from muon spectroscopy to study the local Li-ion diffusion kinetics of $x = 0$, 0.5 and 1. These samples were chosen to understand how the Li-ion diffusion kinetics varied over a large x range. Muon spectroscopy (Section 3.7) is used to complement impedance data due to its ability to probe local Li-ion diffusion without the inclusion of additional contributions such as electronic or grain boundary conductivity.

5.2. Experimental

Li-ion diffusion mechanisms in the $Li_{2+x}Ni_{2-2x}Cr_xV_2O_8$ (x = 0, 0.5 and, 1) inverse spinel series were investigated using neutron diffraction and/or muon spectroscopy techniques. All studied compositions were synthesised at 500 °C for 24 h via the same citric acid sol-gel route reported in Chapter 4.

5.2.1. Variable-Temperature Neutron Powder Diffraction

Variable-temperature time-of-fight (ToF) neutron powder diffraction (ND) data were collected on the Polaris powder diffractometer at the ISIS Neutron and Muon Facility, Rutherford Appleton Laboratory.[8] In order to minimise the possibility for reactions between sample and container, in place of vanadium cans silica glass tubes were used to hold powder samples of *ca.* 2 g (*x* = 0.5 and, 1) and mounted within an evacuated high-temperature furnace. For the duration of the experiment, compressed air was passed over the samples to avoid a reducing atmosphere and potential decomposition of the inverse spinel phase. Data were collected on cooling for *ca.* 250 µAh between 250 to 500 °C and *ca.* 500 µAh at 550 and 600 °C for $Li_3CrV_2O_8$ (*x* = 1) and $Li_{2.5}NiCr_{0.5}V_2O_8$ (*x* = 0.5), respectively. The maximum temperature was selected to avoid decomposition of the inverse spinel structure, established in Chapter 4 to be *ca.* 650 °C for $Li_3CrV_2O_8$. Data were then corrected to subtract background contributions from the silica glass tube and for sample absorption.

The EXPGUI interface for GSAS was used for Rietveld refinements using data collected via the backscattering, 90° and low angle detector banks (banks 5, 4 and 3).[9], [10] Multi-histogram refinements were used to obtain more reliable statistics and easier identification of intermediate Li sites. Fourier difference maps were generated and analysed in GSAS, with the FOX 'Free Objects for Crystallography' software also used to visualise the Fourier difference maps in three dimensions.[11]

5.2.2. Muon Spectroscopy

Muon spectroscopy (µSR) measurements were performed using the EMU instrument at the ISIS Neutron and Muon Facility.[12] Due to the ongoing Covid-19 pandemic, all samples investigated were measured remotely, with on-site sample mounting and data collection performed by the instrument scientist Dr Peter Baker.

Approximately 2 g of x = 0, 0.5 and, 1 were packed into separate Ti sample holders to form disk-shaped samples of *ca.* 30 mm diameter and 1.5 mm thickness. The samples were then implanted with 3.2 MeV spin-polarised positively-charged muons, whose decay into positrons was detected by 96 scintillator segments arranged in two circular arrays. Data were collected using a closed cycle refrigerator from 100 – 600 K in three different applied longitudinal magnetic fields (0, 5, 10 G). Initial symmetry calibrations were conducted using a 20 G transverse magnetic field at 300 K. Data analysis was conducted using the Mantid program.[13]

5.3. Results and Discussion

5.3.1. Variable-temperature Neutron Diffraction Rietveld Refinements

For easier identification of intermediate sites in the Li-ion conduction pathway the highest temperature datasets were refined first (600 °C for x = 0.5 and 550 °C for x = 1). Heating at these high temperatures encourages thermal activation of Li-ions, with Li therefore likely to spend longer on average in interstitial sites within the migration pathway. The initial Rietveld refinement used the same strategy as room temperature combined X-ray and neutron refinements (Chapter 4). The model placed Li, Cr and/or Ni on octahedral 16*c* sites, V on tetrahedral 8*b* sites and oxygen on 32*e* sites. Occupancies were adjusted depending on the chemical formula and initial isotropic thermal displacement parameters, U_{iso}, were fixed to the default value of 0.005 Å^2.

For both compositions, the background and scale factors were refined first, using a shifted Chebyschev function with eight, ten and twelve terms for banks five, four and three, respectively. This was followed by lattice parameters and DIFC for banks three and four. DIFC was kept fixed for the backscattering bank due to the high degree of correlation between DIFC and lattice parameters. The peak profile parameters and DIFA were then refined until

convergence. Atomic positions for oxygen were refined first, followed by U_{iso} values in order of decreasing scattering length magnitude. U_{iso}s for atoms occupying the 16c site were constrained together to share the same value.

During the refinement of $Li_3CrV_2O_8$, the U_{iso}s for the 16c Li/Cr site were initially refined without any damping. This resulted in a large U_{iso} value of 0.166(5) Å^2, suggesting the site requires less scattering in the model at this site. This may be due to lithium motion and/or migration, as well as the small total scattering contribution from the 16c site, as previously discussed in Chapter 4 (-0.525 fm $vs.$ 1.84 fm for $Li_{2.5}NiCr_{0.5}V_2O_8$). Therefore, a damping parameter was added during the initial stages of the refinement. Anisotropic thermal displacement parameters, U_{ij}s, might have been more appropriate to account for the large thermal motion seen at these temperatures. However, when attempted this led to either an unstable refinement or elongated thermal ellipsoids spread over multiple crystallographic sites. This effect was not observed in $Li_{2.5}NiCr_{0.5}V_2O_8$, which may suggest there is more distortion on the 16c sites in $x = 1$ than $x = 0.5$. The thermal ellipsoids for the $Li_3CrV_2O_8$ crystal structure refined using U_{ij}s for the 16c sites are displayed in Figure 5.1. This highlights the model attempting to attribute additional scattering between 16c and 8a sites by using elongated thermal ellipsoids, which might otherwise be attributed to separate sites. Hence, the use of small isotropic U_{iso}s assisted in the identification of distinct intermediate Li sites in the conduction pathway.

Attempts to refine the U_{iso} for the V site resulted in either negative values (-0.00180 Å^2) or values with a larger error than the refined value for both compositions. This is again most likely due to the small scattering length of V (-0.38 fm) when using ND data. Therefore, for V the U_{iso} was kept fixed at 0.005 Å^2. The refinements at this point gave good visual fits, Figure 5.2 and 5.3, and statistical measures for all three detector banks, maintaining an inverse spinel structure (Table 5.1 and 5.2). Refined U_{iso} values were reasonable, though now considerably larger than room temperature refinements, due to increased thermal vibrations of atoms at high temperatures.
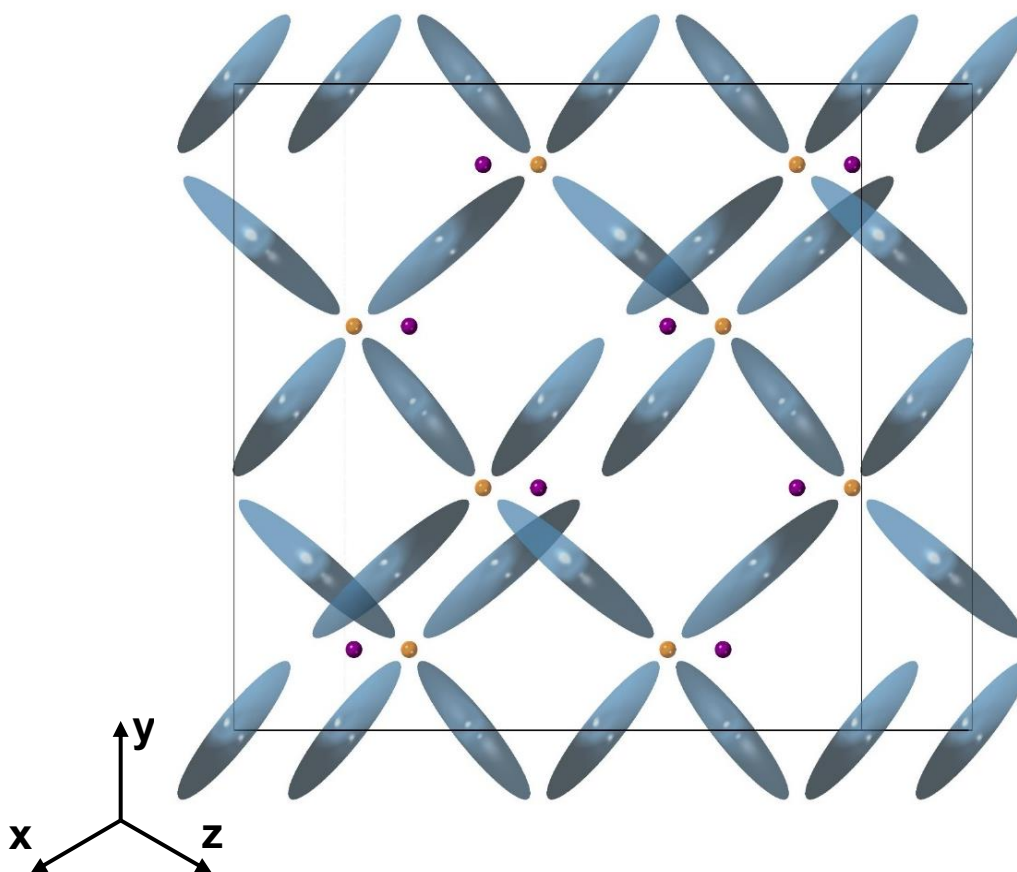
Figure 5.1. Refined crystal structure of $Li_3CrV_2O_8$ at 550°C using U_{ij}s, showing elongated thermal ellipsoids of Li/Cr $16c$ sites (light blue) pointing towards $8a$ sites (orange). V atoms residing on $8b$ sites are shown in purple, and oxygen thermal ellipsoids have been omitted for clarity.

Table 5.1. Refined structure parameters and calculated bond lengths for $Li_{2.5}NiCr_{0.5}V_2O_8$ at 600°C using ND data, with Li occupying a single crystallographic site in the standard model for an inverse spinel.

Li₂.₅NiCr₀.₅V₂O₈, 600 °C, Fd3̄m a = 8.27816(10) Å, Total R_{wp} = 2.57%, χ^2 = 4.094								
Atom	**Site**	**x**	**y**	**z**	**Occ.**	U_{iso} **(Å²)**	**Bond Length**	**(Å)**
V	$8b$	0.375	0.375	0.375	1	0.005	V-O x 4	1.7369(7)
Li	$16c$	0	0	0	0.625	0.00284(13)	(Li/Ni/Cr)-O x	2.1020(4)
							6	
Ni	$16c$	0	0	0	0.250	0.00284(13)		
Cr	$16c$	0	0	0	0.125	0.00284(13)		
O	$32e$	0.2539(1)	0.2539(1)	0.2539(1)	1	0.02102(8)		

Table 5.2. Refined structure parameters and calculated bond lengths for $Li_3CrV_2O_8$ at 550°C using ND data, with Li occupying a single crystallographic site in the standard model for an inverse spinel.

Atom	Site	x	y	z	Occ.	U_{iso} (Å^2)	Bond Length	(Å)
V	8b	0.375	0.375	0.375	1	0.005	V-O x 4	1.7441(9)
Li	16c	0	0	0	0.75	0.1061(21)	(Li/Cr)-O x 6	2.0957(5)
Cr	16c	0	0	0	0.25	0.1061(21)		
O	32e	0.2533(1)	0.2533(1)	0.2533(1)	1	0.02249(8)		

$Li_3CrV_2O_8$, 550 °C, Fd$\overline{3}$m a = 8.27280(10) Å, Total R_{wp} = 2.79%, χ^2 = 3.972
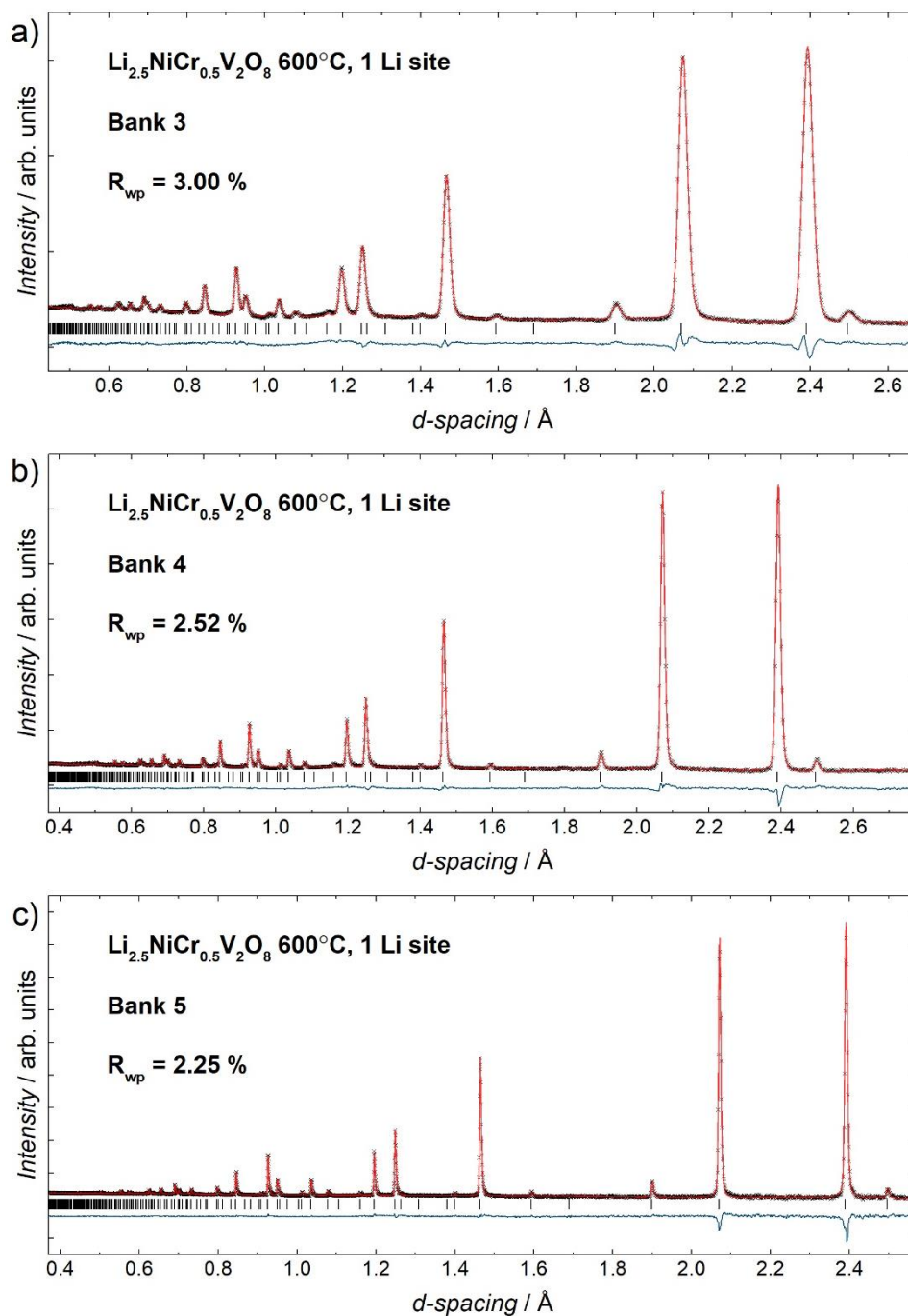
Figure 5.2. Observed, calculated and difference profiles from ToF ND data for $Li_{2.5}NiCr_{0.5}V_2O_8$ at 600°C with Li occupying a single crystallographic site in the standard model for an inverse spinel, collected on detector banks a) 3, b) 4 and c) 5. Observed data are shown in black crosses, calculated in red, difference in blue and calculated reflection positions as black tickmarks.
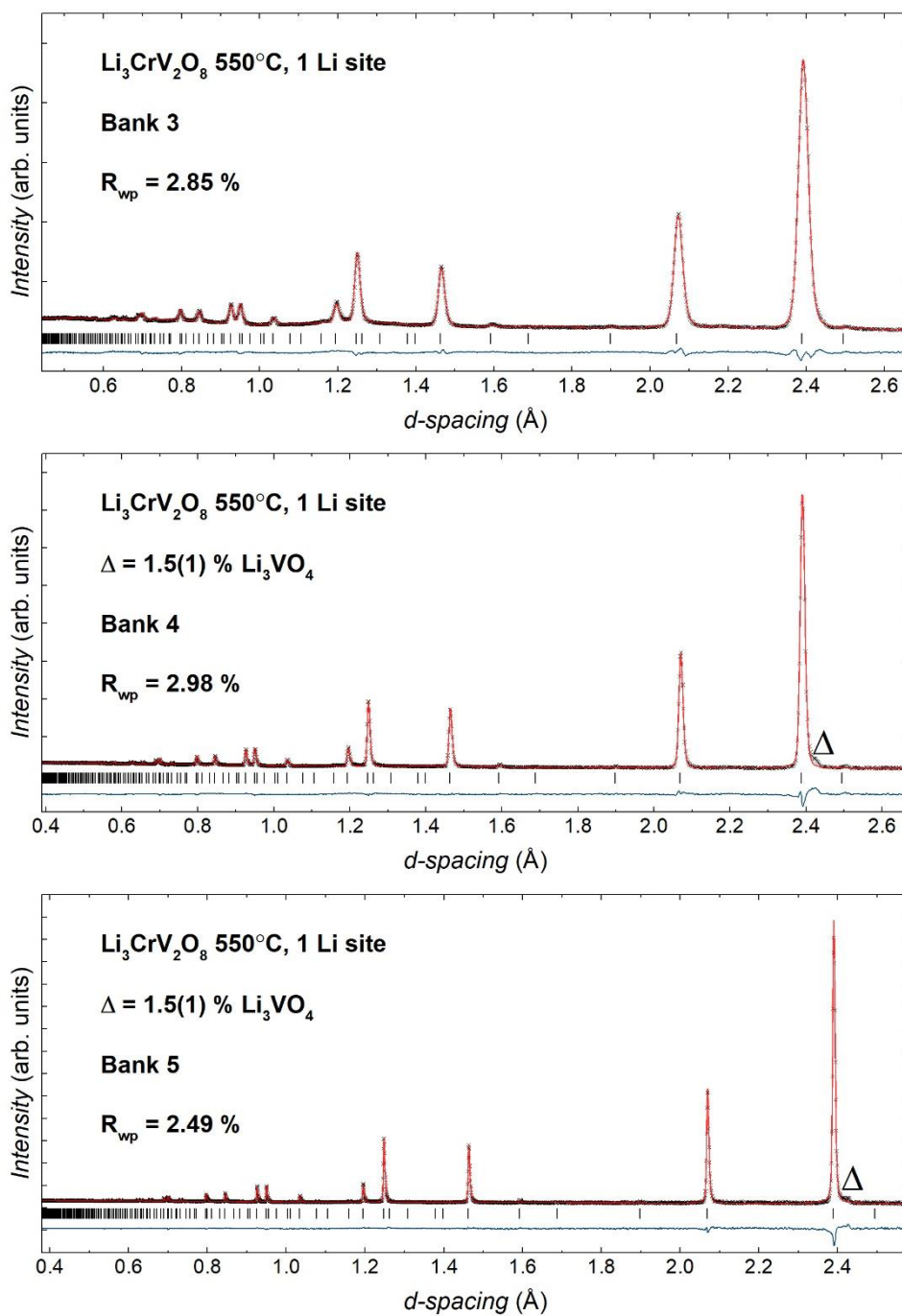
Figure 5.3. Observed, calculated and difference profiles from ToF ND data for $Li_3CrV_2O_8$ at 550°C with Li occupying a single crystallographic site in the standard model for an inverse spinel, collected on detector banks a) 3, b) 4 and c) 5. Observed data are shown in black crosses, calculated in red, difference in blue and calculated reflection positions as black tickmarks.

After this point, U_{iso}s for the 16c sites were kept fixed and the fractional occupancy of Li was refined, giving a value of 0.587(2) for x = 0.5 at 600 °C and 0.668(5) for x = 1 at 550 °C. This decrease of *ca.* 4 to 8 % in site occupancy can be attributed to thermally activated hopping of lithium ions. Difference Fourier maps at this stage showed a peak of significant negative density for both x = 0.5 (ρ = -1.48) and x = 1 (ρ = -0.62) at approximately 0.1265, 0.1265, 0.1265 and equivalent positions related by symmetry. This additional negative scattering was attributed to an additional Li site, since (i) the scattering lengths for Ni, Cr and O are all positive (10.3, 3.64 and 5.80 fm, respectively) and (ii) Li has a larger negative scattering length than V (-1.90 *vs* -0.38 fm). Li is also the more likely mobile species at these temperatures. Difference Fourier maps showed no other atoms close to this position in the ideal inverse spinel model, indicating it is a distinct site and not a poorly fitted atom. This second Li site corresponds to a 32e position, which is located midway between vanadium 8b sites (Figure 5.4 and 5.5). In this site, Li is coordinated to four oxygen atoms in a slightly distorted tetrahedron with Li-O bond lengths of 1.854(24) Å x 3 and 1.82(7) Å.

The fractional occupancy of Li on 32e sites was then refined, resulting in an occupancy of approximately 1 % for both x = 0.5 and 1. Attempts to refine the atomic positions of the 32e site was unsuccessful, leading to an unstable refinement which deviated from convergence. Therefore, due to the very weak scattering observed, the second Li position was instead shifted by a small amount and placed onto an 8a special position at 0.125, 0.125, 0.125 (*ca.* 0.02 Å from the 32e site), which remains tetrahedrally coordinated by oxygen. 32e sites are positioned near the tetrahedral faces between 8a and 16c sites. This spread of negative scattering density observed in both compositions, likely indicates that the migration of Li-ions occurs between the shared faces of octahedral 16c and tetrahedral 8a sites.

Figure 5.4. Difference Fourier map calculated during the Rietveld refinement of the $Li_{2.5}NiCr_{0.5}V_2O_8$ crystal structure at 600 °C. Centre of reference is 0.125, 0.125, 0.125, with a map size of 10 Å × 10 Å. Solid and dash lines represent contours of positive and negative scattering density, respectively. Significant negative scattering is located between V1 atoms, which can be attributed to Li in 8a tetrahedral sites.
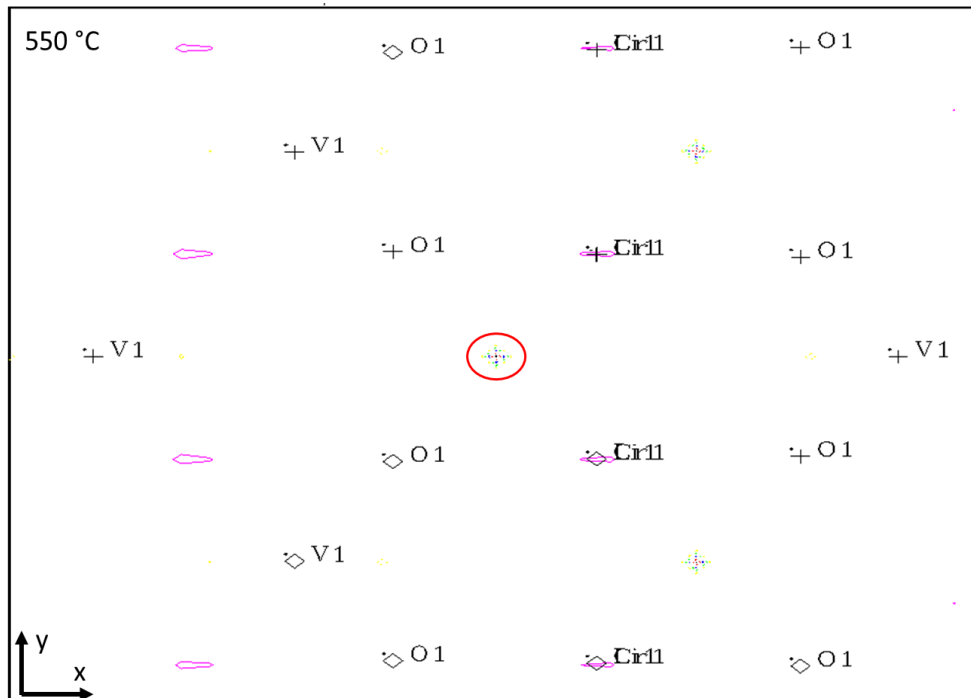
Figure 5.5. Difference Fourier map calculated during the Rietveld refinement of the $Li_3CrV_2O_8$ crystal structure at 550 °C. Centre of reference is 0.125, 0.125, 0.125, with a map size of 10 Å × 10 Å. Solid and dash lines represent contours of positive and negative scattering density, respectively. Significant negative scattering is located between V1 atoms, which can be attributed to Li in 8a tetrahedral sites.

The refinement was continued with a second distinct Li site at 0.125, 0.125, 0.125 and equivalent positions. The U_{iso} values were kept fixed at 0.005 Å^2 due to the correlation between site occupancy and thermal displacement parameters. The occupancy for the second Li site was refined, giving a value of 0.04(1) and 0.05(1) or *ca.* 4 to 5 % for *x* = 0.5 and 1, respectively. Finally, fractional occupancies for both Li sites were then refined together with U_{iso} and atomic coordinates for oxygen. The new structural model showed an improved fit and statistical measures (lower R_{wp} and χ^2) when compared to the initial structural model (Table 5.3 and 5.4, Figure 5.6 and 5.7).

Table 5.3. Refined structure parameters and calculated bond lengths for $Li_{2.5}NiCr_{0.5}V_2O_8$ at 600°C using ND data, with Li occupying two crystallographic sites in the inverse spinel structure.

Atom	Site	X	Y	z	Occ.	U_{iso} (Å^2)	Bond Length	(Å)
$Li_{2.5}NiCr_{0.5}V_2O_8$, 600 °C, Fd$\overline{3}$m *a* = 8.27819(2) Å, Total R_{wp} = 2.50%, χ^2 = 3.862
V	8*b*	0.375	0.375	0.375	1	0.005	V-O x 4	1.7383(7)
Li	16*c*	0	0	0	0.583(2)	0.00284(13)	(Li/Ni/Cr)-O x 6	2.1012(4)
Ni	16*c*	0	0	0	0.250	0.00284(13)	Li$_{8a}$-O x 4	1.8463(7)
Cr	16*c*	0	0	0	0.125	0.00284(13)	Li$_{16c}$-Li$_{8a}$	1.7923(1)
O	32*e*	0.2538(1)	0.2538(1)	0.2538(1)	1	0.02079(7)		
Li	8*a*	0.125	0.125	0.125	0.04(1)	0.005		

Table 5.4. Refined structure parameters and calculated bond lengths for $Li_3CrV_2O_8$ at 550°C using ND data, with Li occupying two crystallographic sites in the inverse spinel structure.

Atom	Site	X	Y	z	Occ.	U_{iso} (Å^2)	Bond Length	(Å)
$Li_3CrV_2O_8$, 550 °C, Fd$\overline{3}$m *a* = 8.27280(10) Å, Total R_{wp} = 2.64%, χ^2 = 3.555
V	8*b*	0.375	0.375	0.375	1	0.005	V-O x 4	1.7447(9)
Li	16*c*	0	0	0	0.668(5)	0.10609(210)	(Li/Cr)-O x 6	2.0953(6)
Cr	16*c*	0	0	0	0.25	0.10609(210)	Li$_{8a}$-O x 4	1.8375(9)
O	32*e*	0.2533(1)	0.2533(1)	0.2533(1)	1	0.02271(7)	Li$_{16c}$-Li$_{8a}$	1.7911(1)
Li	8*a*	0.125	0.125	0.125	0.05(1)	0.005		
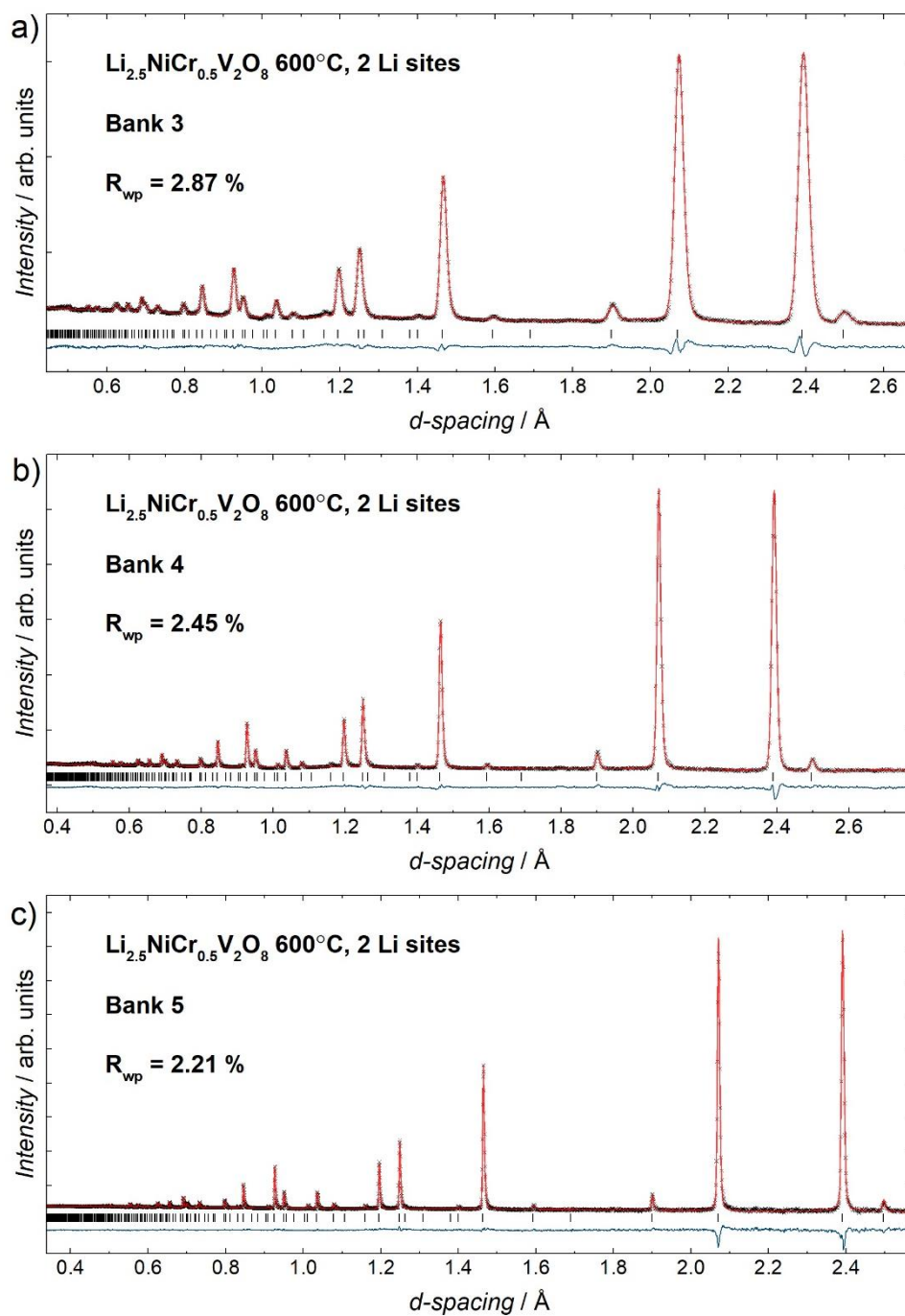
Figure 5.6. Observed, calculated and difference profiles from ToF ND data for $Li_{2.5}NiCr_{0.5}V_2O_8$ at 600°C with an additional Li 8*a* site in the inverse spinel model, collected on banks a) 3, b) 4 and c) 5. Observed data are shown in black crosses, calculated in red, difference in blue and calculated reflection positions as black tickmarks.
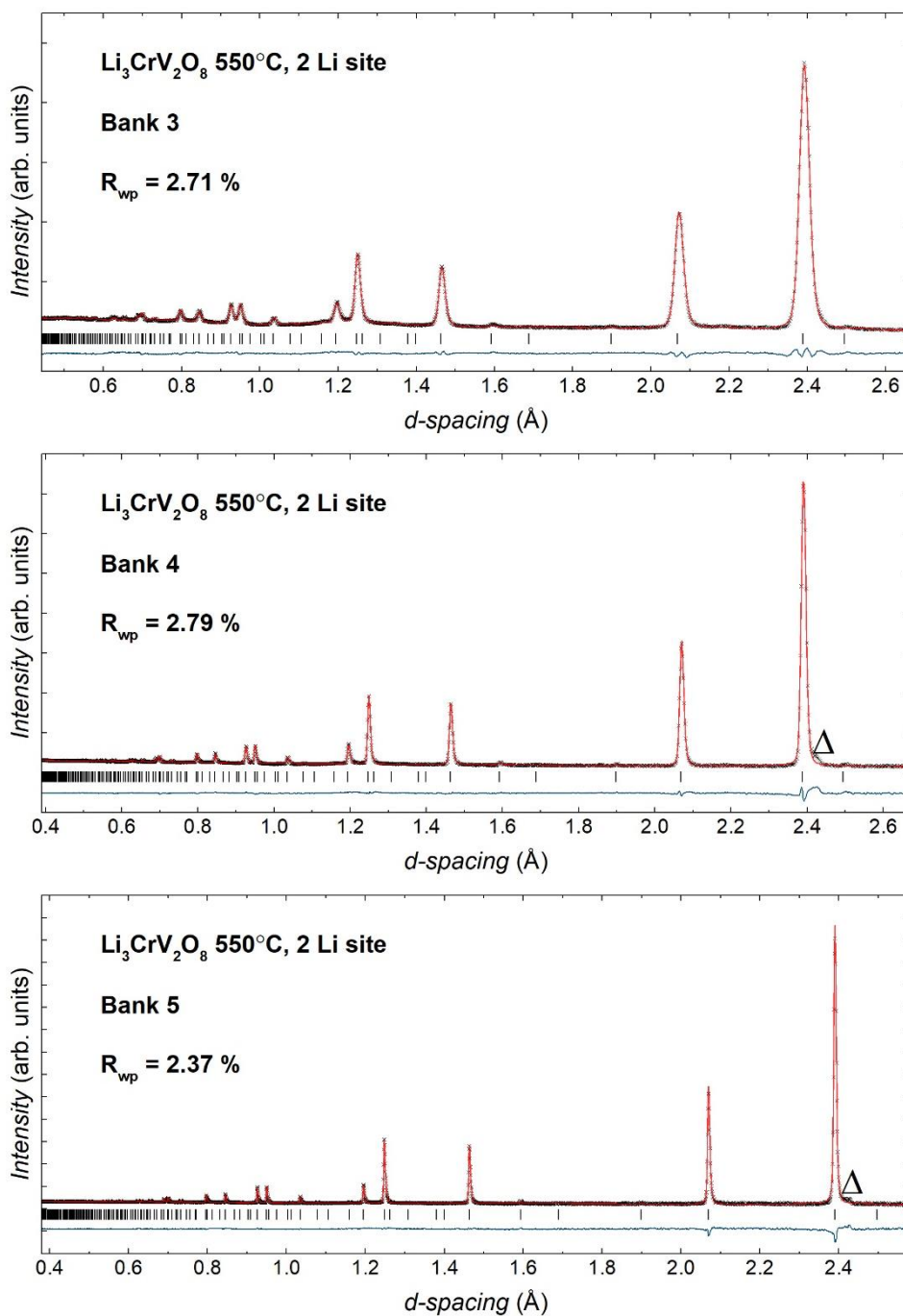
Figure 5.7. Observed, calculated and difference profiles from ToF ND data for $Li_3CrV_2O_8$ at 550°C with an additional Li 8*a* site in the inverse spinel model, collected on banks a) 3, b) 4 and c) 5. Observed data are shown in black crosses, calculated in red, difference in blue and calculated reflection positions as black tickmarks. Δ indicates small impurity peaks associated with Li_3VO_4.

The new structural model with a second distinct Li 8*a* site was refined using ToF ND data collected at various temperatures from 250 °C to 600 °C. Difference Fourier maps were generated for the whole temperature range investigated. For *x* = 0.5, negative scattering density corresponding to Li 8*a* sites were observed in refinements at every temperature from

600 °C to 250 °C (See Appendix, Section 5.6). While for $x = 1$, significant negative scattering was only observed at 500 °C and above, at lower temperatures any negative density was indistinguishable from the background. This could potentially be due to the larger diffuse scattering around 16c sites as a result of the weaker scattering in $x = 1$ when compared to $x =$ 0.5. Nevertheless, it was possible to refine the Li 8a site in both compositions for the whole temperature range studied. At all temperatures, the statistical measures were significantly improved with the addition of the second distinct Li site (Table 5.5).

Figures 5.8 and 5.9 show the structural evolution with temperature. Lattice parameters, U_{iso}s and bond lengths all display a linear increase with temperature. This linear increase indicates there is no cation mixing/ordering and that the new inverse spinel model describes the average structure well at all temperatures. For $x = 0.5$, the oxygen U_{iso} was considerably higher than those for the 16c site and attempts to use anisotropic thermal parameters for oxygen were unsuccessful, with the refinement deviating from convergence. This suggests oxygen atoms are not significantly distorted by the introduction of Li on additional 8a sites at high temperatures. Difference Fourier maps also indicated no additional scattering around oxygen atoms, meaning the higher U_{iso} for oxygen is likely due to greater thermal vibration. For $x = 1$ the opposite trend was found, with 16c site U_{iso} being significantly larger than oxygen U_{iso}s. As previously discussed, this likely suggests there is considerable distortion on 16c sites due to Li migration as well as the poorer total scattering from 16c sites in $x = 1$ than $x = 0.5$. Bond lengths for the 16c site displayed the largest gradient change with temperature, suggesting an expansion of the octahedra to facilitate Li-ion migration.

Table 5.5. Summary of χ^2 for refinements using one or two Li sites in the inverse spinel structure.

Temperature (°C)	$Li_3CrV_2O_8$ χ^2		$Li_{2.5}NiCr_{0.5}V_2O_8$ χ^2	
	One Li site	Two Li sites	One Li site	Two Li sites
600			4.094	3.862
550	3.972	3.555	3.180	3.065
500	3.136	2.883	3.651	3.534
450	2.819	2.576	3.156	3.062
400	2.990	2.749	3.587	3.458
350	3.362	3.134	4.101	3.986
300	2.930	2.725	3.517	3.406
250	3.063	2.988	5.257	5.133
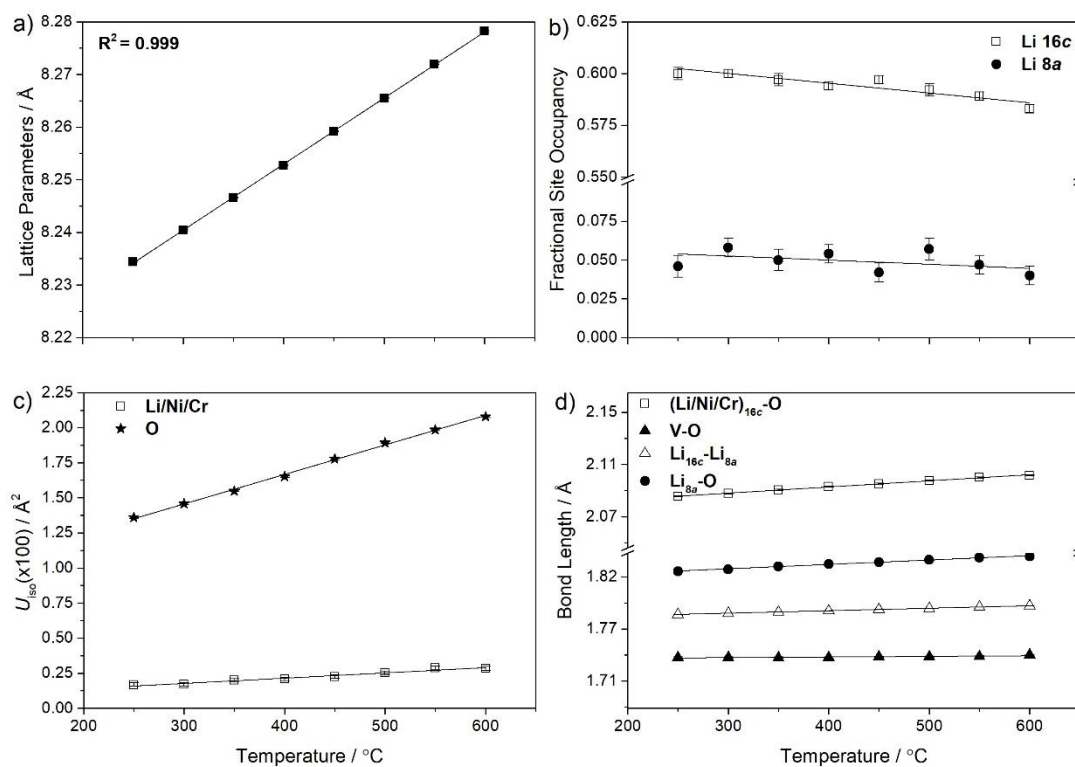
Figure 5.8. Structural evolution of Li$_{2.5}$NiCr$_{0.5}$V$_2$O$_8$ with temperature, a) lattice parameters, b) fractional site occupancy of Li in 16c and 8a sites, c) thermal displacement parameters and d) variation of bond lengths. Some estimated standard deviations are smaller than the symbols.
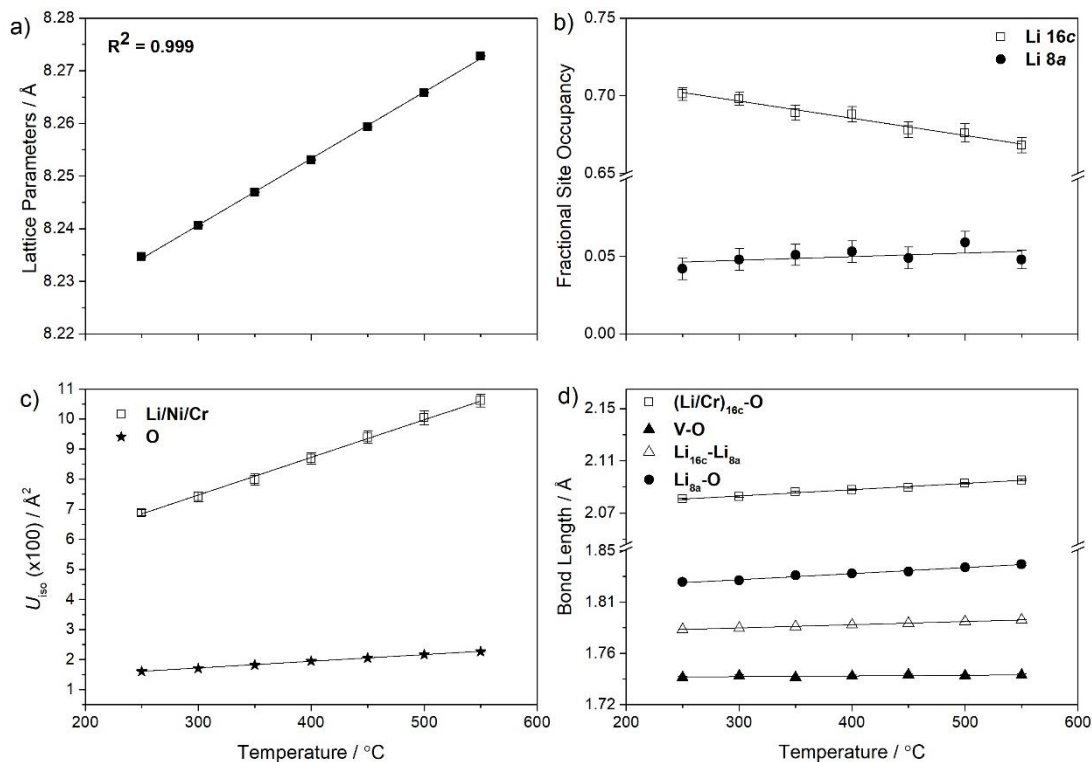
Figure 5.9. Structural evolution of Li$_3$CrV$_2$O$_8$ with temperature, a) lattice parameters, b) fractional site occupancy of Li in 16c and 8a sites, c) thermal displacement parameters and d) variation of bond lengths. Some estimated standard deviations are smaller than the symbols.

Fractional occupancy of Li in 16*c* and 8*a* sites as well as total Lithium content are shown in Figures 5.8b, 5.9b and 5.10. Occupancy of the Li 16*c* site decreases linearly with increasing temperature for both compositions, as thermal activation increases and enables the migration of Li into interstitial sites. A trend in the occupancy of 8*a* Li sites is more tentative, but this is possibly because of the low occupancy *ca.* 3 to 5 % which subsequently results in a very small degree of scattering from this site.

Total Li content remains close to $Li_{2.5}$ up to 500 °C for *x* = 0.5, even without constraining the two Li sites in the refinement. Meanwhile, in *x* = 1 the total Li content remains less than Li_3 at all temperatures, likely due to the greater difficult in refining 16*c* sites, as well as due to the small amount Li_3VO_4 impurity phase found (1.5 %), which suggests *x* = 1 may be slightly non-stoichiometric to begin with. The small differences observed in total Li content at higher temperature are unlikely to be due to Li volatilisation as ND measurements were collected on cooling for both samples. Instead, the differences observed may be explained by some Li being mobile within the inverse spinel structure and therefore poorly captured by the refinement. For example, a small fraction of Li may occupy intermediate positions between 16*c* and 8*a* sites, where the occupancy is too small to refine on average and the nuclear density too small to spot amidst the background of Difference Fourier maps.
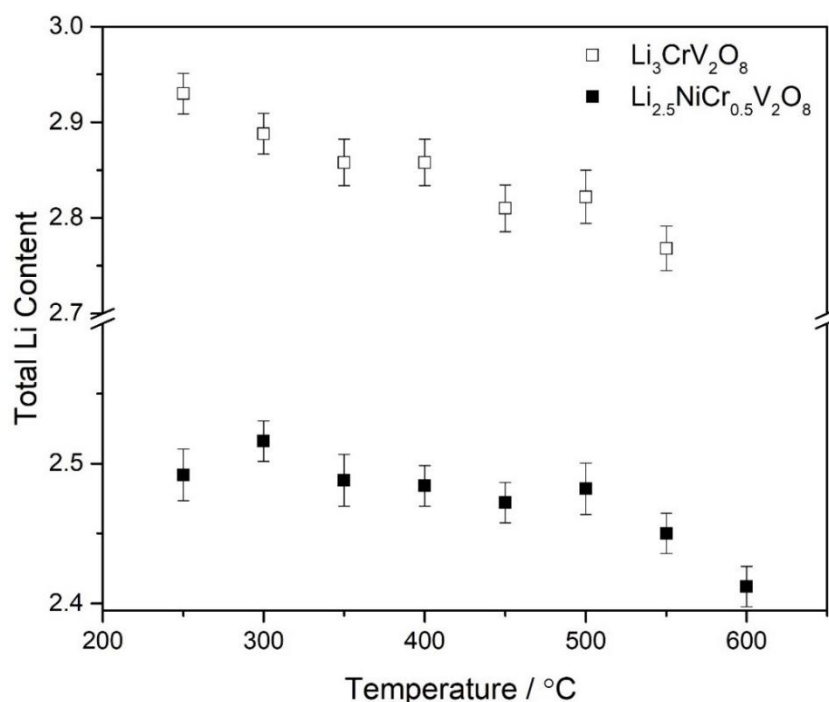
Figure 5.10. Refined Li content for $Li_3CrV_2O_8$ and $Li_{2.5}NiCr_{0.5}V_2O_8$ as a function of temperature. All ND data were collected on cooling.

Room temperature ND refinements of $Li_{2+x}Ni_{2-2x}Cr_xV_2O_8$ were revisited in an attempt to refine the Li site occupancy with the introduction of Li $8a$ sites (Table 5.6). The refinements were attempted using the same strategy as high temperature refinements. For x = 0, 0.25 and 0.5, the $16c$ site U_{iso}s were first refined, without any damping, before being fixed and the Li fractional occupancy refined. Following this, the Li $8a$ site was added to the model and refined separately before refining both Li sites together. For x = 0.75, attempts to refine $16c$ site U_{iso}s using only ND data were unsuccessful, resulting in negative values even with the use of a damping parameter, therefore U_{iso}s were fixed to the value obtained from X-ray data only (Chapter 4). Attempts to refine the Li $16c$ site occupancy required the use of a damping parameter, as attempts without one suggested the site was extremely Li deficient. Nevertheless, it was still possible to refine the occupancy of Li $8a$ sites separately. For x = 1, a damping parameter for both $16c$ site U_{iso}s and Li occupancies were required, though similarly to x = 0.75 it was possible to refine the Li $8a$ site occupancy independently. The difficulties in refining x = 0.75 and x = 1 using ND data are likely due to the small total scattering on $16c$ sites, although x = 1 was easier to refine as the data was collected for slightly longer. Fractional site occupancies for Li on $16c$ sites suggested it was slightly Li deficient for all compositions, with Li on $8a$ sites increasing with increasing x. The total Li content was also close to the target compositions. The small amount of Li occupying $8a$ sites, difficulties in refining x = 0.75 and 1 ND data, and the small differences in statistical measures between both models indicates the existence of Li on $8a$ tetrahedral sites at room temperature is ambiguous but cannot be completely ruled out.

Table 5.6. Summary of Li 16*c* and Li 8*a* site occupancies during attempted room temperature ND refinements of $Li_{2+x}Ni_{2-2x}Cr_xV_2O_8$.

Composition $Li_{2+x}Ni_{2-2x}Cr_xV_2O_8$	Li1 (16*c*) Occupancy	Li2 (8*a*) Occupancy	Refined Li content	Statistical measures Total R_{wp} and χ^2
x = 0, i.e. Li$_2$	0.479(3)	0.008(4)	Li$_{1.93(1)}$	2.15%, 3.661 (one Li site)
				2.15%, 3.629 (two Li sites)
x = 0.25, i.e. Li$_{2.25}$	0.560(2)	0.022(5)	Li$_{2.28(1)}$	2.07%, 3.652 (one Li site)
				2.07%, 3.641 (two Li sites)
x = 0.5, i.e. Li$_{2.5}$	0.606(2)	0.038(6)	Li$_{2.50(1)}$	2.32%, 4.134 (one Li site)
				2.31%, 4.084 (two Li sites)
x = 0.75, i.e. Li$_{2.75}$	0.655(2)	0.044(7)	Li$_{2.71(2)}$	2.95%, 5.289 (one Li site)
				2.94%, 5.268 (two Li sites)
x = 1, i.e. Li$_3$	0.727(2)	0.057(7)	Li$_{3.02(2)}$	3.29%, 3.843 (one Li site)
				3.28%, 3.822 (two Li sites)

The new inverse spinel crystal structure and Li-ion conduction pathway are shown in Figures 5.11 and 5.12. The results of the refinements presented here highlight how variable-temperature neutron powder diffraction allow the capture of an average snapshot of the distribution of mobile cations in the crystal structure. In the $Li_{2+x}Ni_{2-2x}Cr_xV_2O_8$ (*x* = 0.5 and 1) inverse spinels. The majority of Li resides in 16*c* octahedral sites alongside Ni and/or Cr, while a small fraction of Li also occupies 8*a* tetrahedral sites. However, the extremely short Li_{16c} – Li_{8a} distance of *ca.* 1.79 Å means it is unlikely adjacent 16*c* and 8*a* sites are simultaneously occupied due to the electrostatic repulsion between Li-ions. As temperature increases, Li-ions have greater vibrational energy, enabling them to hop from their ideal position into vacant 8*a* sites. Oxygen atoms can also vibrate more, enabling the polyhedral face to widen and increasing the bottleneck for which Li-ions can diffuse through. In the refined inverse spinel crystal structure, 16*c* octahedral sites are connected to two 8*a* tetrahedral sites via face-sharing. An expansion of this face within the polyhedral window enables lithium to migrate from 16*c* sites into two possible 8*a* sites; once in an 8*a* site, lithium can again diffuse through polyhedral faces into four available 16*c* sites, resulting in a three-dimensional 16*c*-8*a*-16*c* conduction pathway. In this case, the complete picture is more complicated as some 16*c* octahedral sites are blocked by Ni and Cr atoms, thereby limiting diffusion. This may

potentially be why only a very small amount of Li-ions (*ca.* 4 %) occupy 8a sites at high temperatures (550 °C to 600 °C) and why oxygen atoms are fairly stable in their ideal position even at high temperature; they are essentially tied down by Ni and Cr, which are heavier and less mobile than Li-ions.
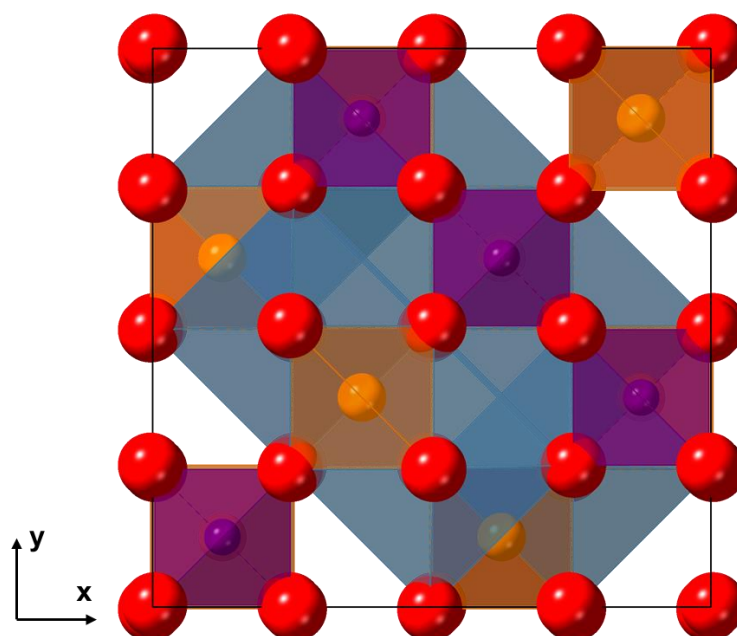
Figure 5.11. Refined average crystal structure of $Li_{2.5}NiCr_{0.5}V_2O_8$ at 600°C, showing purple VO_4 tetrahedra, light blue $(Li/Ni/Cr)_{16c}O_6$ octahedra, orange $Li_{8a}O_4$ tetrahedra, and oxygen atoms in red.
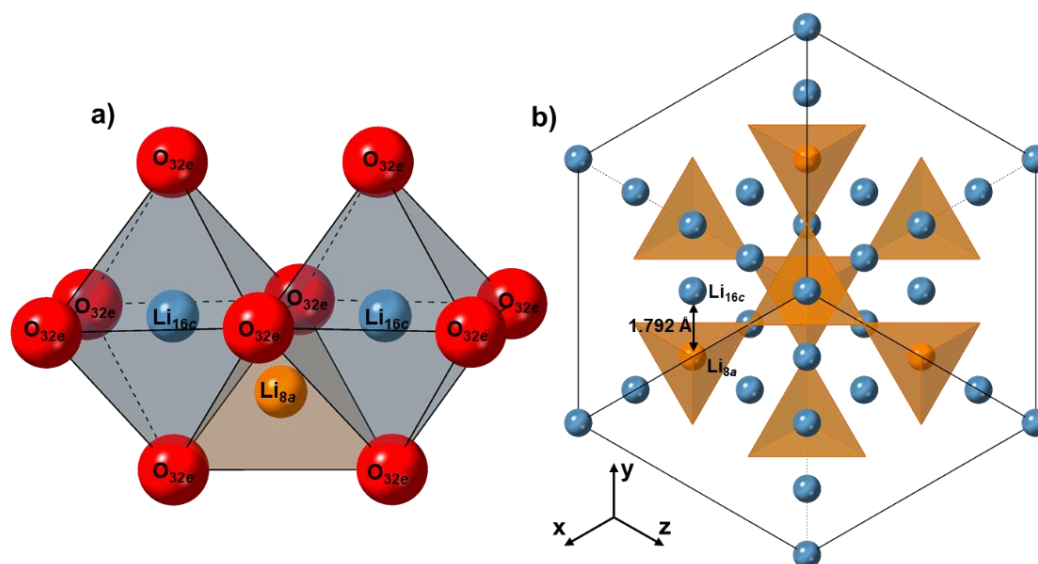
Figure 5.12. a) Portion of the $Li_{2+x}Ni_{2-2x}Cr_xV_2O_8$ (*x* = 0.5 and 1) inverse spinel crystal structure, showing the possible Li-ion conduction pathway through the octahedra face of Li_{16c} sites (blue) into intermediate Li_{8a} sites (orange); b) Simplified crystal structure, orientated in the {111} plane, showing all possible Li positions in the unit cell. Each 16c site is surrounded via two Li_{8c} sites, and each Li_{8a} site is surrounded by four 16c sites randomly occupied by Li, Ni and/or Cr. All other atoms within the crystal structure were omitted for clarity.

The Li-ion diffusion pathway in the $Li_{2+x}Ni_{2-2x}Cr_xV_2O_8$ inverse spinels appear to be fairly simple on average and similar to their normal spinel counterparts such as $Li_2NiGe_3O_8$, $Li_4Ti_5O_{12}$ and $LiMn_2O_4$. In these systems Li-ions solely occupy tetrahedral sites which can hop into adjacent empty octahedral sites allowing for a 3D (tet-oct-tet) conduction pathway.[1]–[3] The results herein suggest that despite sharing octahedral sites with transition metals *e.g.* Cr and/or Ni, the conduction pathway is similar to normal spinels but in reverse. This may explain why they have comparable activation energies for Li-ion diffusion *ca.* 0.5 eV, as discussed in Chapter 4. These results are in contrast to other spinel systems where Li-ions share sites with other atoms such as $Li_2ZnGe_3O_8$ ($[Li/Zn]^{tet8c}[Li]^{oct4b}[Ge_3]^{oct12d}O_8$) which has a large activation energy for Li-ion conduction (2.14 eV).[1], [14] In $Li_2ZnGe_3O_8$, the Li-ions that are disordered alongside Zn in tetrahedral sites do not take part in the conduction pathway due to being blocked by Zn^{2+} cations. Instead, Li-ions occupying octahedral sites are involved in a longer and more tortuous conduction pathway which severely limits Li-ion diffusion.[1] The results presented here show that these Li/TM mixed sites can take part in the conduction pathway and this may again be evidence for local ordering between Li, Ni and/or Cr cations on octahedral sites in the inverse spinel model, as reported by Page *et al.* for $LiNiVO_4$ and $LiCoVO_4$.[7] Future work should investigate the degree of local ordering as a function of Li content in the $Li_{2+x}Ni_{2-2x}Cr_xV_2O_8$ inverse spinels using techniques such as pair distribution function (PDF analysis).

5.3.2. Muon Spectroscopy

Information on the previously discussed conduction pathway can be used alongside muon spectroscopy (μSR) to determine the local Li-ion diffusion kinetics for these inverse spinels. Raw muon decay asymmetry data and subsequent fits for x = 0, 0.5 and 1 are presented in Figures 5.13 to 5.15. At every temperature (100 K to 600 K) the raw asymmetry data, collected in a zero field and two longitudinal fields (5 and 10 Gauss), were simultaneously modelled using a Dynamic Kubo Toyabe (DKT) function, as described by Equation 5.1.[15], [16]

$$A(t) = AG^{DKT}(\Delta, \nu, t, H_{LF}) \times e^{(-\lambda t)} + A_{BG} \qquad \text{(Equation 5.1)}$$

Simultaneous fitting of multiple fields enabled the fitting parameters to be more easily constrained. Within Equation 5.1, the DKT function contains terms describing the local field distribution, Δ, and the fluctuation rate, ν, for mobile species e.g. Li-ions. An exponential relaxing term with a relaxation rate, λ, was multiplied by the DKT function to account for the paramagnetic response associated with the unpaired electrons of Ni^{2+} and Cr^{3+} species. A background term was also added during the fitting process to account for muons which stop in the Ti sample holder. Initially, λ was allowed to vary freely within the fits. However, only a small increase in λ was observed at higher temperatures (>500 K), which may be due to a correlation between λ and ν. Therefore, λ was kept fixed to an average value of 0.05 μs^{-1}, and only Δ and ν were allowed to vary at all temperatures.
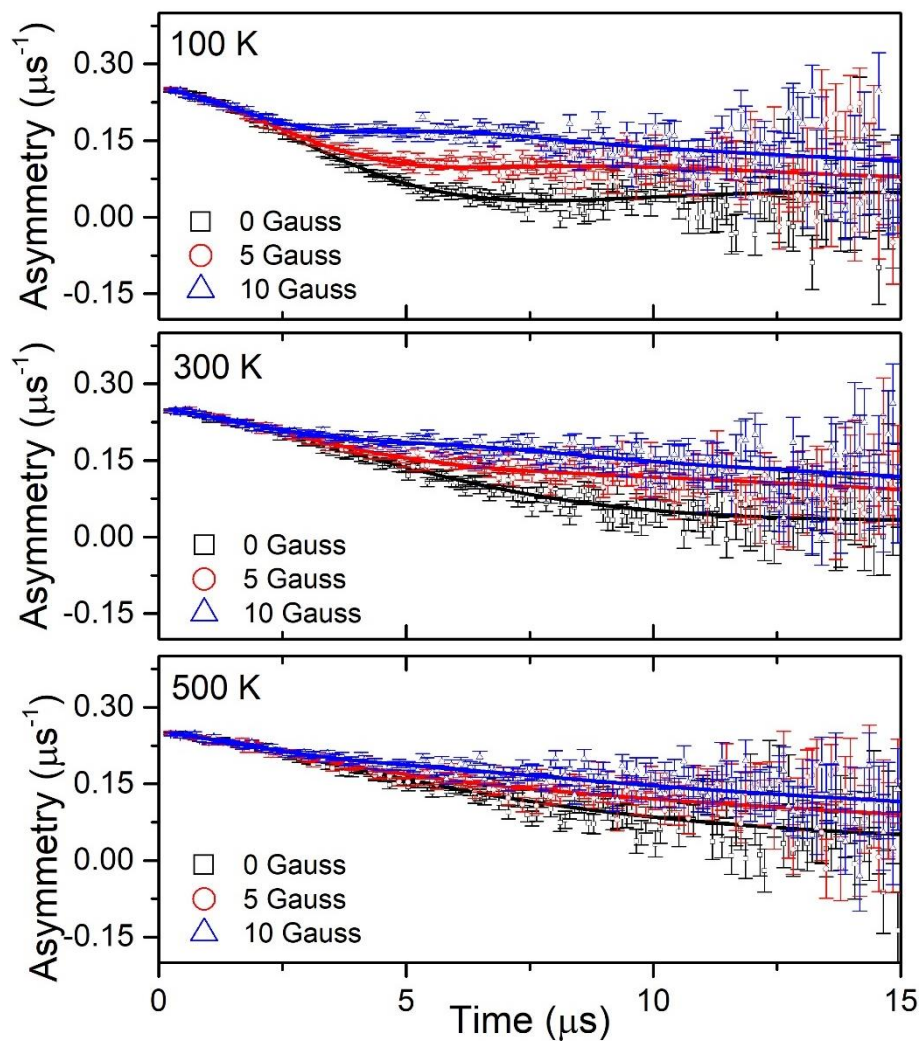
Figure 5.13. Raw muon spectroscopy data for $Li_{2+x}Ni_{2-2x}Cr_xV_2O_8$, $x = 0$, collected at 100 K, 300 K and 500 K in a zero field (squares), and applied longitudinal fields of 5 G (circles) and 10 G (triangles). Raw data was fitted using Equation 5.1.
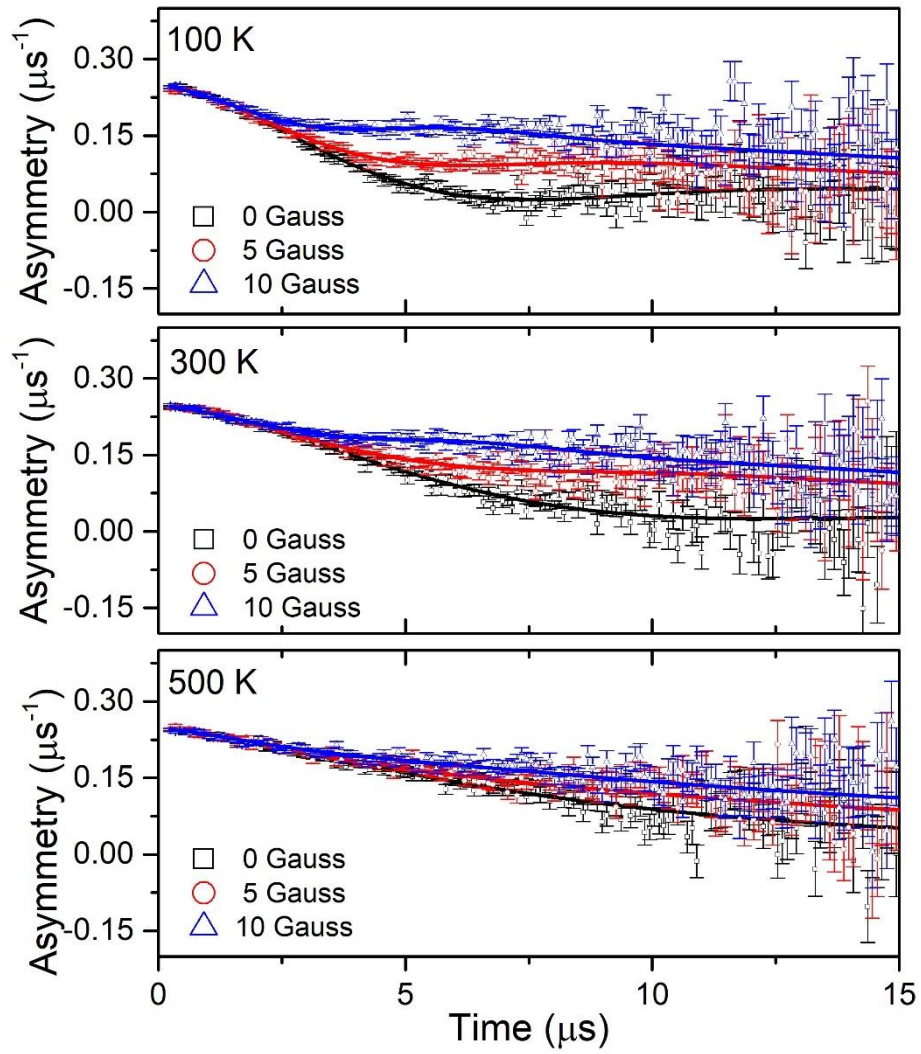
Figure 5.14. Raw muon spectroscopy data for $Li_{2+x}Ni_{2-2x}Cr_xV_2O_8$, $x = 0.5$, collected at 100 K, 300 K and 500 K in a zero field (squares), and applied longitudinal fields of 5 G (circles) and 10 G (triangles). Raw data was fitted using Equation 5.1.
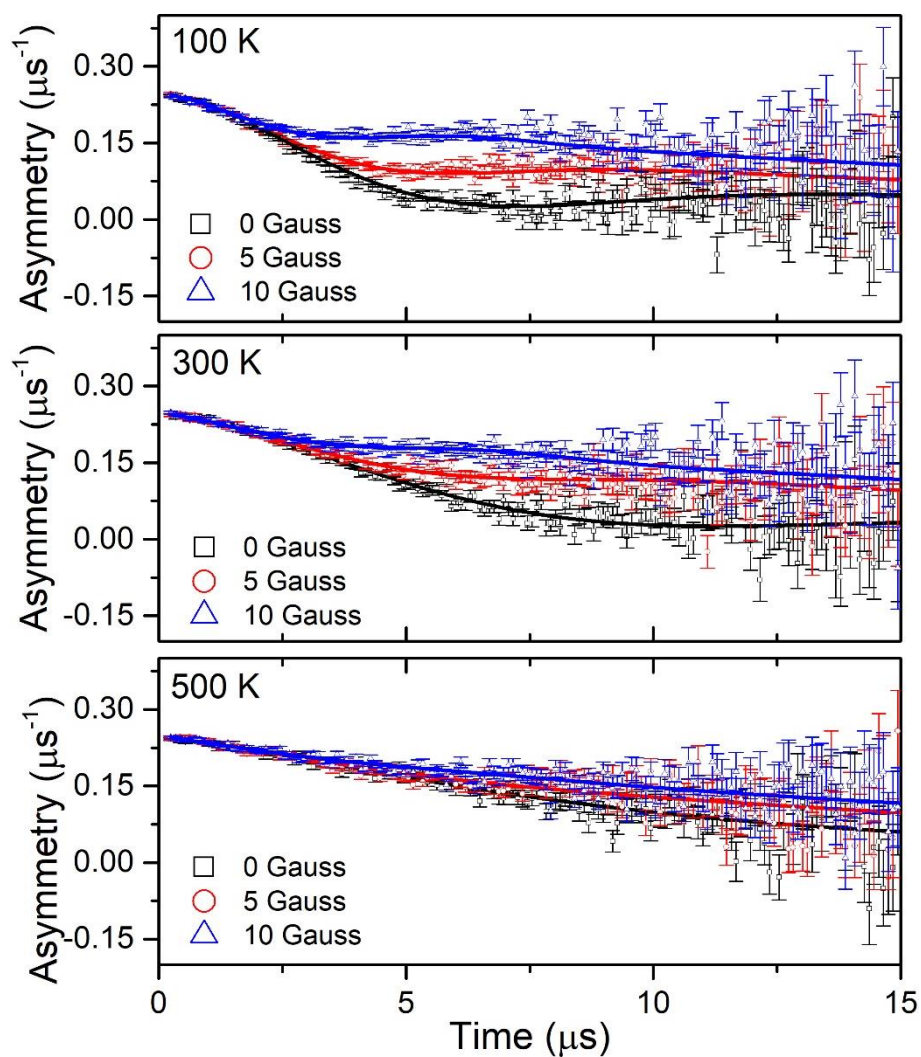
Figure 5.15. Raw muon spectroscopy data for $Li_{2+x}Ni_{2-2x}Cr_xV_2O_8$, $x = 1$, collected at 100 K, 300 K and 500 K in a zero field (squares), and applied longitudinal fields of 5 G (circles) and 10 G (triangles). Raw data was fitted using Equation 5.1.

From the resulting fits, the fitting parameters v and Δ can then be extracted and plotted *vs.* temperature. These parameters describe the environment around the implanted muons, and as such the muon can be used as a local probe. Typically, in battery materials the fluctuation rate, v, is related to the hopping rate of Li-ion diffusion. For example, in materials such as $Li_2NiGe_3O_8$, $LiCoO_2$, and $Li_{6.5}Al_{0.25}La_{2.92}Zr_2O_{12}$, the fluctuation rate shows a low temperature plateau, followed by an Arrhenius-like increase.[17]–[20] The Arrhenius-type behaviour is due to the thermal activation of Li-ions as they begin to hop increasingly rapidly with increasing temperature. The local field distribution, Δ, is related to the stability of the environment around the muon stopping sites and is typically correlated with the fluctuation rate. At low temperatures, Δ is constant due to the static environment around implanted muons, as Li-ion diffusion is slow. As the temperature increases, Δ shows a significant decrease over the thermally activated region. This behaviour is likely due to local changes in the magnetic field the muons experience, caused by the onset on Li-ion diffusion.[15], [21]

The temperature dependence of v and Δ for the inverse spinel series $Li_{2+x}Ni_{2-2x}Cr_xV_2O_8$, $x = 0$, 0.5 and 1 are displayed in Figures 5.16 to 5.18. Plots of v and Δ differ in all three compositions at low temperatures compared to the battery materials described above. Instead of being relatively constant before the thermally activated region, there appears to be three distinct regions within the plots. For $x = 0$ in the first region, v remains relatively constant between 100 K to *ca.* 240 K. In the second region, v values increase to *ca.* 0.1 MHz at 280 K before levelling off until ca. 400 K. Finally, in the third thermally activated region at *ca.* 400 K, a sharp increase in v is observed due to the rapid onset of Li-ion diffusion. Within x = 0.5 and 1, the onset of the thermally activated region shifts to lower temperatures and the second region (between *ca.* 240 K to 400 K) becomes less pronounced with increasing x. There is also an additional region within x = 0.5 and 1, where above 500 K v rapidly decreases and is likely due to Li-ion hopping becoming so fast that it cannot be detected by the implanted muons. For all compositions, calculated values of Δ initially show a significant decrease at low temperatures (*ca.* 100 K to 280 K) before then plateauing between ca. 300 K to 400 K. Finally, Δ values begin to decrease again at high temperatures (*ca.* 440 K). As previously discussed, the high temperature decrease in Δ is correlated to the thermally activated region. Similar to plots of v, the behaviour of Δ experiences a shift to lower temperatures with increasing x (*e.g.* the high temperature decrease begins at *ca.* 460 K for $x = 0$ compared to *ca.* 400 K for $x = 1$).

Compared to other battery materials such as the complex spinel, $Li_2NiGe_3O_8$ (Chapter 2), the high temperature thermally activated region is most similar for $x = 1$ with an onset temperature of *ca.* 320 K compared to 340 K for $Li_2NiGe_3O_8$.[18] However, for $x = 0$ and 0.5 the thermally activated region is shifted to higher temperatures compared to $Li_2NiGe_3O_8$, and suggests a higher temperature is required to reach the same hopping rate (*ca.* 0.25 MHz) of Li-ions in these inverse spinels. An explanation for the low temperature behaviour observed in plots of *v* and *Δ* is currently unclear, as this behaviour has not previously been seen in battery materials studied using the µSR technique. Nevertheless, one possible explanation could be the presence of a range of muon stopping sites which experience different fluctuations, *e.g.* from nuclear or magnetic moments, with increasing temperature. Alternatively as previously discussed, Page *et al.* reported that $x = 0$ and other inverse spinels form a locally cation-zigzag-ordered structure (space group *P4$_1$22*) up to 8 Å.[7] The results presented here may suggest local structural changes with temperature *e.g.* ordered/disordered transitions, which thereby alter the local fields that implanted muons experience. It should be noted that the low temperature phenomena observed in µSR data was not evident within impedance spectroscopy data, likely due to this being a short range effect or occurring outside of the temperature range investigated. Further work could use solid-state NMR or PDF techniques to investigate the effect of temperature on any local structural changes within the inverse spinel system.
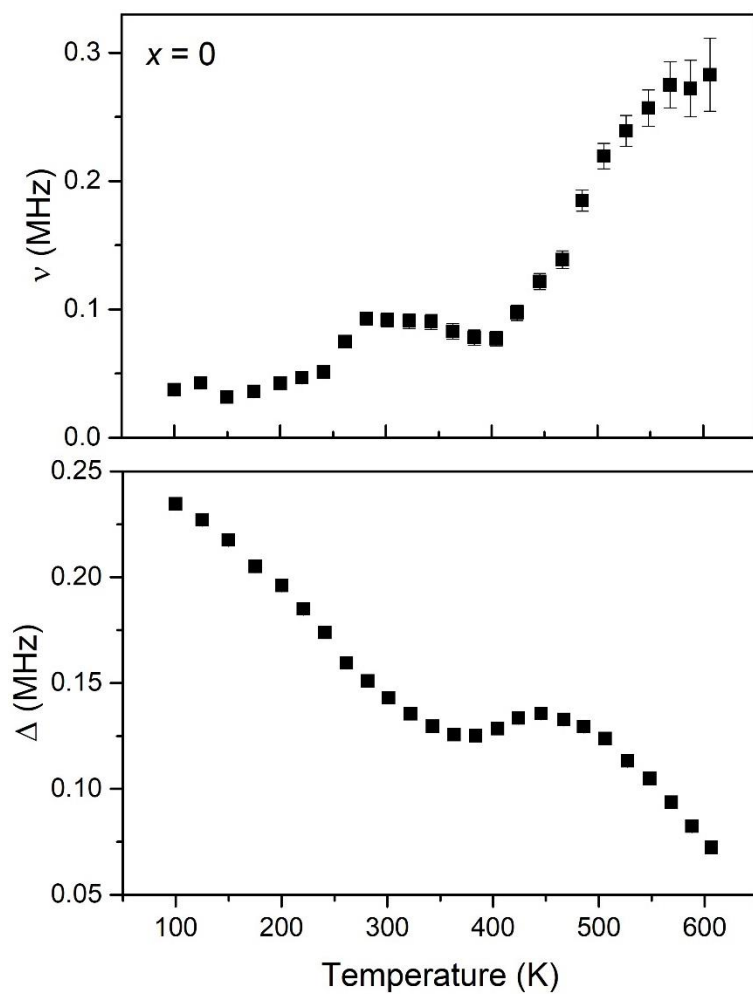
Figure 5.16. Variation of *v* and *Δ* with temperature obtained from the fitting of raw asymmetry data to Equation 5.1 for $Li_{2+x}Ni_{2-2x}Cr_xV_2O_8$, *x* = 0, measured from 100 K to 600 K.
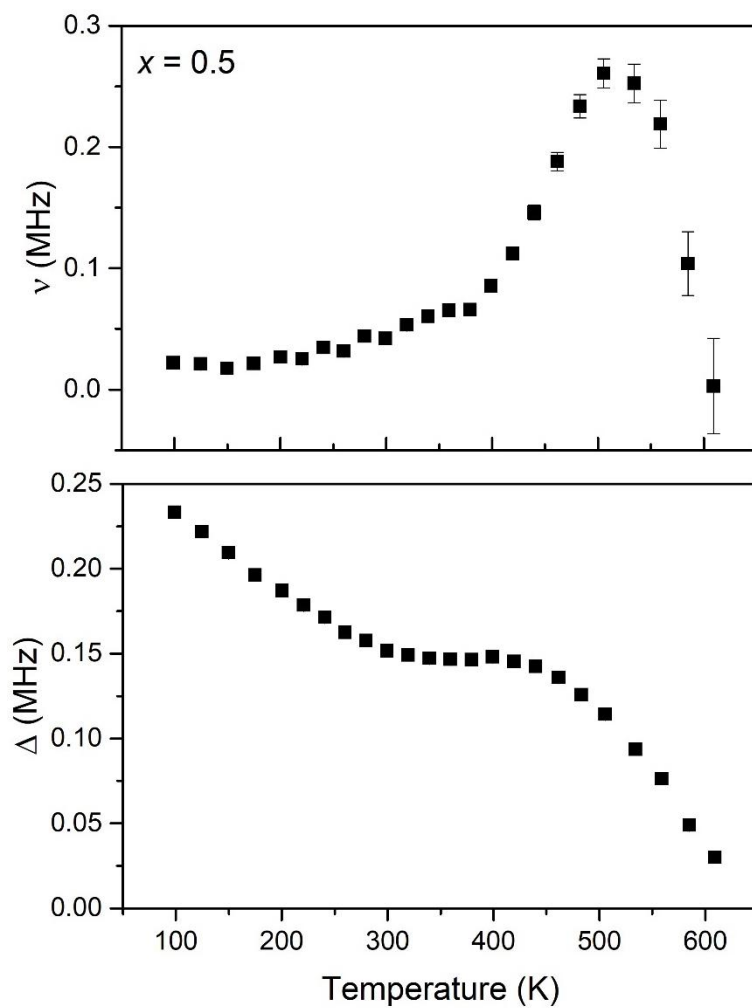
Figure 5.17. Variation of *v* and *Δ* with temperature obtained from the fitting of raw asymmetry data to Equation 5.1 for Li$_{2+x}$Ni$_{2-2x}$Cr$_x$V$_2$O$_8$, *x* = 0.5, measured from 100 K to 600 K.
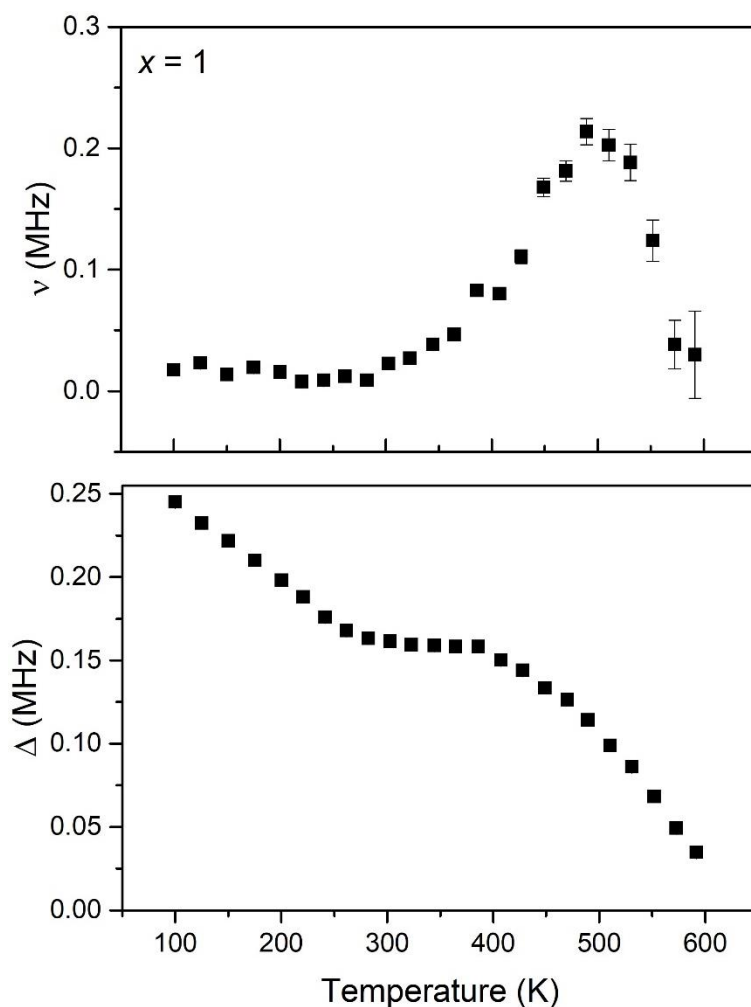
Figure 5.18. Variation of *v* and *Δ* with temperature obtained from the fitting of raw asymmetry data to Equation 5.1 for $Li_{2+x}Ni_{2-2x}Cr_xV_2O_8$, *x* = 1, measured from 100 K to 600 K.

Arrhenius plots of the thermally activated region versus 1000/T for $Li_{2+x}Ni_{2-2x}Cr_xV_2O_8$, *x* = 0, 0.5 and 1 are shown in Figure 5.19. Calculated activation energies were similar for all three compositions, ranging between 0.17 to 0.19 $\pm$ 0.01 eV. These values are significantly lower than those calculated from impedance spectroscopy data, where values range from 0.49 eV to 0.53 eV (Chapter 4, Section 4.3.4). This is likely due to the different sample preparations or Li-ion motion length scales measured by μSR and impedance spectroscopy techniques.[15], [22] Impedance spectroscopy measurements are also sensitive to preparation conditions such as the sintering temperature and pellet density. These discrepancies have also been observed in the solid electrolyte, $Li_{6.5}Al_{0.25}La_{2.92}Zr_2O_{12}$, where an activation energy of 0.19 eV was deduced from μSR compared with 0.55 eV from impedance spectroscopy measurements.[17] The activation energies for these inverse spinels are also

significantly lower than that calculated for $Li_2NiGe_3O_8$ (0.43 eV) from μSR, despite requiring a higher temperature to reach the same hopping rate.[18] The hopping rate is governed by the number of charge carriers and their mobility. This could indicate that while the barrier for hopping is lower in $Li_{2+x}Ni_{2-2x}Cr_xV_2O_8$, the number of Li-ions available to hop may also be lower, as some Li-ions are trapped due to the mixed occupancies between Li and metal cations on average.
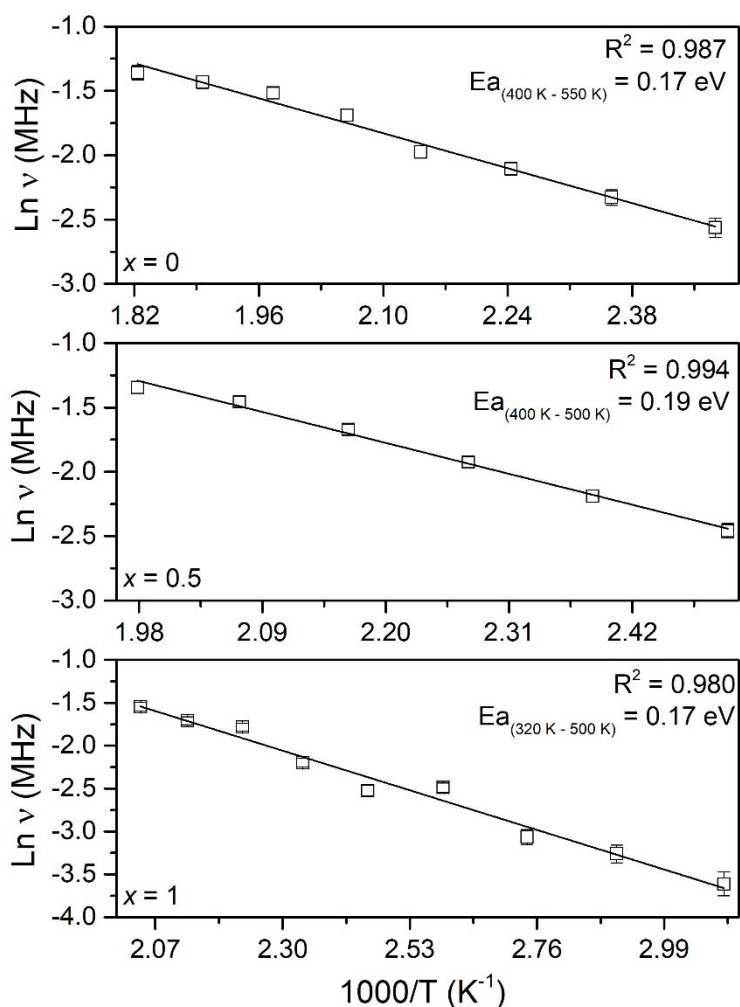
Figure 5.19. Arrhenius plot of v (MHz) vs. 1000/T (K^{-1}) of the thermally activated region for the inverse spinel series, $Li_{2+x}Ni_{2-2x}Cr_xV_2O_8$, x = 0, 0.5 and 1. The error in the activation energy was calculated to be 0.01 eV for all compositions.

The Li-ion diffusion coefficient (D_{Li}) for $Li_{2+x}Ni_{2-2x}Cr_xV_2O_8$, x = 0, 0.5 and 1 was calculated using Equation 5.2. N_i is the number of available sites calculated from the three-dimensional 16c-8a-16c conduction pathway, where each 16c site is surrounded by two 8a sites. $Z_{v,i}$ is the

vacancy fraction of destination sites, assumed to be 1 at 300 K. S_i is the hopping distance between 16c and 8a sites (1.79 Å). Finally, v is the fluctuation rate, calculated by extrapolating the Arrhenius plots of the thermally activated region to 300 K.

$$D_{Li} = \Sigma_{i=1}^{n} \frac{1}{N_i} Z_{v,i} S_i^2 v \qquad \text{(Equation 5.2)}$$

By using the crystal structure information obtained from variable temperature ToF ND and μSR as a local probe for Li-ion hopping, diffusion coefficients of 2.36 ± 0.86 x 10^{-12} cm^2 s^{-1} (x = 0), 2.25 ± 0.64 x 10^{-12} cm^2 s^{-1} (x = 0.5) and 1.96 ± 0.21 x 10^{-12} cm^2 s^{-1} (x = 1) can be obtained for these inverse spinels. Table 5.7 displays D_{Li} and activation energies for several Li-ion conductors calculated using the μSR technique. The results herein are comparable to previous work on the complex spinel, $Li_2NiGe_3O_8$ and have similar activation energies for local Li-ion diffusion to the Li-stuffed garnet, $Li_{6.5}Al_{0.25}La_{2.92}Zr_2O_{12}$ and the normal spinel, $Li_4Ti_5O_{12}$.[17], [18], [23] The similar activation energies of the solid solution $Li_{2+x}Ni_{2-2x}Cr_xV_2O_8$ reported here in comparison to $Li_4Ti_5O_{12}$ are expected due to the related conduction pathways found from variable-temperature ND refinements in this work. This suggests that they are modest Li-ion conductors despite the mixed occupancy of 16c sites by Li and transition metals, and that this should not be the limiting factor for determining their applications as Li-ion battery materials.

Table 5.7. Comparison of activation energies and Lithium diffusion coefficients (D_{Li}) at 300 K for several battery materials calculated from muon spectroscopy data.

Material	D_{Li} (cm^2 s^{-1})	Ea (eV)	Reference
$Li_2Ni_2V_2O_8$	2.36 x 10^{-12}	0.17	This work
$Li_{2.5}NiCr_{0.5}V_2O_8$	2.25 x 10^{-12}	0.19	This work
$Li_3CrV_2O_8$	1.96 x 10^{-12}	0.17	This work
$Li_2NiGe_3O_8$	3.89 x 10^{-12}	0.43	[18]
$Li_4Ti_5O_{12}$	3.2 x 10^{-11}	0.12	[23]
$Li_{6.5}Al_{0.25}La_{2.92}Zr_2O_{12}$	4.62 x 10^{-11}	0.19	[17]
$LiCoO_2$	2.5 x 10^{-10}	0.09	[19]
$LiFePO_4$	10^{-10}-10^{-9}	0.1	[22]

5.4. Conclusions

In this work the Li-ion diffusion mechanisms and kinetics in the inverse spinel series, $Li_{2+x}Ni_{2-2x}Cr_xV_2O_8$, x = 0, 0.5 and 1, were investigated, for the first time, using variable-temperature neutron powder diffraction alongside muon spectroscopy.

Rietveld refinements of x = 0.5 and 1 revealed the inverse spinel structure is maintained throughout all measured temperatures (250 to 600 °C). There was also no indication of cation mixing and/or ordering as a function of temperature. However, difference Fourier maps generated during Rietveld refinements showed significant negative scattering, which was identified as Li-ions occupying additional 8a tetrahedral sites. As a result, the conduction pathway appears to be relatively simple and similar to their normal spinel counterparts. In these materials, Li-ions occupying 16c octahedral sites can diffuse into vacant 8a tetrahedral sites through polyhedral faces, forming an 16c-8a-16c conduction pathway. This is despite the random distribution of Li-ions together with Cr and/or Ni cations in 16c sites.

Muon spectroscopy was then utilised as a local probe for Li-ion diffusion in x = 0, 0.5 and 1. Li-ions were found to rapidly diffuse at *ca.* 400 K for x = 0 and 0.5 and ca. 320 K for x = 1, corresponding to calculated activation energies between 0.17 to 0.19 eV. Li-ion diffusion coefficients of between 1.96×10^{-12} cm^2 s^{-1} and 2.36×10^{-12} cm^2 s^{-1} were determined using structural information obtained from neutron diffraction data alongside the hopping rate obtained from muon spectroscopy data. These results are comparable to other normal spinel materials such as $Li_2NiGe_3O_8$ and $Li_4Ti_5O_{12}$, where Li-ions solely occupy tetrahedral sites. Therefore, this suggests that the random distribution of Li and transition metal cations in octahedral sites should not be the limiting factor in determining their potential applications in LiBs.

Further studies are required to investigate the effect of altering the Li/Transition metal ratio on the local ordering in these materials. This could be conducted through the use of techniques such as PDF theory and solid-state MAS NMR. These techniques could also help gain insight into the low temperature phenomena seen in muon spectroscopy data.

5.5. References

[1]   N. Reeves-Mclaren, R. I. Smith, and A. R. West, "Lithium-ion conduction pathways in complex lithium spinels $Li_2MGe_3O_8$ (M = Ni or Zn)," *Chem. Mater.*, vol. 23, no. 15, pp. 3556–3563, 2011.

[2]   M. Nakayama, R. Jalem, and T. Kasuga, "Electronic structure of spinel-type $LiNi_{1/2}Ge_{3/2}O_4$ and $LiNi_{1/2}Mn_{3/2}O_4$ as positive electrodes for rechargeable Li-ion batteries studied by first-principles density functional theory," *Solid State Ionics*, vol. 262, pp. 74–76, 2014.

[3]   A. Laumann, H. Boysen, M. Bremholm, K. T. Fehr, M. Hoelzel, and M. Holzapfel, "Lithium migration at high temperatures in $Li_4Ti_5O_{12}$ studied by neutron diffraction," *Chem. Mater.*, vol. 23, no. 11, pp. 2753–2759, 2011.

[4]   G. T. K. Fey and D. L. Huang, "Synthesis, characterization and cell performance of inverse spinel electrode materials for lithium secondary batteries," *Electrochim. Acta*, vol. 45, no. 1, pp. 295–314, 1999.

[5]   G. T. K. Fey, P. Muralidharan, and C. Z. Lu, "Synthesis and characterization of a new inverse spinel $LiNi_{1/3}Co_{1/3}Mn_{1/3}VO_4$ for lithium-ion batteries," *Mater. Lett.*, vol. 60, no. 9–10, pp. 1209–1212, 2006.

[6]   A. Kitajou, J. Yoshida, S. Nakanishi, S. Okada, and J. I. Yamaki, "Cathode properties of Mn-doped inverse spinels for Li-ion battery," *J. Power Sources*, vol. 244, pp. 658–662, 2013.

[7]   J. Liu *et al.*, "Unified View of the Local Cation-Ordered State in Inverse Spinel Oxides," *Inorg. Chem.*, vol. 58, no. 21, pp. 14389–14402, 2019.

[8]   R. I. Smith *et al.*, "The upgraded Polaris powder diffractometer at the ISIS neutron source," *Rev. Sci. Instrum.*, vol. 90, no. 11, 2019.

[9]   T. Brian. H, "EXPGUI, a graphical user interface for GSAS," *J. Appl. Crystallogr.*, vol. 34, no. 2, pp. 210–213, 2001.

[10]   A. C. Larson and R. B. Von Dreele, "General Structure Analysis System (GSAS)," *Los Alamos National Laboratory Report LAUR*. pp. 86–748, 2004.

[11]   V. Favre-Nicolin and R. Cerný, "FOX, `free objects for crystallography': a modular approach to ab initio structure determination from powder diffraction," *J. Appl. Crystallogr.*, vol. 35, pp. 734–743, 2002.

[12]   S. R. Giblin *et al.*, "Optimising a muon spectrometer for measurements at the ISIS pulsed muon source," *Nucl. Instruments Methods Phys. Res. Sect. A Accel. Spectrometers, Detect. Assoc. Equip.*, vol. 751, pp. 70–78, 2014.

[13]   O. Arnold *et al.*, "Mantid - Data analysis and visualization package for neutron scattering and μ SR experiments," *Nucl. Instruments Methods Phys. Res. Sect. A Accel. Spectrometers, Detect. Assoc. Equip.*, vol. 764, pp. 156–166, 2014.

[14]   H. Kawai, M. Tabuchi, M. Nagata, H. Tukamoto, and A. R. West, "Crystal chemistry and physical properties of complex lithium spinels $Li_2MM'_3O_8$ (M=Mg, Co, Ni, Zn; M'=Ti, Ge)," *J. Mater. Chem.*, vol. 8, no. 5, pp. 1273–1280, 1998.

[15]   I. McClelland, B. Johnston, P. J. Baker, M. Amores, E. J. Cussen, and S. A. Corr, "Muon Spectroscopy for Investigating Diffusion in Energy Storage Materials," *Annu. Rev. Mater. Res.*, vol. 50, pp. 371–393, 2020.

[16]   R. . Hayano, Y. . Uemura, J. Imazato, T. Yamazaki, and R. Kubo, "Zero-and low-field spin relaxation studied by positive muons," *Phys. Rev. B*, vol. 20, no. 3, p. 850, 1979.

[17]   M. Amores, T. E. Ashton, P. J. Baker, E. J. Cussen, and S. A. Corr, "Fast microwave-assisted synthesis of Li-stuffed garnets and insights into Li diffusion from muon spin spectroscopy," *J. Mater. Chem. A*, vol. 4, no. 5, pp. 1729–1736, 2016.

[18]   D. Z. C. Martin *et al.*, "Evaluating lithium diffusion mechanisms in the complex spinel $Li_2NiGe_3O_8$," *Phys. Chem. Chem. Phys.*, vol. 21, no. 41, pp. 23111–23118, 2019.

[19]   J. Sugiyama, K. Mukai, Y. Ikedo, H. Nozaki, M. Månsson, and I. Watanabe, "Li diffusion in Li_xCoO_2 probed by Muon-Spin spectroscopy," *Phys. Rev. Lett.*, vol. 103, no. 14, pp. 1–4, 2009.

[20]   C. T. Kaiser *et al.*, "Li mobility in the battery cathode material $Li_x[Mn_{1.96}Li_{0.04}]O_4$ studied by muon-spin relaxation," *Phys. Rev. B*, vol. 62, no. 14, pp. R9236–R9239, 2000.

[21]   M. Mansson and J. Sugiyama, "Muon-spin relaxation study on Li- and Na-diffusion in solids," *Phys. Scr.*, vol. 88, no. 068509, pp. 1–13, 2013.

[22]   P. J. Baker *et al.*, "Probing magnetic order in $LiMPO_4$ (M = Ni , Co , Fe) and lithium diffusion in Li_xFePO_4," *Phys. Rev. B*, vol. 84, no. 174403, pp. 1–8, 2011.

[23]   J. Sugiyama *et al.*, "Li-ion diffusion in $Li_4Ti_5O_{12}$ and $LiTi_2O_4$ battery materials detected by muon spin spectroscopy," *Phys. Rev. B*, vol. 92, no. 014417, pp. 1–9, 2015.

5.6. Appendix
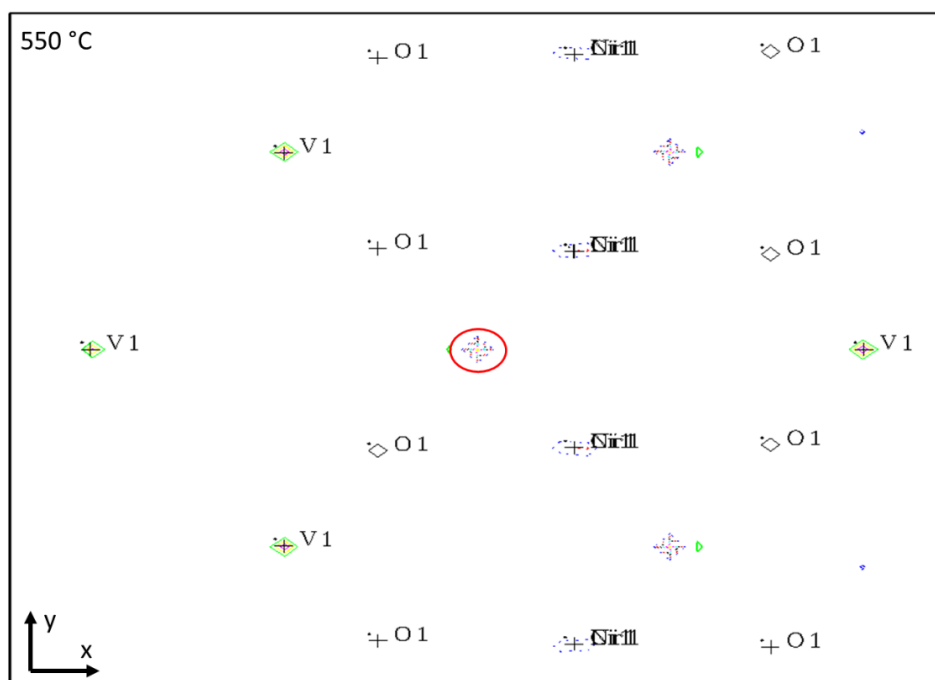
Figure 5.20. Difference Fourier map calculated during the Rietveld refinement of the $Li_{2.5}NiCr_{0.5}V_2O_8$ crystal structure at 550 °C. Centre of reference is 0.125, 0.125, 0.125, with a map size of 10 Å × 10 Å. Solid and dash lines represent contours of positive and negative scattering density, respectively. Significant negative scattering is located between V1 atoms, which can be attributed to Li in 8a tetrahedral sites.
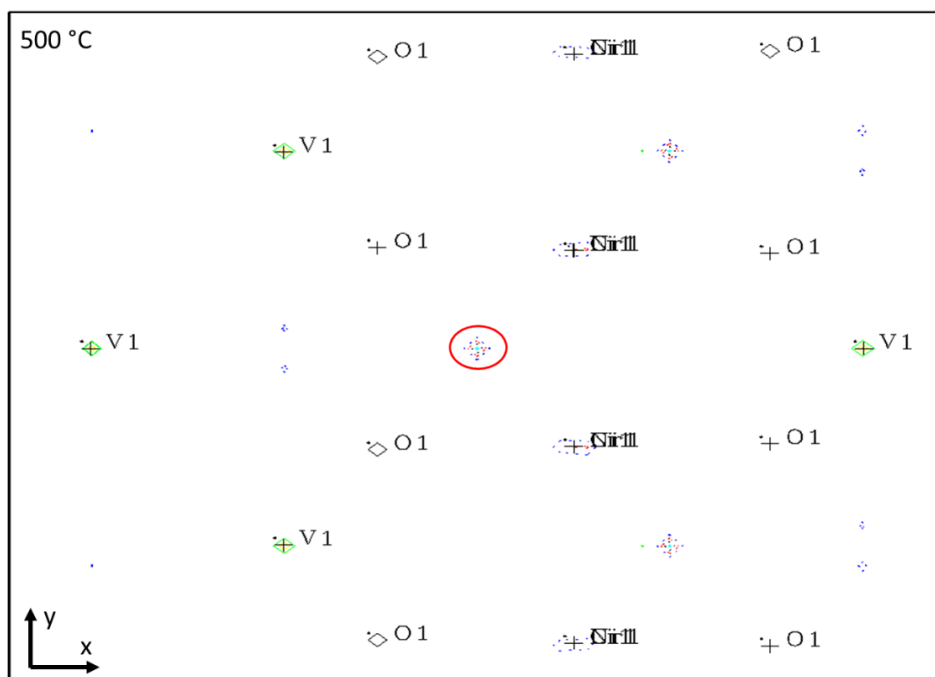
Figure 5.21. Difference Fourier map calculated during the Rietveld refinement of the $Li_{2.5}NiCr_{0.5}V_2O_8$ crystal structure at 500 °C. Centre of reference is 0.125, 0.125, 0.125, with a map size of 10 Å × 10 Å. Solid and dash lines represent contours of positive and negative scattering density, respectively. Significant negative scattering is located between V1 atoms, which can be attributed to Li in 8a tetrahedral sites.

Figure 5.22. Difference Fourier map calculated during the Rietveld refinement of the $Li_{2.5}NiCr_{0.5}V_2O_8$ crystal structure at 450 °C. Centre of reference is 0.125, 0.125, 0.125, with a map size of 10 Å × 10 Å. Solid and dash lines represent contours of positive and negative scattering density, respectively. Significant negative scattering is located between V1 atoms, which can be attributed to Li in 8a tetrahedral sites.

Figure 5.23. Difference Fourier map calculated during the Rietveld refinement of the $Li_{2.5}NiCr_{0.5}V_2O_8$ crystal structure at 400 °C. Centre of reference is 0.125, 0.125, 0.125, with a map size of 10 Å × 10 Å. Solid and dash lines represent contours of positive and negative scattering density, respectively. Significant negative scattering is located between V1 atoms, which can be attributed to Li in 8a tetrahedral sites.

Figure 5.24. Difference Fourier map calculated during the Rietveld refinement of the $Li_{2.5}NiCr_{0.5}V_2O_8$ crystal structure at 350 °C. Centre of reference is 0.125, 0.125, 0.125, with a map size of 10 Å × 10 Å. Solid and dash lines represent contours of positive and negative scattering density, respectively. Significant negative scattering is located between V1 atoms, which can be attributed to Li in 8a tetrahedral sites.
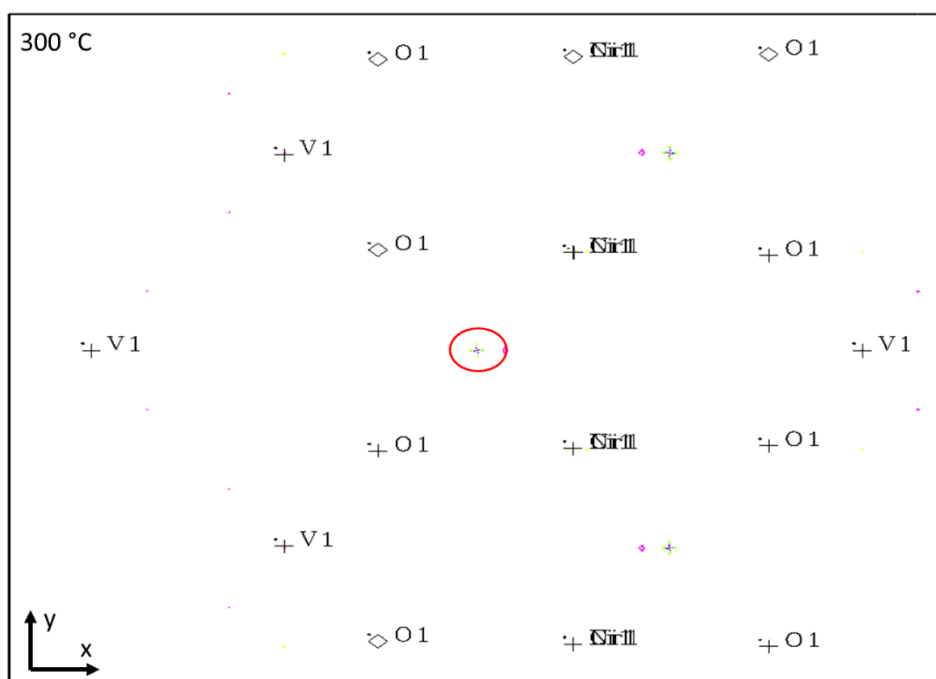
Figure 5.25. Difference Fourier map calculated during the Rietveld refinement of the $Li_{2.5}NiCr_{0.5}V_2O_8$ crystal structure at 300 °C. Centre of reference is 0.125, 0.125, 0.125, with a map size of 10 Å × 10 Å. Solid and dash lines represent contours of positive and negative scattering density, respectively. Significant negative scattering is located between V1 atoms, which can be attributed to Li in 8a tetrahedral sites.
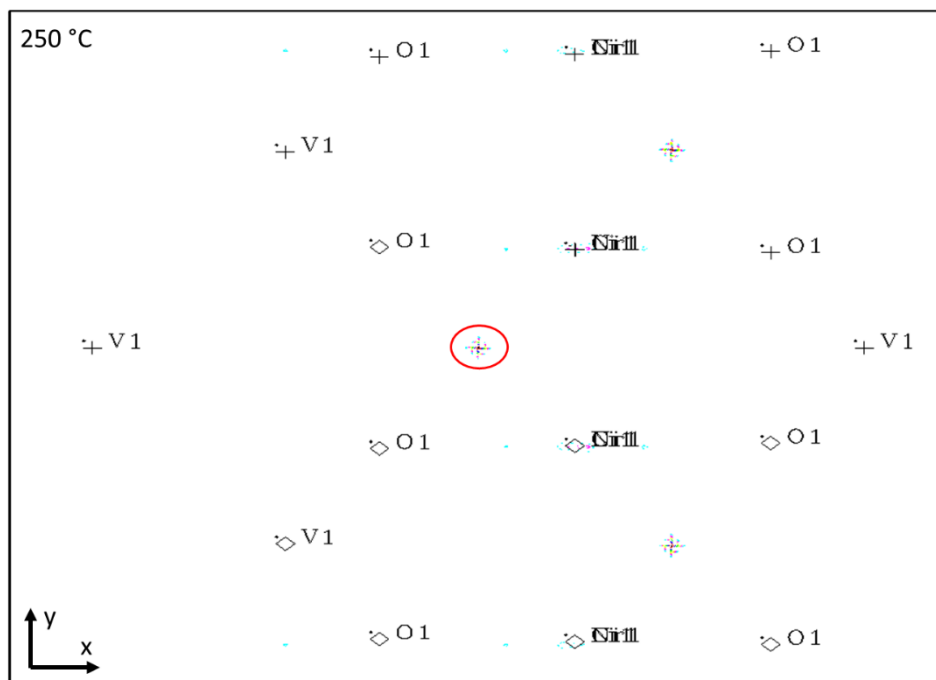
Figure 5.26. Difference Fourier map calculated during the Rietveld refinement of the $Li_{2.5}NiCr_{0.5}V_2O_8$ crystal structure at 250 °C. Centre of reference is 0.125, 0.125, 0.125, with a map size of 10 Å × 10 Å. Solid and dash lines represent contours of positive and negative scattering density, respectively. Significant negative scattering is located between V1 atoms, which can be attributed to Li in 8a tetrahedral sites.
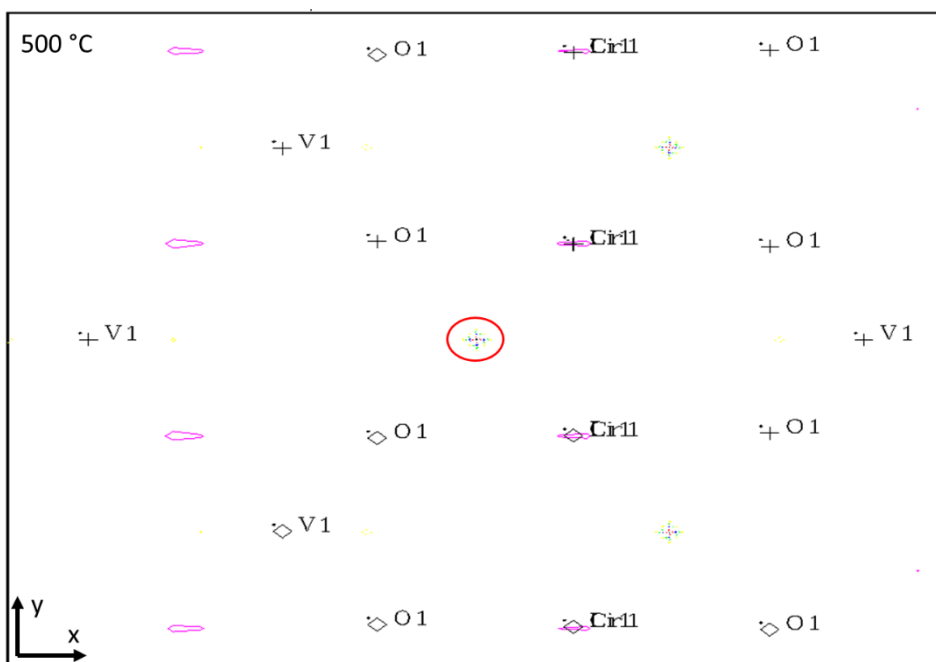
Figure 5.27. Difference Fourier map calculated during the Rietveld refinement of the $Li_3CrV_2O_8$ crystal structure at 500 °C. Centre of reference is 0.125, 0.125, 0.125, with a map size of 10 Å × 10 Å. Solid and dash lines represent contours of positive and negative scattering density, respectively. Significant negative scattering is located between V1 atoms, which can be attributed to Li in 8a tetrahedral sites.

Chapter 6: Electrochemical Performance of the $Li_{2+x}Ni_{2-2x}Cr_xV_2O_8$ Solid Solution

6.1. Introduction

Current cathode materials are typically the limiting component in LiBs due to their lower capacity compared to the anode. The choice of cathode material also usually determines the operating voltage, and thus the overall energy density of full cells. The two main approaches to increase energy density are therefore 1) to use high voltage materials e.g. $Li_2NiMn_3O_8$ with an operating voltage and theoretical capacity of 4.7 V vs. Li/Li^+ and 147 mAh g^{-1}, respectively; or 2) increase the amount of Li-ions that can be extracted during charge, thereby increasing capacity e.g. Li-rich cathode materials, which can have specific capacities > 250 mAh g^{-1}.[1], [2]

As previously discussed in Section 2.4.5, the inverse spinels, $LiMVO_4$ (M = Mn Co and/or Ni) have also been investigated as potential cathode materials due to their relatively high operating voltages of between 3.8 to 4.8 V *vs.* Li/Li^+ and theoretical capacities of ca. 148 mAh g^{-1}, depending on the transition metal.[3], [4] However, the limited discharge capacities (between 40 to 90 mAh g^{-1}) and significant capacity fade observed has meant that less focus has been given to materials with the inverse spinel structure.[5] Instead, focus has shifted to materials with greatly increased capacities such as Li-rich disordered rocksalts, with a Li to transition metal ratio greater than one.[6]

More recently, there has been renewed interest in inverse spinel vanadates as potential anode materials due to the possibility of a multivalent $V^{5+/3+}$ redox process. This would enable theoretical capacities greater than 200 mAh g^{-1} at operating voltages between 1 to 0.8 V, offering an enticing alternative to the normal spinel $Li_4Ti_5O_{12}$ (theoretical capacity = 175 mAh g^{-1} and operating voltage 1.5 V *vs.* Li/Li^+). Examples of inverse spinels which have previously been investigated as anode materials include $LiNiVO_4$, $LiMgVO_4$ and $LiZnVO_4$.[7], [8] The choice of M^{2+} transition metal appear to have a significant influence on initial discharge capacities as well as capacity retention and cycle life. For instance, $LiNiVO_4$ and $LiZnVO_4$ have initial discharge capacities of between 850 to 1110 mAh g^{-1} and 1008 mAh g^{-1}, respectively.[5], [8] Despite the high initial capacities observed, these materials typically suffer from huge capacity fade (> 50 %) during subsequent cycles. On the other hand, $LiMgVO_4$

displays a lower initial discharge capacity of 581 mAh g^{-1}, but with a capacity retention of 91 % after 30 cycles. These materials also suffer low initial coulombic efficiencies, with LiMgVO$_4$ displaying a charge capacity of *ca.* 202 mAh g^{-1}, corresponding to a coulombic efficiency of 35 %.[8] The observed differences in cycling behaviour of these materials have been attributed to different reaction mechanisms (*e.g.* intercalation or conversion-like mechanisms), as previously discussed in Chapter 2, Section 2.2.1.

In this chapter, the compositions Li$_{2+x}$Ni$_{2-2x}$Cr$_x$V$_2$O$_8$ (0 ≤ x ≤ 1) were investigated using electrochemical cycling as potential cathode and anode materials. Particular focus was made on studying how the electrochemical properties vary with increasing Li/Cr content. XANES was then used to investigate the in-situ cycling performance the of x = 0.5 and x = 0.75 compositions as cathode materials. These compositions were chosen because they displayed the best electrochemical behaviour during initial cell testing.

6.2. Experimental

The inverse spinel series $Li_{2+x}Ni_{2-2x}Cr_xV_2O_8$ (x = 0, 0.25, 0.5 0.75 and 1) were investigated as both cathode and anode materials through galvanostatic cycling experiments. All studied compositions were synthesised at 500 °C for 24 h *via* the same citric acid sol-gel route reported in Chapter 4.

6.2.1. Electrochemical Measurements

Galvanostatic cycling experiments were performed in Swagelok type cells on a Biologic VSP potentiostat. For both cathode (positive) and anode (negative) electrode tests, 10 mm diameter pellets of approximately 20 mg of electrode material were pressed outside the glovebox and dried for *ca.* 12 h in a vacuum oven at 80 °C. The electrode mixture consisted of 75 wt% active material, 15 wt% carbon black, and 10 wt% polyvinylidene fluoride (PVDF). Half cells were then fabricated in an Ar filled glovebox using the pellets of electrode material, a Whatman glass microfibre separator, and a 10 mm diameter lithium metal disk (Sigma-Aldrich, 99 %) pressed on a stainless steel plate as the counter electrode. The electrolyte solution consisted of 1 M $LiPF_6$ dissolved in ethylene carbonate (EC) and dimethyl carbonate (DMC) 1:1 v/v (Sigma-Aldrich, battery grade). A C-rate of C/10 was used for all experiments with a voltage range of 3 to 4.9 V for cathode experiments and 2.5 to 0.02 V for anode experiments. The theoretical capacity was calculated using Equation 6.1:

$$Q_{Theoretical} = \frac{nF}{M_W \times 3.6} \qquad \text{(Equation 6.1)}$$

Where *n* is the number of electrons transferred during cycling per unit formula, *F* is the Faraday constant (9.6485 x 10^4 C mol^{-1}), M_w is the molecular mass of electrode material and 3.6 is the factor required to convert from coulomb (CA g^{-1}) to mAh g^{-1}. The number of electrons transferred were calculated using Equations 6.2 and 6.3 and the theoretical capacities are summarised in Table 6.1.

(Li$^+$ extraction) $Li_3Cr^{3+}V_2O_8 \rightarrow Cr^{6+}V_2O_8 + 3Li^+ + 3e^-$ (Equation 6.2)

(Li$^+$ insertion) $Li_3CrV^{5+}{}_2O_8 + 4e^- + 4Li^+ \rightarrow Li_7CrV^{3+}{}_2O_8$ (Equation 6.3)
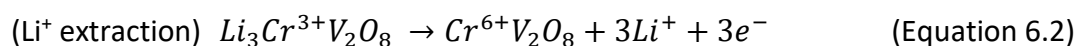
Table 6.1. Theoretical capacities for $Li_{2+x}Ni_{2-2x}Cr_xV_2O_8$ as cathode and anode materials, calculated assuming a three (cathode) and four (anode) electron transfer using Equations 6.1, 6.3 and 6.4.

Composition	Theoretical Capacity (mAh g^{-1})	
($Li_{2+x}Ni_{2-2x}Cr_xV_2O_8$)	Cathode	Anode
0	148	297
0.25	174	309
0.5	202	323
0.75	232	338
1	266	354

6.2.3. In-situ Cycling XANES

In-situ XANES data were collected during electrochemical cycling on the B18 beamline at the Diamond Light Source synchrotron facility (Harwell Science & Innovation Campus, Oxfordshire, UK), for V, Cr, and Ni *K*-edges of $Li_{2.75}Ni_{0.5}Cr_{0.75}V_2O_8$ and $Li_{2.5}NiCr_{0.5}V_2O_8$ as cathode materials using a multichannel potentiostat (3 to 4.9 V). Powder electrodes were prepared via mixing with carbon black (1:1 wt%) and cycled at a C-rate of C/20 for $Li_{2.75}Ni_{0.5}Cr_{0.75}V_2O_8$ and C/15 for $Li_{2.5}NiCr_{0.5}V_2O_8$. The C-rate was altered due to beamline time constraints. Electrochemical cells were again prepared in an Ar filled glovebox using a specially designed cell for synchrotron radiation, fitted with a Be window to allow X-rays to pass through (Figure 6.1).[9]
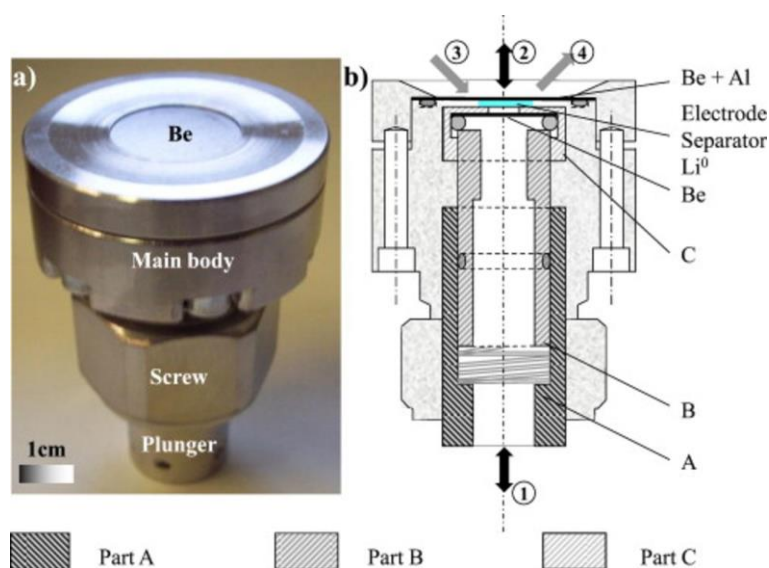
Figure 6.1. Electrochemical cell schematic for in-situ measurements.[9]

Further XANES spectra were collected to act as standard reference materials of known valence (VO_2, V_2O_5, NiO, $LiNiO_2$, $Ni(OCOCH_3)_2 \cdot 4H_2O$, Cr_2O_3, CrO_2 and K_2CrO_4), as well as powder samples of $Li_{2+x}Ni_{2-2x}Cr_xV_2O_8$ (x = 0, 0.25, 0.5, 0.75 and 1) to provide a baseline dataset for comparison. Samples were prepared by mixing with appropriate amounts of an inert, low molecular weight binder (cellulose) and pressed into 10 mm diameter pellets. All measurements were carried out in fluorescence mode, using a Si single crystal (111) monochromator. The collected XANES spectra were then normalised and calibrated against the metallic foil (V, Cr or Ni) within the Athena software package.[10] For fitting of Cr and V pre-edge regions, the program Fityk was used.[11] Due to the Covid-19 pandemic, all samples investigated were measured remotely, with on-site sample preparation and data collection performed by the instrument scientists Dr Maria Diaz-Lopez and Dr Veronica Celorrio.

6.3. Results and Discussion

6.3.1. Electrochemical Cycling of $Li_{2+x}Ni_{2-2x}Cr_xV_2O_8$ (x = 0, 0.25, 0.5, 0.75 and 1) as potential cathode materials

Electrochemical cycling data for the $Li_{2+x}Ni_{2-2x}Cr_xV_2O_8$ solid solution as potential cathode materials are presented in Figure 6.2. Galvanostatic cycling experiments for $Li_{2+x}Ni_{2-2x}Cr_xV_2O_8$ were carried out due to previous interest in x = 0 as a high voltage (4.8 V *vs.* Li^+/Li) cathode material (Chapter 2, Section 2.4.5). For x = 0, an initial charge (Li^+ extraction) capacity of *ca.* 80 mAh g^{-1} was obtained, with a voltage plateau at *ca.* 4.75 V due to a $Ni^{2+/3+}$ oxidation process. During discharge (Li^+ insertion), a plateau at *ca.* 4.7 V was observed, with a discharge capacity of *ca.* 23 mAh g^{-1}. This suggests only a limited amount of the Li-ions present can be reversibly extracted/inserted during cycling. These results are consistent with previous reports for x = 0, with initial charge capacities between 80 to 40 mAh g^{-1}, and discharge capacities between 30 to 20 mAh g^{-1}, depending on the synthesis method and electrochemical cell setup.[3], [5], [12] Capacities during the 2nd and 10th cycles were further reduced significantly to below 5 mAh g^{-1}, suggesting the material rapidly deteriorates after the 1st cycle. Previous research efforts have suggested this irreversible capacity loss during the first and subsequent cycles, observed here and in previous studies, is likely due to mixing of $Ni^{2+/3+}$ and V^{5+} cations on octahedral and tetrahedral sites, as well as side reactions such as electrolyte oxidation during cycling at high voltages.[3], [13]

For x = 0.25, 0.5, and 0.75, a similar pattern was observed, with 1st cycle charge capacities between 100 to *ca.* 80 mAh g^{-1}. However, two plateaus were observed during charge, one between 4.5 V to 4.6 V, and one at *ca.* 4.8 V. The first voltage plateau shifts to lower voltages with increasing x, although the explanation for this is currently not understood. The different voltage plateaus are likely due to Cr^{3+}/Ni^{2+} and/or electrolyte oxidation during charge. These processes appear to be largely irreversible on discharge, with limited capacities of between 23 to 9 mAh g^{-1}. The discharge capacity seen is the largest for x = 0.75, which displays a capacity of ca. 23 mAh g^{-1} between 3.7 and 3 V. A similar pattern is observed in the discharge curves for x = 0.5 and 0.25 between 3.5 and 3 V, with reduced capacities of ca. 11 and 9 mAh g^{-1}, respectively. This behaviour may be due to side reactions and/or an oxygen (O^{2-}/O_2^{2-}) redox process, which has been suggested in the inverse spinel $LiNi_{1/3}Co_{1/3}Mn_{1/3}VO_4$ and to a greater extent in Li-rich layered oxide cathode materials.[1], [12] A computational study of electronic structure changes for $LiNiVO_4$ and $LiCoVO_4$ during discharge (lithiation) also suggested that while reduction of the transition metal is the dominant redox process, oxygen ions can also be reduced.[14] The results herein may suggest this is more evident in Cr-containing inverse spinels.

During subsequent cycles, the lower voltage plateau present on charge is absent and capacities are likewise significantly reduced, again suggesting that these materials rapidly deteriorate after the initial charge. The additional charge capacity observed at high voltages (between 4.8 V to 4.9 V) for x = 0.25 and 0.75 are most likely due to side reactions, such as reactions between the electrolyte and stainless steel Swagelok cells.[15] For x = 1, a small slope between 4.4 V and 4.5 V is observed, with charge/discharge capacities of *ca.* 10 mAh g^{-1} and 4 mAh g^{-1}. This indicates x = 1 is not redox active in the studied voltage window and the small capacities observed are likely due to electrolyte oxidation.
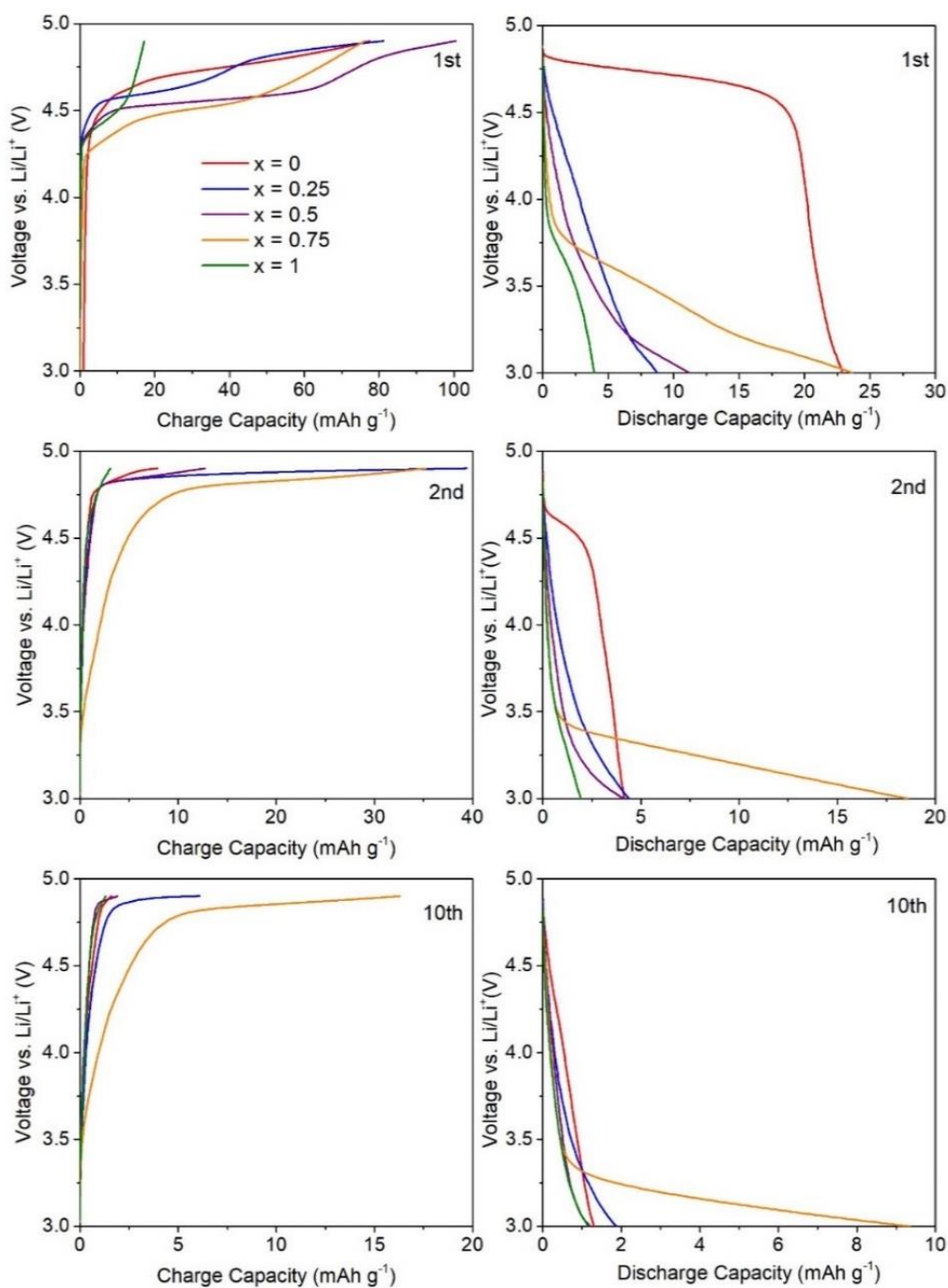
Figure 6.2. Electrochemical data for $Li_{2+x}Ni_{2-2x}Cr_xV_2O_8$ (x = 0, 0.25, 0.5, 0.75 and 1) cycled as a cathode between 3 V to 4.9 V at a C-rate of C/10.

6.3.1.1. In-situ XANES Analysis of Li$_{2+x}$Ni$_{2-2x}$Cr$_x$V$_2$O$_8$ (x = 0.75 and 0.5) as Potential Cathode Materials

To investigate the poor cycling performance of Li$_{2+x}$Ni$_{2-2x}$Cr$_x$V$_2$O$_8$ as cathode materials, in-situ transition metal *K*-edge XANES for compositions *x* = 0.75 and 0.5 were collected during initial cycling. Figure 6.3 displays Cr *K*-edge normalised XANES spectra for powder samples of *x* = 0.25, 0.5, 0.75 and 1 as well as for the reference materials Cr$_2$O$_3$, CrO$_2$ and K$_2$CrO$_4$. For many metal absorption edges, the edge position (E$_{\frac{1}{2}}$, here determined as the energy at one half the edge step) follows a linear trend with oxidation state; however, Farges reported variations in the absorption edge position of up to a 2.6 eV for several Cr^{3+} compounds in octahedral coordination, which brings into question the reliability of using the absorption edge position as a measure of oxidation state.[16] Farges suggested that the centroid position and area of the lower energy pre-edge features are a better indicator of Cr oxidation state than the edge position.[16] A similar trend to that found in previous reports is observed in Figure 6.3, with the absorption edge positions of the Li$_{2+x}$Ni$_{2-2x}$Cr$_x$V$_2$O$_8$ series differing by up to 1.5 eV. The spectra of all compositions are shifted to higher energies compared to the Cr^{3+} reference compound, Cr$_2$O$_3$. Despite these differences, the lower energy pre-edge feature at *ca.* 5990 eV is almost identical in Li$_{2+x}$Ni$_{2-2x}$Cr$_x$V$_2$O$_8$ compositions and Cr$_2$O$_3$.
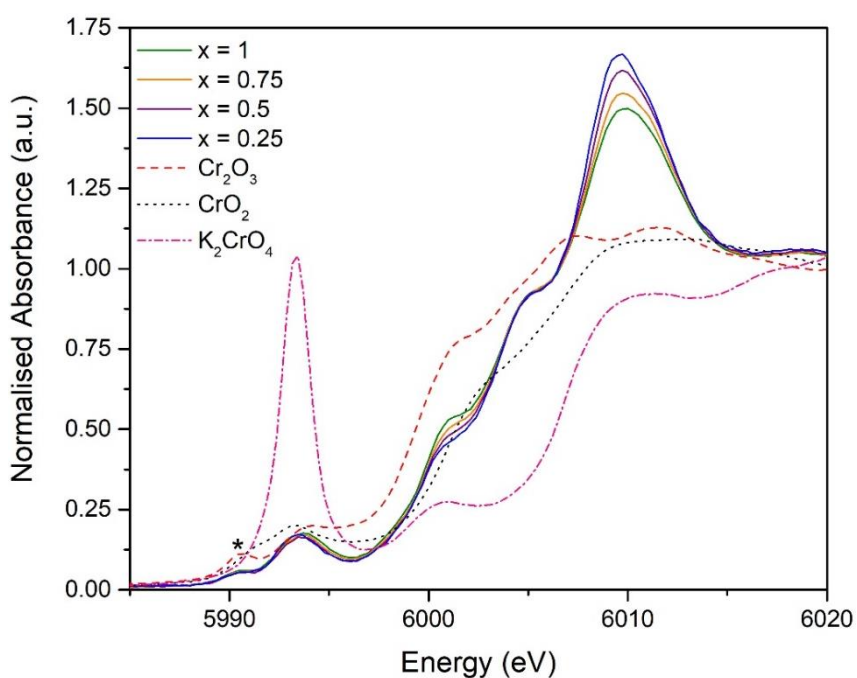
Figure 6.3. Normalised Cr *k*-edge XANES spectra for powder samples of Li$_{2+x}$Ni$_{2-2x}$Cr$_x$V$_2$O$_8$ (*x* = 0.25, 0.5, 0.75, and 1) and the standard reference materials Cr$_2$O$_3$ (Cr^{3+}), CrO$_2$ (Cr^{4+}) and K$_2$CrO$_4$ (Cr^{6+}). * = first pre-edge feature.

The pre-edge features were fitted using multiple pseudo-Voigt functions to calculate the centroid position and integrated area, examples of which are shown in Figure 6.4. It should be noted that the fitting parameters were not intended to be related to any physical phenomenon. For lower valence Cr species, the higher energy pre-edge feature was excluded as the pre-edge information was inconsistent with its inclusion, *i.e.* the centroid position for Cr^{3+} species shifted beyond CrO_2. Three pseudo-Voigts were required to accurately describe the intense pre-edge feature observed in the spectrum of K_2CrO_4, with the centroid position and area calculated using a weighted average of the different pseudo-Voigts. Table 6.2 summarises the pre-edge information for all measured materials. The centroid positions of the standard reference materials Cr_2O_3, CrO_2 and K_2CrO_4 shift to higher energies as the oxidation state of Cr shifts from Cr^{3+} to Cr^{6+}, which is consistent with trends observed by Farges.[16] The area of the pre-edge peaks are related to the coordination of Cr, with K_2CrO_4 displaying the largest area due to Cr^{6+} being present in a tetrahedral coordination. Cr_2O_3 and CrO_2 are both in an octahedral environment and exhibit similar pre-edge peak areas. The centroid position and area for powder samples of $x = 0.25$, 0.5, 0.75 and 1 are comparable to Cr_2O_3, indicating Cr has a 3+ oxidation state in an octahedral coordination, as expected in the inverse spinel structure.
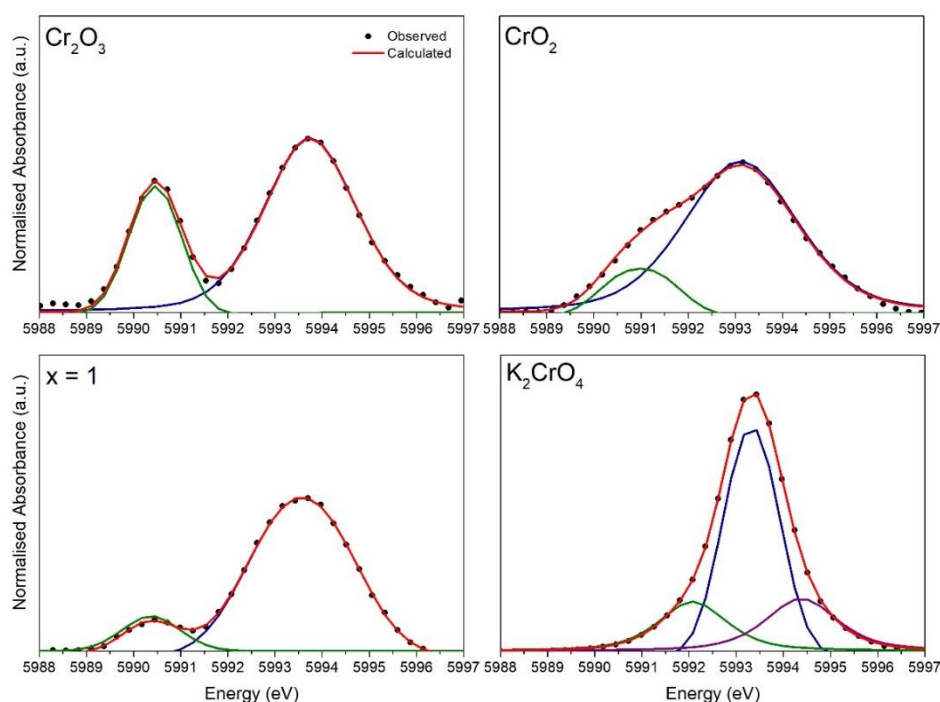
Figure 6.4. Example fits of the Cr pre-edge features for the standard reference materials Cr_2O_3, CrO_2, K_2CrO_4 and $Li_{2+x}Ni_{2-2x}Cr_xV_2O_8$, $x = 1$ using multiple pseudo-Voigt peak shape functions in the Fityk software. The background of the pre-edge was manually defined and subtracted before fitting.

Table 6.2. Pre-edge information of Cr k-edge XANES spectra for $Li_{2+x}Ni_{2-2x}Cr_xV_2O_8$ (x = 0.25, 0.5, 0.75, and 1) and the standard reference materials Cr_2O_3, CrO_2 and K_2CrO_4, calculated from fitting the first pre-edge feature.

Sample	Centroid Position (eV)	Total Area
x = 1	5990.36	0.038
x = 0.75	5990.42	0.024
x = 0.5	5990.32	0.022
x = 0.25	5990.26	0.011
Cr_2O_3	5990.45	0.055
CrO_2	5990.98	0.035
K_2CrO_4	5993.31	2.002

V K-edge normalised XANES spectra for powder samples of x = 0, 0.25, 0.5, 0.75 and 1 as well as the spectra of the reference materials VO_2 and V_2O_5 are shown in Figure 6.5. Similar to Cr K-edge XANES spectra, the complicated absorption edge position means it is not a reliable measure of oxidation state, as seen by the shift in edge position at $E_{1/2}$ with x in the $Li_{2+x}Ni_{2-2x}Cr_xV_2O_8$ series. As such, the V K-edge XANES spectra were analysed by fitting the pre-edge feature with three pseudo-Voigt functions, in a similar manner to the Cr XANES spectra discussed above. The V K-edge XANES spectra presented here are additionally complicated by the varying coordination environments between the reference compounds and the $Li_{2+x}Ni_{2-2x}Cr_xV_2O_8$ series *e.g.* V^{5+} in V_2O_5 is in a square pyramidal coordination, while the expected coordination in inverse spinels is tetrahedral. As a result, there is little overlap of the pre-edge feature centroid positions of the V reference materials and $Li_{2+x}Ni_{2-2x}Cr_xV_2O_8$ compositions. Instead, the centroid position, and relative and total areas (normalised to V_2O_5) were used to compare the results herein to previous reports for V K-edge XANES spectra of differing oxidation states and environments.[17], [18]

The pre-edge information from the resulting fits are summarised in Table 6.3. The pre-edge peak area of $Li_{2+x}Ni_{2-2x}Cr_xV_2O_8$ compositions are of the same magnitude as the V_2O_5 standard reference material, with the centroid position shifted to slightly lower energies, *ca.* 1 eV. The VO_2 standard reference has a slightly lower relative area compared to V_2O_5

however, the overlap in the centroid position between VO_2 and V_2O_5 may indicate the VO_2 standard used is a mixture of V^{4+}/V^{5+} oxidation states.[17] When compared to previous analysis of differing V containing species by Chaurand *et al.* – who also observed a *ca.* 1 eV shift to lower energies for V^{5+} species in tetrahedral coordination compared to V_2O_5 – this suggested V in $Li_{2+x}Ni_{2-2x}Cr_xV_2O_8$ compositions is present as V^{5+} in a tetrahedral coordination.[17] These results are also consistent with previously reported V *K*-edge XANES spectra for *x* = 0.[7], [19] This is in good agreement with the expected coordination within the inverse spinel structure.
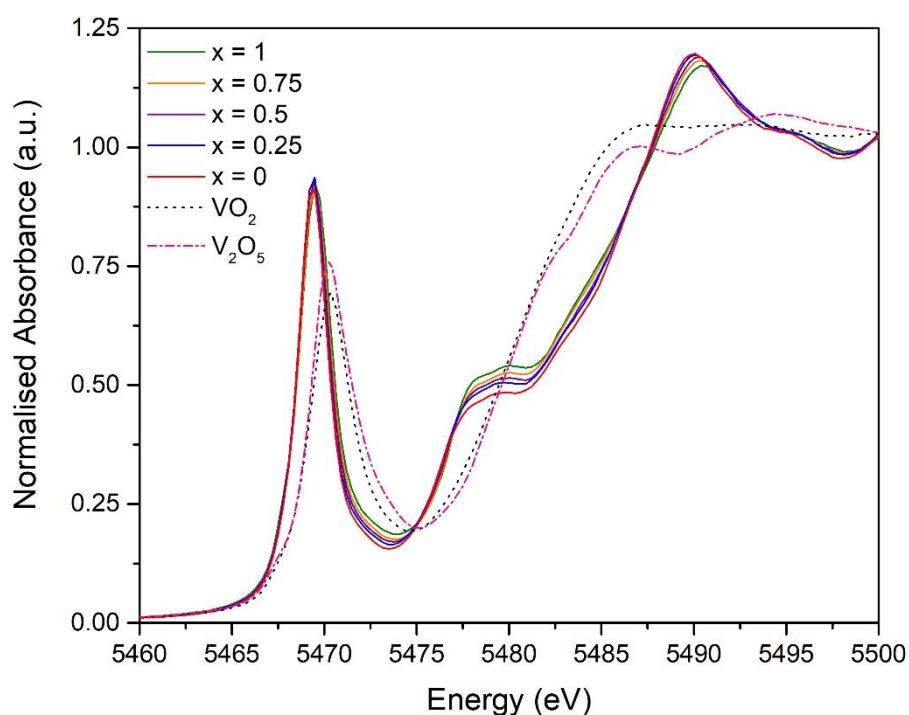
Figure 6.5. Normalised V *k*-edge XANES spectra for $Li_{2+x}Ni_{2-2x}Cr_xV_2O_8$ (*x* = 0, 0.25, 0.5, 0.75, and 1) and the standard reference materials, VO_2 and V_2O_5.

Table 6.3. Pre-edge information of V *k*-edge XANES spectra for $Li_{2+x}Ni_{2-2x}Cr_xV_2O_8$ (*x* = 0.25, 0.5, 0.75, and 1) and the standard reference materials, VO_2 and V_2O_5. *Note that it appears that some of the VO_2 standard has oxidised from V^{4+} to V^{5+} as observed by the intense pre-edge feature.

Sample	Oxidation State	Centroid Position (eV)	Relative area	Total Area
x = 1	5	5469.61	0.99	1.964
x = 0.75	5	5469.58	0.98	1.937
x = 0.5	5	5469.52	0.96	1.892
x = 0.25	5	5469.48	0.95	1.869
x = 0	5	5469.46	0.94	1.846
VO_2	4/5*	5470.37	0.87	1.711

V_2O_5	5	5470.51	1	1.968

Ni K-edge normalised XANES spectra for $Li_{2+x}Ni_{2-2x}Cr_xV_2O_8$ $x = 0.5$ and 0.75, as well as the reference compounds NiO, $LiNiO_2$ and $Ni(OCOCH_3)_2 \cdot 4H_2O$ are presented in Figure 6.6. Ni K-edge XANES spectra for $x = 0$ and 0.25 were not collected due to technical difficulties and time constraints during the experiment. The absorption edge positions for $x = 0.5$ and 0.75 are similar, in contrast to those of the Cr and V K-edge XANES spectra. Nevertheless, the edge position is also complicated due to the differences in coordination environments compared to the Ni reference compounds. For instance, NiO (Ni^{2+}) and $LiNiO_2$ (Ni^{3+}) are both in octahedral coordination, with a shift to higher energy in the edge position observed for $LiNiO_2$; however, for $Ni(OCOCH_3)_2 \cdot 4H_2O$ (Ni^{2+}) the edge position is shifted beyond that of $LiNiO_2$, possibly because Ni^{2+} is in a distorted octahedral coordination.[20] The edge position of $x = 0$ and 0.25 is most similar to $Ni(OCOCH_3)_2 \cdot 4H_2O$, indicating a Ni^{2+} oxidation state, and likely a distorted octahedral environment, *i.e.* likely located on the 16c site alongside Li/Cr due to the shared occupancy in these inverse spinels. These results are also consistent with previous Ni K-edge XANES spectra for $x = 0$.[7], [19] Due to similarities in the XANES spectra between the $Li_{2+x}Ni_{2-2x}Cr_xV_2O_8$ compositions, it can be inferred that x = 0.25 and x = 0 would also be Ni^{2+} in an octahedral coordination.
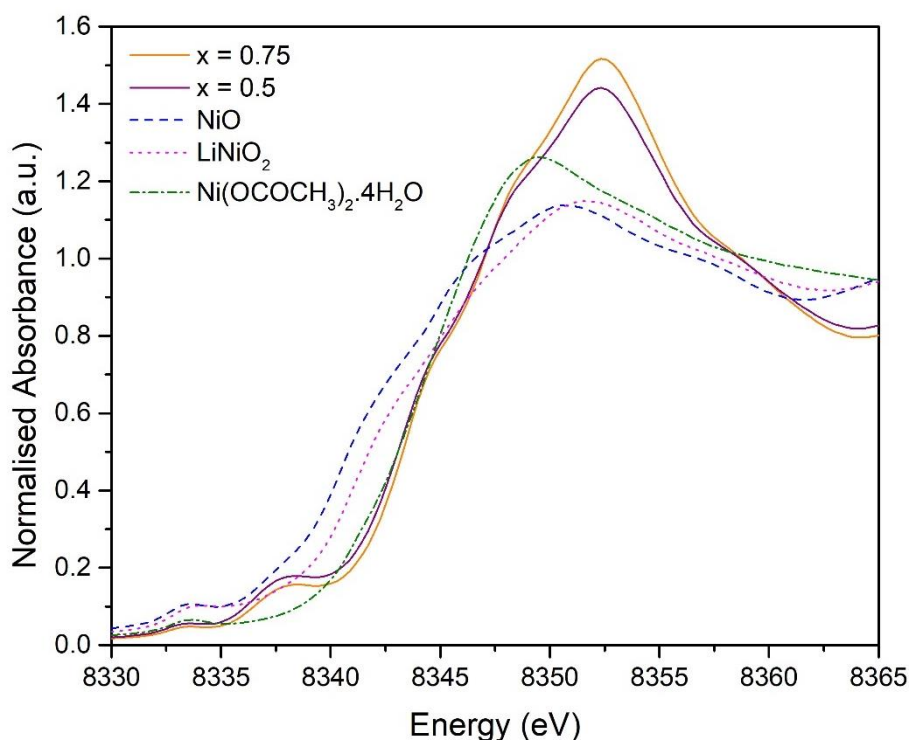
Figure 6.6. Normalised Ni *k*-edge XANES spectra for $Li_{2+x}Ni_{2-2x}Cr_xV_2O_8$ (*x* = 0.5 and 0.75) and the standard reference materials, NiO, LiNiO₂ and Ni(OCOCH₃)₂·4H₂O.

In-situ electrochemical cycling data for *x* = 0.75 and 0.5 during initial cycles are presented in Figure 6.7. For *x* = 0.75, only the first charge data is available due to the cell failing during discharge. Nevertheless, both compositions have comparable voltage profiles to those in Figure 6.2, indicating the in-situ electrochemical cell is an accurate reflection of the electrochemical mechanisms that occur during standard operation. Cr, V and Ni *K*-edge normalised XANES spectra collected during in-situ cycling are displayed in Figures 6.8, 6.10 and 6.11.

For both compositions the largest change is observed within Cr *K*-edge XANES spectra during the first charge. From 4.5 to 4.9 V, a systematic shift in edge position to higher energies is observed and the higher energy pre-edge peak at *ca.* 5993 eV increases in intensity with increasing voltage. The lower energy pre-edge peak at *ca.* 5990 eV is concealed at higher voltages, as the higher energy pre-edge peak at *ca.* 5993 eV becomes the dominant feature. For *x* = 0.5 during the subsequent discharge and second charge, only a very small change is observed in the pre-edge intensity and edge position. Figure 6.10 summaries the changes in the pre-edge centroid position and area with voltage. From 3 to 4.5 V, the pre-edge

information indicates Cr largely remains Cr^{3+}, but at voltages higher than 4.5 V the pre-edge regions begins to resemble a Cr^{6+} species. The increase in the pre-edge peak area is largest for x = 0.5, possibly due to the different reaction kinetics as a slower C-rate of C/20 was used, compared to C/15 for x = 0.75. These changes in the pre-edge features, alongside the shift to higher energies in the edge position suggests that, on charge, Cr^{3+} is oxidised to Cr^{6+} as Li-ions are extracted and Cr^{6+} ions shift from octahedral to tetrahedral sites in the inverse spinel structure. This process is largely irreversible, likely because the majority of Cr^{6+} ions are unable to be reduced back to Cr^{3+}, and explains the limited capacities obtained on discharge. A similar $Cr^{3+/6+}$ process has been reported for the normal spinel series, $LiMn_{2-x}Cr_xO_4$.[21] The transition of Cr^{6+} ions from octahedral 16c to neighbouring tetrahedral 8a sites may also impede the Li-ion (16c-8a-16c) conduction pathway discussed in Chapter 5.
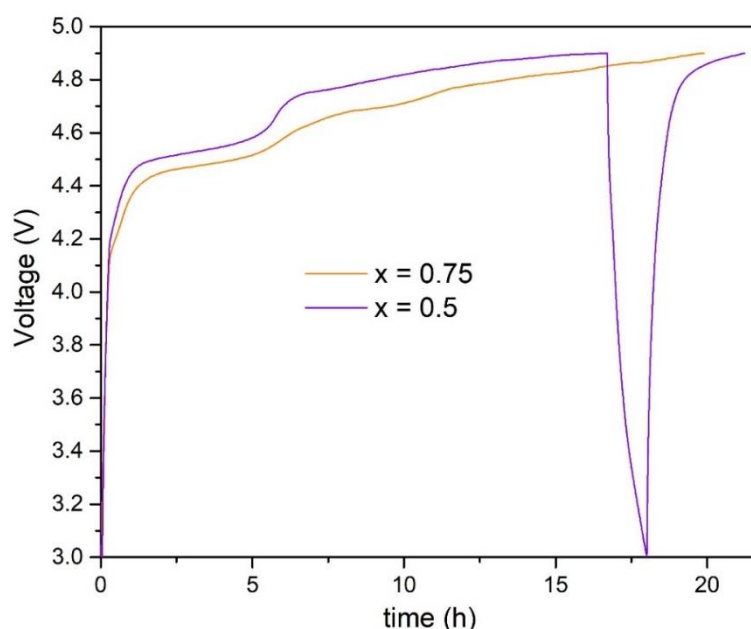
Figure 6.7. In-situ electrochemical data for x = 0.75 and x = 0.5, cycled between 3 V to 4.9 V at a C-rate of C/20 and C/15 respectively.
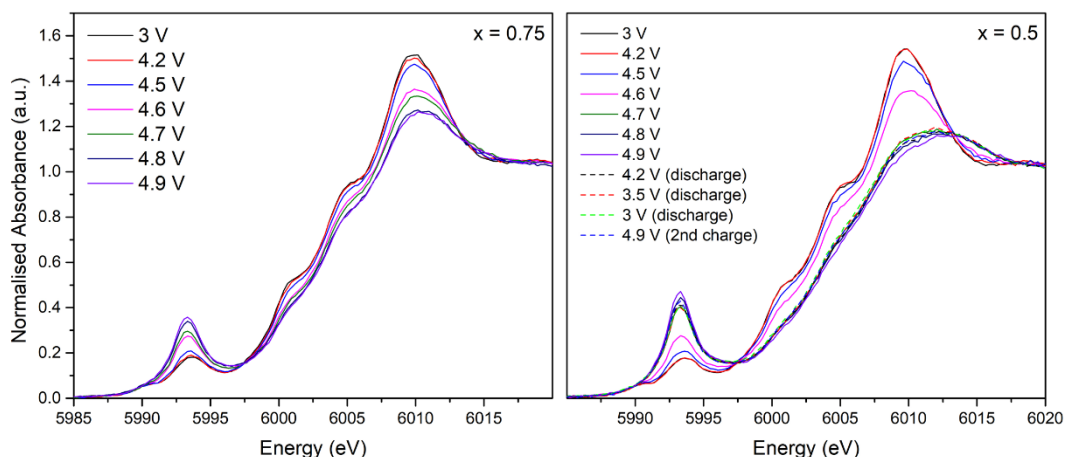
Figure 6.8. Normalised Cr *k*-edge XANES spectra collected during in-situ cycling for *x* = 0.75 and *x* = 0.5.
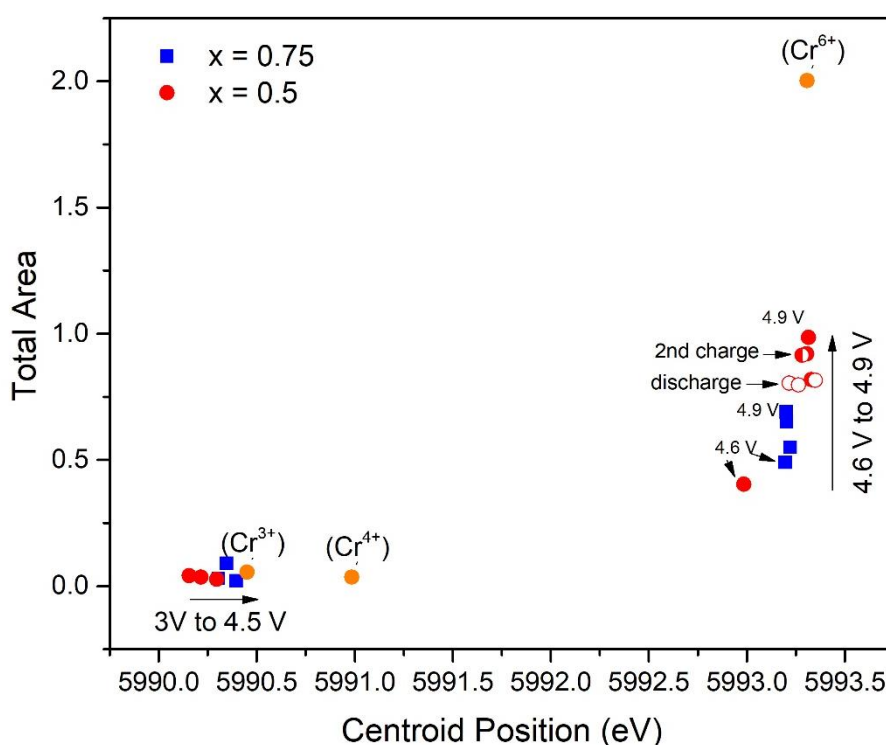
Figure 6.9. Summary of pre-edge information for Cr *k*-edge XANES spectra collected during in-situ cycling. The data highlights that for both *x* = 0.75 and 0.5, Cr pre-edge regions begin to resemble the Cr^{6+} standard with increasing voltage. Data for *x* = 0.75 is shown in blue squares and *x* = 0.5 data is shown red circles, with discharge and 2nd charge data in open and half-closed circles, respectively. Data for Cr standard reference materials are shown in orange circles.

In the V *K*-edge XANES spectra, a small decrease in the pre-edge peak is observed on charge; however, no systematic trend in the edge position is observed. This may indicate a small percentage of V^{5+} ions in tetrahedral sites shifting into octahedral sites, which has previously been suggested to occur in similar inverse spinel compounds.[7], [13] The Ni *K*-

edge XANES spectra appear relatively unchanged during cycling with only a very small decrease in the peak after the absorption edge, indicating the majority of Ni remains in its 2+ oxidation state. Similar results have been obtained by Kitajou *et al.* for $LiNi_{1/3}Co_{1/3}Mn_{1/3}VO_4$, who instead suggested the higher voltage plateau may be due to an oxygen (O^{2-}/O_2^{2-}) redox process, as discussed above.[12] As a result of these findings, the majority of capacity loss observed in these materials after the first charge appears to be due to the oxidation of Cr^{3+} to Cr^{6+}. Subsequently, Cr^{6+} transitions from octahedral to neighbouring tetrahedral sites, thereby blocking Li-ion diffusion through these sites.
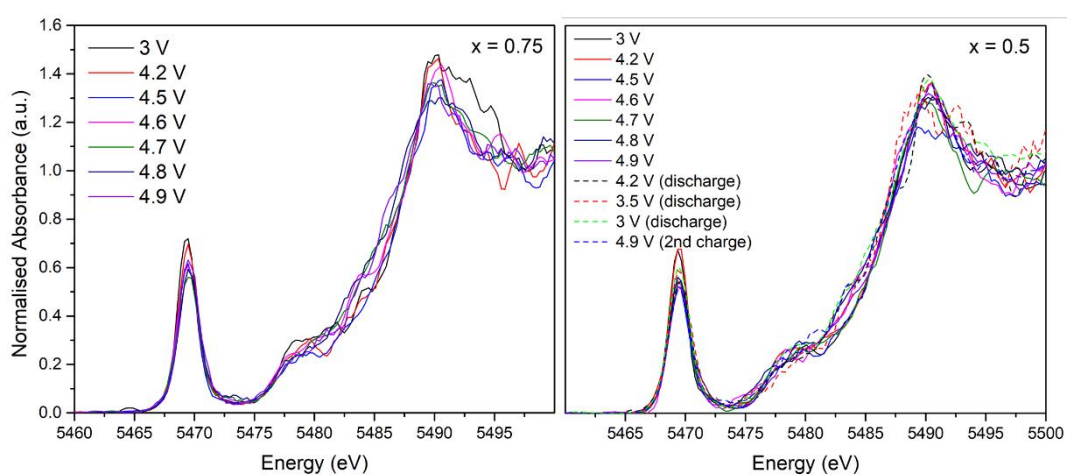
Figure 6.10. Normalised V *k*-edge XANES spectra collected during in-situ cycling for *x* = 0.75 and *x* = 0.5.
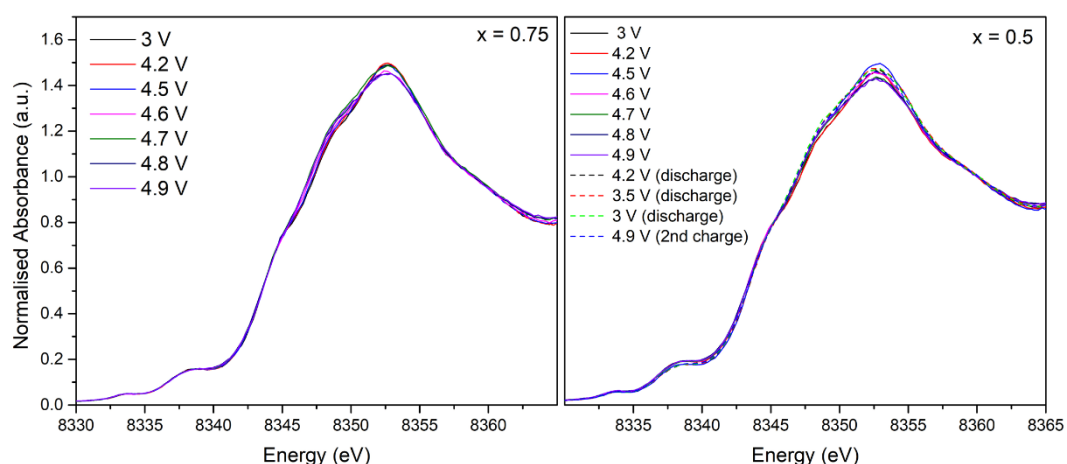
Figure 6.11. Normalised Ni *k*-edge XANES spectra collected during in-situ cycling for *x* = 0.75 and *x* = 0.5.

6.3.2. Electrochemical Cycling of Li$_{2+x}$Ni$_{2-2x}$Cr$_x$V$_2$O$_8$ (x = 0, 0.25, 0.5, 0.75 and 1) as Potential Anode Materials

Following the investigation of the inverse spinel series Li$_{2+x}$Ni$_{2-2x}$Cr$_x$V$_2$O$_8$ as potential cathode materials, the question arose as to whether the series would function more effectively as anode materials. This was driven by previous studies into LiMVO$_4$ (M = Ni, Cu, Zn and Mg), where the possibility of a two-electron V^{5+}/V^{3+} redox process would enable greater capacities than other spinels such as Li$_4$Ti$_5$O$_{12}$.[7], [8], [22]

Figures 6.12a to 6.16a show discharge and charge curves for *x* = 0, 0.25, 0.5, 0.75 and 1 between a voltage range of 2.5 to 0.02 V. For x = 0, on the 1st discharge the voltage rapidly decreases to *ca.* 0.9 V where it then displays two regions, the first with a decrease between *ca.* 0.9 to 0.6 V, and the second where the voltage more gradually decreases between *ca.* 0.6 to 0.5 V. After this, a sharp decrease is observed until 0.02 V. For *x* = 0.25, 0.5 and 0.75, a similar behaviour is observed, however, the second voltage region decreases more rapidly with increasing *x*. For *x* = 1, the voltage sharply decreases to 1 V and then gradually decreases to *ca.* 0.5 V. After this, the voltage swiftly drops to *ca.* 0.06 V, where it levels off to 0.02 V. The resulting 1st cycle discharge capacities are 968, 712, 721, 764, and 406 mAh g^{-1} for *x* = 0, 0.25, 0.5, 0.75 and 1, respectively. These values are all significantly higher than theoretical capacities calculated assuming a V$^{5+/3+}$ redox couple and suggests additional reduction processes are occurring during the 1st discharge, such as the reduction of transition metal cations to their metallic state. For *x* = 1, if the voltage plateau at 0.06 V is excluded, a discharge capacity of 355 mAh g^{-1} is obtained, in excellent agreement with its theoretical capacity of 354 mAh g^{-1}. This indicates the additional *ca.* 50 mAh g^{-1} of capacity obtained at low voltages may be due to further reduction processes. Further work should investigate the capacity retention and structural stability of these materials at differing voltage cut-offs.

The voltage curves on the subsequent charge differ significantly from discharge, with the slope for *x* = 0 occurring between *ca.* 1 to 1.5 V. As *x* increases, the voltage range of the charge slope decreases until between 0.6 to 1.1 V for *x* = 1. This indicates the operating voltage or average voltage decreases with increasing *x,* and is *ca.* 1.25, 1.2, 1.1, 1 and 0.8 V for *x* = 0, 0.25, 0.5, 0.75 and 1, respectively. The resulting 1st cycle charge capacity are 615, 417, 437, 450 and 165 mAh g^{-1} for *x* = 0, 0.25, 0.5, 0.75 and 1, respectively. This represents a

substantial irreversible capacity loss during charge, with Coulombic efficiencies of *ca.* 60 % for *x* = 0, 0.25, 0.5 and 0.75 and *ca.* 40 % for *x* = 1.

Capacity and Coulombic efficiency *vs.* cycle number are shown in Figures 6.12b to 6.16b. For *x* = 0, 0.25, and 0.5 charge/discharge capacities rapidly fade over the first five cycles before plateauing for the remaining cycles. For *x* = 0.75, the capacity rapidly fades during the first five cycles and after this, experiences a more gradual decline for the remaining cycles. *x* = 1 displays the greatest stability *vs.* cycle number, experiencing a relatively stable decline after the first cycle. Coulombic efficiencies *vs.* cycle number are also the highest for *x* = 1, indicating the discharge/charge processes are the most reversible for this composition. Capacity retention after 30 cycles increases with increasing *x, e.g.* for x = 0 a capacity retention of 14 % is obtained compared to 61 % for x = 1. This implies Li/Cr doping may help stabilise the crystal structure during cycling as anode materials.
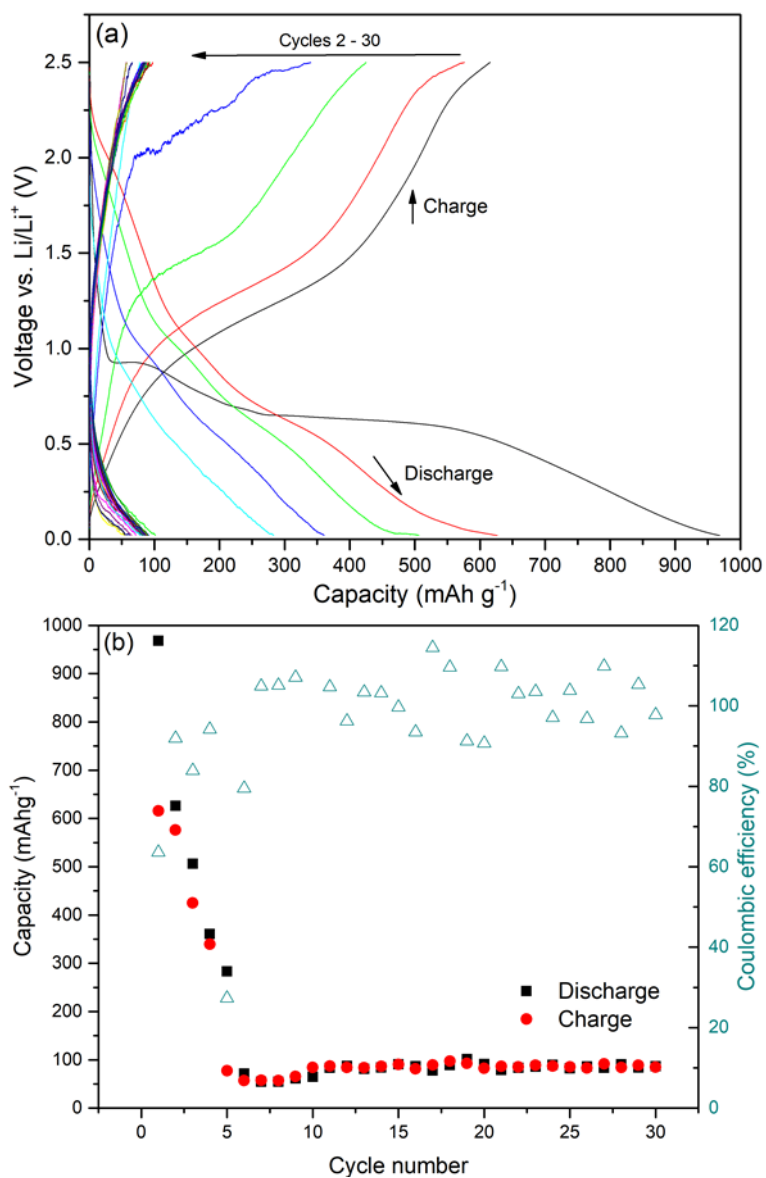
Figure 6.12. Electrochemical data for $Li_2Ni_2V_2O_8$ cycled as an anode between 2.5 to 0.02 V at a C-rate of C/10.
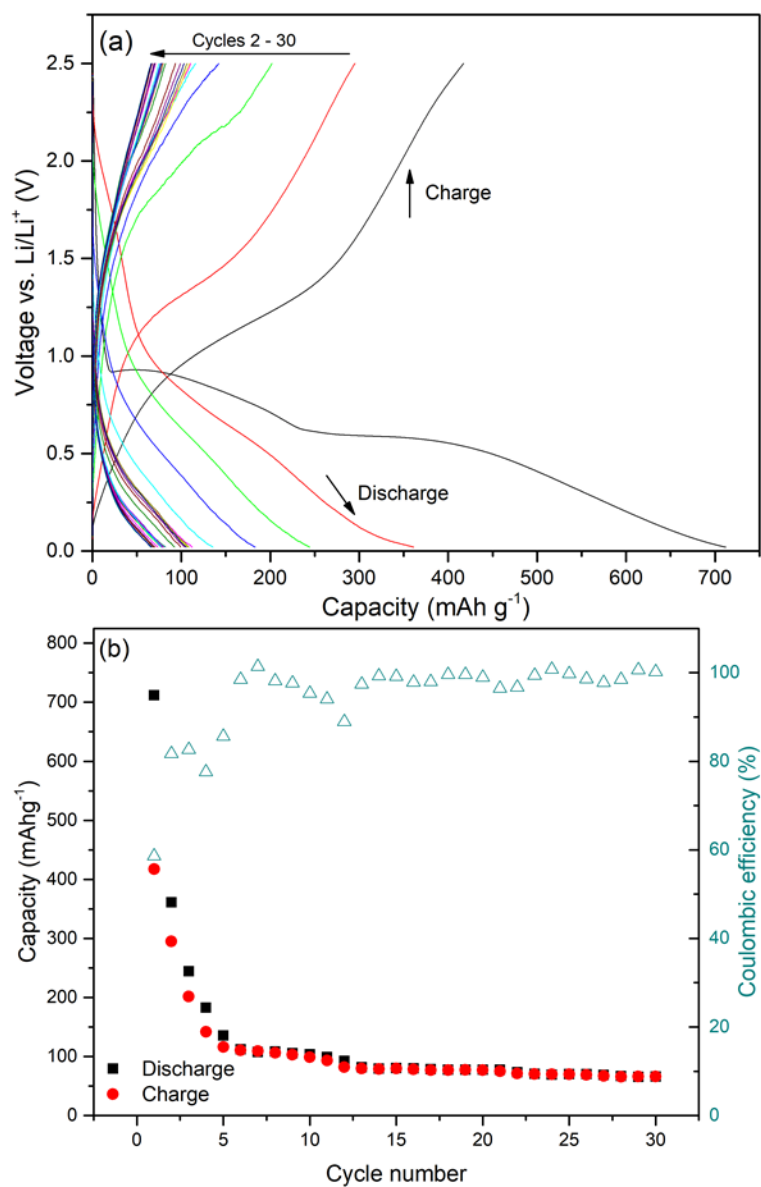
Figure 6.13. Electrochemical data for $Li_{2.25}Ni_{1.5}Cr_{0.25}V_2O_8$ cycled as an anode between 2.5 to 0.02 V at a C-rate of C/10.

181
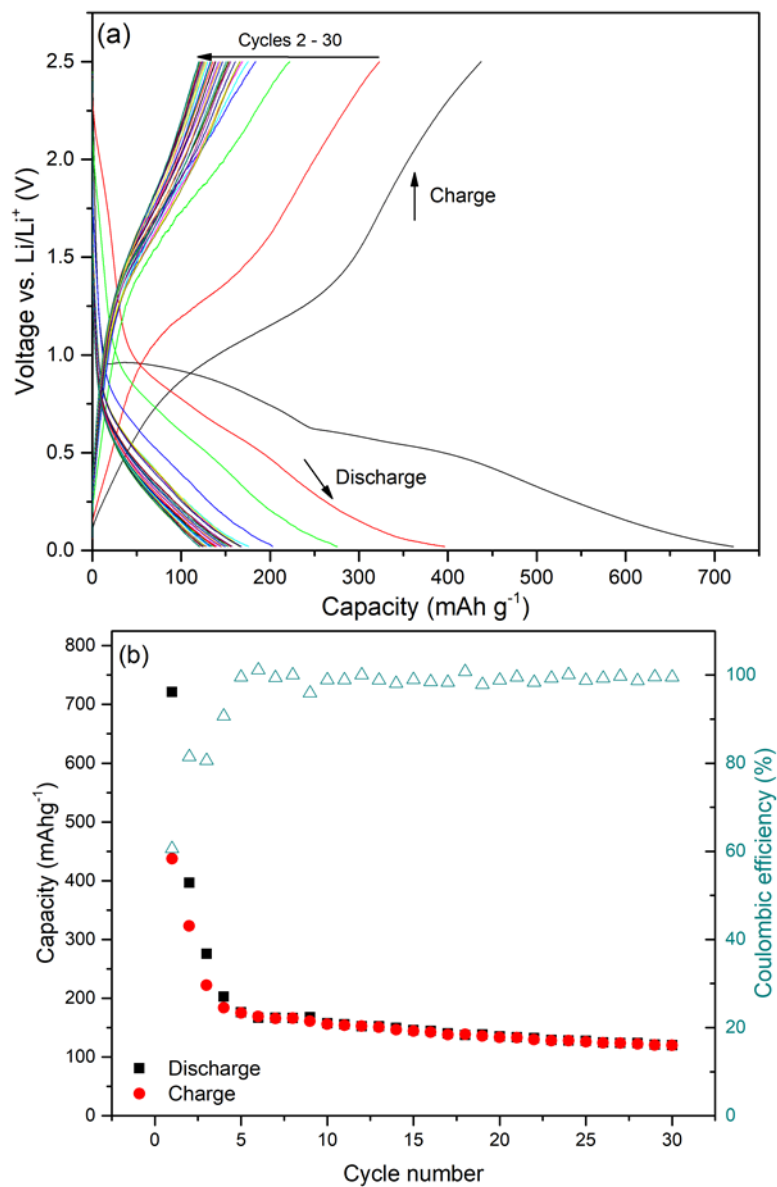
Figure 6.14. Electrochemical data for $Li_{2.5}NiCr_{0.5}V_2O_8$ cycled as an anode between 2.5 to 0.02 V at a C-rate of C/10.
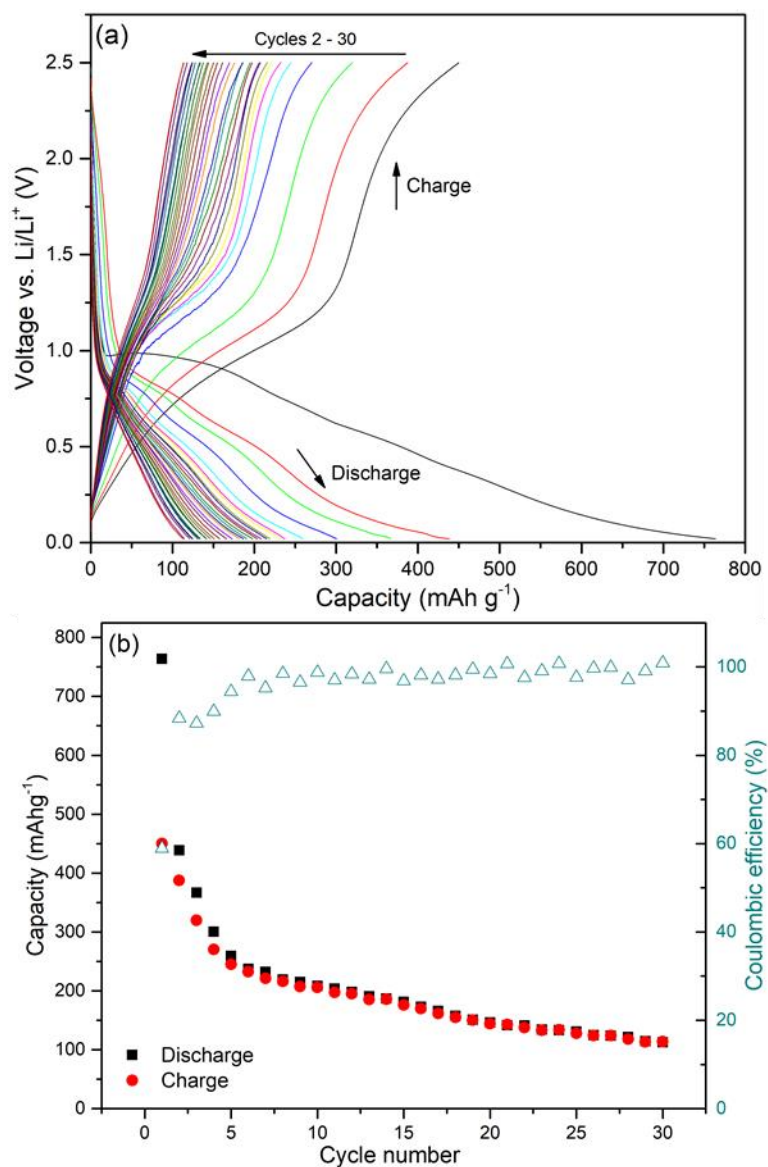
Figure 6.15. Electrochemical data for $Li_{2.75}Ni_{0.5}Cr_{0.75}V_2O_8$ cycled as an anode between 2.5 to 0.02 V at a C-rate of C/10.
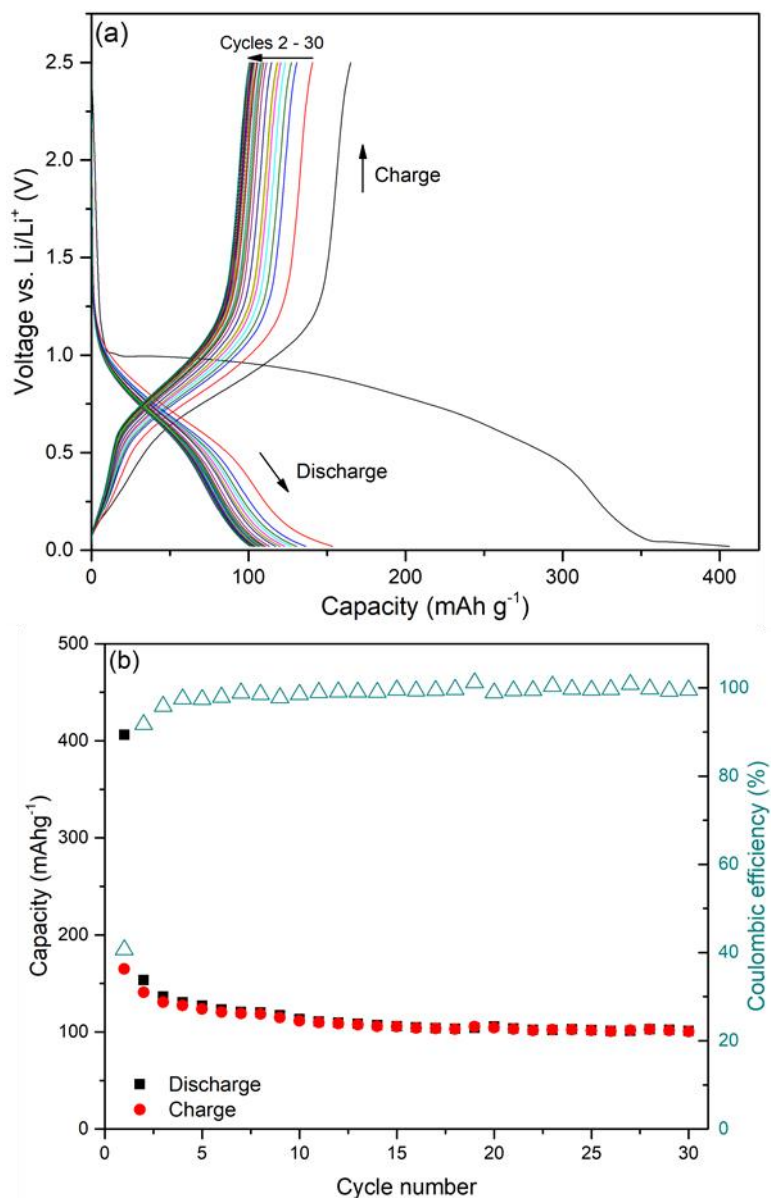
Figure 6.16. Electrochemical data for $Li_3CrV_2O_8$ cycled as an anode between 2.5 to 0.02 V at a C-rate of C/10.

In previous reports of $x = 0$ cycled as an anode material between 3 to 0.02 V, the 1st cycle discharge capacities obtained were between 850 to 1110 mAh g^{-1}, depending on the synthesis method.[5], [7] These results are comparable to the 968 mAh g^{-1} obtained herein, and likewise display poor capacity retention during cycling. Rossignol *et al.* investigated the charge/discharge mechanism of $x = 0$ during cycling using X-ray absorption spectroscopy (XAS) and suggested that during discharge, vanadium atoms are reduced and shift from tetrahedral sites to distorted octahedra, whilst nickel atoms are reduced close to their metallic state. During charge, XAS data revealed only vanadium atoms are oxidised, shifting back to a

tetrahedral environment.[7] XRD data also revealed $x = 0$ is amorphised during discharge, suggesting x = 0 behaves like a conversion anode material. Uyama *et al.* investigated the inverse spinel series LiMg$_{1-x}$Zn$_x$VO$_4$ (x = 0 to 1) as potential anode materials using ex-situ XRD (Chapter 2, Section 2.1.1).[8] Herein, ex-situ XRD revealed LiZnVO$_4$ behaves similarly to LiNiVO$_4$, where on discharge LiZnVO$_4$ is amorphised. Uyama *et al.* suggested LiZnVO$_4$ undergoes a two stage reaction mechanism during cycling. The first is an intercalation-type mechanism (Equation 6.4) in which V^{5+} ions are reduced to V^{4+} and shift from tetrahedral sites to empty octahedral sites and are subsequently reduced to V^{3+} as more Li-ions are inserted into the inverse spinel structure. As the reaction proceeds, a second conversion-like reaction occurs and the spinel structure is destabilised, forming a rocksalt type phase (Equation 6.5).[8] A similar mechanism has also been observed in the normal spinel, LiMnTiO$_4$.[23] The formation of the rocksalt phase leads to additional lattice strain due to differences between the rocksalt and spinel structures, as well as significant volume expansion as more Li-ions are inserted on discharge.[8], [23] These changes may explain the degradation in capacity retention *vs.* cycle number due to factors such as the active material isolating from the conducting carbon. In contrast, during discharge Uyama *et al.* suggested LiMgVO$_4$ only undergoes the first intercalation-type reaction mechanism and displays a substantial increase in capacity retention compared to LiZnVO$_4$.

$$[V^{5+}]_{tet}[LiM]_{oct}O_4 + 2Li^+ + 2e^- \rightarrow [Li]_{tet}[LiV^{3+}]_{oct}[LiM]_{oct}O_4 \qquad \text{(Equation 6.4)}$$

$$[Li]_{tet}[LiV^{3+}]_{oct}[LiM]_{oct}O_4 + xLi^+ + xe^- \rightarrow x(Li_a,Zn_b,V_c)O \qquad \text{(Equation 6.5)}$$
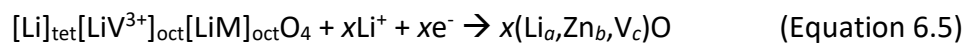
In comparison to the previous inverse spinels investigated, the data presented here for Li$_3$CrV$_2$O$_8$ (x = 1) display behaviour similar to LiMgVO$_4$, with 1st cycle discharge/charge capacities > 350 mAh g^{-1} and < 200 mAh g^{-1}, respectively.[8] During subsequent cycles, both materials display greater capacity retention than their Zn or Ni containing counterparts. This may indicate that like LiMgVO$_4$, Li$_3$CrV$_2$O$_8$ also undergoes an intercalation-type mechanism. *Uyama et al.* suggested the poor first cycle Coulombic efficiency is due to difficulty in oxidising V^{4+} to V^{5+} and shifting back into tetrahedral sites during charge.[8] This could explain the reduced capacity during the 1st cycle charge for x = 1, as the charge capacity of 165 mAh g^{-1} is close to the theoretical capacity of 177 mAh g^{-1} assuming a one electron V$^{3+/4+}$ redox couple. However, this is in contrast to XAS data collected by Rossignol *et al.* for LiNiVO$_4$ (x = 0), which shows vanadium atoms in tetrahedral environments, suggesting an oxidation state of 5+ for

vanadium atoms during charge. Rossignol *et al.* instead suggested the limited reversible capacity on charge is due to reduced Ni atoms remaining in their metallic state.[7] As for x = 0.75, 0.5 and 0.25, their discharge/charge curves appear to behave more similarly to x = 0 with decreasing x. This could potentially indicate, with increasing Ni content, the reaction mechanisms are more conversion-like due to the larger capacities observed.

This work highlights the potential of inverse spinel materials as moderate voltage, high capacity anodes. Further work should investigate the full $Li_{2+x}Ni_{2-2x}Cr_xV_2O_8$ series using techniques such as XAS alongside operando XRD to elucidate the role of transition metal ions in octahedral sites on the reaction mechanism in inverse spinels during cycling. Further work on mitigating the low 1st cycle coulombic efficiencies is also required, *e.g.* through different doping strategies and altering the voltage cut-off window. Rate capabilities of these materials should also be studied to assess their competitiveness against other anode materials such as $Li_4Ti_5O_{12}$.

6.4. Conclusions

In this work the electrochemical performance of the $Li_{2+x}Ni_{2-2x}Cr_xV_2O_8$ ($0 \leq x \leq 1$) solid solution as potential cathode and anode materials were assessed through galvanostatic cycling with potential limits experiments. As cathode materials cycled between 3 to 4.9 V, $x = 0$ displayed comparable charge/discharge capacities to those previously reported, with a single voltage plateau. For $x = 0.25$, 0.5 and 0.75, initial charge capacities were similar to $x = 0$ (between 80 to 100 mAh g^{-1}), although two voltage plateaus were observed within charge curves. On discharge, these processes were largely irreversible, with limited discharge capacities between 9 to 23 mAh g^{-1}. For Cr and Ni-containing samples, the majority of the discharge capacity was observed between 3 to 3.7 V, which may be indicative of an oxygen (O^{2-}/O_2^{2-}) redox process based on comparisons to similar materials reported in the literature. $x = 1$ appears to be redox inactive as a cathode material in the studied voltage window.

XANES of $Li_{2+x}Ni_{2-2x}Cr_xV_2O_8$ ($0 \leq x \leq 1$) powders were collected to confirm the oxidation states of Cr, Ni and V in these materials. Analysis of the XANES Cr, V and Ni K-edge spectra revealed the present of Cr^{3+}, Ni^{2+} and V^{5+}, which was expected for the inverse spinel structure. In-situ XANES of $x = 0.5$ and 0.75 during cycling as cathode materials between 3 and 4.9 V were conducted to investigate the changing oxidation states during (dis)charge processes and to help explain the irreversible capacity loss. During charge, the largest change was seen in the Cr K-edge spectra. Analysis of the pre-edge information and edge position indicated an increase in the pre-edge peak intensity and a shift to higher energies in the edge position. As a result, on charge the Cr K-edge spectra, for both $x = 0.5$ and 0.75, more resembled the Cr^{6+} standard reference spectra. A small decrease in the pre-edge intensity of V k-edge XANES spectra was also observed on charge, which may be suggestive of a small percentage of V^{5+} cations shifting from tetrahedral sites to octahedral sites. Ni K-edge XANES spectra remained relatively unchanged during cycling. For x = 0.5 on the subsequent discharge, the Cr, V and Ni K-edge spectra largely remained unchanged. These results indicate that on charge, Cr^{3+} is oxidised to Cr^{6+} and shifts from octahedral to tetrahedral sites. On discharge, the majority of Cr^{6+} is unable to be reduced back to Cr^{3+}. The presence of Cr^{6+} in tetrahedral sites may also impede the oct-tet-oct Li-ion conduction pathway found in Chapter 5.

Preliminary results of $Li_{2+x}Ni_{2-2x}Cr_xV_2O_8$ ($0 \leq x \leq 1$) as anode materials revealed the largest 1st cycle discharge capacity was observed for $x = 0$ at *ca.* 968 mAh g^{-1}, which again is

comparable to previous studies. The 1st cycle discharge capacities for x = 0.25, 0.5, 0.75 and 1 were 712, 721, 764, and 406 mAh g^{-1}, respectively. Despite the lower initial capacity for x = 1, it was found to have the highest capacity retention (61 %) over 30 cycles. The operating voltage also decreased with increasing x. These results indicate x = 1 is the most promising composition as a potential anode material. Nevertheless, further work is required to better understand the structural stability of inverse spinels during cycling *e.g.* through the use of in-situ XRD or XANES experiments during cycling as anode materials. Future work should also focus on optimising and evaluating the voltage window and rate capabilities, as well as reducing the low initial coulombic efficiency. An obvious next step would be to investigate the effect of dopants on the electrochemical performance. For instance, substitution of Li$^+$ and Cr^{3+} for a small amount of Ti^{4+} would create vacancies on the octahedral sites, which may in turn increase the Li-ion conduction by reducing the blocking effect of transition metals in octahedral sites.

6.5. References

[1]   W. Zuo *et al.*, "Li-rich cathodes for rechargeable Li-based batteries: Reaction mechanisms and advanced characterization techniques," *Energy Environ. Sci.*, vol. 13, no. 12, pp. 4450–4497, 2020.

[2]   G. Liang, V. K. Peterson, K. W. See, Z. Guo, and W. K. Pang, "Developing high-voltage spinel $LiNi_{0.5}Mn_{1.5}O_4$ cathodes for high-energy-density lithium-ion batteries: current achievements and future prospects," *J. Mater. Chem. A*, no. 8, pp. 15373–15398, 2020.

[3]   G. T. Fey, W. Li, and J. R. Dahn, "$LiNiVO_4$: A 4.8 Volt Electrode Material for Lithium Cells," *J. Electrochem. Soc.*, vol. 141, no. 9, pp. 2279–2282, 1994.

[4]   a K. Padhi, W. B. Archibald, K. S. Nanjundaswamy, and J. B. Goodenough, "Ambient and High-Pressure Structures of $LiMnVO_4$ and Its $Mn^{3+/2+}$ Redox Energy," *J. Solid State Chem.*, vol. 128, pp. 267–272, 1997.

[5]   G. T. K. Fey and D. L. Huang, "Synthesis, characterization and cell performance of inverse spinel electrode materials for lithium secondary batteries," *Electrochim. Acta*, vol. 45, no. 1, pp. 295–314, 1999.

[6]   J. Huang *et al.*, "Non-topotactic reactions enable high rate capability in Li-rich cathode materials," *Nat. Energy*, vol. 6, no. 7, pp. 706–714, 2021.

[7]   C. Rossignol, G. Ouvrard, and E. Baudrin, "X-Ray Absorption Spectroscopy Study of the Structural and Electronic Changes upon Cycling of $LiNiVO_4$ as a Battery Electrode," *J. Electrochem. Soc.*, vol. 148, no. 8, p. A869, 2001.

[8]   T. Uyama and K. Mukai, "Synthesis of $LiMg_{1-x}Zn_xVO_4$ with $0 \leq x \leq 1$ for application to the negative electrode of lithium-ion batteries," *Mater. Today Energy*, vol. 14, pp. 1–10, 2019.

[9]   J. B. Leriche *et al.*, "An Electrochemical Cell for Operando Study of Lithium Batteries Using Synchrotron Radiation," *J. Electrochem. Soc.*, vol. 157, no. 5, p. A606, 2010.

[10]   B. Ravel and M. Newville, "ATHENA, ARTEMIS, HEPHAESTUS: Data analysis for X-ray absorption spectroscopy using IFEFFIT," *J. Synchrotron Radiat.*, vol. 12, no. 4, pp. 537–541, 2005.

[11]   M. Wojdyr, "Fityk: A general-purpose peak fitting program," *J. Appl. Crystallogr.*, vol. 43, no. 5 PART 1, pp. 1126–1128, 2010.

[12]   A. Kitajou *et al.*, "Capacity improvement by deficit of transition metals in inverse spinel $LiNi_{1/3}Co_{1/3}Mn_{1/3}VO_4$ cathodes," *J. Power Sources*, vol. 302, pp. 240–246, 2016.

[13]   N. V Landschoot, "Synthesis and characterization of inverse spinels, intercalation materials for Li-ion batteries," 2006.

[14]   Z. Chen and Z. Zhang, "First principles investigation of electronic structure change and energy transfer by redox in inverse spinel cathodes $LiNiVO_4$ and $LiCoVO_4$," *J. Mater. Chem.*, vol. 22, no. 36, pp. 18968–18974, 2012.

[15]   N. N. Sinha, J. C. Burns, R. J. Sanderson, and J. Dahn, "Comparative Studies of Hardware Corrosion at High Potentials in Coin-Type Cells with Non Aqueous Electrolytes," *J.*

Electrochem. Soc., vol. 158, no. 12, p. A1400, 2011.

[16] F. Farges, "Chromium speciation in oxide-type compounds: Application to minerals, gems, aqueous solutions and silicate glasses," *Phys. Chem. Miner.*, vol. 36, no. 8, pp. 463–481, 2009.

[17] P. Chaurand *et al.*, "New methodological approach for the vanadium K-edge X-ray absorption near-edge structure interpretation: Application to the speciation of vanadium in oxide phases from steel slag," *J. Phys. Chem. B*, vol. 111, no. 19, pp. 5101–5110, 2007.

[18] J. Li, Y. Li, P. K. Routh, E. Makagon, I. Lubomirsky, and A. I. Frenkel, "Comparative analysis of XANES and EXAFS for local structural characterization of disordered metal oxides," *J. Synchrotron Radiat.*, vol. 28, no. 5, pp. 1511–1517, 2021.

[19] R. S. Liu, Y. C. Cheng, R. Gundakaram, and L. Y. Jang, "Crystal and electronic structures of inverse spinel-type $LiNiVO_4$," *Mater. Res. Bull.*, vol. 36, no. 7–8, pp. 1479–1486, 2001.

[20] K. Tirez *et al.*, "Speciation and fractionation of nickel in airborne particulate matter: comparison between selective leaching and XASspectroscopy," *J. Anal. At. Spectrom.*, vol. 26, no. 3, pp. 517–527, 2011.

[21] C. Sigala, A. Verbaere, J. L. Mansot, D. Guyomard, Y. Piffard, and M. Tournoux, "The Cr-Substituted Spinel Mn Oxides $LiCr_yMn_{2-y}O_4$ (0< y <1): Rietveld Analysis of the Structure Modifications Induced by the Electrochemical Lithium Deintercalation," *J. Solid State Chem.*, vol. 132, pp. 372–381, 1997.

[22] R. Kanno, Y. Takeda, M. Hasegawa, Y. Kawamoto, and O. Yamamoto, "Mechanistic studies on the electrochemically lithiated spinel $LiCuVO_4$," *J. Solid State Chem.*, vol. 94, no. 2, pp. 319–328, 1991.

[23] R. Chen *et al.*, "Reversible Li+ storage in a $LiMnTiO_4$ spinel and its structural transition mechanisms," *J. Phys. Chem. C*, vol. 118, no. 24, pp. 12608–12616, 2014.

Chapter 7: Conclusions and Future Work

7.1. Conclusions

In this thesis, the inverse spinel, $Li_3CrV_2O_8$ was revisited to fully investigate its crystal structure. Its electrical and electrochemical properties were investigated for the first time. A novel solid solution between the two end members $Li_2Ni_2V_2O_8$ and $Li_3CrV_2O_8$, of the form $Li_{2+x}Ni_{2-2x}Cr_xV_2O_8$ ($0 \leq x \leq 1$), was also synthesised using a citric acid sol-gel route. Room-temperature combined X-ray and neutron refinements revealed a disordered inverse spinel structure, crystallising in the $Fd\overline{3}m$ space group with an average lattice parameter of 8.2103(1) Å, and no indication of cation ordering on 16c octahedral sites. The variation in total conductivity and activation energies with Li and transition metal content was investigated using impedance spectroscopy. Activation energies for total conductivity were between 0.50 and 0.56 eV, with total and bulk conductivities increasing with x. The similar activation energies calculated likely indicates that Li-ions diffuse via the same conduction mechanism(s) within the $Li_{2+x}Ni_{2-2x}Cr_xV_2O_8$ ($0 \leq x \leq 1$) solid-solution. The highest bulk conductivity was obtained for $x = 1$ with a value of 1.68×10^{-7} S cm^{-1} at 75 °C.

The diffusion mechanisms of these inverse spinels were investigated using a combination of variable-temperature neutron powder diffraction and muon spectroscopy measurements. In the former, difference Fourier maps enabled the determination of interstitial conduction sites for $x = 0.5$ and 1 at 0.125, 0.125, 0.125 and equivalent positions, corresponding to an additional Li 8a site within the inverse spinel structure. A 16c-8a-16c conduction pathway was subsequently deduced. In the latter, muon data was able to probe the local Li-ion kinetics and the activation energies for Li-ion hopping were determined for each to be, within error, between 0.17 – 0.19 eV for $x = 0$, 0.5 and 1, again suggesting that the same conduction mechanism(s) are followed across the solid solution series. These activation energies are significantly lower than those determined from impedance spectroscopy measurements, likely because impedance measurements are highly dependent on the sintering conditions and density of pellets, whereas muon spectroscopy measurements requires the material to be in powder form. This highlights the advantages of using multiple different probes for materials characterisation at differing length scales. Additional features were observed within ν and Δ plots at low temperatures (< 400 K) that have not previously been reported in other battery materials investigated using muon

spectroscopy. An explanation for these features are currently unknown however, it may be an indication of local ordered/disordered transitions within the inverse spinel structure or local magnetic effects. The combination of structural information from Rietveld analysis of neutron powder diffraction data, alongside the hopping rate obtained from muon spectroscopy, has enabled diffusion coefficients of between 1.96×10^{-12} cm^2 s^{-1} and 2.36×10^{-12} cm^2 s^{-1} to be determined. This is an important finding because the similarity of both the diffusion pathway and the activation energies to that of normal spinels implies that the random distribution of Li and transition metal ions on octahedral sites in inverse spinels does not impede their potential in Li-ion batteries. This emphasises the influence of cation distribution on the Li-ion diffusion properties. If the distribution of cations on octahedral sites were randomly distributed at all length scales, then the 16c-8a-16c conduction pathway found in this work would be blocked. Likewise, if the cations were fully ordered then the conduction pathway would also be blocked due to the lack of empty tetrahedral sites, as is the case for LiZnNbO$_4$. Therefore it is likely that some degree of local order/disorder between cations on octahedral sites plays a role in enabling the diffusion of Li-ions.

The electrochemical performance of x = 0, 0.25 and 0.75 as potential cathode materials is limited by the large irreversible capacity observed during discharge, as demonstrated via galvanostatic cycling. The x = 1 composition, on the other hand, was found to be redox inactive as a cathode. The origin of the poor cathodic cycling performance of Cr and Ni containing samples was revealed through in-situ XANES Cr, V and Ni K-edge spectra. The results indicated that Cr^{3+} in octahedral sites is oxidised to Cr^{6+} on charge, which subsequently migrates to occupy tetrahedral sites. The inability for the reverse process to occur on discharge is likely what inhibits their function as effective cathodes. Furthermore, there was an indication that a small percentage of V^{5+} cations may be able to shift from tetrahedral to octahedral sites during charge. On the other hand, there was no evidence for a change in the oxidation state of Ni during (dis)charge processes.

Further measurements were conducted to assess the ability of the Li$_{2+x}$Ni$_{2-2x}$Cr$_x$V$_2$O$_8$ inverse spinels as anode materials. For all compositions, the initial discharge capacities obtained were greater than their theoretical capacities, assuming a V^{5+} to V^{3+} redox process. For example, specific discharge capacities of $ca.$ 968 mAh g^{-1} and 406 mAh g^{-1} for x = 0 (theoretical capacity = 297 mAh g^{-1}) and x = 1 (theoretical capacity = 354 mAh g^{-1}),

respectively, were obtained. It can be inferred that additional redox processes occur during discharge. All compositions were found to suffer from low Coulombic efficiencies during the first cycle (between 60 – 40 %). However, the capacity retention over 30 cycles was found to increase with increasing x, *e.g.* capacity retentions of 14 and 61 % were obtained for $x = 0$ and 1, respectively. This electrochemical behaviour may imply that Li/Cr doping helps stabilise the inverse spinel structure during cycling.

Overall, this work demonstrates the importance of utilising multiple techniques to investigate potential battery materials. In fact, for the first time it has been shown that the conduction pathway in inverse spinels is not impeded by the mixed cation distribution, despite previous suggestions that no obvious tunnels exist for Li-ion diffusion. In particular, if the migration of other cationic species can be mitigated, for example through the investigation of new compositions, then the inverse spinel structure holds great potential to be implemented in future LiB technologies.

7.2. Future Work

Regarding future studies, there are many different avenues that could be explored to expand upon this work on the $Li_{2+x}Ni_{2-2x}Cr_xV_2O_8$ compositions. These materials show promise as potential anode materials. Therefore, the optimisation of cell parameters such as the voltage window and active material content within electrodes is required. Optimising the voltage window may enable improved coulombic efficiencies and life cycle. At the same time, further studies on the rate capabilities and structural stability of these materials during cycling through techniques such as in-situ XRD are also necessary. In particular, the role of different transition metals, which are randomly distributed together with Li over octahedral sites, on the structural stability, capacity and nominal voltage requires clarification. In this regard, modelling studies *e.g.,* density functional theory (DFT) could be used to investigate the stability of the host inverse spinel structure with the introduction of different dopants. DFT modelling could also be used to calculate the electrochemical potential as a function of Li (de)intercalation. This could provide a snapshot of how the structure is altered during cycling. DFT or molecular dynamics simulations could also be implemented to confirm the energetic favourability of different conduction pathways and interstitial sites to those determined experimentally within this work. This may additionally provide insight into the different Li

insertion/extraction mechanisms during (dis)charge cycles. These modelling techniques should be linked to experimental data through the comparison of modelled and practical voltage curves, as well as through the differences between calculated and experimental collected XRD patterns.

One doping strategy which should be studied is the substitution of Li^+ and Cr^{3+} for higher valance cations such as Ti^{4+} to introduce cation vacancies in octahedral sites and create additional sites for Li-ions to occupy during electrochemical cycling. More broadly, this work may inspire further investigations into other systems where Li and transition metals are disordered over crystallographic sites *e.g.* Li-rich disordered rocksalts. Both Layered and disordered rocksalts have primarily received attention as potential cathode materials. However, their performance as anode materials still requires further investigation, particularly the role of cation order/disorder over differing length scales on the ability of these materials to accept additional Li-ions during cycling. This could be investigated using a combination of the insights gained from any potential modelling studies and by attempting to synthesise novel $V^{4+/3+}$ containing compositions which adopt a rocksalt or spinel structure to create new anode materials with greatly improved electrochemical properties such as reduced capacity loss over (dis)charge cycles.

Finally, the role that local and/or average cation ordering plays on the electrical and electrochemical properties is crucial to the understanding of materials which adopt the inverse spinel structure. For example, the variation in local ordering with temperature and Li content will enable the future design of new materials. This could be achieved by techniques such as solid-state NMR, Raman spectroscopy, and/or PDF theory. This may help enable future researchers to find the ideal cation distribution for Li-ion diffusion during cycling. To this end, a greater understanding of the differences between obtained diffusion properties across techniques such as impedance and muon spectroscopy is required. The electrochemical properties of ordered inverse spinels should also be investigated. For instance, there have been no previous studies on Li insertion/extraction in $LiZnNbO_4$, where Li and Nb are ordered over octahedral sites. This could provide a direct comparison to the materials investigated herein and may help elucidate the role of cation ordering on the resulting electrochemical properties in Li-containing inverse spinels.

Chapter 8: Appendix

8.1 Publication

As part of the initial stages of my PhD, work into fully understanding the Li-ion diffusion mechanisms in the complex spinel, $Li_2NiGe_3O_8$ (Chapter 2, Section 2.3.2.4) was conducted alongside collaborators from the University of Sheffield, Durham University, and the ISIS Neutron and Muon Facility. This work led to the publication: D. Z. C. Martin *et al.*, "Evaluating lithium diffusion mechanisms in the complex spinel $Li_2NiGe_3O_8$," *Phys. Chem. Chem. Phys.*, vol. 21, no. 41, pp. 23111–23118, 2019.

Within this work, the Li-ion diffusion mechanisms in the complex spinel, $Li_2NiGe_3O_8$ were investigated using multiple complementary techniques. $Li_2NiGe_3O_8$ crystalises into the $P4_332$ space group, in which Li-ions occupy tetrahedral 8*c* sites, Ni and Ge occupy 4*b* and 12*d* octahedral sites, respectively. A 1:3 ordering between Ni and Ge occurs on octahedral sites. $Li_2NiGe_3O_8$ was previously reported as a moderate Li-ion conductor (*ca.* 10^{-7} S cm^{-1} at 60 °C) and is not redox active up to 5 V.[1] Thus, it may have potential applications as a solid electrolyte within an all-solid-state spinel-based LiB. Muon spectroscopy was used to study the local Li-ion hopping, and it was found that Li-ions start to rapidly hop into interstitial sites at *ca.* 340 K. Below *ca.* 300 K the hopping rate, *v*, was relatively constant (unlike the work presented for the inverse spinels, $Li_2Ni_2V_2O_8$, $Li_{2.5}NiCr_{0.5}V_2O_8$ and $Li_3CrV_2O_8$ in Chapter 5). *v* alongside previously obtained structural information was used to determine a Li-ion diffusion coefficient of 3.89 x 10^{-12} cm^2 s^{-1} at 300 K.[2] An activation energy for local Li-ion hopping of 0.43(3) eV was determined from Arrhenius plots of the diffusion coefficient. This activation energy was slightly lower than those obtained from impedance spectroscopy (between 0.46(1) to 0.53(1) eV) and therefore highlights the advantages of using multiple techniques to probe Li-ion diffusion.

My contributions towards this publication are outlined as followed: analysis of muon spectroscopy data and writing the introduction, experimental, results and discussion and conclusions (excluding sections concerning solid-state NMR). This work formed the initial inspiration for investigating Li-ion diffusion within inverse spinels using a range of complementary techniques.

PCCP

Check for updates

Evaluating lithium diffusion mechanisms in the complex spinel Li$_2$NiGe$_3$O$_8$†

Daniel Z. C. Martin, [a] Abby R. Haworth, [b] Whitney L. Schmidt, [c] Peter J. Baker, [d] Rebecca Boston, [a] Karen E. Johnston [*b] and Nik Reeves-McLaren [*a]

Lithium-ion diffusion mechanisms in the complex spinel Li$_2$NiGe$_3$O$_8$ have been investigated using solid-state NMR, impedance, and muon spectroscopies. Partial occupancy of migratory interstitial 12d sites is shown to occur at lower temperatures than previously reported. Bulk activation energies for Li$^+$ ion hopping range from 0.43 ± 0.03 eV for powdered samples to 0.53 ± 0.01 eV for samples sintered at 950 °C for 24 h, due to the loss of Li during sintering at elevated temperatures. A lithium diffusion coefficient of 3.89 × 10^{-12} cm^2 s^{-1} was calculated from muon spectroscopy data for Li$_2$NiGe$_3$O$_8$ at 300 K.

1 Introduction

Since Sony's successful commercialisation of lithium-ion batteries (LIBs) in 1990, their numerous desirable properties have been widely reported.[1-3] However, despite becoming ubiquitous in modern society, several safety concerns still remain, predominantly related to the use of flammable and corrosive organic liquid electrolytes in close proximity to highly energetic electrode materials.[4-6] Whilst accidents are relatively rare, these liquid electrolytes can pose significant dangers to consumers and other end-users, as well as reputational damage for device manufacturers.[7]

An all-solid-state battery utilising a solid electrolyte could alleviate many of these concerns, whilst offering improved shock resistance and durability.[8] To date, research has primarily focused on the development and optimisation of materials with room-temperature Li$^+$ ion conductivities (σ_i) of $\geq 10^{-3}$ S cm^{-1}, in order to compete with current commercial liquid electrolytes.[8] Several such materials exist, for instance thio-LISICONs (*e.g.*, Li$_{10}$GeP$_2$S$_{12}$, σ_i = 1.2 × 10^{-2} S cm^{-1}) and Li-stuffed garnets (*e.g.*, Li$_{6.4}$La$_3$Zr$_{1.4}$Ta$_{0.6}$O$_{12}$, σ_i = 10^{-3} S cm^{-1}).[9-11] Nevertheless, many of these candidate materials suffer a number of drawbacks, which are preventing their commercialisation. For example,

thio-LISICONs are unstable in air and decompose at cell voltages >4 V *vs.* Li/Li$^+$.[12,13] Many are also reported to react with lithium metal.[12] Li-stuffed garnets can undergo proton exchange (H$^+$/Li$^+$), substantially reducing levels of Li$^+$ ion conductivity.[14,15] They are also widely reported to exhibit high interfacial resistance with electrode materials (up to ~2000 Ω cm^2).[16] One solution to lowering this interfacial resistance is to use materials with the same crystal structure to enable lattice matching, for example by developing an all-spinel solid-state battery.

The spinel structure, AB$_2$O$_4$, has been studied extensively and is known to consist of cubic close packed O^{2-} anions, with A-site cations occupying an eighth of the tetrahedral sites and B-site cations filling half of the available octahedral sites for 'normal' spinels.[17,18] Depending on the cations present, the spinel structure may also be inverse ([B]^{tet}[A,B]^{oct}O$_4$) or random ([B$_{0.67}$A$_{0.33}$]^{tet}[A$_{0.67}$B$_{1.33}$]^{oct}O$_4$). Cubic spinels generally crystallise in the $Fd\bar{3}m$ space group. In Li-based spinels, Li$^+$ ion conductivity typically follows a two-step conduction mechanism involving Li ions in 8a tetrahedral sites hopping into empty 16c octahedral sites and then onto adjacent 8a sites, forming a three-dimensional 8a-16c-8a pathway for ionic migration[19] that means spinels often exhibit interesting and useful electrical properties. As a result, several manganese-based spinels have been considered as potential high voltage cathode materials (>4.7 V *vs.* Li$^+$/Li), *e.g.*, LiCoMnO$_4$ and LiNi$_{0.5}$Mn$_{1.5}$O$_4$.[20-22] However, these are incompatible with current LIB cell designs due to the breakdown of organic electrolytes above *ca.* 4.5 V *vs.* Li$^+$/Li. Spinel-based titanates such as Li$_4$Ti$_5$O$_{12}$ are currently of interest as anode materials in LIB applications, as they exhibit excellent dimensional stability during Li (de)intercalation.[23,24] In contrast, spinel-based materials for solid electrolyte applications have received considerably less attention, since they often incorporate redox active transition metals. One potential candidate material is Li$_2$NiGe$_3$O$_8$, previously

^{a} Department of Materials Science and Engineering, University of Sheffield, Sheffield, S13JD, UK. E-mail: n.reeves@sheffield.ac.uk

^{b} Department of Chemistry, Durham University, Durham, DH1 3LE, UK. E-mail: karen.johnston@durham.ac.uk

^{c} Division of Natural Sciences and Mathematics, Kentucky Wesleyan College, 3000 Frederica St., Owensboro, KY 42301, USA

^{d} ISIS Facility, Science and Technology Facilities Council, Rutherford Appleton Laboratory, Harwell Science and Innovation Campus, Didcot, Oxfordshire, OX11 0QX, UK

† Electronic supplementary information (ESI) available. See DOI: 10.1039/c9cp02907a

This journal is © the Owner Societies 2019

Phys. Chem. Chem. Phys., 2019, **21**, 23111–23118 | 23111

reported by Kawai *et al.* to exhibit a modest Li$^+$ ion conductivity of ~10^{-7} S cm^{-1} at 63 °C (comparable to the tetragonal phase of the Li-stuffed garnet Li$_7$La$_3$Zr$_2$O$_{12}$) and which is electrochemically inactive below 5 V *vs.* Li$^+$/Li.[25]

Li$_2$NiGe$_3$O$_8$ can be described as an ordered or 'complex' spinel in space group $P4_3$32, with Li$^+$ ions occupying tetrahedral 8c sites, and 1:3 cation ordering of Ni and Ge on the 4b and 12d octahedral sites, respectively.[25] Conduction pathways in complex spinels are less well studied compared to normal spinels, but can involve additional steps depending on the nature of the ordering present. Previous work using variable-temperature time-of-flight neutron powder diffraction (ToF ND) indicated the presence of a second Li 12d octahedral site in Li$_2$NiGe$_3$O$_8$ at high temperatures (~350–850 °C), leading to the proposition of a three-dimensional 8c-12d-8c conduction pathway.[26] Theoretical studies by Nakayama *et al.* predicted the activation energy for this particular pathway to be 0.47 eV, lower than other previously proposed pathways.[19]

An improved understanding of ionic diffusion mechanisms in spinel materials, and Li$^+$ ion conductors at large, is crucial if such materials are to be improved and optimised for use as solid electrolytes in all-solid-state LIBs. To this end, we have used a combination of techniques, including impedance, muon and solid-state NMR spectroscopies to enhance our understanding of the crystal structure of the complex spinel Li$_2$NiGe$_3$O$_8$ and the Li$^+$ ion diffusion dynamics therein.

2 Experimental methods

2.1 Synthesis and characterisation

Samples of Li$_2$NiGe$_3$O$_8$ were synthesised *via* traditional solid state methods. Stoichiometric amounts of Li$_2$CO$_3$ (Sigma-Aldrich, 99%), NiO (Alfa Aesar, 99%) and GeO$_2$ (Sigma-Aldrich, 99.999%) were mixed and ground in an agate mortar and pestle, placed into Au boats and fired at 923 K for 5 hours. Prior to heating, the starting reagents were dried at either 453 (for Li$_2$CO$_3$) or 773 K (for oxides) for 12 hours. The samples were then calcined at 1173 K for 36 hours, with intermediate regrinding. Identical specimens of Li$_2$NiGe$_3$O$_8$ were used for all XRD, impedance, solid-state NMR and μSR studies.

Samples were characterised by X-ray diffraction (XRD) using a Bruker D2 Phaser diffractometer with Cu Kα (λ = 1.5418 Å) radiation. The ICDD's PDF-4+ database (2019 edition) and SIeve+ software were used for phase analysis. Rietveld refinements were performed using the GSAS-II software.[27]

2.2 Impedance spectroscopy

Pellets of Li$_2$NiGe$_3$O$_8$ were prepared for impedance spectroscopy measurements by uniaxial pressing. Pellets were placed onto sacrificial powder in an alumina crucible and sintered at 1223 K for 6 or 24 hours, resulting in pellets with 66% and 81% density, respectively. Both pellet faces were polished and gold electrodes applied to each as a paste. Each pellet was then annealed at 1123 K for 2 hours. All heating steps described used heating/cooling rates of 5 °C min^{-1}. Impedance measurements were collected using a Solartron Analytical/Ametek ModuLab XM MTS

system from 1 MHz to 30 mHz with a 100 mV applied AC voltage. Measurements were taken during heating from 336 to 541 K.

2.3 Solid-state NMR spectroscopy

Solid-state NMR spectra were acquired using a Bruker 500 Avance III HD spectrometer, equipped with a wide-bore 11.7 T Oxford magnet, using Larmor frequencies of 194.4 MHz for ^{7}Li (I = 3/2) and 73.6 MHz for ^{6}Li (I = 1). Powdered samples were packed into conventional 4.0 or 1.3 mm ZrO$_2$ rotors and magic-angle spinning (MAS) rates of 10 and 60 kHz were employed, respectively. Both ^{6}Li and ^{7}Li chemical shifts were referenced to 1 M LiCl$_{(aq)}$.

Conventional ^{7}Li MAS NMR spectra were obtained using a single-pulse experiment with typical pulse lengths of 3 μs. ^{6}Li MAS NMR spectra were acquired using a Hahn echo experiment (90$_x$–τ–180$_y$) with a typical π/2 pulse length of 3 μs. Typical radiofrequency field strengths of 84 kHz were employed and an experimentally optimised recycle interval of 0.2 s was used for both ^{7}Li and ^{6}Li. Standard variable-temperature (VT) ^{6}Li MAS NMR experiments were completed between 260 and 412 K using conventional hardware and the parameters stated above. In all cases, temperatures were calibrated using the ^{1}H signal of MeOH; quoted temperatures thus reflect the true sample temperature during the experiment.

Additional static variable-temperature ^{6}Li NMR experiments were completed for Li$_2$NiGe$_3$O$_8$ over the temperature range 204 to 609 K using a Bruker 400 Avance III HD spectrometer, equipped with a wide-bore 9.7 T magnet, using a Larmor frequency of 58.9 MHz for ^{6}Li. The sample was packed into a 5.0 mm glass tube and placed into a Bruker 5.0 mm static probe. The static NMR spectra were acquired using a standard solid echo experiment (90$_x$–τ–90$_y$), with a typical π/2 pulse length of 5 μs. Here, τ represents an echo delay of 200 μs between 197 and 542 K and 250 μs at 609 K. The interpulse delay was increased in order to acquire the whole echo at higher temperatures. Typical radiofrequency field strengths of 50 kHz were employed and the experimentally optimised recycle interval was 0.05 s. In all cases, true sample temperatures during experiments have been determined using a lead nitrate calibrant.

2.4 Muon spin relaxation (μSR) spectroscopy

All μSR measurements were performed using the EMU instrument at the ISIS pulsed muon facility. Around ~1 g of sample was packed into a disk of 30 mm diameter and 1.5 mm thickness and sealed in a Ti sample holder with a ~25 μm thick Ti foil window. The sample was implanted with 3.2 MeV spin-polarised positive muons, and the out-coming positrons detected by 96 scintillator segments arranged in two circular arrays. Data were collected from 39–555 K using a closed cycle refrigerator under three different applied longitudinal magnetic fields (0, 5 and 10 G). Initial symmetry calibrations were conducted using a 20 G transverse magnetic field. Data analysis was conducted using the WiMDA program.[28] Collection of data in multiple longitudinal fields enabled (i) the controlled decoupling of interactions between the implanted muons and any local magnetic field distributions, and (ii) additional constraints in and hence more reliable results from the fitting process.

23112 | *Phys. Chem. Chem. Phys.,* 2019, 21, 23111–23118

This journal is © the Owner Societies 2019

3 Results and discussion

Room-temperature powder XRD data for $Li_2NiGe_3O_8$ are shown in Fig. 1. Bragg peaks were indexed to the $P4_332$ space group, with no additional or missing reflections, giving a refined lattice parameter a = 8.1848(5) Å, in good agreement with previous reports.[25,26] Details of the corresponding Rietveld refinement and a list of refined structural parameters are given in the ESI.† A $Li_2NiGe_3O_8$ pellet sintered at 1223 K for 24 h showed small additional Bragg peaks which are likely caused by lithium volatilisation, resulting in the onset of thermal decomposition and formation of impurities. Despite a rigorous search of the 2019 edition of the ICDD PDF-4+ database, we were unable to identify the additional phases present. It is noted that these peaks were not observed in data collected for a pellet sintered at the same temperature for 6 h.

3.1 Lithium-ion conductivity analysis by impedance spectroscopy

Impedance data were collected for $Li_2NiGe_3O_8$ pellets sintered for 6 and 24 h. Owing to the lack of mixed valence Ni and Ge species in $Li_2NiGe_3O_8$, the electrical conductivity is expected to be negligible, as previously reported.[19,25] Hence, the responses observed in impedance data are likely due to Li^+ ion conduction. The complex impedance spectra obtained in Fig. 2(a) show two partly resolved arcs followed by a low frequency spike.

Irrespective of the sintering time, the arc observed at higher frequencies has an associated capacitance of $\sim 3.1 \times 10^{-12}$ F, indicative of bulk, intra-granular responses. The second, intermediate frequency arc, with capacitance $\sim 1 \times 10^{-11}$ F, is attributed to the response from the grain boundary component.[29] Under both sintering conditions, a subsequent low-frequency Warburg spike, inclined at $\sim 50°$ to the horizontal axis, was observed with associated capacitance of $\sim 10^{-6}$ F, indicative of complete or partial ion blocking at the electrode, representative of ionic conductivity in $Li_2NiGe_3O_8$.[29]

Fig. 2 (a) Complex impedance spectra collected at ~ 523 K for $Li_2NiGe_3O_8$ pellets prepared using different sintering times: 24 hours (blue circles) and 6 hours (black squares). (b) Arrhenius plots bulk and grain boundary conductivities for $Li_2NiGe_3O_8$ pellets prepared using different sintering times: 24 hours (circles) and 6 hours (squares). Grain boundary activation energies of 0.56 ± 0.02 eV and 0.49 ± 0.02 eV were calculated for pellets sintered at 24 hours and 6 hours, respectively.

To extract conductivities from the arcs attributed to intra-granular and grain boundary responses in the complex impedance spectra, fitting was performed using Z-View. Bulk conductivities were taken from the intersection of two manually fitted parallel RC semicircles, with errors calculated from the intersection of the semicircles with the Z' axis. The extracted bulk conductivities, as a function of inverse temperature, are shown in Fig. 2(b). For both samples, the data follows typical Arrhenius-type behaviour, enabling activation energies to be calculated. The pellet sintered for 6 h exhibited an activation energy of 0.46 ± 0.01 eV, whilst the pellet fired for 24 h showed a higher value, 0.53 ± 0.01 eV, closer to that previously reported by Kawai et al. (0.55 eV) for $Li_2NiGe_3O_8$ sintered for 24 h.[25] Assuming all Li in the spinel unit cell contribute to diffusion, an intra-grain diffusion coefficient, D_{Li}, of 2.26×10^{-13} cm s^{-1} can be estimated from impedance data at 336 K using the Nernst–Einstein equation:[30]

$$D = \frac{\sigma k_B T}{n_{Li} e^2}$$

Fig. 1 XRD patterns obtained for (a) powdered $Li_2NiGe_3O_8$ and pellets sintered for (b) 6 h and (c) 24 h. Additional unknown reflections are denoted by *. An expansion of the 2θ range in (c) highlights the additional Bragg peaks present for the 24 h sintered pellet.

This journal is © the Owner Societies 2019

Phys. Chem. Chem. Phys., 2019, 21, 23111–23118 | 23113

198

It is evident from Fig. 2(a) and (b) that longer sintering times leads to a concomitant decrease in both bulk and grain boundary conductivities. This difference is attributed to the loss of lithium and subsequent formation of additional phases during sintering at temperatures close to the reported melting point of $Li_2NiGe_3O_8$ (1243 K).[25]

3.2 Probing Li diffusion using solid-state NMR

Using solid-state NMR spectroscopy it is possible to probe both local structural changes and ion mobility. Both lithium nuclides (^6Li and ^7Li) are suitable for NMR spectroscopy, however, one is often preferred over the other, depending on the specific system under investigation. Typically, ^7Li is favoured because of its higher natural abundance (92.5%) when compared to ^6Li (7.5%). However, its large quadrupole moment can give rise to relatively broad lines when Li is in a low symmetry site. In such cases, ^6Li is often preferred because it can allow close or overlapped resonances to be resolved. Moreover, because of its smaller quadrupolar interaction, the ^6Li shift may be more closely approximate to the isotropic chemical shift, thereby providing a better measure of the Li bonding environment.[31] The ^7Li and ^6Li MAS NMR spectra obtained for $Li_2NiGe_3O_8$ are shown in Fig. 3(a) and (b), respectively. The ^7Li MAS NMR spectrum acquired at 10 kHz exhibits a lineshape characteristic of a

Fig. 3 (a) ^7Li and (b) ^6Li MAS NMR spectra acquired for $Li_2NiGe_3O_8$. In (a), two different MAS rates were used, 10 and 60 kHz, respectively. In (b), a MAS rate of 10 kHz was used and an expansion of the central transition is also shown as a comparison. All spinning sidebands are denoted by *.

23114 | Phys. Chem. Chem. Phys., 2019, 21, 23111–23118

This journal is © the Owner Societies 2019

paramagnetic-containing species, i.e., a complex manifold of spinning sidebands. The spectrum obtained indicates the presence of two resonances at $\delta \approx -25$ and 0 ppm, likely corresponding to two distinct Li sites, in good agreement with the reported $P4_332$ phase of $Li_2NiGe_3O_8$.

The variation in $^{6,7}Li$ chemical shift with coordination number is well reported for a variety of crystalline systems.[32] Typically, in diamagnetic systems, LiO_4 environments exhibit chemical shifts between $\delta_{iso} = 0–3$ ppm, whilst LiO_6 environments are between -1 and 0 ppm.[31,32] In paramagnetic systems, these shifts can be altered substantially by the presence of a paramagnetic species, i.e., the presence of an unpaired electron(s).[33,34]

Based on the chemical shifts reported in the literature, coupled with the X-ray diffraction data presented here, and the relative intensities of each resonance, the resonance at $\delta \approx -25$ ppm is believed to correspond to the tetrahedral 8c site and the resonance at $\delta \approx 0.0$ ppm corresponds to the octahedral 12d site. Hence, at room temperature, it appears that small amounts of Li occupy the vacant octahedral site, which is in contrast to previous diffraction studies.[26] In the spectrum, the tetrahedral site is shifted from its expected position, indicating that it is directly affected by the presence of paramagnetic Ni^{2+}, i.e., it is experiencing a Knight shift, although the shift observed here is relatively small when compared to similar reported systems where the resonance can be shifted by several hundreds of ppm.[33,34] A fast spinning (60 kHz) ^7Li MAS NMR spectrum was also acquired for $Li_2NiGe_3O_8$ (shown as an inset in Fig. 3(a)), which revealed the presence of two resonances, one broad resonance at $\delta = -25.3$ ppm, belonging to the tetrahedral Li site and a sharper resonance at $\delta = -3.9$ ppm corresponding to the octahedral Li site. It is noted that the extra resolution afforded by faster MAS rates indicates that a Knight shift is also observed for the octahedral site. At slower MAS rates the lineshape is broadened, which hinders the extraction of an accurate shift for this site. Again, the intensities indicate that a small quantity of Li is occupying the octahedral sites. To verify the quantity of Li on each site, the spectrum was fitted to determine the approximate ratio of tetrahedral to octahedral sites. It is noted that this is somewhat challenging based on the broadened nature and overlap of the two sites. Occupancies of 0.024 and 0.976 were obtained for the octahedral and tetrahedral sites, respectively (Fig. S4, ESI†). This is in good agreement with the slow spinning (10 kHz) ^7Li MAS NMR spectrum.

Initial variable-temperature ^6Li MAS NMR studies of $Li_2NiGe_3O_8$ were completed over the temperature range 260 to 412 K. The corresponding spectra are shown in Fig. 4(a). Between 260 and 357 K, a single broad resonance is observed. As the temperature is increased to 379 K a second resonance appears at $\delta = -1.1$ ppm, indicating the presence of a second Li site, believed to correspond to the octahedral Li site. The appearance of this site upon heating indicates diffusion of the Li ions from the tetrahedral 8c site onto one of the three neighbouring vacant 12d octahedral sites via a hopping mechanism. The presence of a second site is in good agreement with previous high temperature (~350–850 °C) ToF ND structural studies of $Li_2NiGe_3O_8$.[26] However, the solid-state NMR data presented

Fig. 4 Variable-temperature ^{6}Li (a) MAS and (b) static NMR spectra obtained for $Li_2NiGe_3O_8$. The spectra in (a) were acquired over the temperature range 260 and 412 K and a MAS rate of 10 kHz was used. All of the spectra shown in (b) were acquired under static conditions over the temperature range 204 to 609 K.

indicate that Li diffusion onto the octahedral site(s) occurs at lower temperatures than previously reported.[26] In fact, our ^{7}Li MAS NMR data (*vide supra*) suggest that, even at room temperature, some of the vacant octahedral $12d$ sites are occupied. However, owing to relatively poor signal-to-noise in the VT ^{6}Li MAS NMR spectra, it is challenging to accurately determine the precise temperature at which Li ions become mobile and move between the $8c$ and $12d$ sites.

As the temperature is increased, there is an obvious, yet gradual, linear change in chemical shift of the resonance corresponding to the tetrahedral site, towards more positive values. For example, the resonance is centred at $\delta = -31.3$ ppm at 260 K and moves to $\delta = -17.2$ ppm at 412 K. This is in contrast to the trend expected with increasing temperature for a paramagnetic system.

Typically, as temperature is increased, Li chemical shift values move to lower (or more negative) values, thereby obeying Curie–Weiss behaviour.[35] As stated earlier, a Knight shift is observed for the tetrahedral site in the ^{7}Li MAS NMR spectrum obtained at room temperature. This indicates that the tetrahedral Li site is closer in the structure to the paramagnetic Ni^{2+} centre. In contrast, the resonance assigned to the octahedral $12d$ site exhibits a very small change in chemical shift, moving from $\delta = -1.1$ ppm to $\delta = -0.9$ ppm, with increasing temperature.

It is noted that, owing to the relatively low intensity and broad nature of the resonance, it is challenging to accurately determine the precise chemical shift observed. However, the resonance is not shifted to the same extent as that corresponding to the tetrahedral Li site. This suggests that the octahedral $12d$ site is positioned further away from the Ni^{2+} in the structure and therefore does not experience the same effect of the paramagnetic species, *i.e.*, no significant Knight shift. As temperature is increased and Li ions increasingly migrate from the tetrahedral site onto the octahedral site they move further and further away from the paramagnetic species. As a result, their chemical shift changes (becoming more positive). In $Li_2NiGe_3O_8$, the octahedral Li site is ~ 4 Å from the Ni centre, compared to a separation of ~ 3.2 Å between the tetrahedral site to the Ni centre. Similar VT ^{7}Li MAS NMR experiments were completed between 260 and 357 K and the same trend in chemical shift was observed, Fig. S5 in the ESI.† Hence, the VT ^{6}Li and ^{7}Li MAS NMR data are in good agreement.

To further investigate Li^+ ion mobility in $Li_2NiGe_3O_8$, additional static variable-temperature ^{6}Li NMR experiments were completed over a greater temperature range (204 to 609 K). It is noted that, due to hardware limitations, it is not possible to acquire ^{6}Li MAS NMR data over this temperature range. The VT static ^{6}Li NMR spectra obtained are shown in Fig. 4(b). Below room temperature, a single broad and relatively featureless lineshape is observed. As the temperature is increased, line narrowing is observed, indicative of Li^+ ion mobility within $Li_2NiGe_3O_8$, in good agreement with the VT ^{6}Li MAS NMR data.

The variation in ^{6}Li chemical shift and full width at half maximum (FWHM) with increasing temperature are shown in Fig. 5, where a linear change in chemical shift is observed and a gradual narrowing of the resonance is also observed, again indicative of Li ion motion. In contrast to the MAS NMR data, it was not possible to resolve distinct Li sites or the individual contributions from the $8c$ tetrahedral and $12d$ octahedral Li sites in the observed lineshape. In this instance, the ^{6}Li NMR data is only capable of identifying the presence of Li^+ ion mobility within $Li_2NiGe_3O_8$ and not the precise contribution of each site. To gain further insight into the ion mobility, ^{6}Li T_1 measurements were attempted for $Li_2NiGe_3O_8$ using a saturation recovery experiment. However, owing to the paramagnetic nature of the sample, the relaxation properties of the system were too fast and could not be accurately measured. Similarly, using the VT NMR data acquired, and analysis of the corresponding FWHM, attempts were made to obtain an activation energy for Li migration. Unfortunately, due to a combination of hardware limitations and the specific characteristics of the system under investigation, we were unable to acquire the full motional narrowing curve for $Li_2NiGe_3O_8$ (Fig. 5(b)). Hence, we were unable to obtain an activation energy.

3.3 Investigation of intra-grain diffusion by μSR

To explore Li^+ ion diffusion in greater depth, muon spectroscopy, μSR, was used. Positively charged muons, μ^+, have a lifetime of 2.197 μs and are 100% spin polarised. They can be implanted ~ 200 μm into a sample and are expected to reside

This journal is © the Owner Societies 2019

Phys. Chem. Chem. Phys., 2019, **21**, 23111–23118 | **23115**

200
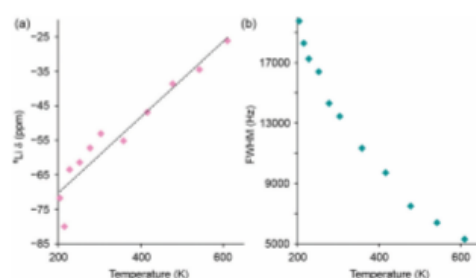
Fig. 5 Variation in (a) ^{6}Li chemical shift and (b) full width at half maximum (FWHM) with increasing temperature for the ^{6}Li static NMR data obtained for Li$_2$NiGe$_3$O$_8$. The corresponding spectra are shown in Fig. 4(b).

near oxygen sites.[36-39] The μ^+ spin can precess depending on the different magnetic fields it experiences, such as external applied fields, fields from nearby nuclei, or those from unpaired electrons in paramagnetic species. The diffusion of Li$^+$ ions leads the μ^+ to undergo a spin flip due to the inherent nuclear magnetic moment of lithium. When the μ^+ decays, the positron produced is most likely to be emitted in the direction of the μ^+ spin at decay. By recording the positrons emitted from opposite sides of the sample, the asymmetry of positrons can then be followed as a function of time and the evolution of the muon spin ensemble deduced.

Muon decay asymmetry data collected in longitudinal magnetic fields of 0, 5 and 10 G at various temperatures were fitted using WiMDA. For each temperature point, data from all three fields were fitted to a single model using Keren's analytic generalisation of the Abragam function, multiplied by an exponential relaxation term to account for the presence of paramagnetic Ni.[40] Example fitted data for Li$_2$NiGe$_3$O$_8$ at room temperature are shown in Fig. 6.

From the different fits, the calculated fluctuation rate, ν, and local magnetic field distribution, Δ, were extracted and their
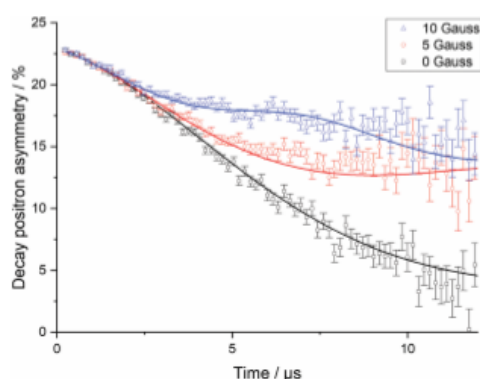
Fig. 6 Raw muon spectroscopy data for Li$_2$NiGe$_3$O$_8$, collected at 300 K in a zero field (squares), and applied longitudinal fields of 5 G (circles) and 10 G (triangles), with fits using the Keren function with a Lorentzian relaxation.
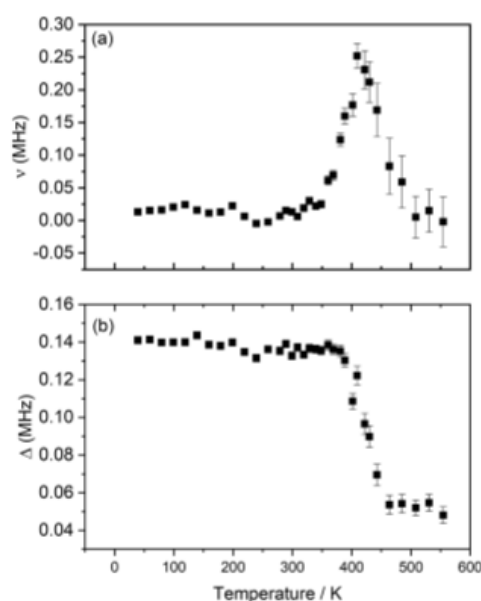
Fig. 7 Variation of ν (a) and Δ (b) with temperature obtained from the fitting of raw asymmetry data to the Keren function for Li$_2$NiGe$_3$O$_8$, measured from 40 K to 555 K.

variation with temperature is shown in Fig. 7(a) and (b). The fluctuation rate shows a plateau at lower temperatures, followed by an Arrhenius-like increase due to thermally activated diffusion of lithium ions above $\sim$300 K. This increase in fluctuation rate continues to 421 K; the subsequent decrease observed at higher temperatures is likely indicative of Li$^+$ ions hopping at rates too fast for μSR to capture.[36,37] The values obtained for Δ, Fig. 7(b), support this hypothesis; Δ is constant, within errors, at low temperatures, due to the slow rate of lithium hopping, but then shows a significant decrease from $\sim$380 K related to the effect of motional narrowing, where Li$^+$ ions are moving quickly and their nuclear spins differ from point to point within the sample. Above 442 K, lithium diffusion coefficients become too large for the muons to capture, and Δ values plateau again.

3.4 Elucidating diffusion mechanisms

The lithium ion diffusion coefficient for Li$_2$NiGe$_3$O$_8$ can be calculated using the equation:

$$D_{Li} = \sum_{i=1}^{n} \frac{1}{N_i} Z_{\nu,i} S_i^2 \nu$$

where N_i is the number of accessible Li sites in the ith path, $Z_{\nu,i}$ is the vacancy fraction of the destination sites in the ith path, S_i is the hopping distance between sites, and ν is the fluctuation rate at 300 K, and assumed to be related to Li$^+$ ions hopping between 8c and 12d crystallographic sites, as reported previously.[26,41]

201

Based on the findings obtained using μSR and solid-state NMR spectroscopy, additional analysis was conducted on the crystal structural refinements, using the ToF ND data previously reported by our group.[26] Therein, refinements conducted on room temperature data had indicated within standard statistical approaches that the 8c site was fully and solely occupied by Li; occupancy of the 12d migratory interstitial had only been noted where datasets had been collected at temperatures above ambient conditions. This does not preclude the possibility of very low concentrations of lithium hopping between the two sites at, or close to, ambient conditions – such results would merely be statistically indistinguishable from the fully ordered structure reported. This assumption is in good agreement with the [6,7]Li MAS NMR and μSR data presented (Fig. 3 and 7). Therefore, in order to calculate the true diffusion coefficient at 300 K, refined occupancies of both the 8c and 12d sites from $350 \leq T/^{\circ}\mathrm{C} \leq 850$ were linearly extrapolated (Fig. S6, ESI†) to give proposed fractional occupancies, or $Z_{v,i}$, of 0.97 and 0.03 for the 8c and 12d sites respectively at 300 K (Table S2, ESI†). This is in good agreement with the occupancies obtained from the ^{7}Li MAS NMR data (vide supra).

The hopping distance, S_i, in $Li_2NiGe_3O_8$ can be calculated by considering that an ion hopping between the 8c and 12d sites likely passes through three saddle points (SP) along the way, in the LiO_4 tetrahedral and LiO_6 octahedral faces, and an empty tetrahedral site. Once in the 12d site, Li^+ ions can hop to one of two neighbouring 8c sites (one of which is the original 8c site). A reasonable hopping distance of 2.95 Å can thus be calculated from the distances between the 8c-SP1-SP2-SP3-12d sites along this proposed conduction pathway (Fig. 8).

By following these assumptions, the calculated diffusion coefficient, D_{Li}, for $Li_2NiGe_3O_8$ at 300 K is found to be 3.89×10^{-12} cm^2 s^{-1} (Table S2, ESI†). This is in good agreement with the figure extracted from impedance spectroscopy data, and is similar to values reported for other spinel-type materials, e.g., $Li_4Ti_5O_{12}$ which has a diffusion coefficient, D_{Li} of between $3.2 \times$

Fig. 9 Arrhenius plot of the diffusion coefficient in the temperature range 340 K to 410 K for the complex spinel, $Li_2NiGe_3O_8$. The calculated activation energy from the slope is 0.43 ± 0.03 eV.

10^{-11} to 4.0×10^{-12} cm^2 s^{-1}, depending on the technique used and precise degree of lithiation.[42,43] By comparison, other solid electrolyte candidate materials based on the Li-stuffed garnet structure, e.g., $Li_{6.5}Al_{0.25}La_{2.92}Zr_2O_{12}$, with a faster ionic conductivity and shorter hopping distance (1.67 Å), has a Li^+ ion diffusion coefficient of 4.62×10^{-11} cm^2 s^{-1}.[39]

An activation energy of 0.43 ± 0.03 eV for lithium hopping in our powdered sample of $Li_2NiGe_3O_8$ was calculated from an Arrhenius plot of log D_{Li} over the thermally activated region (Fig. 9), in good agreement with the value obtained from EIS data on a pellet sintered for 6 h (0.46 ± 0.01 eV), but considerably lower than that observed after a 24 h sinter (0.53 ± 0.01 eV). This is further evidence that long dwell times at temperatures close to the melting point result in Li loss through volatilisation. As a result, additional studies aimed at identifying less extreme consolidation methods are currently underway. Length-scale dependent ion dynamics are well known in the literature with $LiFePO_4$ being a particular prominent example,[44] where the activation energy changes several-fold and the diffusion constant by several orders-of-magnitude. In $Li_2NiGe_3O_8$ the change in activation energy is far less pronounced.

4 Conclusions

Lithium-ion diffusion mechanisms in the complex spinel $Li_2NiGe_3O_8$ have been investigated using a range of complementary techniques. Building on previous reports of an 8c-12d-8c conduction pathway, using μSR and [6,7]Li solid-state NMR spectroscopy, we have shown that Li^+ ion hopping becomes thermally activated at ~300 K, resulting in partial occupancy of the migratory interstitial site at lower temperatures than previously reported. A lithium diffusion coefficient of 3.89×10^{-12} cm^2 s^{-1} at 300 K and an activation energy for lithium hopping of 0.43 ± 0.03 eV were determined using μSR on powdered samples. This energy is considerably lower than that observed for sintered pellets (0.46 ± 0.01 and 0.53 ± 0.01 eV,

Fig. 8 Portion of $Li_2NiGe_3O_8$ crystal structure showing the proposed 8c-SP1-SP2-SP3-12d conduction pathway. A Li_{12d}–O_6 octahedron is shown in orange and the two nearest Li_{8c}–O_4 tetrahedral are shown in red. A hopping distance of 2.95 Å can be calculated from a Li_{8c}-ion hopping between three possible saddle points (grey) into the neighbouring Li_{12d} site.

depending on the sintering conditions), suggesting that the investigation of an alternate consolidation route, avoiding Li volatilisation, may be worthwhile. This work also highlights the necessity of using multiple complementary techniques, such as impedance spectroscopy, solid-state NMR and μSR, as local probes in order to gain a more complete understanding of hopping mechanics in important ionic conductors.

Conflicts of interest

There are no conflicts to declare.

Acknowledgements

References

1 M. Armand and J.-M. Tarascon, *Nature*, 2008, **451**, 652–657.
2 J. B. Goodenough and K. Park, *J. Am. Chem. Soc.*, 2013, **135**, 1167–1176.
3 N. Nitta, F. Wu, J. T. Lee and G. Yushin, *Mater. Today*, 2015, **18**, 252–264.
4 P. G. Balakrishnan, R. Ramesh and T. P. Kumar, *J. Phys. Chem. Lett.*, 2006, **155**, 401–414.
5 J. B. Goodenough and Y. Kim, *Chem. Mater.*, 2010, **22**, 587–603.
6 Q. Li, J. Chen, L. Fan, X. Kong and Y. Lu, *Green Energy Environ.*, 2016, **1**, 18–42.
7 Samsung, 2016, http://www.samsung.com/us/note7recall/.
8 J. C. Bachman, S. Muy, A. Grimaud, H. Chang, N. Pour, S. F. Lux, O. Paschos, F. Maglia, S. Lupart, P. Lamp and L. Giordano, *Chem. Rev.*, 2016, **116**, 140–162.
9 N. Kamaya, K. Homma, Y. Yamakawa, M. Hirayama, R. Kanno, M. Yonemura, T. Kamiyama, Y. Kato, S. Hama and K. Kawamoto, *Nat. Mater.*, 2011, **10**, 682–686.
10 Y. Li, J.-T. Han, C.-A. Wang and J. B. Goodenough, *J. Mater. Chem.*, 2012, **3**, 15357–15361.
11 R. Kanno and M. Murayama, *J. Electrochem. Soc.*, 2001, **148**, 742–746.
12 A. C. Luntz, J. Voss and K. Reuter, *J. Phys. Chem. Lett.*, 2015, **6**, 4599–4604.
13 J. Kasemchainan, P. G. Bruce and J. Matthey, *Technol. Rev.*, 2018, **62**, 177–180.
14 V. Thangadurai, S. Narayanan and D. Pinzaru, *Chem. Rev.*, 2014, **43**, 4714–4727.
15 A. Orera and J. Campo, *Inorg. Chem.*, 2016, **55**, 1324–1332.
16 K. Hofstetter, A. J. Samson, S. Narayanan and V. Thangadurai, *J. Power Sources*, 2018, **390**, 297–312.
17 W. H. Bragg, *Philos. Mag.*, 1915, **30**, 305–315.
18 S. Nishikawa, *Proc. Math. Phys. Soc. Tokyo*, 1915, **8**, 199–209.
19 M. Nakayama, R. Jalem and T. Kasuga, *Solid State Ionics*, 2014, **262**, 74–76.
20 H. Kawai, M. Nagata, H. Tukamoto and A. R. West, *Electrochem. Solid-State Lett.*, 1998, **1**, 212–214.
21 A. Manthiram, K. Chemelewski and E. Lee, *Energy Environ. Sci.*, 2014, **7**, 1339–1350.
22 M. M. Thackeray, *J. Am. Ceram. Soc.*, 1999, **54**, 3347–3354.
23 B. M. Wagemaker, D. R. Simon, E. M. Kelder, J. Schoonman, C. Ringpfeil, U. Haake, D. Lützenkirchen-hecht, R. Frahm and F. M. Mulder, *Adv. Mater.*, 2006, **18**, 3169–3173.
24 T. Ohzuku, A. Ueda and N. Yamamota, *J. Electrochem. Soc.*, 1995, **142**, 1431–1435.
25 H. Kawai, M. Tabuchi, M. Nagata, H. Tukamoto and A. R. West, *J. Mater. Chem.*, 1998, **8**, 1273–1280.
26 N. Reeves-Mclaren, R. I. Smith and A. R. West, *Chem. Mater.*, 2011, **23**, 3556–3563.
27 B. H. Toby and R. B. Von Dreele, *J. Appl. Crystallogr.*, 2013, **46**, 544–549.
28 F. L. Pratt, *Phys. B*, 2000, **289–290**, 710–714.
29 J. T. S. Irvine, D. C. Sinclair and A. R. West, *Adv. Mater.*, 1990, **2**, 132–138.
30 M. M. Ahmad, *RSC Adv.*, 2015, 25824–25829.
31 K. MacKenzie and S. Mark, *Multinuclear Solid-State Nuclear Magnetic Resonance of Inorganic Materials (Pergamon Materials Series)*, Elsevier Science Ltd, 2002, pp. 629–639.
32 Z. Xu and J. F. Stebbins, *Solid State Nucl. Magn. Reson.*, 1995, **5**, 103–112.
33 Y. J. Lee, F. Wang and C. P. Grey, *J. Am. Chem. Soc.*, 1998, **120**, 12601–12613.
34 C. P. Grey and Y. J. Lee, *Solid State Sci.*, 2003, **5**, 883–894.
35 L. S. Cahill, R. P. Chapman, C. W. Kirby and G. R. Goward, *Appl. Magn. Reson.*, 2007, **32**, 565–581.
36 P. J. Baker, I. Franke, F. L. Pratt, T. Lancaster, D. Prabhakaran, W. Hayes and S. J. Blundell, *Phys. Rev. B: Condens. Matter Mater. Phys.*, 2011, **84**, 1–8.
37 M. Mansson and J. Sugiyama, *Phys. Scr.*, 2013, **88**, 1–13.
38 M. J. Ariza, D. J. Jones, J. Roziere, J. S. Lord and D. Ravot, *J. Phys. Chem. B*, 2003, **107**, 6003–6011.
39 M. Amores, T. E. Ashton, P. J. Baker, E. J. Cussen and S. A. Corr, *J. Mater. Chem. A*, 2016, **4**, 1729–1736.
40 A. Keren, *Phys. Rev. B: Condens. Matter Mater. Phys.*, 1994, **50**, 10039–10042.
41 R. J. Borg and G. J. Dienes, *An Introduction to Solid State Diffusion*, Academic, San Diego, CA, 1988.
42 J. Sugiyama, H. Nozaki, I. Umegaki, K. Mukai, K. Miwa, S. Shiraki, T. Hitosugi, A. Suter, T. Prokscha, Z. Salman, J. S. Lord and M. Martin, *Phys. Rev. B: Condens. Matter Mater. Phys.*, 2015, **92**, 1–9.
43 W. J. H. Borghols, M. Wagemaker, U. Lafont and E. M. Kelder, *J. Phys. Chem. B*, 2009, **12**, 17786–17792.
44 G. Krishna, P. Dathar, D. Sheppard, K. J. Stevenson and G. Henkelman, *Chem. Mater.*, 2011, 4032–4037.

23118 | *Phys. Chem. Chem. Phys.*, 2019, **21**, 23111–23118

This journal is © the Owner Societies 2019

203

8.2 References

[1]   H. Kawai, M. Tabuchi, M. Nagata, H. Tukamoto, and A. R. West, "Crystal chemistry and physical properties of complex lithium spinels $Li_2MM'_3O_8$ (M=Mg, Co, Ni, Zn; M'=Ti, Ge)," *J. Mater. Chem.*, vol. 8, no. 5, pp. 1273–1280, 1998.

[2]   N. Reeves-Mclaren, R. I. Smith, and A. R. West, "Lithium-ion conduction pathways in complex lithium spinels $Li_2MGe_3O_8$ (M = Ni or Zn)," *Chem. Mater.*, vol. 23, no. 15, pp. 3556–3563, 2011.